UNDERSTANDING QUANTUM PROCESSES IN SEMICONDUCTORS THROUGH THE USE OF SELECTIVE MULTIDIMENSIONAL SPECTROSCOPY

JONATHAN TOLLERUD

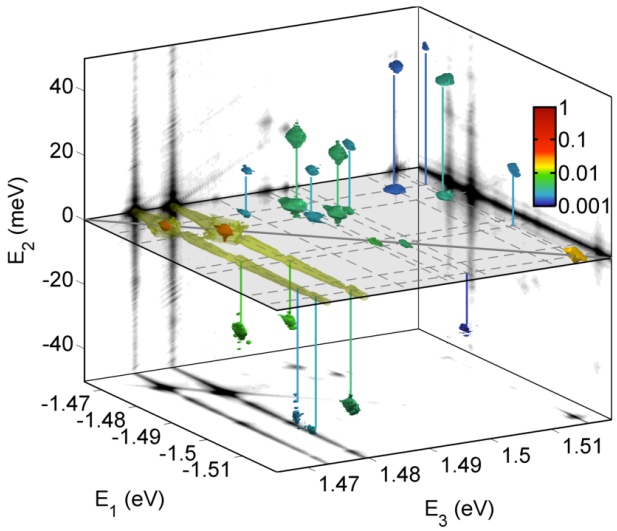

Doctor of Philosophy
Faculty of Science Engineering and Technology
Centre for Quantum and Optical Science
Swinburne University of Technology

December 2015

Jonathan Tollerud: *Understanding quantum processes in semiconductors through the use of selective multidimensional spectroscopy ,* Doctor of Philosophy, December 2015

ABSTRACT

The work presented in this thesis is motivated by two inter-related goals: to develop techniques capable of selectively measuring coherent interactions and to understand the coherent interactions in semiconductor double quantum wells.

Coherent multidimensional spectroscopy (CMDS) techniques are developed which can be used to selectively excite and then measure a variety of otherwise hidden quantum states in solid-state or molecular systems. A CMDS apparatus which utilizes a diffraction based pulse-shaper to control the inter-pulse delays is implemented. The pulse-shaper is also used to individually shape the amplitude of excitation spectra, allowing the possibility to selectively excite particular quantum pathways. The usefulness of the selective approach is demonstrated by observing and then quantifying inter-well coherent superpositions in an AlGaAs/GaAs double quantum well. Spectral shaping of the excitation beams is also used to isolate mixed two-exciton states in a selective two-quantum experiment, which is a complementary tool for studying coherent interactions between spectrally distinct states.

Spatially indirect 'dark' excitons are studied in a GaAs/InGaAs double quantum well. While these 'dark' excitons are difficult to study in a linear experiment, they can be easily detected in a coherent multidimensional spectroscopy experiment through their strong coupling to 'bright' exciton transitions. We also identify coherent superpositions of the 'dark' and 'bright' states. The strong coupling of these spatially indirect excitons to the bright quantum well and barrier excitons suggests that the 'dark' excitons play a role in the relaxation of excitons into the quantum wells.

The intrinsic stability of the CMDS apparatus enables us to study GaAs/InGaAs and AlGaAs/GaAs double quantum wells at extremely low excitation densities, several orders of magnitude lower than typical excitation densities used in CMDS measurements of excitons in quantum wells. Several striking changes to the 2D spectra are observed. Inter-well coherent superpositions of excitons are observed to be much more prevalent at low excitation density in GaAs/InGaAs and AlGaAs/GaAs samples. In a GaAs/InGaAs double quantum well, a narrowing of two-quantum linewidths reveals tilted peaks shapes, which to our knowledge have never been observed in two-quantum 2D spectra of quantum wells. Finally, what appears to be an extended 2D delocalized exciton state is observed in disordered AlGaAs/GaAs double quantum wells. Excitation density dependence suggests that this delocalized state is related to the enhanced inter-well coupling at low excitation densities.

It is worthwhile for anyone to have behind him
a few generations of honest, hard-working ancestry.

— John Phillips Marquand

Dedicated to my family. . .

. . . and to the loving memory of Manley Owen Tollerud.
1921 – 2014

ACKNOWLEDGMENTS

There are many people who have made the four years of my PhD at Swinburne enjoyable, fulfilling, and memorable.

I would first and foremost like to thank my PhD supervisor, Jeff Davis, for providing me the opportunity to pursue a PhD at Swinburne, but more importantly for his continual support guidance, enthusiasm and generosity with time (especially over the last few months). I have learned an extraordinary amount from him, and will be a far better physicist as a result of his supervision. His generosity and implicit confidence in my abilities in deciding to send me to several overseas conferences is also greatly appreciated.

I am also extremely grateful for the scholarship funding provided to me by Swinburne University, which made this entire journey possible.

I would like to thank Chennupati Jagadish and Hoe Tan from Australian National University for supplying the AlGaAs/GaAs samples that were studied in this thesis. I am also indebted to Steve Cundiff, Gaël Nardin, and François Morier-Genoud for several very fruitful discussions, and for providing the GaAs/InGaAs samples that were studied in this thesis.

I would never have been able to put together the CMDS experiment without the continual help of Chris and Gethin over the first couple years. Their constant willingness to lend a hand (no matter how late in the day), understanding of the nuances of the experimental equipment, and intrinsic ability to get things working got me through some of the toughest parts of the early experimental development. Beyond this, their friendship from the start made me feel welcome from the first day I arrived in Australia. To Professor Lap van Dao, Fabio, Michael, Naylyn, Ashkan, Pavel, Huang, Khuong, Evelyn and everyone else who worked in the Ultrafast lab, I have greatly appreciated the always friendly and supportive working environment.

I am very grateful to the many friends I have made at Swinburne: Marcus, Alex, Kristian, Ashkan, Gethin, Chris, Emma, Will, Rodney, Mirren, Nick, Evelyn (and many more). The tea-time and lunch-time conversations were usually memorable, and always entertaining-whether they strayed towards the profound, the hilarious or the absurd. When is the next barbecue in Rocket Park?

To my parents, Barb and Ed, who instilled in me a love of science from a young age and who have always supported me and given me invaluable guidance. Thank you for the encouragement and love and for backing my crazy decision to move to Australia.

Finally, I feel a sense of immeasurable gratitude for my soon-to-be wife Kathryn. Getting to know you and growing ever closer has been a highlight of the last four years. I thank you for your constant support, encouragement and understanding (especially over the final few months), for our walks, for showing me Australia, for the laughter, for the Love, for switching me out of 'Matlab-mode', for your never-ending excitement and interest in my work, for being an inspiration. I love you and I cannot wait for our next adventure together.

DECLARATION

I, Jonathan Owen Tollerud, declare that this thesis entitled:

"Understanding quantum processes in semiconductors through the use of selective multidimensional spectroscopy "

contains no work that has been accepted for any other academic award. All the work presented is primarily the work of the author.

I warrant that I have obtained, where necessary, permission from the copyright owners to use any third party copyright material reproduced in the thesis (such as artwork, images, unpublished documents), or to use any of my own published work (such as journal articles) in which the copyright is held by another party (such as publisher, co-author).

Jonathan Tollerud
Centre for Quantum and Optical Science
Faculty of Science Engineering and Technology
Swinburne University of Technology
Melbourne, Australia
December 2015

CONTENTS

LIST OF FIGURES

LIST OF TABLES

ACRONYMS

0Q 0-quantum
1Q 1-quantum
2Q 2-quantum
2LS Two-level system
4LS Four-level system
6LS Six-level system
AOM Acousto-optic modulator
BB Broadband
CCD Charge-coupled device
CF Carrier frequency
CMDS Coherent multidimensional spectroscopy
CP Cross-peak
CS Coherence specific
CS-CP Coherent superposition cross-peak
CW Continuous-wave
DP Diagonal-peak
DQW Double quantum well
EID Excitation induced decoherence
EIS Excitation induced shift
EHP Electron-hole pair
ESA Excited state absorption
fs femtosecond
FFT Fast Fourier transform
FPD Free-polarization decay
FWHM Full width at half max
FWM Four-wave mixing
HH Heavy-hole
GS Ground state
GSB Ground state bleach
LFE Local field effects
LH Light-hole
LHC light harvesting complex
MBE Molecular beam epitaxy
MOCVD Metal-organic chemical vapour deposition
MQW Multi-quantum well
NIR Near-infrared
NMR Nuclear magnetic resonance
NW Narrow well
OPA Optical parametric amplifier
PE Photon echo
PL Photoluminescence
PLE Photoluminescence excitation spectroscopy
ps picosecond
QCL Quantum cascade laser
RMSE Root mean square error
SLM Spatial light modulator
SNR Signal-to-noise
TISE Time-independent Schrödinger equation
Ti:Sapph Titanium-sapphire
TG Transient grating
THz Terahertz
QB Quantum beat
QD Quantum dot
QW Quantum well
WW Wide well

1

INTRODUCTION

Physical phenomena are typically split into two regimes: the classical and the quantum. At the quantum level, the world is governed by the Schrödinger equation, and outcomes are probabilistic. While in principle *everything* can be described by the Schrödinger equation, the deterministic rules of classical physics are typically more convenient for explaining the macroscopic world. There are, however, many examples of macroscopic effects that can only be adequately explained using quantum mechanics [1]: superfluidity, superconductivity, the phenomena of stimulated emission (without which there would be no lasers), the transistors that enable modern computers, the emission spectra of stars, and the structure of DNA (to name just a few). One of the fundamental tenets of quantum mechanics is that particles can be described by a wavefunction. Coherent superposition of particle is a 'smoking gun' proving that wavefunctions are necessary to describe a particle, and is therefore is an entirely non-classical effect. It is also important in a number of different macroscopic contexts, ranging from the fundamental [1] to the applied [2–5]. Fundamentally, coherent superpositions are an interesting tool for understanding how the quantum world transitions into the classical world through decoherence [1]. Coherent superpositions also play a role in many applied contexts including the operation of devices such as quantum cascade lasers [2] and quantum tunnelling diodes [3]. Coherent superposition is the integral concept that differentiates classical and quantum computing, and is also what allows the potential performance gains that quantum computing has been accorded so much attention [4].

While it is relatively straightforward to understand how particles that are spatially overlapped can form coherent superpositions, the formation of coherent superpositions between particles that are *spatially separated* presents additional challenges, and requires detailed understanding of the mechanisms governing the interactions. Understanding these mechanisms could also open the door to a great many applications. The study of such **coherent superpositions** of **spatially separated states** will be central theme of the work in this thesis.

An example of a system in which coherent superpositions of spatially separated particles may be studied is the double quantum well (DQW), which is shown in Fig. 1.1. A semiconductor quantum well (QW) is a material with a 2D region that confines charged particles in one direction, and thereby forces the particle to take on

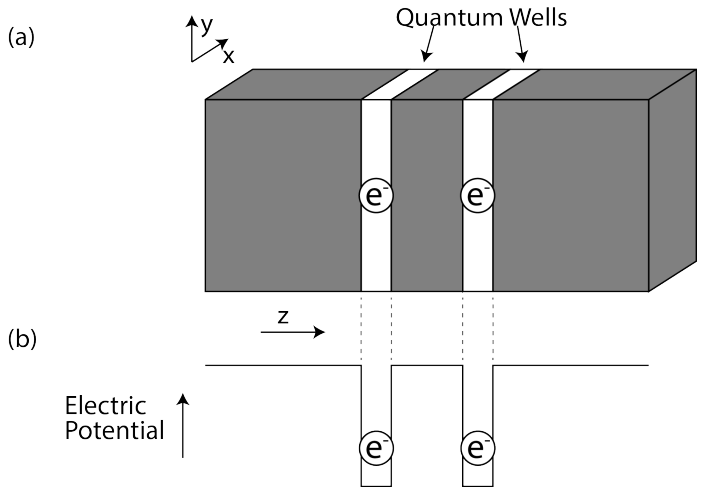

Figure 1.1: A cartoon of a double quantum well (DQW). The layered DQW structure (a), is made up of two layers of one type of material (white color) sandwiched between layers of a different material (grey). (b) The electrons are confined in potential wells as a function of the z-direction created by the sandwich structure.

intrinsically quantum mechanical traits (quantized states, for example). QWs are an important concept in quantum mechanics, and are particularly interesting because they can be easily and precisely built with modern growth techniques. In fact, QW based lasers have become very widespread, and are commonly used in computer mice and in optical telecommunication. DQWs are also very useful in fundamental studies because we can control the shape of the potential very precisely.

A natural system where spatially separated coherent superpositions may play a role is in photosynthesis, where coherent superposition may be involved in the transfer of energy from the chromophores that absorb the sunlight to the reaction center which initiates all the biochemical reactions [5–8]. Several experiments have observed evidence of coherent superpositions in a variety of different light harvesting complexes (LHCs) [6–9] and within the reaction center [10, 11]. In part due to experimental limitations, the role of these coherent superpositions (and in some cases even the identification of the states involved) is still controversial and research in this area is evolving rapidly. One of the goals of the work in this field is understanding if and how coherent superpositions are involved in the fast and efficient transfer of energy from the chromophores to the reaction center. Efficient extraction of energy from light absorbers also happens to be one of the bottlenecks in some man made photovoltaic devices [12], so an understanding of how energy is transferred in natural light harvesters could be advantageous in the design of future devices.

To achieve a detailed understanding of coherent superpositions of spatially separated states, we first need methods to excite and then measure them. To do this we exploit the coherence of femtosecond (fs, 10^{-15} s) pulses generated by an ultrafast laser: a pulse of light incident upon the sample generates a large number of coherent superpositions, which we can then 'check' on later. These coherent super-

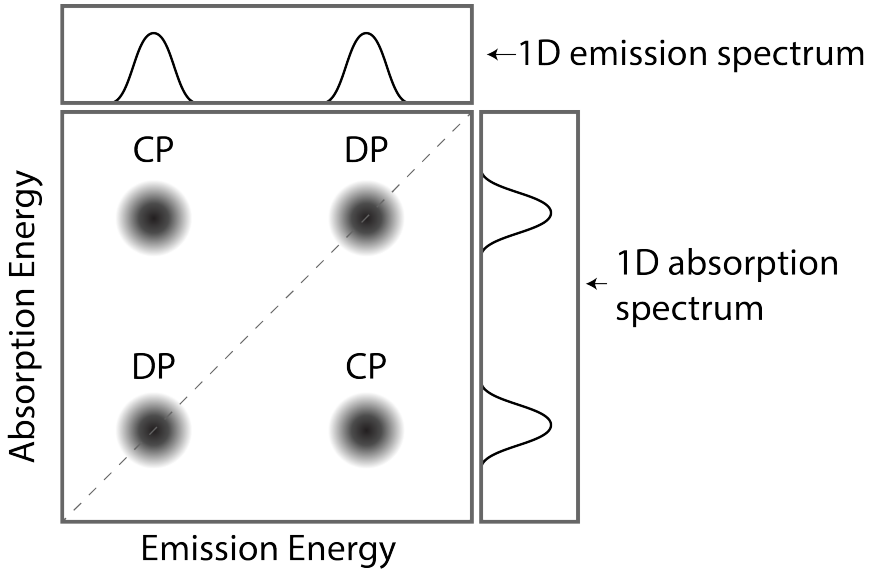

Figure 1.2: A cartoon 2D spectrum for a system with two coupled transitions. Interactions between two transitions can be observed as cross-peaks (CPs). The diagonal-peaks (DPs) indicate signals involving only one of the transitions. Linear absorption and emission measurements cannot be used to separate the interactions between the two transitions from the signals involving only one transition.

positions then evolve according to the Schrödinger equation and eventually become incoherent as they interact with their environment, so the longer we wait before we 'check' on the superpositions, the less signal we observe. This process is often called dephasing or decoherence. In order to observe these coherent superpositions, our measurement needs to be faster than the dephasing/decoherence processes, which (in many electronic systems), happens on the ultrafast time-scale: fs to picoseconds (ps, 10^{-12} s).

In a system with multiple states that are all interacting there can be many signals that look the same in linear spectroscopy. We therefore also need a way to separate out the signal we are interested in observing. One way to separate out the interactions is by expanding the information onto two frequency directions using 2D spectroscopy. In the most common type of 2D spectroscopy, one axis represents the absorption energy and the other represents the emission energy (as shown in Fig. 1.2). As a result, signals in which absorption and emission occur in the same state appear along the diagonal (often called diagonal-peaks or DPs), while signals involving absorption and emission from different states appear away from the diagonal (often called cross-peaks or CPs). This separation of signals is the main power of 2D spectroscopy - peaks which would be overlapped on either an absorption or emission spectrum can now be separated and interactions can be clearly identified. Multiple experimental techniques can be used to generate 2D spectra. However, to directly observe coherent superpositions we must use a *coherent* 2D spectroscopy technique. Further separation of signals can also be realized by expanding the data into additional frequency axes. The generalized set of multidimensional techniques are therefore given the name **coherent multidimensional spectroscopy (CMDS)**.

CMDS has been conducted across a wide range of excitation wavelengths to study coherent phenomena in different types of transitions: nuclear spin transitions at radio wavelengths [13–15], vibrational transitions at infrared wavelengths [16] and (most recently) electronic transitions at near-infrared and visible wavelengths [17, 18]. Multidimensional techniques were first developed at radio frequencies to study nuclear spin interactions, where they have proven to be incredibly powerful. Multidimensional NMR has resulted in two Nobel prizes [14, 15], and plays an integral role in determining the structure of complex molecules (including proteins). The success of multidimensional NMR comes from the many variations of CMDS that have been developed since its inception 60 years ago. CMDS at optical wavelengths introduces new experimental challenges, and was only first realized in the late 1990's and 2000's [19, 20]. As a result, many of these CMDS techniques and variations have not yet been developed at visible/near-infrared wavelengths.

Still, CMDS of electronic transitions[1] satisfies some pre-requisites for studying coherent superpositions of spatially separated systems: it is a coherent technique which can be conducted with fs resolution, and many signals can be separated. There are, however, still some challenges. For example, some of the different signals excited in the experiment can still overlap the coherent superpositions signal and therefore introduce ambiguity into interpretation of the experimental results. Even if they don't directly overlap the coherent superposition signal, other signals can result in congested spectra and hence obscure the coherent superposition signals. To overcome these challenges, we can emulate some of the techniques which have been developed in multidimensional NMR. Of the varied tools in the NMR arsenal, one of the most useful is the ability to use pulse sequences which isolate signals due to interaction between different states (i.e. those signals that produce CPs) from those that are due to a single state (i.e. those that produce DPs). This can be thought of as a 'selective' experiment in that we are selectively exciting particular signals. While there are several ways to achieve this selection experimentally, one of the most common is through controlling which transitions are excited by each subsequent pulse. While some information is lost (we are not collecting all the signals), the information that we do collect can be more informative. The philosophy behind selective and non-selective experiments can thus be summarized in the following way. We can either set out to:

- Perform a simple experiment which results in a wide variety of data, but which may not be easily interpreted (the non-selective approach).
- Perform a somewhat more complicated experiment which results in less data, but which is more easily interpreted (the selective approach).

Both approaches can be useful depending on what is known about the sample *a priori* and what information we want to obtain with the experiment. The flexibility

1 Which we will refer to simply as CMDS from here on out.

of modern NMR spectrometers allows both selective and non-selective experiments to be conducted on the same sample consecutively. An advantageous approach is, therefore, to start with a simple non-selective experiment to get a 'birds-eye-view' of the sample, followed by sets of increasingly specific, selective experiments [21].

The study of spatially separated coherent superpositions of excitons[2] can also benefit from the selective approach. By using a slightly more complicated experiment, we can probe only the coherent superpositions of spatially separated states, and thereby simplify the data analysis and unambiguously identify the source of the signals. Furthermore, the experimental apparatus that we have implemented is also capable of some of the same flexibility of the NMR spectrometers described above, in that we can perform the non-selective experiment and selective experiments using the same apparatus with no changes to the optical setup. The details of the series of selective and non-selective experiments can then be tailored to the needs of the sample and the information of interest, mirroring the flexibility of an NMR spectrometer.

The work in this thesis describes the development, demonstration and utilization of such techniques to selectively study interactions between distinct states. The results in this thesis can thus be divided into two general categories:

1. Development and demonstration of selective techniques.

2. Utilization of those techniques to open up new avenues of investigation into the coherent response of excitons in DQWs.

The first part of this thesis we will show how such an experiment is implemented using a pulse-shaper based CMDS experiment. Spectral amplitude shaping of the pulses allows us to generate pulse sequences which can be used to isolate single quantum pathways. Although this can in principle be used to isolate a wide variety of signals, we use it in this thesis to study excited state coherent superpositions of spatially separated excitons. The development of this novel technique is included predominately in Ch. 2, Ch. 4 and Ch. 5. In Ch. 2, the experimental implementation of pathway selection is described. In Ch. 4 pathway selection in the 1-quantum and 0-quantum multidimensional spectra[3] is demonstrated, and isolated coherent superposition signals are observed. In Ch. 5, pathway selection in the 2-quantum 2D spectra[4] is demonstrated and then used to isolate signals from spatially separated mixed two-exciton states.

To demonstrate how useful the selective technique can be, we study coherent superpositions in DQWs. As was noted previously, DQWs are a very convenient template system for exploring coherent effects because they can be very precisely grown using modern growth techniques. Excitons in QWs have spectrally narrow

2 An exciton is a quasi-particle made up of an electron and a hole.

3 1-quantum, 0-quantum and 2-quantum are three common types of CMDS spectroscopy techniques currently used to study electronic transitions, which will be described in detail in Ch. 2.

4 See 3.

resonances which can be easily separated and identified. Though the results cannot be directly extrapolated to biological light harvesting complexes, our results suggest that this selective technique could be useful there as well.

The initial goal of this project was the establishment of the experimental apparatus and demonstration of the selective technique. Using this suite of techniques, we have also been able to observe some very interesting phenomena and explore new areas of the coherent physics of excitons in semiconductor QWs along the way. In Ch. 4, we show that inter-well coherent superpositions can be observed using pathway selection in two separate DQW samples. We observe inter-well coherent superpositions even when the barrier is wide enough that the QWs can be considered as non-overlapping quantum systems. We also show that the shape of the inter-well coherent superposition CPs provides a great deal of information about the nature of the broadening of the coupled transitions, and that the peak-shape of inter-well CPs is very different from shape of the intra-well CPs. In Ch. 6 we to investigate spatially indirect 'dark' states which are strongly coupled to 'bright' QW states by exploiting the power of CMDS to detect coherent superpositions. In Ch. 7 we exploit the intrinsic stability and sensitivity of the CMDS apparatus to investigate how coherent dynamics change in the extremely low excitation density regime which has remained mostly unexplored. Our observations at low density are strikingly different from those at high density.

Collectively, these studies explore coherent interactions between quantum systems that are separated to different extents: In Ch. 4 and Ch. 7 we explore inter-well coherent superpositions. In Ch. 5 signals are isolated that involve a state made of one exciton in the QW and one in the barrier. In Ch. 6 we explore coherent superpositions involving carriers in different layers of the DQW. Finally, in Ch. 7 we study coherent interactions of excitons separated by large distances in the plane of a single QW. So, we have been able to learn about coherent superpositions in several different contexts, each of which reveal different physics and contribute to the overall understanding of coherent interactions between spatially separated particles. Furthermore, the continued development and use of the techniques developed here should allow us to better understand how the fundamentally quantum mechanical phenomenon of coherent superposition of spatially separated states contributes to macroscopic effects in a range of systems from semiconductor DQWs to photosynthetic light harvesting complexes.

2

EXPERIMENTAL METHODS

A quantum mechanical coherent superposition is a coherent phenomenon, which must be separated from incoherent signals to be clearly observed. To explain what is meant by the distinction between coherent and incoherent phenomena, consider Fig. 2.1, which depicts a sample excited by a coherent light source (e.g. a laser). The light is absorbed by the sample and then re-emitted as an optical signal after undergoing some sort of evolution in the sample. If the evolution within the sample is entirely coherent, then the re-emitted radiation will have a well-defined phase (ϕ) relative to the electric field that initiated the evolution in the sample. This means that ϕ should always be the same. If, on the other hand, the there is some random phase jump due to interactions in the sample, then the emitted radiation will no longer have a well-defined phase relative to the input waveform and is considered to be incoherent. Coherent processes are therefore processes for which ϕ is constant, while incoherent processes are those for which ϕ varies randomly.

Incoherent and coherent processes could therefore be separated by simply comparing the time evolution of the emitted electric field with the time evolution of the electric field of the light source to identify any well-defined phase difference. Unfortunately, this is impossible in the visible/near-infrared (NIR) region of the electromagnetic spectrum because no instrument exists that is fast enough to directly measure the oscillations of the electric field in real time. We can, however, use interferometric techniques to measure the emitted electric field in the frequency

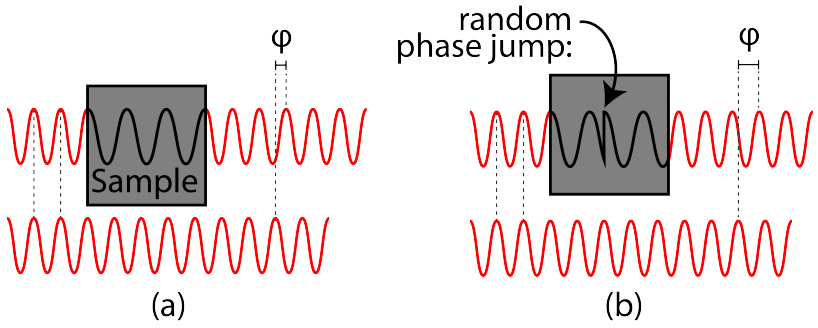

Figure 2.1: Coherent phenomena produce an output that has a constant phase relative to the coherent excitation. Incoherent phenomena involve some random phase jumps which randomly change the relative phase.

domain[1], from which the time evolution of the electric field can be extracted using a Fourier transform. This type of signal detection, (also called heterodyne detection) involve recording a spectral interferogram between the emitted electric field and a reference electric field which is phase-locked[2] to the excitation electric field. Interferometric detection intrinsically isolates the emission from coherent processes because emission from incoherent processes average out over the course of a measurement. However, interferometric detection alone is not particularly useful for measuring dynamics or for separating out the many coherent signals that can be produced.

Heterodyne detection of visible/NIR in ultrafast experiments is a relatively recent development [22–24]. Long before it was devised, other methods of measuring coherent phenomena were developed, which do not require the use of interferometric detection. These techniques use transient non-linear spectroscopy with multiple pulses, which can be designed so that emission of a signal is only possible when the interactions in the sample are coherent. The delays between some of the pulses can then be scanned to change the amount of time the coherent excitation evolves in the sample before subsequent pulses arrive to provide the additional photons required to produce the nonlinear signal. As a result, slow detectors can be used along with relatively simple tools to control the inter-pulse delays (such as translation stages) to measure coherent dynamics [25]. The key to the success of these measurements is that they can observe coherent dynamics *without* directly measuring the electric field.

To resolve the coherent dynamics, the laser pulses used in the experiment must be much shorter in time than the dynamics of interest. In many condensed matter systems this means they must be on the picosecond (ps) or femtosecond (fs) time scale. The development of the mode-locked dye laser in the 1970's [26] produced pulses well down into the ps regime. The arrival of Kerr-lens mode-locked titanium-sapphire lasers in the early 1990's pushed the pulses down in the 10's of fs [27]. More recently titanium-sapphire oscillators have been optimized to produces pulses as short as just a few fs [28], and with additional spectral broadening and pulse compression (and considerable effort), sub-1 fs pulses have been demonstrated in the visible [29]. These ultrafast laser technologies, (particularly development the titanium-sapphire laser) have enabled the development of many different non-linear techniques for measuring coherent (as well as incoherent) dynamics.

A good example of such a technique is transient four-wave mixing (FWM) spectroscopy, which uses two or three pulses to generate a third order non-linear signal. Coherent dynamics can then be measured by scanning the delay between arrival time of the first and second pulse to measure coherent dynamics. This technique has proven to be very useful for studying coherent effects in QWs [30–33] and many other systems [34–38]. Several variants of FWM also have also emerged to

1 There are also interferometric techniques that operate in the time domain.
2 which is to say, the two electric fields have a constant relative phase.

study different transient phenomena (both coherent and incoherent). Some of these techniques are transient grating spectroscopy [39], femtosecond stimulated Raman spectroscopy [40], femtosecond coherent anti-Stokes Raman spectroscopy [41], and pump-probe spectroscopy [42].

Coherent multidimensional spectroscopy (CMDS), combines non-linear multi-pulse spectroscopy with interferometric detection to correlate the evolution of the emitted signal as a function of both the 'real' time (i.e. the time evolution of the electric field of the emitted signal) with the evolution during one or more inter-pulse delays. This is a powerful extension of non-interferometric non-linear spectroscopy techniques, in that it allows us to more clearly separate the many coherent signals that can be produced. In particular, it allows us to clearly identify coherent interactions between different states.

To experimentally realize CMDS, the relative phase of the excitation pulses must remain constant to a precision well below the period of an optical cycle. To understand why, we must consider that the phase of the emitted signal in a multi-pulse nonlinear experiment depends on the phase of all of the input fields. As a result, if the phase any of the excitation fields shifts randomly relative to all the other excitation fields, then so too will the phase of the emitted signal. This randomly fluctuating signal phase causes the phase of the interference pattern to randomly fluctuate over the course of the measurement. The interferogram will average out and no interference between the signal and the reference will be observed. This stability requirement is the main experimental challenge in CMDS, which we will discuss in more detail in Section 2.2.

The rest of this chapter aims to give a brief overview of FWM and CMDS, and then describe the techniques and apparatus established at Swinburne as a part of this PhD project.

2.1 Four-wave mixing

While in principle, CMDS can be applied to many different non-linear spectroscopic techniques, most common implementation so far have been based on FWM. The goal of this section, therefore, is to describe the fundamental concepts of FWM which are necessary for understanding the CMDS.

FWM is the name given to a range of non-linear processes that involve the interaction of three different light fields (in this case fs pulses[3]) with a material through its third order susceptibility ($\chi^{(3)}$) to generate a signal (which is the fourth wave). Assuming that each pulse interacts only once (which is not always the case) the frequency of resulting FWM signal is a linear combination of the frequency of the three different light fields (i.e. $\nu_{FWM} = \pm\nu_1 \pm \nu_2 \pm \nu_3$). If the three light fields

3 FWM can be conducted with either CW or pulsed excitation, but since the purpose of this thesis is understanding ultrafast phenomena, the discussion will be limited to FWM with fs pulses. This form of FWM mixing is often referred to as transient Four wave mixing (TFWM), but for simplicity the 'T' will be dropped for this thesis.

all have the same frequency ($\nu = \nu_1 = \nu_2 = \nu_3$), the signal will be generated at the same frequency.[4] FWM is a phase sensitive process, so macroscopic generation of signal requires that phase-matching conditions be met (or equivalently, must obey momentum conservation). For the FWM signal to conserve momentum, the signal must be emitted with the wave vector: $k_{FWM} = \pm k_1 \pm k_2 \pm k_3$. Thus, if a non-collinear geometry is used, many of the possible FWM signals are emitted in directions spatially separated from the excitation beams. In this way, the FWM signals can can be detected mostly free of background contributions (such as lower order signals and scattered light from excitation beams), which will not have the same well defined directionality [43].

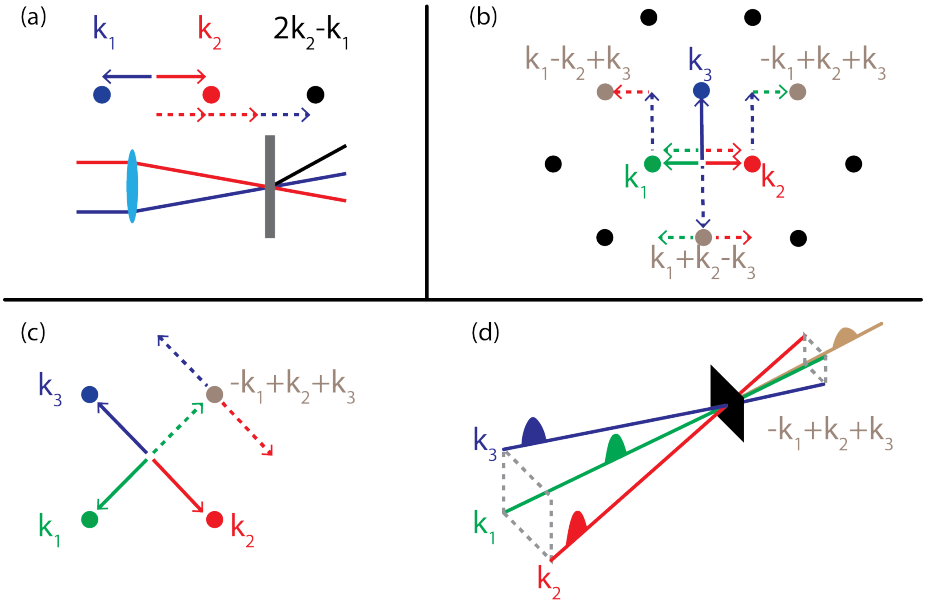

Figure 2.2: Typical beam geometries used in FWM experiments. Colors are used to identify beams, not to indicate spectral content. (a) two beam FWM in which one pulse supplies two photons, and the other supplies one for each FWM photon generated. (b) Equilateral triangle beam geometry for a three pulse FWM experiment. Each pulse supplies a single photon for each signal photon generated. The three pulse FWM signal directions are shown in grey. The two pulse signal directions are also shown in black (but not labeled). (c) 2D and (d) 3D depictions of the box geometry that is used in most CMDS experiments - only the FWM signal that makes up the final corner of the box is shown, since usually this is the only one collected when box geometry is used.

This spatial discrimination is utilized in two-beam FWM (shown in Fig. 2.2a). In this configuration, two beams with wave vectors k_1 and k_2 are incident upon the sample. FWM is a $\chi^{(3)}$ process, which requires three photons, so in this two beam configuration, one beam supplies one photon and the other supplies two. FWM is a $\chi^{(3)}$ process which requires three photons. In this two beam configuration, one beam supplies one photon and the other supplies two. In this case, the k_2 pulse supplies two photons, and a FWM signal with $\nu_{FWM} = 2\nu_2 - \nu_1$ is generated in the $k_{FWM} = 2k_2 - k_1$ direction, which is well separated from each of the excitation

4 ν_{FWM} can also be generated at 3ν, but this is usually referred to as third harmonic generation rather than FWM.

beams [43]. If this technique is extended to include three beams instead of two, all of the possible FWM signals that involve all three pulses are separated from the excitation beams. Typically, either a box or triangle geometry is used, which generates a signal pattern like the one shown in Fig. 2.2b,c. Box beam geometry is especially useful, as the FWM process simultaneously conserves energy as well as momentum, which enhances the FWM efficiency compared with other geometries [43]. The three pulse box geometry is typically used in CMDS experiments, so the rest of this discussion will concern that particular implementation of FWM.

FWM is typically conducted resonantly, meaning that the pulse excitation spectra overlap one or more transitions in the sample being studied. If multiple transitions are excited, FWM signals can be spectrally resolved so that the dynamics of different transitions can be separated. The temporal evolution of the FWM signal (the 'real-time' dynamics) will depend on both the amount of broadening and the nature of the broadening of the transition(s) which are resonant with the pulse spectrum. The FWM signal can be time resolved to measure these real-time dynamics or measured with a slow detector (often called time-integrated). Time-resolved detection of FWM signals is accomplished by either cross-correlating the FWM signal with a reference pulse [44–46], or through spectral interferometry [22–24]. If the temporal dynamics of the signal are not of interest, it can be measured using a time-integrating detector such as a CCD or a photodiode. Regardless of the detection method, a variety of dynamical information can be gleaned by scanning the time delays between the excitation pulses while monitoring the intensity, spectral content and/or (in the case of time-resolved FWM) temporal evolution of the signal.

The light-matter interactions in a FWM experiment for a two-level system (2LS) can be described as follows: The first pulse generates a coherent superposition of the ground and excited state (also called a 'coherence' for simplicity). The phase of this coherence oscillates as a function of time with a starting phase set by the excitation pulse. After a time t_1 (also called the 'coherence time') the second pulse interacts with this coherence to generate a population, either in the ground state or excited state. The third pulse returns the system to a coherence which then emits in the signal direction.[5]

FWM experiments typically must excite on the order of 10^9 carriers per pulse to generate a measurable signal [46], so FWM is fundamentally an ensemble measurement. Because the pulses have a single well-defined phase, all of the coherences generated by the first pulse have the same initial phase. This ensemble of in-phase coherences oscillate together and form a macroscopic polarization. The FWM signal is proportional to the number of coherences within the ensemble, as well as the phase-coherence across the ensemble. Thus, the phase initially set by the laser must be maintained to generate a FWM signal. During the first time period, individual

5 In many FWM experiments, τ is used for the coherence time instead of t_1, T is used for the waiting time instead of t_2. In this thesis t_1 and t_2 are used to be consistent with the labelling that is often used in CMDS.

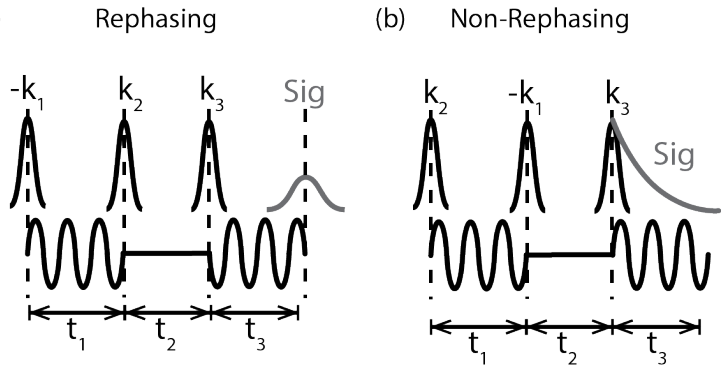

Figure 2.3: Two typical FWM orderings.(a) Rephasing show a reversal of the phase oscillations in t_1 and t_3, and generate a photon echo at $t_3 = t_1$. (b) Non-rephasing pulse ordering has no phase reversal, so the signal is a free-induction decay instead of a photon echo.

scattering events occur which randomly change the phase of the coherences within the ensemble. Aggregated across the ensemble, these random phase changes manifest as a reduction in the phase-purity of the macroscopic polarization and subsequently the FWM signal amplitude. As t_1 is increased, more scattering events occur, thereby reducing the overall signal strength. Once t_1 is large enough, the phase of coherences within ensemble are evenly distributed across all 2π possible phase values, and no signal will be generated. For a homogeneously broadened transition, the decay of the FWM signal as a function of t_1 can be used to measure the decoherence time of the transition. The relationship between the decoherence time (T_2) and the homogeneous linewidth (Γ_H) is given by Eq. 2.1 [46][6].

$$T_2 = 2\hbar/\Gamma_H \tag{2.1}$$

However, many real ensembles involve some amount of inhomogeneous broadening which leads to more rapid dephasing of the macroscopic polarization as a function of t_1. This additional dephasing is due to the broad range of oscillation frequencies which fall out of phase with a decay constant inversely proportional to the inhomogeneous linewidth (Γ_{IH}), thus leading to a reduction of the macroscopic polarization. Dephasing due to to inhomogeneity is completely distinct to the decoherence discussed above, and occurs even in the absence of the interactions that lead to the homogeneous linewidth. Unlike the pure decoherence, which involves random changes to the phases in the ensemble, the dephasing due to inhomogeneity is an ordered process. The individual phases of the emitters do not change randomly, but the differences in frequency gradually push the different spectral components out of phase as t_1 increases. The phase of the original pulse is still embedded in the individual coherences, even though no macroscopic polarization remains. This ordered process can be reversed with what is called the photon echo effect [34, 47].

6 T_2 depends on the excited state lifetime (T_1) and the pure dephasing time (T_2^*). This will be discussed in the following chapter.

The photon echo effect occurs only in the rephasing pulse ordering (Fig. 2.3a). After the different inhomogeneous spectral components of the signal have fallen out of phase, the second pulse arrives and puts all of the different components of the inhomogeneous ensemble into populations, over which time there is no phase evolution. The interaction with the third pulse (k_3) has the opposite sign from the first interaction ($-k_1$)[7], so the coherence that it induces has a phase evolution in t_3 which is opposite (in sign) the phase evolution in t_1. The dephasing due to inhomogeneity that 'winds up' during t_1 therefore 'un-winds' during t_3, and the phase of all the inhomogeneous spectral components eventually come back into phase at $t_3=t_1$. With all the inhomogeneous components back in phase, a macroscopic polarization is again present, which then generates a FWM signal. A hallmark of the inhomogeneous broadening is therefore a FWM signal which does not appear immediately after the third pulse, but instead centred at $t_3=t_1$. This delayed signal emission is what leads to the name 'photon echo'.

The decoherence due to scattering processes are not reversed, so when a photon echo is present, the decay of the time integrated signal as a function of t_1 is again a measure of the decoherence time and therefore Γ_H. The intensity of the photon echo is proportional to e^{-4t_1/T_2}, so there is an additional factor of '2' in the relationship between the measured decoherence time (T_2^{IH}) and the homogeneous linewidth Γ_H when the transition is inhomogeneously broadened [46].

$$T_2^{IH} = 4\hbar/\Gamma_H \tag{2.2}$$

Due to the factor of '2' difference between Eq. 2.1 and Eq. 2.2, there is some uncertainty in determining the homogeneous linewidth using FWM, when the nature of the broadening is either unknown, or when Γ_H is comparable to Γ_{IH} [46].

In the non-rephasing pulse ordering (Fig. 2.3b), the first and third light-matter interactions (interactions involving k_2 and k_3, respectively) have the same sign. For that reason, no photon echo is present as the sign of the phase evolution in t_3 is in the same direction as in t_1. The decay of the non-rephasing signal is therefore related to Γ_{IH}, instead of Γ_H. The rephasing pulse ordering is most commonly used in FWM experiments exploring coherent dynamics, because (unlike the non-non-rephasing pulse ordering) it can be used to separate Γ_H from Γ_{IH} [46].

Scanning t_2 for a fixed t_1 can also provide insight into both the coherent and population dynamics of the resonant transitions. The populations created by the

7 The negative sign placed in front of k_1 does *not* indicate that the beam used in the experiment is travelling in the $-k_1$ direction, but is rather a means of identifying which pathways in contribute to the signal in the detected direction. As Section 2.1.1 will show in detail, when we perturbatively solve the Shrodinger equation, we end up with three nested commutators which when multiplied out result in an array of terms including all of the linear combinations of the three pulses with positive or negative signs. Each of those terms has a wavevector that is a linear combination of the wavevectors of the excitation pulses. The negative sign for k_1 (positive signs for k_2 and k_3) in Fig. 2.3 indicates that only terms with a negative k_1 (positive k_2 and k_3) will contribute to the signal when collecting only along the $-k_1+k_2+k_3$ direction. This also means that the phase evolution set in motion by the $-k_1$ pulse will have the opposite sign to the phase evolution set in motion by k_2 or k_3, (i.e. $e^{ik_1x-i\omega_1t}$ becomes $e^{-ik_1x+i\omega_1t}$).

second pulse will decay as a function of t_2 by radiative and non-radiative processes, but are convolved with an additional signal decay due to carrier diffusion. The populations in t_2 are not actually evenly distributed through the focal spot of the laser, but rather occur as a spatial 1D grating [43]. The spacing of this grating is set by the wave-vectors of the first two pulses, and the signal is only generated if the population grating is still in place when the third pulse arrives. The grating can decay in two different ways: the populations can relax or the carriers that make up the grating can diffuse.[8] Therefore, the decay of the FWM signal as a function of t_2 is a convolution of the grating decay and the population decay. These two effects can be deconvolved through measurements taken using different grating spacings (set by the angle of the beams used in the measurement) [48] or making separate measurements of the lifetime.

If multiple, coherently coupled transitions are excited by the first two excitation pulses, the second pulse can put the system into a coherent superposition of excited states instead of a population [46]. Unlike the populations, which have a phase that does not evolve in t_2, the phase of the coherent superposition evolves with a period (T_{CS}) set by the energy difference of the two coupled transitions (ΔE_{1-2}):

$$T_{CS} = \frac{h}{\Delta E_{1-2}} \tag{2.3}$$

The coherent superposition pathway can then interfere with one of the pathways that involve a population during t_2, and lead to oscillations of the intensity of the FWM signal as a function of t_2 with a period equal to T_{CS} [49, 50]. These oscillations form the basis for the identification of transitions that are coherently coupled using 0-quantum 2D spectroscopy and 3D spectroscopy, which are described in Sections 2.2.1.2 and 2.2.2 respectively.

2.1.1 *Formal description of FWM and Feynman-Liouville diagrams*

This section contains a formal treatment for FWM signals. Density matrix formalism is typically used to describe FWM signals for semiconductor nanostructures, as it can be used to describe mixed states [51]. The detected quantity in the FWM experiment is the 3^{rd}-order polarization ($P^{(3)}$), which can be calculated using the 3^{rd}-order density matrix ($\rho^{(3)}$):

$$P^{(3)}(t) = Tr[\mu\rho^{(3)}(t)] \tag{2.4}$$

8 Incidentally, this population grating serves as a useful tool for conceptualizing the FWM process. The signal can be thought of as the diffraction of the third pulse off of the population grating created by the first two pulses. In this way, the FWM signal is imbued with the wave-vector dependences of the three excitation beams.

To calculate $\rho^{(3)}$ we must solve the Liouville-von Neumann equation for the system Hamiltonian (H).

$$\frac{\partial \rho}{\partial t} = -\frac{i}{\hbar}[H, \rho] \tag{2.5}$$

To do so, we will follow the perturbative approach laid out by Peter Hamm [52], which is the Hilbert space version of the derivation given by Shaul Mukamel in *Principles of Nonlinear Optical Spectroscopy* [51, Ch. 5 p. 115] in Liouville space.

The pulses (even with the relatively large pulse energies produced by fs oscillators) can be treated perturbatively, as the amplitude of the pulse electric fields are dwarfed by the internal electric fields in the semiconductor lattice [46, 51]. In the perturbative regime we can split the system Hamiltonian (H) into two parts,

$$H(t) = H_0(t) + H'(t) \tag{2.6}$$

where H is the total Hamiltonian of the system, H_0 is the unperterbed Hamiltonian and H' represents the light matter interactions, which can be defined classically as

$$H'(\tau) = \int E(\mathbf{r}, \tau) P(\mathbf{r}) \tag{2.7}$$

Where $P(\mathbf{r})$ is the classical polarization density which can be related to the dipole operator μ. After making the dipole approximation it can be written as

$$H'(\tau) = -E(\mathbf{r}, \tau) \cdot \mu \tag{2.8}$$

In the interaction picture, the time dependence of H_0 can be determined using the time evolution operator:

$$U_0(t, t_0) = e^{-\frac{i}{\hbar} H_0 \cdot (t - t_0)} \tag{2.9}$$

The perturbative interaction Hamiltonian can then be defined as:

$$H'_I(t) = U_0^*(t, t_0) H'(t) U_0(t, t_0) \tag{2.10}$$

The dipole operator in the interaction picture ($\check{\mu}(\tau)$) is defined as:

$$\check{\mu}(\tau) = U_0^*(t, t_0) \mu U_0(t, t_0) = e^{\frac{i}{\hbar} H_0 \tau} \mu e^{-\frac{i}{\hbar} H_0 \tau} \tag{2.11}$$

To describe the dynamics, we start with the Liouville-von Neumann equation of motion for the perturbative Hamiltonian in the interaction picture:

$$\frac{\partial \rho_I}{\partial t} = -\frac{i}{\hbar}[H'_I, \rho_I] \tag{2.12}$$

Which can be expanded by power into:

$$\rho_I(t) = \rho_I(t_0) + \sum_{n=1}^{\infty} \left(-\frac{i}{\hbar}\right)^n \int_{t_0}^{t} d\tau_n \int_{t_0}^{\tau_n} d\tau_{n-1} \cdots \int_{t_0}^{\tau_2} d\tau_1 \\ [H'_I(\tau_n), [H'_I(\tau_{n-1}), \cdots [H'_I(\tau_n), \rho(t_0)] \cdots]] \tag{2.13}$$

The interaction density matrix is related to the full density matrix by the time evolution operator:

$$\rho(t) = U_0(t, t_0)\rho_I(t)U_0^*(t, t_0) \tag{2.14}$$

so we can now write the power expanded density matrix by combining Eq. 2.13 and Eq. 2.14.

$$\rho(t) = \rho^{(0)}(t) + \sum_{n=1}^{\infty} \left(-\frac{i}{\hbar}\right)^n \int_{t_0}^{t} d\tau_n \int_{t_0}^{\tau_n} d\tau_{n-1} \cdots \int_{t_0}^{\tau_2} d\tau_1 \\ U_0(t, t_0) \cdot [H'_I(\tau_n), [H'_I(\tau_{n-1}), \cdots [H'_I(\tau_1), \rho(t_0)] \cdots]] \cdot U_0^*(t, t_0) \tag{2.15}$$

We can now make the assumption that the system was in equilibrium before the first pulse arrived so that we can replace t_0 with $-\infty$, and substitute Eq. 2.10 (definition of perturbative Hamiltonian) and Eq. 2.11 (definition of interaction dipole operator) into Eq. 2.15.

$$\rho(t) = \rho^{(0)}(-\infty) + \\ \sum_{n=1}^{\infty} \left(-\frac{i}{\hbar}\right)^n \int_{-\infty}^{t} d\tau_n \int_{-\infty}^{\tau_n} d\tau_{n-1} \cdots \int_{-\infty}^{\tau_2} d\tau_1 E(\tau_n)E(\tau_{n-1}) \cdots E(\tau_1) \cdot \\ U_0(t, t_0) \cdot [\check{\mu}(\tau_n), [\check{\mu}(\tau_{n-1}), \cdots [\check{\mu}(\tau_1), \rho(-\infty)] \cdots]] \cdot U_0^*(t, t_0) \tag{2.16}$$

Each term in the sum represents an order of the density matrix. For FWM experiments presented in this thesis, we are only concerned with the third order, which is the n=3 term of the sum in equation. The third order density matrix is therefore given by:

$$\rho^{(3)}(t) = \left(-\frac{i}{\hbar}\right)^3 \int_{-\infty}^{t} d\tau_3 \int_{-\infty}^{\tau_3} d\tau_2 \int_{-\infty}^{\tau_2} d\tau_1 E(\tau_3)E(\tau_2)E(\tau_1) \cdot U_0(t, t_0) \cdot \\ [\check{\mu}(\tau_3), [\check{\mu}(\tau_2), [\check{\mu}(\tau_1), \rho(-\infty)]]] \cdot U_0^*(t, t_0) \tag{2.17}$$

Using $\rho^{(3)}$ we can then calculate the observable third order polarization ($P^{(3)}$) by substituting Eq. 2.17 into Eq. 2.4.

$$P^{(3)}(t) = \left(-\frac{i}{\hbar}\right)^3 \int_{-\infty}^{t} d\tau_3 \int_{-\infty}^{\tau_3} d\tau_2 \int_{-\infty}^{\tau_2} d\tau_1 E(\tau_3)E(\tau_2)E(\tau_1)\cdot \left\langle \check{\mu}(t)\cdot[\check{\mu}(\tau_3),[\check{\mu}(\tau_2),[\check{\mu}(\tau_1),\rho(-\infty)]]]\right\rangle \tag{2.18}$$

It is more convenient to discuss the dynamics as a function of the delays between pulses rather than according to the absolute arrival time of the pulses. We can recast Eq. 2.18 using the two inter-pulse delays (t_1 and t_2) and the time after the third pulse (t_3), which are defined based on the arrival times of the three pulses (τ_1, τ_2, τ_3).

$$\tau_1 = 0,\ \ t_1 = \tau_2 - \tau_1,\ \ t_2 = \tau_3 - \tau_2,\ \ t_3 = t - \tau_3 \tag{2.19}$$

Using these new time variables, Eq. 2.18 becomes:

$$\begin{aligned} P^{(3)}(t) = \left(-\frac{i}{\hbar}\right)^3 \int_0^{\infty} dt_3 \int_0^{\infty} dt_2 \int_0^{\infty} dt_1 \\ E(t-t_3)E(t-t_3-t_2)E(t-t_3-t_2-t_1)\cdot\theta(t_1)\theta(t_2)\theta(t_3)\cdot \\ \langle \check{\mu}(t_3+t_2+t_1))\cdot[\check{\mu}(t_2+t_1),[\check{\mu}(t_1),[\check{\mu}(0),\rho(-\infty)]]]\rangle \end{aligned} \tag{2.20}$$

Where $\theta(\tau)$ is the heavyside step function, which ensures causality (i.e. that interactions happen in the order the pulses arrive and that $t_1, t_2, t_3 \geqslant 0$).

$$\theta(\tau) = \begin{cases} 1 & \text{if } \tau \geqslant 0 \\ 0 & \text{if } \tau < 0 \end{cases} \tag{2.21}$$

Eq. 2.20 can also be written as a convolution of the electric fields of the three pulses with a 3rd-order response function ($S^{(3)}$):

$$\begin{aligned} P^{(3)}(\mathbf{r},t) = \int_0^{\infty} dt_3 \int_0^{\infty} dt_2 \int_0^{\infty} dt_1 S^{(3)}(t_3,t_2,t_1)\cdot \\ E(\mathbf{r},t-t_3)E(\mathbf{r},t-t_3-t_2)E(\mathbf{r},t-t_3-t_2-t_1) \end{aligned} \tag{2.22}$$

$$\begin{aligned} S^{(3)}(t_3,t_2,t_1) = \left(\frac{i}{\hbar}\right)^3 \theta(t_1)\theta(t_2)\theta(t_3)\cdot \\ \langle \check{\mu}(t_3+t_2+t_1)\,[\check{\mu}(t_2+t_1),[\check{\mu}(t_1),[\check{\mu}(0),\rho(-\infty)]]]\rangle \end{aligned} \tag{2.23}$$

The operators in Eq. 2.23 all act from the left. That need not be the case, so there is also an equivalent response function for operators acting from the right. This

alternate response function is the complex conjugate of Eq. 2.23, but is otherwise the same. The nested commutators when multiplied out give $2^3 = 8$ terms. Each of those terms represents a 'pathway' or specific sequence of interactions. Closer inspection shows that half of the terms are actually complex conjugates of the others, so we have a total of 4 possible terms.

For our three beam box configuration there are three possible pulses (labelled E_A, E_B, E_C) which are incident on the sample at τ_A, τ_B, τ_C, respectively. The full electric field perturbing the system can be defined according to Eq. 2.24.

$$\begin{aligned}
E(\mathbf{r},\tau) =& E_A(\tau-\tau_A)e^{+ik_1\mathbf{r}-i\omega(\tau-\tau_A)}+ && (2.24.1)\\
& E_A(\tau-\tau_A)e^{-ik_1\mathbf{r}+i\omega(\tau-\tau_A)}+ && (2.24.2)\\
& E_B(\tau-\tau_B)e^{+ik_2\mathbf{r}-i\omega(\tau-\tau_B)}+ && (2.24.3)\\
& E_B(\tau-\tau_B)e^{-ik_2\mathbf{r}+i\omega(\tau-\tau_B)}+ && (2.24.4)\\
& E_C(\tau-\tau_C)e^{+ik_3\mathbf{r}-i\omega(\tau-\tau_C)}+ && (2.24.5)\\
& E_C(\tau-\tau_C)e^{-ik_3\mathbf{r}+i\omega(\tau-\tau_C)} && (2.24.6)
\end{aligned}$$

For now, we assume that all three pulses have an identical Gaussian time envelop function with a width of *T*:

$$E_A(\tau) = E_B(\tau) = E_C(\tau) = E_0 e^{\frac{-\tau^2}{2T^2}} \tag{2.25}$$

The six terms in Eq. 2.24 can in principle act in any order, and the pulses can each act more than once (i.e. provide a photon for more than one of the interactions). This leads to an additional $6^3 = 216$ terms for each term/pathway in the response function. Multiplying the number of terms in the response function with the terms in the electric field, we get a total of $4 \times 6^3 = 864$ terms.

Most of these terms, however, do not contribute to the signal in a box geometry three-beam FWM experiment for two main reasons: the pulses typically appear in a well-defined pulse ordering (i.e. the delays t_1 and t_2 are much larger than the pulse width *T*), and with a well-defined wave vector.

The wave vector of the signal generated by each of the 216 electric field combinations is defined by the wave-vector of the electric field terms which contributed. For example, if the three electric field terms from Eq. 2.24 that contribute to the signal are terms 2.24.3 ($e^{+ik_2\mathbf{r}-i\omega(\tau-\tau_B)}$), 2.24.5 ($e^{+ik_3\mathbf{r}-i\omega(\tau-\tau_C)}$) and 2.24.2($e^{-ik_1\mathbf{r}+i\omega(\tau-\tau_A)}$), then the spatial component of the signal electric field will be given by:

$$e^{-ik_s\mathbf{r}} = e^{-ik_1\mathbf{r}} \cdot e^{+ik_2\mathbf{r}} \cdot e^{+ik_3\mathbf{r}} \tag{2.26}$$

The wave vector of the signal is therefore $k_s = -k_1 + k_2 + k_3$. If instead, terms 2.24.4 ($e^{-ik_2\mathbf{r}+i\omega(\tau-\tau_B)}$), 2.24.5 ($e^{+ik_3\mathbf{r}-i\omega(\tau-\tau_C)}$), and 2.24.1 ($e^{ik_1\mathbf{r}-i\omega(\tau-\tau_A)}$) contribute to the signal, then the emission will be in the $k_s = k_1 - k_2 + k_3$ direction.

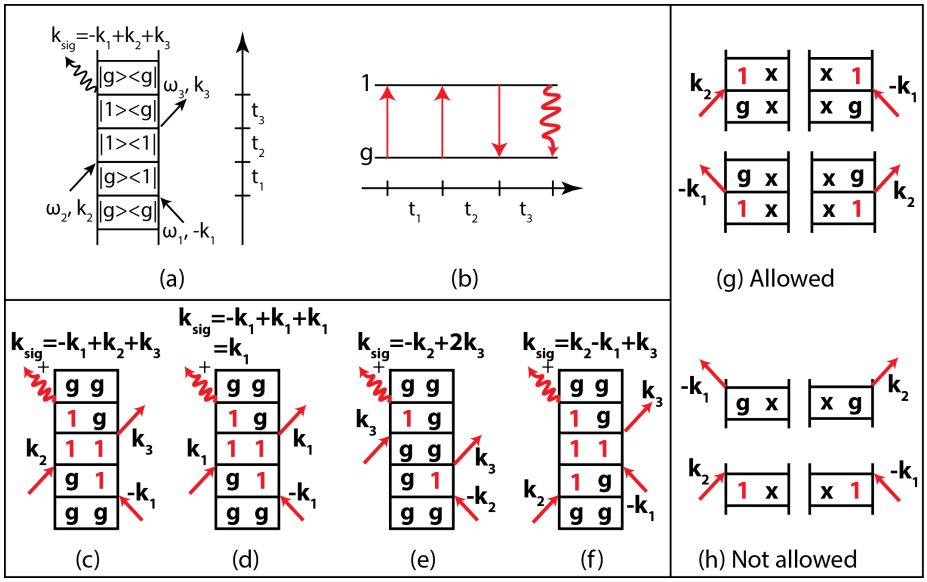

Figure 2.4: A few examples of Feynman-Liouville diagrams. (a) shows a typical representation of a F-L diagrams, with an equivalent energy level diagram shown in (b). (c)-(f) show a set of different possible pathways for some selected phasematching directions and pulse orderings. The syle of these diagrams will be continued through the rest of this thesis. In many cases, the energy of the interacting photon will be indicated by the color of the angled arrow in some cases, so the explicit frequency dependence is dropped. (a) and (c) are equivalent pathways. In some cases where only one signal direction is discussed and pulse ordering is known, the wave vectors will also be dropped. (g) Shows the allowed interactions for a two-level system. (h) Shows examples of interactions which are not allowed. They involve either de-exciting the ground state (top row) or exciting the already excited state (bottom row) when there are no higher energy states.

We can therefore differentiate between these two sets of signals by detecting in either the $k_1 - k_2 + k_3$ or the $-k_1 + k_2 + k_3$ direction (as long as $k_1 \neq k_2$).

This ability to choose which pathways we detect based on the signal direction illustrates the importance of the box beam geometry. If we used a collinear beam geometry ($k_1 = k_2 = k_3$) all of the electric field terms would be spatially overlapped. By detecting in the $-k_1 + k_2 + k_3$ direction in the box geometry shown in 2.2c, we can isolate a small number of the electric field terms (specifically, terms that involve exactly one contribution each from terms 2, 3 and 5 in Eq. 2.24). In the box geometry, there is no other combination of wave-vectors that lead to a signal wave-vector in the $-k_1 + k_2 + k_3$ direction[9]. Thus, out of the 216 total electric field terms, there are a total of only six that lead to signal in the $-k_1 + k_2 + k_3$ direction.

So far we have ignored the time ordering of the pulses. We can further reduce the six electric field combinations to just one if the delays between the pulses are much larger than the pulse widths (i.e. we know which order the pulses are interacting). The terms in the response function that can lead to signal also depend on the ordering of the pulses.

9 There are terms from higher order odd Polarizations that could share this wave-vector ($P^{(5)}$, $P^{(7)}$, $P^{(9)}$, etc.). Due to the weak power scaling of the nonlinear response of most materials it is assumed that $P^{(5)}$ only contributes at high powers and that any higher contribution is negligible.

To understand how pulse ordering and wave-vector dependence combine to limit the pathways in an experiment, it is more convenient to use Feynman-Liouville (F-L) diagrams than equations [51, 52]. Each F-L diagram is used to identify a single pathway, which represents a single term in $P^{(3)}$ (Eq. 2.22). A few example F-L diagrams are presented in Fig. 2.4a and Fig. 2.4c-f. The specific stylings of these diagrams vary, but the key parts are the same. The diagram takes the form of a ladder, with the vertical lines representing time (running from bottom to top) and the timing of the light matter interactions indicated by the rungs. The spacing between the rungs is the time delays between interactions, (t_1,t_2 and t_3 from bottom to top), and the bra and ket in the box indicate the quantum state of the system during each time delay. If both bra and ket are in the same state, then the system is in a population. If the bra and ket are in different states, then the system is in a coherent superposition of states (often referred to simply as a coherence). The system must start and end in either a ground state population or an excited state population. In FWM experiments it is normally assumed that the system starts in a ground state population, but may end in any population.

The arrows represent the interactions with the laser pulses. Arrows pointing to the right represent a term of the form $e^{+i\mathbf{k}\mathbf{r}-i\omega\tau}$ (i.e. terms 1, 3, and 5 in Eq. 2.24) while arrows pointing to the left represent a term of the form $e^{-i\mathbf{k}\mathbf{r}+i\omega\tau}$ (i.e. terms 2, 4, and 6 in Eq. 2.24). Arrows pointing inwards represent absorption of a photon and an increasing excitation of the system, while arrows pointing away from the ladder represent emission of photon and a de-excitation of the system[10]. For this reason, the FWM signal is always represented by an arrow pointing outwards.

The F-L diagrams can be related back to terms in the response as follows. The arrows on the left (right) side of the diagram represent dipole operators in the response function that act from the left (right). The dipole operators act on the equilibrium density matrix in order. The diagrams shown in Fig. 2.4c-f therefore represent the following terms in the response function:

$$\check{\mu}(t_3+t_2+t_1)\check{\mu}(t_1)\rho(-\infty)\check{\mu}(0)\check{\mu}(t_2+t_1) \text{ (Fig. 2.4c-d)}$$

$$\check{\mu}(t_3+t_2+t_1)\check{\mu}(t_2+t_1)\rho(-\infty)\check{\mu}(0)\check{\mu}(t_1) \text{ (Fig. 2.4e)}$$

$$\check{\mu}(t_3+t_2+t_1)\check{\mu}(0)\rho(-\infty)\check{\mu}(t_1)\check{\mu}(t_2+t_1) \text{ (Fig. 2.4f)}$$

The labels next to the arrows indicate the wave-vector of the electric field interacting with the system. The wave-vector of the resulting signal can be found by adding the wave-vectors of the first three electric field terms (as shown in Fig. 2.4c-f). The energy of each electric field interaction is sometimes included in label next to each of the arrows (as in Fig. 2.4a). In this thesis, the energy label is left off. Instead, the energy of the photon that interacts with the system is represented by the color of

10 Note that interactions other than the signal field which point outwards (such as k_3 in 2.4c) do not indicate incoherent spontaneous emission, but rather the coherent stimulated emission, driven by one of the excitation pulses.

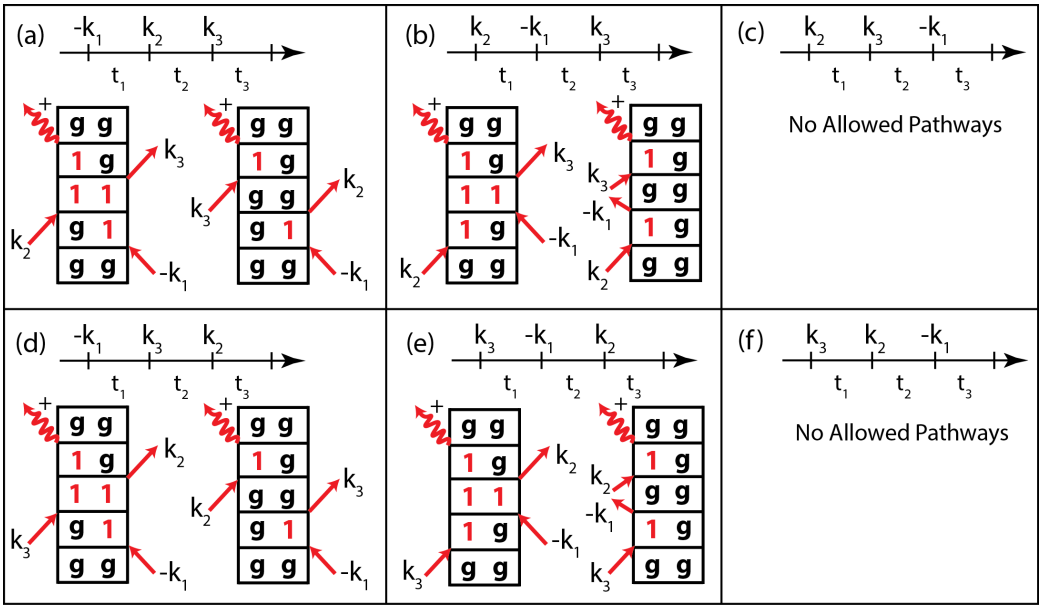

Figure 2.5: All the possible pathways for a two level system, detected in the $-k_1 + k_2 + k_3$ direction for the six possible pulse orderings. (a) and (d) are the rephasing pulse ordering which lead to a photon echo in inhomogeneously broadened systems. (b) and (e) are the non-rephasing pulse orderings which produce a free-induction decay regardless of the broadening in the system. In a strictly two-level system, there are no allowed pathways in pulse orderings in which $-k_1$ arrives last (shown in (c) and (f)). This pulse ordering is often called the 2-quantum pulse ordering for reasons that will be made clear in Section 2.2.1.3. When we consider coupling between the two-level systems further along, we will see that there are in-fact allowed pathways in the 2-quantum pulse orderings. If pulses in the k_2 and k_3 are identical, the pathways in (a), (b) and (c) provide the same information as the pathways in (d), (e) and (f), respectively.

the arrow. For a two-level system, all of the interactions happen at the same photon energy (the energy of the g $\leftrightarrow$ 1 transition), so all of the arrows have the same color. When additional transitions are included, they are indicated by different colors.

The only allowed interactions for a two-level system involve the excitation of the system from the ground state to the single excited-state or de-excitation of the system from the single excited state to the ground state (as shown in Fig. 2.4g). Any pathways that involve de-excitation of the ground state or increasing the excitation of an already excited state are not allowed (as shown in Fig. 2.4h). We note here, that the former (de-exciting the ground state) is never allowed, but the latter (increasing the excitation of an already excited state) is possible if there are additional higher-energy states. As we will see later in this chapter, there are often higher energy states for excitons in QWs, so additional pathways and transitions are allowed.

With these rules in mind, the full set of pathways for a two-level system is presented in Fig. 2.5 for all six possible pulse orderings. The pathways in Fig. 2.5a and Fig. 2.5d are for the rephasing pulse orderings, in which the conjugate pulse arrives first. The pathways in Fig. 2.5b,e show the non-rephasing pulse-orderings. The conjugate pulse arrives last in the pulse-orderings in Fig. 2.5c,f. In this pulse ordering, there are no allowed pathways for a two-level system. If more states are considered,

however, this need not necessarily be the case. We will see in the following sections and the experimental results chapters that signals are in fact generated in the pulse ordering. An explanation of where these signals come from is provided in Section 2.2.1.3. If the k_2 and k_3 pulses are identical, the pathways in Fig. 2.5a-c provide the same information as the pathways in Fig. 2.5d-f, respectively, because they involve the same term in the response function.

The density matrix (ρ), transition dipole moment (μ) and interaction Hamiltonian (H'_{int}) used in the previous equations each represent an n×n matrix, where n is the number of states in the system. So far we have been considering a two level system consisting of one ground state and 1 excited state. The number of terms contributing to the signal increases significantly as more transitions are added to the system. The matrix elements of μ are defined as $\mu_{i,i} = 0$, and $\mu_{i,j}$ is the transition dipole moment from transition i to j (for i≠j). Assuming that all non-diagonal matrix-elements are non-zero, the matrix multiplication in the commutators in Eq. 2.23 results in an additional n-1 terms for each commutator. This leads to a total number of terms equal to $(2(n-1))^3$ in $S^{(3)}$. Ignoring phase-matching and pulse-ordering, this leads to a total of $(2(n-1))^3 \cdot 6^3$ pathways. For a two, three or four level system this results in 8 (1728), 64 (13,824), and 216 (46,656) terms/pathways with (without) considering phase-matching. Many of these pathways can be removed by restricting which matrix-elements are included for μ, but this obviously still represents a difficult problem to solve completely when many states must be considered. Due to this complexity, the resulting system of interdependent differential equations must be solved numerically in most cases.

Inclusion of multiple states increases the number of allowed diagrams significantly (just as it introduced many new terms to $S^{(3)}$). A few selected pathways from a three-level system are shown in Fig. 2.6. The main difference is the introduction of more pathways that involve multiple transitions and therefore imply interactions between the associated excited states. These interactions can take the form of a coherent superposition of excited states (Fig. 2.6a) or population relaxation during during t_2 (Fig. 2.6e), excited state absorption of the third pulse (Fig. 2.6d) or ground state bleach through a shared ground state (Fig. 2.6c). The main shared characteristic of these pathways (and difference from the types described in Fig. 2.5) is that they involve emission from a state other than the one in which the first absorption took place. This is a key feature that is exploited by CMDS to separate the pathways that involve multiple excited states from pathways that involve only a single excited state. This feature of CMDS will be described in more detail in the following section.

This Section has presented a basic formal description of FWM, with the intention of providing a basic understanding of the measurement technique. This basic description unfortunately misses a lot of important and interesting physics. For example, it ignores the relaxation of the coherences and populations. Relaxation terms can be included in the Hamiltonian as an additional perturbation [46, 51],

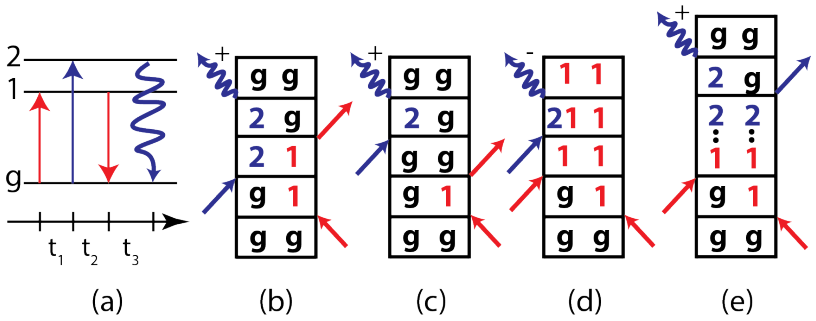

Figure 2.6: Selected F-L diagrams for a two coupled 2LS's. The color indicates the energy of the interacting photon. The energy level diagram shown in (a) is equivalent to the the F-L diagram in (b). (b-e) represent the coherent superposition, ground state bleach, excited states absorption and population transfer pathways, respectively.

but complicate the resulting response function so they were left out here for the sake of simplicity. Rigorous inclusion of such effects in the system Hamiltonian is computationally intractable, but can be introduced phenomenologically after integration [53, 54]. Phenomenological inclusion of these excitation induced effects in the Hamiltonian as population/excitation dependent relaxation terms might be a good compromise, and is an avenue that could be pursued to explain some of the results in this thesis.

2.2 Coherent Multi-dimensional Spectroscopy

In standard spectrally-resolved FWM, the signal is typically measured using a time-integrating detector (such as a CCD), which measures the signal intensity, but not the signal phase [46]. To perform CMDS, the full complex signal must be measured (amplitude and phase) [17]. In order to measure the signal phase, the FWM signal must be detected interferometrically. In such a scheme (often called heterodyne detection), the signal co-propagates with a reference pulse (called the local oscillator or LO) into a spectrometer. The signal then appears as a spectral interferogram on top of the LO spectrum. From this interferogram, the signal phase can be backed out, and the phase evolution tracked as a function of the inter-pulse delays. This is the key difference between a standard FWM experiment and CMDS, and is also the origin of the main experimental difficulties [17, 55]. In order to determine the phase of the signal, the excitation pulses and the reference pulse must all be phase-locked for the duration of the experiment to a degree of precision well below the period of the optical cycle (a few fs at optical frequencies). By 'phase-locked', we mean that the relative phases of k_1, k_2, k_3 and the LO must remain constant. The absolute phase of the pulses may drift from shot-to-shot, but they must all drift by the same amount, so the relative phase of the four beams remains constant [17, 55].

For the pulses to remain phase locked all the way to the sample, any experimental instabilities (such as vibrations or air currents) that do not affect all the pulses equally must be avoided (passive phase stabilization) or compensated (active phase

stabilization). Passive phase stabilization can be further split into two categories: implementations in which all beams pass through the same optics and those in which beams are routed so that all phase drifts are intrinsically compensated in the final signal.

Several experimental implementations of both active and passive phase stabilized CMDS have been demonstrated in the last decade [55]. In some implementations of CMDS, the phase is actively stabilized using nested interferometers and additional CW lasers [20, 56]. Another approach uses a geometry that intrinsically cancels any phase drifts that appear by clever routing of the beams through multiple translation stages [57, 58]. Most other approaches rely on passive phase stabilization, in which all the beams pass through as many of the same optics as possible. The difficulty in this case is then controlling the delays individually. In some experiments wedge pairs are used to control the delays and the only optics the beams do not share are the wedges themselves, and an ND filter in the LO beam [59, 60]. Typically, in these prism pair based implementations, k_1 and k_2 take different paths to k_3 and the LO. The coherence time (the delay between k_1 and k_2) is controlled by a prism pair, and the waiting time (the time between the arrival of k_2 and k_3) is controlled with a delay stage. In this implementation, k_1 and k_2 are phase locked and k_3 and the LO phase locked, but $k_{1/2}$ are not phase locked with k_3/LO.

Utilizing a diffraction based pulse-shaper [61] to control the inter-pulse delays is arguably the best passively phase stabilized implementation of CMDS, since there are no non-shared optics aside from the ND filter in the LO beam. In this experimental setup, four beams in a box geometry are all independently delayed by a single diffraction based pulse-shaper with a 2D SLM [62, 63]. The experimental section of this chapter will describe this implementation in more detail. All of the beams are fully phase locked, so two-quantum spectroscopy can be performed. The pulse-shaper can also be used for spectral shaping and pulse compression.

Another different way of using a pulse-shaper for CMDS is in the two beam pump-probe geometry [64–67]. The pump is passed through a pulse-shaper, which is used to split it into two separate collinear pulses using a sinusoidal phase pattern. The probe acts as both the third excitation pulse and the LO, in what is called self-heterodyne detection. The delay between first pulse and the second pulse is scanned by changing the periodicity of the phase pattern. The delay between the pump pulses and the probe pulse is controlled by a delay stage, so there is no phase stability between the pump and the probe. This implementation is experimentally simple compared with the diffraction based pulse shaping described in the previous paragraph, but does not have the same flexibility. Another benefit of the pump-probe geometry is that the recorded spectra are intrinsically phased, (i.e. Φ_G is always 0). The pump can also be split into more than two pulses to perform higher order ($\chi^{(5)}$ for example) measurements. $\chi^{(5)}$ 3D spectroscopy in pump probe geometry was also recently demonstrated [68].

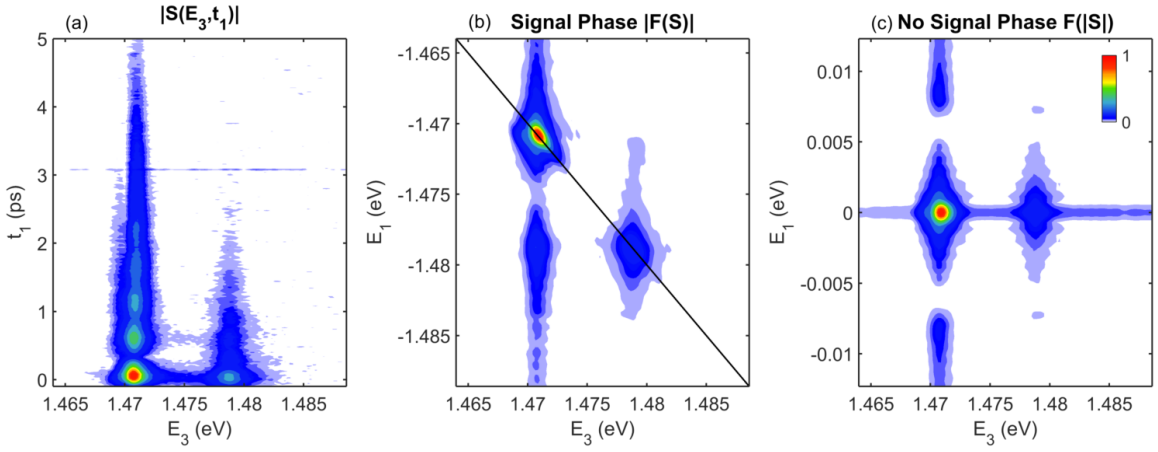

Figure 2.7: (a) A scan of the coherence time, which is Fourier transformed as (b) complex signal and (c) absolute value of the signal.

The previously described CMDS experiments use phase matching to separate the signal of interest from other signals. The phase matching requirements, however, limit the spatial resolution that can be achieved because the FWM signal must be well separated from the excitation beams. Furthermore, the signal from a nanostructure that is much smaller than the wavelength of light being used will intrinsically have a very well defined position and consequently a very a poorly defined wave vector (i.e. it acts more like a point source than a macroscopic polarization). CMDS with better spatial resolution can be achieved if a co-linear pulse geometry is used and some other signal from the sample is detected instead of the FWM signal itself. The co-linear pulses can be focused to a much smaller spot, and a well defined emission wave-vector is no longer required. Experiments have been performed using photocurrent [69, 70], photoluminescence [71–73] and electron photoemission [74] as detection. In these experiments, the desired FWM signal is separated from the background using phase cycling along with AOMs and lock-in amplifiers.

A completely different experimental approach to CMDS involves non-interferometric measurement of the FWM signal, followed by the use of iterative phase retrieval algorithms [75]. This approach has shown some success in the case of semiconductor nanostructures with well defined electronic structure, but has been less effective in more complex molecular systems [76, 77].

As in FWM, CMDS spectra are acquired by collecting the spectrally resolved signal as a function of the two time delays between the excitation pulses: $\mathbf{E}(t_1, t_2, E_3)$. A key difference between CMDS and FWM is that in CMDS the signal electric field is detected (because of the interferometric detection) whereas in standard FWM the signal intensity is detected (direct detection). In CMDS, the data recorded in the t_1 and/or t_2 time domains is then Fourier transformed into the associated frequency/energy domains: $\mathbf{E}(E_1, E_2, E_3)$. Because the signal phase has been collected, the solution to the Fourier transform from $\mathbf{E}(t_1, t_2, E_3)$ to $\mathbf{E}(E_1, E_2, E_3)$ is unique, which

leads to much more easily interpreted results as well as intuitive representation of couplings between transitions through the appearance of cross-peaks. Figure 2.7 shows a Fourier transform of a FWM signal recorded as a function of t_1 with and without inclusion of the signal phase. A wealth of new information can be extracted when the phase information is included. For example, the exact absorption energy and the shapes of all of the peaks can now be determined. In both Figs. 2.7b and 2.7c, there is evidence of coupling of the peak at $E_3 = 1.471$ eV to another peak as there are of multiple peaks with the same emission energy. When the phase information is not included, however, it is unclear whether that represents coupling to a transition at higher energy or lower energy. When the phase information is included, the 2D spectrum definitively shows that the state at 1.471 eV is coupled to a state at higher energy (1.479 eV to be exact)[11]. We can also intuitively identify the transition to which it is coupled by looking for peaks along the diagonal at the same value of E_1.

The phase of the recorded complex signal has an additional offset related to the phase differences between the excitation beams and the LO, which is generally referred to as the 'global phase offset' (Φ_G) [78]. The position of the features in 2D spectra depend on the phase evolution, rather than the absolute phase, so not knowing this offset makes little difference for absolute value spectra. However, much information can be gleaned from analysing the 'real' and 'imaginary' parts separately. For example, excited state absorption signals generate negative valued peaks in 'real' spectra, and can therefore be separated from other processes which generate positive valued peaks. Furthermore, in semiconductor nano-structures, the 'real' peak-shape can be an important indicator of the type of interactions present in the system. For example, dispersive peaks have been shown to be an indicator of the presence of many body effects such as EIS or EID [53, 54, 79–82].

The measured 'real' and 'imaginary' signals will be rotated relative to the real and imaginary parts of $\chi^{(3)}$ by Φ_G. In box beam geometry FWM experiments at $t_1 = t_2 = t_3 = 0$ fs, Φ_G is defined as:

$$\Phi_G = -\Phi_{k_1} + \Phi_{k_2} + \Phi_{k_3} \tag{2.27}$$

Where Φ_{k_1}, Φ_{k_2} and Φ_{k_3} are the phase differences between the LO and k_1, k_2 and k_3, respectively. Therefore, if all of the beams are perfectly in phase, Φ_G goes to zero, which means that the real/imaginary parts of the measured signal correspond to the real/imaginary parts of $\chi^{(3)}$. Φ_G can be corrected (a process called 'phasing') by measuring the relative phase of all the beams before the experiment, and then rotating the phase of the multidimensional spectra by the appropriate amount dur-

11 Negative E_1 values are used by convention in some parts of the CMDS field. The reason for this convention traces back to the fact that the sign of the phase evolution during t_3 is opposite that of t_1, which leads to a negative frequency. While the some 2D spectra are presented with positive E_1 values (which is arguably more intuitive), many papers (particularly those involving semiconductor nanostructures) use negative E_1 values. For consistency with previous work in the field, the negative E_1 convention is therefore used throughout this thesis.

ing data analysis. In pulse-shaper based experiments, additional phase offsets can also be added to set Φ_G at $t_1 = t_2 = t_3 = 0$ fs to zero when the data is acquired.

Another way of phasing the multidimensional spectra is through comparison with a pump-probe signal [20, 83]. In this technique, a pump-probe measurement is recorded with $t_{PP} = t_2$, where t_{PP} is the delay between the pump and the probe and t_2 is the waiting time at which the the 2D spectrum was collected. If $\Phi_G = 0$, the pump probe signal is equivalent to a projection of the real part of a the sum of the rephasing and non-rephasing 2D spectra onto the E_3 axis. This is due to projection-slice theorem which states that if $\hat{S}$ is the projection of a 2D function (S) onto one dimension (x) and S_t is a slice the 2D Fourier transform of S at k_x=0 (where k_x is the Fourier domain of x), then $\hat{S}$ is equivalent to the Fourier transform of $\hat{S}_t$ ($\hat{S} = \mathcal{F}[\hat{S}_t]$).

We can apply the projection-slice theorem to 2D spectra. $S_{t_2}(E_1, E_3)$ is the real part of the a 2D spectrum (rephasing+non-rephasing) at a particular waiting time t_2. $\hat{S}_{t_2}(E_3)$ is the projection of $S_{t_2}(E_1, E_3)$ onto the E_3 axis:

$$\hat{S}_{t_2}(E_3) = \int_{-\infty}^{\infty} dE_1 S_{t_2}(E_3, E_1) \tag{2.28}$$

$\tilde{S}_{t_2}(t_1, E_3)$ is the inverse Fourier transform of $S_{t_2}(E_1, E_3)$ along E_1. The projection-slice theorem then tells us that $\tilde{S}_{t_2}(0, E_3) = \hat{S}_{t_2}(E_3)$. A two pulse pump-probe measurement is a $\chi^{(3)}$ measurement in which the first pulse supplies both of the first two photons and the signal emits in the probe direction. Pump-probe is therefore a FWM experiment with t_1=0. The pump-probe signal is also self-heterodyne detected, with a global phase offset which is intrinsically 0 ($\Phi_G^{PP} = 0$), and therefore always measures the real part of $\chi^{(3)}$. As a result, the pump-probe signal at t_2=0 is equivalent to $\tilde{S}_{t_2}(0, E_3)$ and therefore also equivalent to $\hat{S}_{t_2}(E_3)$ if Φ_G=0. Φ_G can therefore be deduced by fitting the amount of phase rotation required such that the projection of the 2D spectrum and the pump-probe coincide [20, 56, 59, 83, 84]. The real part of $\chi^{(3)}$ can then be extracted by rotating the recorded spectra by the Φ_G extracted from the fits of the projection of the 2D spectrum to the recorded pump-probe for each t_2 in the experiment.

It was recently demonstrated that phasing can also be accomplished using transient grating (TG) measurements in samples with weak pump-probe signals [85]. Transient grating refers to three beam FWM experiments in which the first two pulses are overlapped temporally and t_2 is scanned. Similar to the pump-probe phasing technique, the TG phasing technique involves recording the TG signal for different t_2 delays. The TG spectrum must be recorded in both the $k_4 = -k_1 + k_2 + k_3$ and $k_5 = k_1 - k_2 + k_3$ directions. The relative phase of k_1 and k_2 is then scanned, until the phase difference between the interferograms measured in the k_4 and k_5 directions is maximized. At this point, the difference between the two is equivalent

to the pump-probe signal for the same t_2, and the Φ_G can then be deduced and corrected for in the same manner described in the previous paragraph.

Although there is a great deal of information in 'real' and 'imaginary' peak-shapes, and hence phasing of the recorded data is useful, it is also not always straightforward to perform. For that reason, for the data presented in this thesis, we do not phase any of the data. There is still a huge amount of information in the amplitude data, as we will see in the following sections and in the experimental results presented in the following chapters.

2.2.1 *Two-dimensional spectroscopy*

CMDS data is typically presented as 2-dimensional spectra. A wide variety of different information can be gleaned by scanning one delay and performing a Fourier transform. The following sections will describe the three most common 2D spectra, which are labelled here as 1-quantum (1Q), 0-quantum (0Q) and 2-quantum (2Q) coherence spectra. The differences between these different types of spectra are in the pulse ordering and the inter-pulse delay that is scanned while recording the signal electric field. Fig. 2.8, shows two of the commonly used pulse orderings (which are also the two that will be used in this thesis): the rephasing pulse ordering and the two quantum pulse ordering. The wavevector of each of the relevant beam is shown above the pulses, and the time delay to be scanned for each type of spectrum is indicated underneath. The frequency of the three pulses are (for now) assumed so all be identical and resonant with the ground to singly excited state ($g \leftrightarrow 1$) transition. The state of the system is indicated by the level diagrams at the bottom of the figure, and the frequency of the phase oscillations is shown in the bottom row. In all cases, the signal is detected in the same $-k_1+k_2+k_3$ direction, which allows separation of the various different types of pathways. It is worth noting that if you detected in a different direction, the same set of pulses would produce a different type of experiment. For example: the two quantum pulse ordering in 2.8b is a rephasing pulse ordering when detected in the $+k_1-k_2+k_3$ direction.

In the rephasing pulse ordering (shown in Fig. 2.8a), the conjugate pulse (the one with the minus sign) arrives first and is followed by the other two pulses. Both 1Q and 0Q scans are performed using this pulse ordering by scanning the first time delay (t_1) or second time delay (t_2) respectively. In this pulse ordering, the system is in a coherent superposition of the ground state (g) and a singly-excited state (1) which produces signal phase oscillations at roughly the laser frequency during t_1. In t_2, the system is in either a population (in g or 1) or an excited state coherent superposition (a superposition of 1 and 1') which produce signal phase oscillations that either don't oscillate or oscillate at frequencies far below the laser frequency in t_2. The frequency of these phase oscillations relative to the laser frequency in these respective time periods are the reason for the names 1Q and 0Q for 2D spectra that

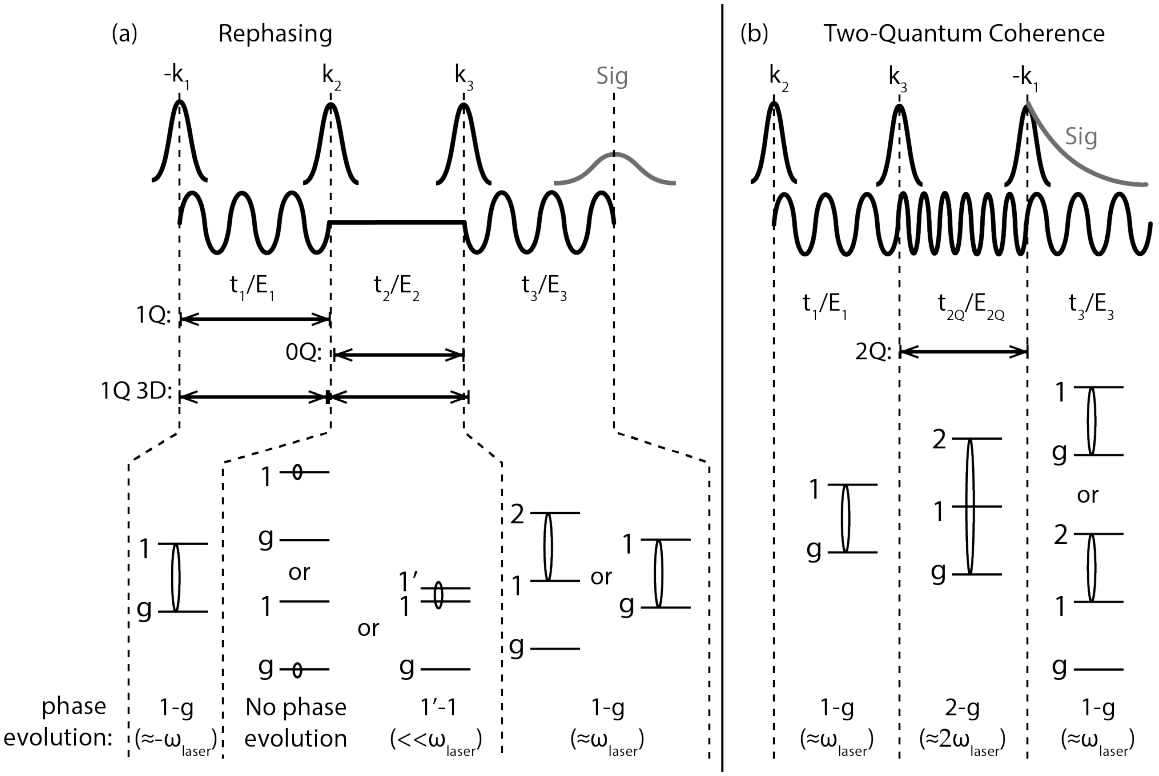

Figure 2.8: Phase evolution of the two CMDS pulse ordering used in this thesis: (a) rephasing, (b) Two-quantum coherence. The time delays that are scanned for each type of spectrum are labeled. For now, all pulses are assumed to have the same frequency. The state of the system in each time period is indicated by the simple level diagram which includes a ground state (g) a singly excited state (1) and a doubly excited state (2). The frequency and sign of the phase oscillations in each time period are shown in the bottom row.

involve the t_1 or t_2, respectively. In the 2Q pulse ordering (shown in Fig 2.8b), the second time delay (t_{2Q}) is typically scanned. In this pulse ordering, the system is in a coherent superposition of a doubly excited state and the ground state (often called a two-quantum coherence), which produces signal phase oscillations at roughly twice the laser frequency, which lead to the 2Q name.

While the following sections give a general description of 2D spectroscopy techniques, more specific explanation involving excitons in QWs can be found in Sections 4.2 and 5.2.

2.2.1.1 *1-Quantum*

As shown in Fig. 2.8a, a 1-Quantum coherence (1Q) 2D spectra are the most commonly used 2D spectra, and are also the most intuitive. A 1Q spectrum can be treated as a photon absorption/emission correlation map of the sample's electronic structure. The E_3 (horizontal) axis is the energy of the emitted signal photon, and the E_1 (vertical) axis is the energy of the photon absorbed from the first pulse. In this way, signals that are overlapped in 1D experiments such as photoluminescence or absorption can be separated, coupling between transitions can be detected, and homogeneous and inhomogeneous broadening can be separated.

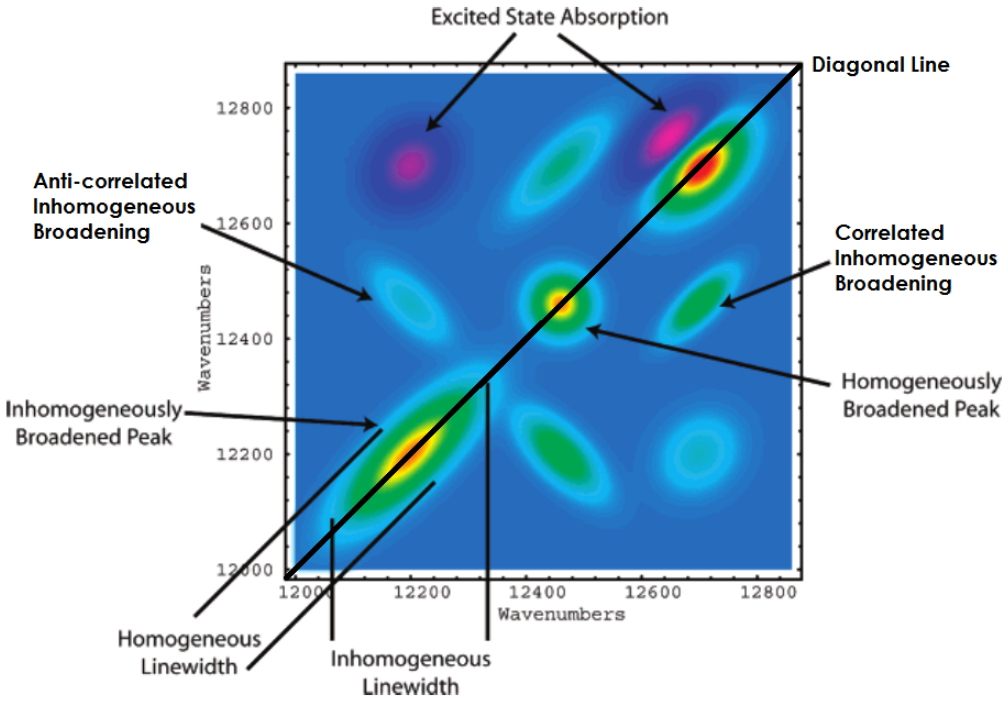

Figure 2.9: A cartoon diagram showing what types of information can be extracted from a 1Q-Rephasing 2D spectrum. Adapted with permission from Cho et al. [17].

To acquire a 1Q spectrum, the delay between the first and second pulses ($-k_1$ and k_2, respectively for rephasing[12]) is scanned, as in a coherence time scan in a FWM experiment described in Section 2.1. A macroscopic polarization is created with a phase set by the first pulse which evolves as a function of t_1 according to the energy of the excited transition. The phase of the emitted FWM signal (Φ_S) depends on the phase of the macroscopic polarization when the second pulse arrives, and as a result Φ_S will oscillate as t_1 is scanned at a frequency set by the energy of the transition excited by the first pulse. Put another way, this means that by measuring the phase and amplitude of the FWM signal as a function of t_1, and then Fourier transforming along t_1, the transition energy of the state excited by the first pulse can be determined and correlated with the state from which the FWM signal was emitted. The resulting 1Q 2D spectrum can therefore be thought of as a correlation map between the photon that initiated the FWM process with the final emitted signal photon.

A good illustration of the depth of information that can be gleaned from 1Q spectra is presented in Fig. 2.9 (which is adapted from Cho et al [17]). The detected peaks can be split into two main categories: diagonal-peaks (DPs) and cross-peaks (CPs). DPs are peaks which involve absorption and emission from the same transition, and therefore appear along the diagonal line (i.e. the E_1:E_3 line indicated in Fig. 2.9). CPs are peaks which involve absorption and emission from different transitions, and therefore appear away from the diagonal line.

12 Like other FWM experiments, 1Q 2D spectroscopy can be conducted in either a rephasing or non-rephasing pulse ordering, but only rephasing spectra are presented in this thesis.

The shape of DPs also contains useful information. Inhomogeneously broadened transitions appear as elongated peaks tilted along the diagonal. The width of the peaks along the diagonal is the inhomogeneous linewidth, while the cross-diagonal width of the peak is the homogeneous linewidth. This ability to separate homogeneous and inhomogeneous broadening is very powerful, and stems from the photon echo effect described in Section 2.1. Transitions which have no inhomogeneous broadening have round peak-shapes with equal diagonal and cross-diagonal widths.

Interactions between transitions can be identified through the presence of CPs. CPs can be generated by a variety of different pathways, including excited state coherent superpositions (CS), population-transfer (PT), excited-state absorption (ESA) or ground-state bleach (GSB), all of which can overlap in a 1Q 2D spectrum.

Additional coherent and incoherent dynamics can be interrogated by acquiring 2D spectra at various t_2 times (also called 'waiting times'). Some CP pathways can be identified based on the evolution as a function of t_2. For example, PT can be identified by CPs that grow in as t_2 increases. Coherent superpositions of excited states can be identified by oscillations in the phase of the CP (though this is accomplished more effectively using 0-quantum 2D or 1-quantum 3D spectroscopy - both of which involve a Fourier transform along t_2 and will be discussed in more detail in sections 2.2.1.2 and 2.2.2 respectively). Unlike PT and CS, ESA and GSB cannot be identified based on measurements as a function of t_2. ESA can, however, be identified based on the sign of the real part of the CP, which will be negative. ESA can appear as a CP well separated from DPs, or (typically in molecular systems) as a negative shoulder to a DP.

As with DPs, analysis of the CP peak-shape can lead to important insights. A peak which is tilted along the diagonal is indicative of correlated inhomogeneous broadening. The degree of correlation of the peak can be extracted from the cross-diagonal width of the peak, while tilting of the peak away from the diagonal indicates that the two transitions have different inhomogeneous linewidth. A CP between two inhomogeneously broadened transitions that is *not* tilted along the diagonal is indicative of uncorrelated inhomogeneous broadening. The presence or lack of correlation in the inhomogeneous broadening can be an important tool for identifying transitions and understanding their interactions. Analysis of CP shapes will be used several times in this thesis.

In some cases, additional information can be extracted from the DP peak-shapes. In semiconductor nanostructures, biexciton (BX) peaks can be identified as either a slightly shifted copy of an exciton (X) DP[13] or as a shoulder on the DP [80, 86]. The real peak-shape can also be very useful in this context as well, as BX has the opposite sign of X (because it is an ESA peak). In molecular systems, excited state absorption often can be identified as a negative peak on the above diagonal side of the DP (as shown in Fig. 2.9).

13 This can also be thought of as a CP.

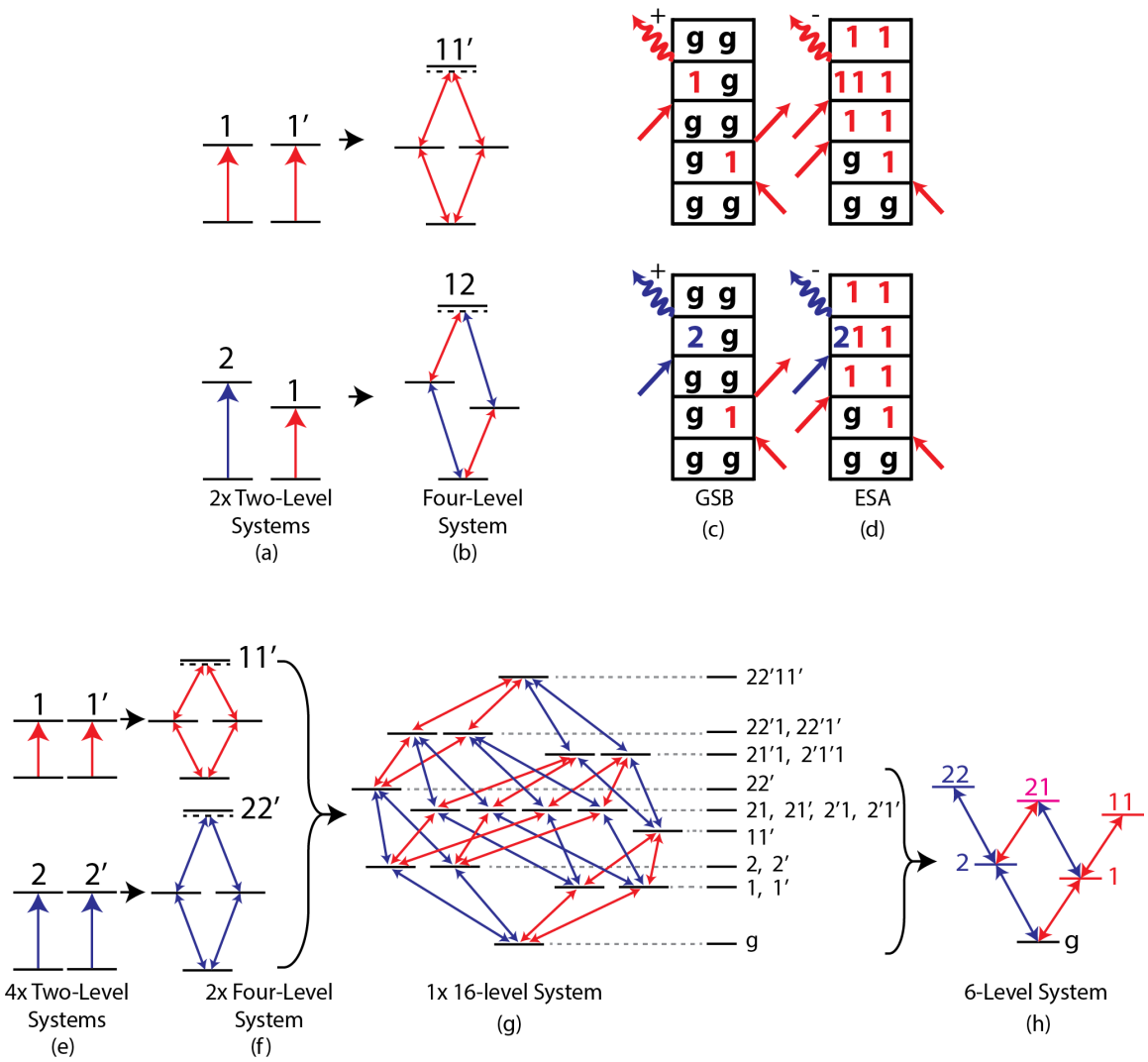

Figure 2.10: (a) Two degenerate (top row) and non-degenerate (bottom row) 2LS's. (b) The pairs of 2LS's in (a) can be re-written as a 4LS. In the absence of any kind of coupling, the pathways shown in (c) will cancel with the pathways in (d) and the 4LS will effectively reduce to a pair of 2LS's. (e) Four 2LS's made up of two pairs of degenerate 2LS's. The 4 2LS's can be rewritten as two 4LS's (f), or a 16LS (g). In the CMDS experiments in this thesis, we only consider correlations of up to two-particles so we ignore all states above 22'. Furthermore, the states that share the same emission energy (e.g. 21, 21', 2'1, and 2'1') are indistinguishable in the experiment, so we treat them as a single state and drop the ' from the notation. The 16LS therefore reduces to the 6LS shown in (h).

We will now briefly discuss the concept of the cancellation of signal pathways. First consider the 2-level systems (2LS) in Fig. 2.10a. The top row represents two systems with equal transition energies while the bottom row represents 2LS's with different transition energies. Focusing first on the top row, the two 2LS's (whether coupled or uncoupled) can be recast as a four level diamond system. If the 2LS's are coupled there is some difference between the $0\leftrightarrow1$ transition and the $1\leftrightarrow11$ transition. This difference could come, for example, in the form a shift of the transition energy, or a difference in the 1 and 11 dephasing rates.

If the 2LS's are uncoupled and the $0\leftrightarrow1$ and $1\leftrightarrow11$ transition energies and dephasing rates are identical, then the GSB and ESA pathways will exactly cancel. If, on the other hand, there is some difference between $0\leftrightarrow1$ and $1\leftrightarrow11$, GSB and ESA will not necessarily cancel. This same concept applies to 2LS's with different transition energies as well. As a result, if the 2LS's are uncoupled, then the ESA and GSB pathways will cancel and no CP will be generated. It should be noted that this concept does not assume anything about the physical mechanism underlying the difference between $0\leftrightarrow1$ and $1\leftrightarrow11$. It could be generated by some coupling of the transitions which shifts the transition energies, or (as has been suggested in [54]) by EID or EIS which affects the $0\leftrightarrow1$ and $1\leftrightarrow11$ differently.

If we have two pairs of degenerate 2LS's (as shown in Fig. 2.10e), each of the pairs can separately be formed into a 4LS (as shown in Fig. 2.10f). These 4LS's can then be combined into a 16 level system (16LS) as shown in Fig. 2.10g. If we consider only excitations of up to 2 particles, we are limited to an 11-level system. If we further consider only levels which have unique energies, this reduces to the 6LS shown in Fig. 2.10. This 6LS is useful in describing the pathways in 1Q, 0Q and 2Q 2D spectroscopy, and forms the basis for concepts discussed in the following paragraphs.

In Fig. 2.11 we show a tree diagram of all of the available pathways for two pairs of 2LS's with different transition energies recast as a 6-level triangle system. The pathways are broken down based on which of the one-exciton states (1 or 2) is excited by each pulse. F-L diagrams for a given pathway can be constructed by following the dashed lines from bottom to top. Time runs from bottom to top and the delays between the pulses are indicated on the right. The ordering of the transitions excited is given by the color of the top panel. This color also indicates where each pathway can be found on the cartoon 1Q and 0Q and 3D spectra in Fig. 2.12, Fig. 2.14 and Fig. 2.17, respectively.

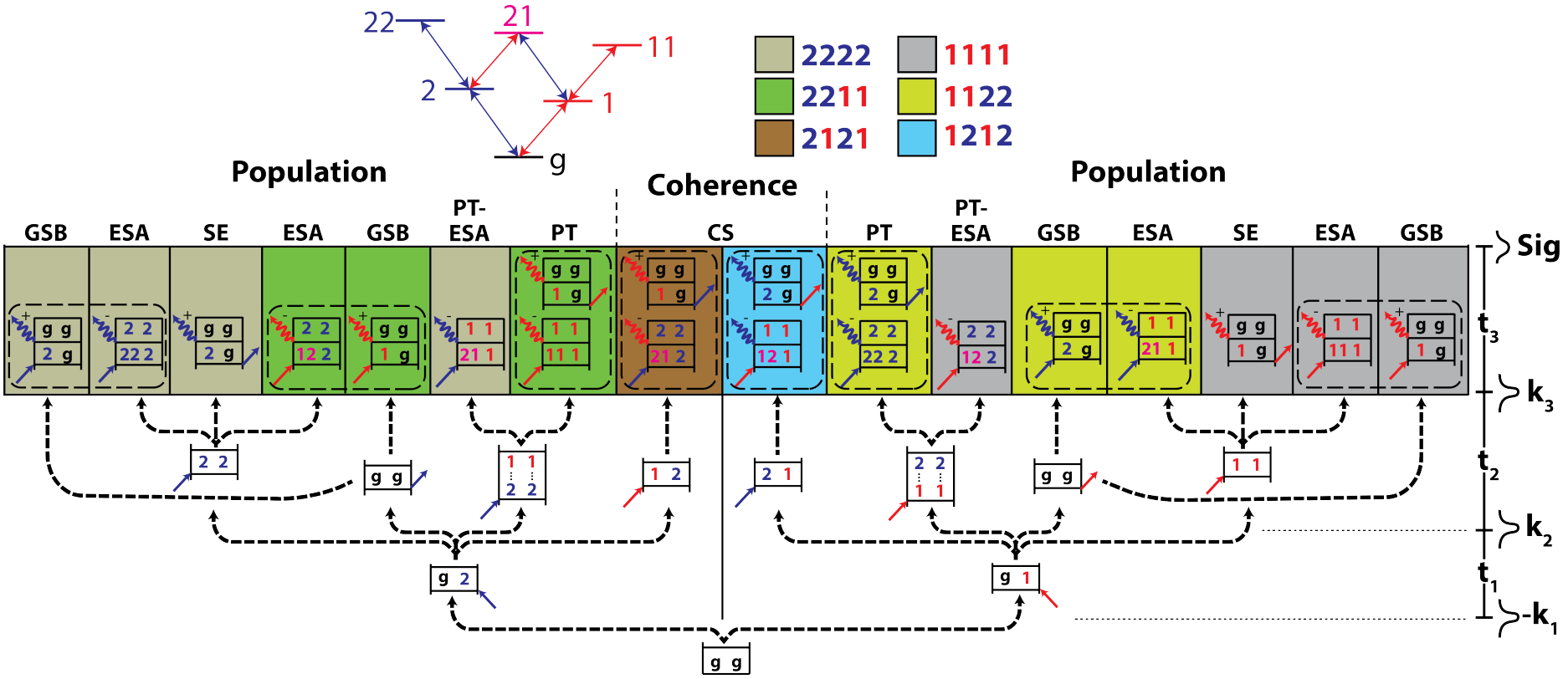

Figure 2.11: A tree diagram of all of the pathways available for two 2LS's recast as a single six-level system. F-L diagrams for each pathway can be constructed by following the tree diagram from bottom to top, following the dashed arrows. Time flows from bottom to top, the arrival of each pulse and the time delays between them are indicated on the right. Pathways are categorized as either population or coherence pathways. Population (Coherence) pathways involve a population (an excited state coherent superposition) during t_2. The color of the top panels indicate the order of the interaction of the pulses with different transitions and the position they appear in the 1Q, 0Q and 3D spectra in Fig. 2.12, Fig. 2.14 and Fig. 2.17, respectively. Pathways are grouped in pairs that cancel if the 2LS's are not coupled. The GSB and ESA involving only 1 or only 2 (in the grey and tan boxes) will cancel if the individual 2LS's within the ensemble are uncoupled. The CP pathways (in the yellow, green, brown and blue boxes) will all cancel unless 1 and 2 are coupled.

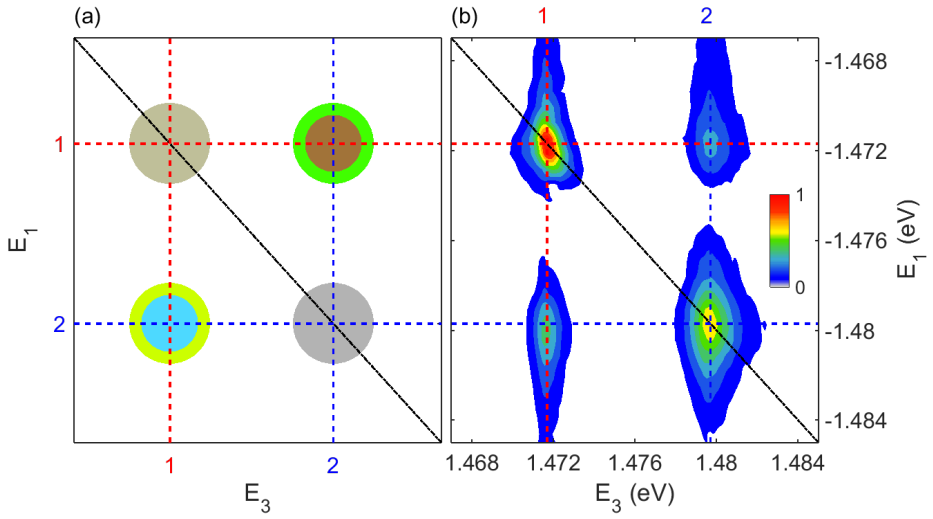

Figure 2.12: (a) A cartoon 1Q spectrum for two coupled 2LS's. The different peaks in the cartoon 2D spectrum are color coded according to the different types of pathways in Fig. 2.11. Teal and brown refer to the coherent superposition cross-peak pathways, yellow and green refer to the population cross-peak pathways, and brown and grey refer to the diagonal-peak pathways. The CPs are made up of both population and coherence pathways. (b) A 1Q spectrum of two coupled transitions in a double QW.

Considering all the available pathways in Fig. 2.11, we find several pairs of pathways with opposite signs that will cancel in the absence of coupling of the transitions. These pairs are indicated by the dashed boxes. This shows that in the absence of coupling, none of the CP pathways will generate signal. It also suggests that if the transitions are coupled we should see some CPs for both ESA-GSB and the difference between the two CS pathways.

We can break the pathways in Fig. 2.11 down into two general categories: 'population pathways' and 'coherence pathways'. Population (coherence) pathways are the pathways that involve a ground state or excited state population (a coherent superposition of excited states) during t_2. The only pathways that involve a coherent superposition of excited states are the four pathways in blue and brown. These coherence pathways are also the only pathways that are excited when the 2121 or 1212 pulse sequences are used.

The cartoon 1Q spectrum in Fig. 2.12a shows where we expect to see the various pathways from Fig. 2.11. The population CP pathways (yellow and green) overlap the coherence CP pathways. This illustrates why detection of CPs in a 1Q spectrum is not enough to definitively identify coupling in the form of coherent superpositions of excited states. A 2D 1Q spectrum with experimental data for two coupled transitions is shown in Fig. 2.12b.

As this cartoon shows, CMDS is capable of revealing many different peaks and is a powerful tool for identifying coupling of transitions. It should also be clear now, however, that there are issues and ambiguities in determining the pathway that lead to the CPs or determining the underlying mechanism. The next sections will

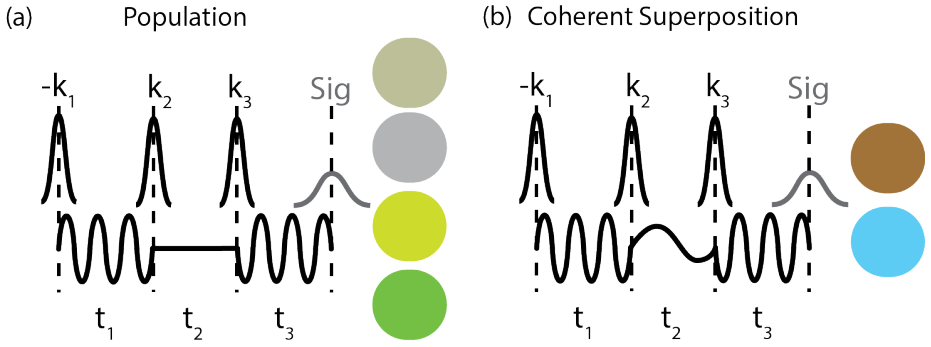

Figure 2.13: The phase evolution associated with (a) population pathways and (b) coherence pathways. The population pathways have no phase evolution in t_2, while the coherence pathways do. The coloured circles in (a) and (b) indicate which pathways appear in Fig. 2.11 involve phase oscillations in t_2, and where in the cartoon 1Q and 0Q spectra they appear.

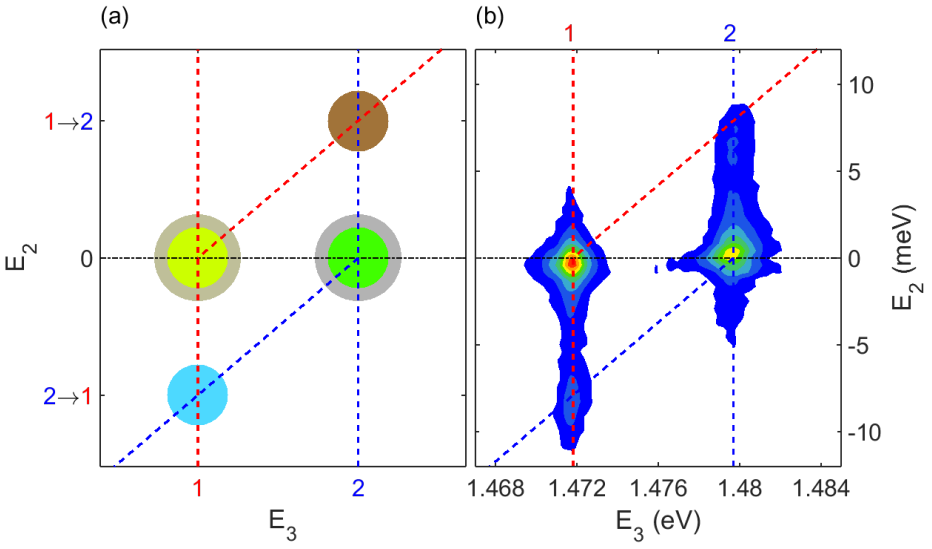

Figure 2.14: (a) A cartoon 0Q spectrum with peaks colored based on the pathways in Fig. 2.12a. (b) Example 0Q 2D spectrum.

show that 0Q and 2Q 2D spectra can add complimentary information that can be used to narrow down the coupling pathways while probing additional details.

2.2.1.2 *0-Quantum Coherence*

0-quantum coherence (0Q) spectra correlate the emission energy with the frequency of phase oscillations during t_2 (E_2), and can be used to separate coherence and population signals. As shown Fig. 2.8a 0Q spectra use the rephasing pulse ordering. However, t_2 is scanned instead of t_1, then data is Fourier transformed along t_2. As shown more clearly in Fig. 2.13a, population pathways do not exhibit phase oscillations as a function t_2, and therefore generate signals at $E_2 = 0$ eV. Coherence pathways, on the other hand involve an excited state superposition during t_2 and therefore do exhibit oscillations as a function of t_2. The period of the phase oscillations is set by the energy separation of the states in the superposition. This energy separation must be smaller than the laser spectral width for the excited state super-

positions in t_2 to be excited. As a result, the E_2 energy values are typically much lower than the E_3/E_1 energy.

When the Fourier transform is applied to the data along t_2, coherence signals are shifted away from $E_2=0$. Signals generated through the coherent superposition pathway can therefore be clearly separated from population signals (which all appear at $E_2=0$). This is a very important capability, as it is one of the only ways to definitively identify coherent superpositions. A cartoon 0Q spectrum is shown in Fig. 2.14d. The coherent superposition peaks can be seen in blue and brown, and are separated from the population signals (tan, light green, grey and dark green). An example of a 0Q spectrum with real data is shown in Fig. 2.14e. In the experimental chapters, coherent superposition peaks in 0Q spectra will be referred to as CPs (also coherent superposition CPs or CS-CPs), and $E_2=0$ signals will be referred to as diagonal-peaks (DPs).

Information can also be gleaned by studying the peak-shapes and widths of 0Q DPs and CS-CPs. DPs typically have a round or oval peak-shape with one of the axes aligned along the $E_2=0$ line. The width along E_3 is set by the full transition linewidth (homogeneous and inhomogeneous contributions), and the width along E_2 is limited by both the population lifetime, and the lifetime of the population grating (which depends on the carrier diffusion rate and the spacing of the population grating). In our experiment, the t_2 delay range is an additional limiting factor. The lifetime of the population grating and population lifetime are long compared with the delay range accessible in our experiment. The width of 0Q DPs along E_2 is thus largely a measurement of the pulse-shaper time window (as described in detail in section 2.4.10), and therefore only provides a lower bound on the population lifetime and the lifetime of the population grating.

Peak-shapes of the CS-CPs have been largely unexplored in the literature, but can be very useful in understanding details of the broadening of the different transitions. We will provide an analysis of some peak-shapes in section 4.3.4, and describe what peak-shapes we expect for homogeneous broadening, and correlated/uncorrelated inhomogeneous broadening.

2.2.1.3 *2-Quantum Coherence*

In 2-Quantum coherence (2Q) spectra, the pulse ordering is flipped so that the conjugate pulse (k_1 when detecting in the $-k_1+k_2+k_3$ direction) arrives last, as shown in Fig. 2.8b. To collect a 2Q 2D spectrum, the inter-pulse delay t_{2Q} is scanned (where t_{2Q} is the delay between the second pulse (k_3) and the third pulse (k_1)). A Fourier transform is then applied as a function of t_{2Q}.

In the 2Q pulse ordering, the first pulse generates a 1Q ground to excited state coherence. The second pulse then transforms this 1Q coherence into a coherence between the ground and doubly excited state, which is called a two-quantum (2Q) coherence. The phase of the 2Q coherence oscillates as a function of t_{2Q} with a

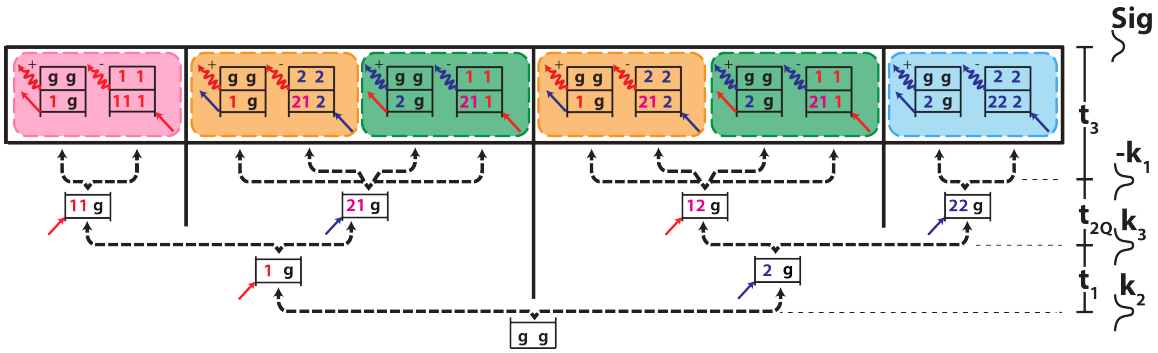

Figure 2.15: (a) shows Feynman diagrams for the full set of pathways in the 2Q pulse ordering. They are again grouped in pairs of overlapping signals with opposite signs, which are color coded according to their positions on the cartoon 2Q spectrum shown in Fig. 2.16a.

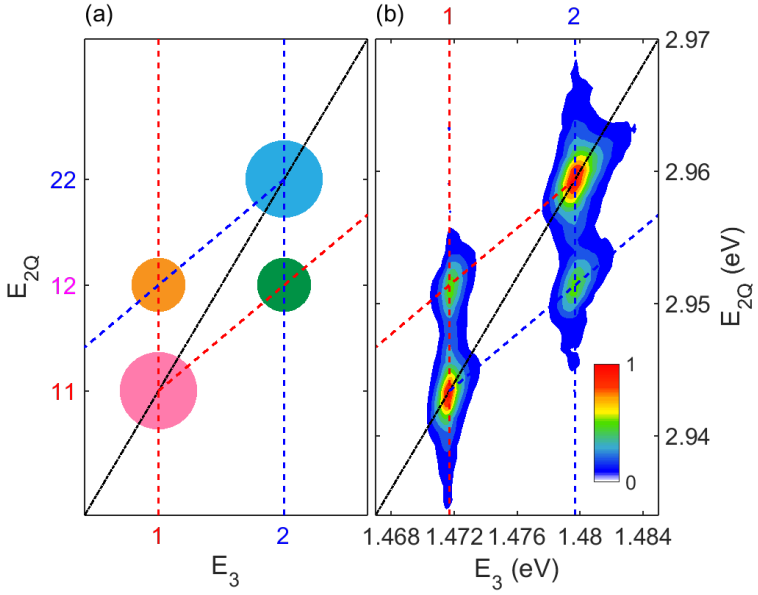

Figure 2.16: (a) A cartoon 2Q spectrum shown in which the pathways are indicated by the color of the peak indicates the pathways in Fig. 2.15. (a) Is an example 2Q spectrum with experimental data for a sample made up of two coupled 2LS's.

period (T_{2Q}) set by the energy difference between the ground and doubly excited states, which is equal the transition energy of the photons in the first two interactions (E_{k_2} and E_{k_3}):

$$T_{2Q} = \frac{\hbar}{(E_{k_2} + E_{k_3})} \tag{2.29}$$

In the simplest view of a 2LS, this pulse ordering should not generate any FWM signal. If we view the macroscopic polarization excited by the laser as an ensemble of isolated non-interacting 2LS's, a 2Q coherence should not be allowed because there is no transition at twice the single transition energy. We can recast these 2LS's as a four level diamond system (as in the top row of Fig. 2.10a), in which there is a state (11) with an energy twice the transition of the individual 2LS. Like similar pathways in the 1Q pulse ordering, all of the 2Q pathways which access the 11 state

have an overlapping pathway with opposite sign. In the absence of interactions between the individual 2LS's, all of the pathways still perfectly cancel, thus leading to no measured signal. This cancellation is illustrated in Fig. 2.15, which shows a tree diagram of all the 2Q pathways for a 6LS. The pathways are separated into pairs which overlap in the 2Q 2D spectrum with opposite sign (as we did for the 1Q pathways in Fig. 2.11). All of the 2Q pathways (including pathways leading to DPs and CPs) appear in pairs with opposite sign so if all the interactions between the transitions are ignored, all of the pathway pairs should exactly cancel and result in no 2Q signal.

However, 2Q signals have been observed in several different types of samples [81, 82, 86–88]. Previously, 2Q signals have also been detected using time-integrated FWM without measuring phase information [31, 89–91]. In QWs, these signals were found to be nearly as strong as signals in the rephasing pulse ordering [31, 91]. These signals have been explained phenomenologically by including many-body or two-body effects [31, 54, 79, 81, 82, 89, 90].

Like 1Q spectra, peaks in 2Q spectra can be separated into DPs and CPs. In 2Q spectra, peaks along the 2:1 line are referred to as DPs and peaks away from the 2:1 line are referred to as CPs. For DPs, the frequency of the phase oscillations of the 2Q coherence are twice that of the emitted photon (i.e. $E_{2Q} \approx 2 \cdot E_3$). This suggests and that all the interactions involved the same transition. In general, pathways in which the first two pulses interact with different transitions generate peaks away from the 2:1 line (i.e. CPs), and for which $E_{2Q} \neq 2 \cdot E_3$. The presence of CPs indicates that the system was in a mixed 2Q coherence during t_{2Q}. The mixed 2Q coherence for states A and B oscillates with a frequency set by the sum of the two transition energies (E_A and E_B).

$$\omega_{2Q} = \frac{E_{2Q}}{\hbar} = E_{k_2} + E_{k_3} \tag{2.30}$$

As a result, 2Q CPs do not occur at the same 2Q energy as either of the DPs for state A or state B. Instead, a CP involving transition A and transitions B will occur at E_{2Q} halfway between $2E_A$ and $2E_B$ (the E_{2Q} of the DP associated with states A and B respectively)[14].

A cartoon 2Q spectrum is shown in Fig. 2.16a. There are a total of four overlapping pathways that lead to each of the CPs. Qualitative and quantitative differences between these pathways have not been examined in detail. In Ch. 5 we will show that it is possible to separate these pathways using a selective approach. The colors of the peaks indicate where we expect to find the different pathways enumerated in Fig. 2.15a. An example 2Q spectrum with experimental data from a coupled double quantum well is shown in Fig. 2.16b. DPs and CPs can clearly be resolved. There

14 Assuming that the only states in the sample are A and B and two-exciton states involving A and/or B (which is typically the case in QW systems). If there are other states at higher energy, then more pathways and CP positions are possible.

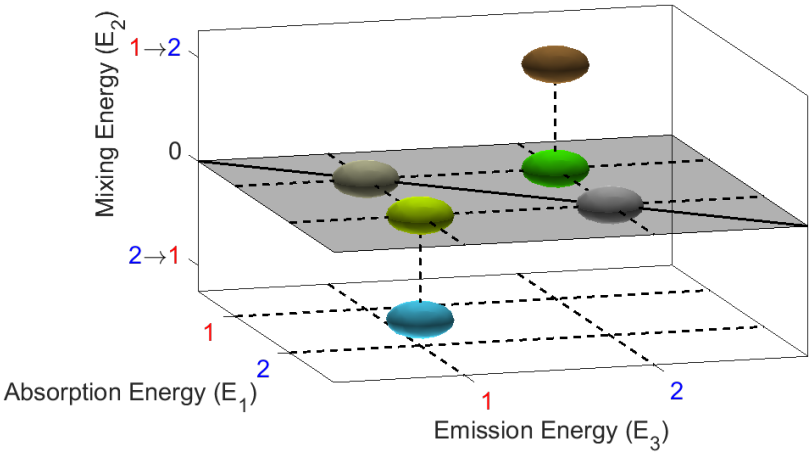

Figure 2.17: A cartoon of a 3D spectrum. Peaks are shaded according to the pathways in Fig. 2.12a. CPs generated by coherence pathways can be separated from CPs generated by population pathways along the E_2 direction.

is also a clear tilt to the peak-shapes. The source of this tilt is different from the source of tilt in 1Q DPs and CPs, and will be discussed in Section 7.3.1.

2.2.2 *Three-dimensional spectroscopy*

In 3D spectroscopy, two different time delays are scanned and signal is resolved along three different frequency directions. 3D electronic spectroscopy based on the $\chi^{(3)}$ nonlinearity is usually applied in the rephasing pulse ordering [76, 77, 92–95], but the 2Q pulse ordering has also been used [96].

A cartoon 3D spectrum for the rephasing pulse ordering is shown in Fig. 2.17. The color of the peaks indicates the F-L diagrams from Fig. 2.12 which appear at each peak position. Unlike the 1Q and 0Q 2D spectra, each of the peaks has only a single color, so there are fewer overlapping pathways. All peaks that arise from population pathways remain in the E_2=0 plane, while all the CPs that arise from coherence pathways are shifted away from E_2=0, as in a 0Q 2D spectrum. The population CPs can be separated from the population DPs in the E_3 and/or E_1 directions, as in a 1Q 2D spectrum.

Though they are much more time consuming to collect, we can access information in 3D spectra that cannot be accessed through the different 2D spectra. Furthermore, in some cases two frequency dimensions is not enough to fully separate signals. For example, samples with closely spaced transitions or significant inhomogeneity can lead to overlapping CPs in 1Q and 0Q spectra. 3D spectroscopy can help can help in separating these pathways, as they can be resolved along a third frequency direction. A good example of this can be seen in the 3D spectrum in Fig. 6.12 in Chapter 6. The CS-CPs are overlapped in the projection of the 3D spectrum onto E_1 vs. E_3 (which is equivalent to the 1Q spectrum at t_2=0 fs), but can be clearly separated in the 3D data.

As the signal is separated over three frequency dimensions instead of two, coherence peaks can also be more easily identified and separated from noise and artifacts. The peak must satisfy the criteria that $E_2 = E_3 - E_1$ to be a coherence CP[15]. In a 3D spectrum we have all three values, which provides an additional confirmation of the peak designation. On the other hand 0Q spectra only give us E_3 and E_2, so we have to assume E_1. In some cases this is reasonable, but in spectra which are noisy and/or congested or in which the coherence signal is very weak, having the additional check is important.

3D spectra also allow us to generate a fourth type of 2D spectrum which is not possible without collecting an entire 3D spectrum. These E_1 vs E_2 spectra can be generated by taking slices from a 3D spectrum for a particular E_3 (emission energy) or t_3 value[16]. This type of 2D spectrum is useful for both separating peaks and confirming that the criteria for coherent superpositions are satisfied.

Finally, if the coherence peak can be isolated in 3D spectral space, we can apply some of the peak-shape analysis tools CMDS provides. In particular, E_3 vs E_1 peak-shape analysis is very useful, and cannot be used on coherent superposition CPs in either 1Q or 0Q 2D spectra. E_3 vs E_2 and E_1 vs E_2 spectra also provide useful information about the nature of the broadening. More details on this type of analysis is provided in section 4.3.4.

2.3 Pathway selection

Generally, CMDS is performed with three identical broadband pulses with either collinear or cocircular polarization. One of the major advantages of this approach is that it simultaneously excites and probes all the available quantum pathways within the pulse bandwidth[17]. This broad excitation provides a rich variety of information simultaneously in a single scan, which can be very advantageous. This ceases to be an advantage if the pathways of interest overlap or are obscured by other pathways in the 2D or 3D spectra. A good example of this is in the CPs of a 1Q 2D spectrum, where at least four separate quantum pathways can lead to overlapping signals as demonstrated in Fig. 2.12. These overlapping signals can introduce ambiguity into the interpretation of CPs when they arise in experimental data. Furthermore, if specific signals can be isolated without having to collect an entire 2D or 3D spectrum then acquisition time can be reduced. This can prove useful when the goal is to study the effect of some other variable on a particular pathway. In such a situation the long acquisition times required for 3D spectroscopy might be prohibitive, while the reduced acquisition time of a selective experiment would make the experiment feasible.

15 Assuming once again that there are only one exciton transitions and two exciton transitions involving the one exciton transitions (which is typically the case in QW systems). If there are other states at higher energy then coherence CPs can appear away from $E_2 = E_3 - E_1$.

16 Or by integrating across all E_3/t_3 values for the entire spectrum, which in many cases is not as useful.

17 Co-circular polarization suppresses some biexciton pathways which must be formed by opposite spin excitons.

For these reasons, considerable effort has gone into the development of methods of limiting the quantum pathways that are excited or enhancing certain pathways while suppressing others. I will call this general set of approaches pathway-selection as they involve selectively exciting the pathways of interest while suppressing others. Pathway selection has been implemented in a number of ways: by spectrally tuning the excitation spectra to different transitions, by controlling the polarization of the beams to limit pathways, or through spectral phase shaping of the beams to enhance pathways. All of these approaches have strengths and weaknesses, and may suit different types of samples or experimental goals.

2.3.1 *Pathway selection using spectrally tuned pulses*

One way that pathway selection can be employed is by using excitation beams which don't all share the same excitation spectrum, and therefore aren't all resonant with the same transitions. Pulse sequences can then be generated that exclusively excite specific signal pathways. For example, by using k_1 and k_2 beams which are resonant with different transitions (e.g. X_1, and X_2 respectively), the coherent interactions between X_1, and X_2 can be studied. This is conceptually similar to heteronuclear NMR, in which different sequences of nuclear spins are selectively excited. The links between heteronuclear NMR and pathway selection with spectrally tuned pulses are explored Section 5.1.

Two examples of such an approach to isolate quantum pathways can be seen in Fig. 2.18, which shows how coherent-superposition and population CPs can be isolated. A more in-depth analysis of the approach, and how it can be applied to 1Q and 0Q spectra to extract additional information is presented in Section 4.2. Pathway selection using shaped pulses can also be used in 2Q spectra to isolate mixed two-exciton states, as shown in Chapter 5.

Pathway selection has been implemented in FWM experiments by using two optical parametric amplifiers (OPAs) tuned to different transitions [97, 98]. However, the instabilities intrinsic to the non-linear processes used to generate the pulses in the OPAs and the application of delays (using translation stages) lead to a lack of phase stability, which prevents the acquisition of the phase information necessary for 2D spectroscopy. This precludes the use of dual OPAs for pathway selective 2D spectroscopy detected in the time domain. This approach has, however, still been used to gain an in-depth understanding of coherent-coupling in light harvesting complexes by allowing access to details that are hidden in 2D spectra with broadband excitation [97, 98]. The Wright group [99–101], has used dual OPAs in a mixed time/frequency domain approach to build up 2D spectra. The spectra are collected by using comparatively narrow (~5-40 meV [99, 101]) spectra out of the OPAs, and then scanning the spectral position of one or both of the OPA spectra.

The lack of stability between the OPAs still prevents them from detecting the phase of the signal, but they can still uncover coupling between transitions in this way.

Another way to generate excitation pulses which don't share the same spectra is to narrow an initially broad spectrum from an ultrafast laser pulse. By individually narrowing the excitation beams, a sequence of pulses can be generated such that the pulses are only resonant with different sample transitions. This approach has the benefit that it can be integrated into passively phase stabilized experiments. One way that the pulse spectra can be individually controlled in this fashion while still maintaining phase stability is using a pulse-shaper capable of spectral amplitude shaping. In Ch. 4 and published in Ref. [95] we demonstrate how this pulse-shaper based method of pathway selection can be applied in 1Q 2D and 3D spectroscopy to isolate coherent interactions between different transitions. The results in this paper are also presented in Chapter in more depth. Senlik et al. [67] have also recently reported a similar experiment using a pulse-shaper to tune the first two pulses to different transitions. Instead of scanning t_1 and performing a Fourier transform along that axis, they scan and Fourier transform t_2. In the language that has been used in this thesis, this could be called a pathway-selective 0Q spectrum. By acquiring data with and without pathway selection, they showed that much of the same information could be extracted from both, but that the signal to noise and acquisition time were both significantly improved when pathway selection was used. They go on to point out that this reduced acquisition time allows them to probe a specific signal pathway while varying some other parameter (e.g. temperature or excitation density).

The coherent dynamics of some systems are also dependent on both the excitation density used in the experiment and which transitions are excited by the laser pulses. For example, the measured linewidths and transition energies of excitons in QWs depends on the excitation density. In particular, linewidths of QW excitons are increased significantly when free carriers are also excited in the QW. For this reason, experiments are usually conducted so that they excite as few free-carriers as possible. In some cases this is not possible (for example if one of the excitonic resonances of interest spectrally overlaps the free-carrier signal). When broadband excitation is used in such experiments, all three of the pulses are necessarily resonant with the free-carriers. By using pathway selection with spectral shaping, we reduce the number of pulses that are resonant with the free-carriers, and thus reduce the overall number of free-carriers excited in the experiment. This can mitigate the effect of the free-carriers on the dynamics of interest while still exciting the signal we are after.

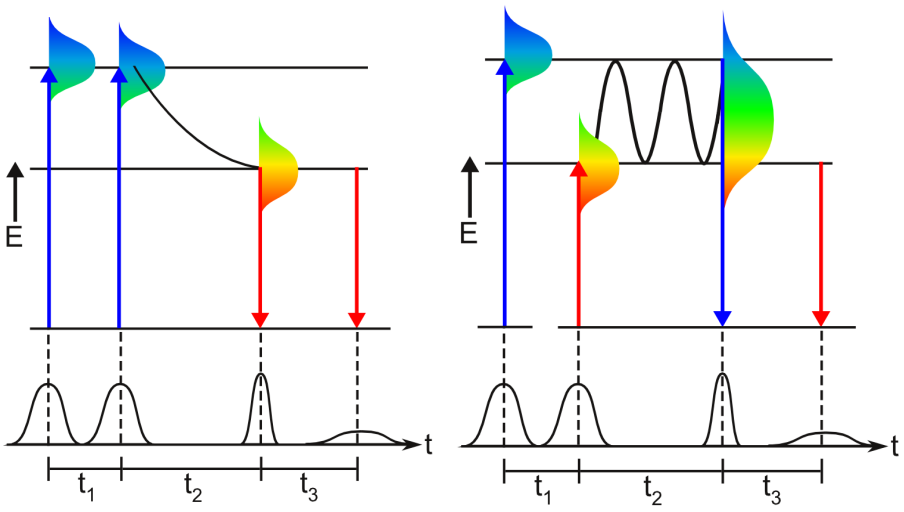

(a) Population Transfer (b) Coherent Superposition

Figure 2.18: Spectral pathway selection sequences to isolate the (a) population transfer and (b) coherent superposition pathways.

2.3.2 *Pathway selection with temporal shaping*

The basic idea of the temporal shaping approach to pathway selection is that the electric field of the excitation pulses can be modified such that particular pathways are either enhanced or suppressed. The new waveform can be a simple change of the input pulse (for instance, splitting the single pulse into a pair of pulses) or much more complex, arbitrary waveforms designed to fulfil some specific role at the sample. To that end, pulse-shapers are used to shape the phase (and in some cases the amplitude) and thereby modify the temporal evolution of the electric field of the excitation pulse(s). The pulse-shaper can be used to split the single input pulse into a train of pulses [102] or shape it into an arbitrary waveform [103].

In many ways, this approach is similar to the idea of coherent control, in which specially shaped pulses are used to control dynamical processes through the interference of quantum pathways in the sample [104, 105]. Typically, a fs pulse is passed through a pulse-shaper and then is incident upon a sample while some sort of output from the sample is monitored (e.g. photoluminescence or photocurrent). Pulse shaping is then used to optimize the electric field of the pulse for a particular output - for example, amplifying the photoluminescence from one chromophore while suppressing photoluminescence from another one. This optimization can be conducted manually (e.g. systematically varying the relative phase or delay of a double pulse) or through iterative/adaptive algorithms to find the ideal pulse shape for a desired output. The original intention of coherent control was to enhance or suppress chemical reactions through the control of wavepackets [105], but it has been now been used to control a variety of processes, including excitons in QWs [106–108] and QDs [109].

Temporal shaping based pathway selection approaches (similar to coherent control) have recently been used in multidimensional spectroscopy experiments. Wen and Nelson [110] recently demonstrated that temporally shaped pulses could be used to enhance different pathways in 1Q and 2Q spectra of a multi-QW. They used a double pulse in place of the third excitation pulse and found that by varying the relative phase and delay they could amplify either the HH or the LH exciton emission, and also in certain cases amplify CPs that were difficult to resolve using standard techniques.

Prokhorenko et al [111, 112] used temporal shaping to study Rhodamine 101. They used a pulse-shaper to generate a pulse with amplitude and phase profiles optimized for energy transfer in a previous experiment [113]. This optimized pulse shape was applied to the first and second excitation pulses. This did not result, however, in the appearance of population transfer CPs, but rather the appearance of fine structure (sharp peaks) along the absorption axis. They were unable to explain this result explicitly, but pointed out that the state preparation had significant effect on the resulting spectra.

The work by Wen and Prokhorenko show that there is some promise in using temporal shaping as a method of pathway selection in multidimensional spectroscopy, particularly as a means of the enhancing CPs from well defined excitonic resonances in QWs. However, there is clearly a lot of work to be done in fully understanding what effect this more complex state preparation has on the 2D spectra that result.

2.3.3 *Pathway selection with polarization control*

The polarization of the four optical fields can also be used as a form of pathway-selection. For instance, in molecular systems, different pathways can be suppressed, enhanced or removed entirely with different sequences of linearly polarized pulses [80, 86, 97, 98, 114]. These approaches were developed in 2D-IR experiments studying vibrational modes [16, 115–117], but have more recently been used in 2D studies of electronic transitions as well [11, 80, 86, 114]. For example, Read et al [114], performed 2D spectroscopy on the Fenna-Matthews-Olson light harvesting complex in which the first two pulses were linearly polarized with angles of $+\pi/3$ and $-\pi/3$, respectively. This sequence was shown to nearly eliminate DPs while simultaneously enhancing CP pathways, which enabled the observation of CPs which were otherwise hidden by the overlapping, much stronger diagonal contributions. Linear polarization sequences can also be used to measure structural characteristics, such as relative dipole angles in isotropic molecular systems [118].

Polarization selectivity has also been combined with spectrally tuned pulses. This has been done in FWM mixing experiments where the additional selectivity helped to determine nature of coherences in a light harvesting complex (vibrational, electronic or vibronic) [97, 98]. This same polarization based pathway selection ap-

proach was used by Westenhoff et al [11] to identify coherent electronic coupling in the reaction center of Rhodobacter sphaeroides bacteria using 2D spectroscopy with co-resonant excitation pulses.

Pathway selection with linear polarization works well on samples with well defined linear dipole moments. In semiconductor nanostructures, excitonic resonances are characterized by angular momentum rather than a linear transition dipole, so circular polarization of the optical fields can provide additional details. Pulse sequences with different circular polarization directions have been used in investigations of QWs to identify contributions from biexcitons [80] and mixed biexcitons [86]. Linear and circular polarization sequences have also led to the observation [81] and reduction [80] of many-body effects in QWs.

2.4 SLM based CMDS apparatus

This section describes the CMDS apparatus that was implemented as part of my PhD research. This experimental setup was used to perform the studies on QW coherent dynamics outlined in the following results chapters, and was modelled on the COLBERT experiment which was developed at MIT by Turner et al [62, 63, 119]. A block diagram of the Swinburne CMDS experiment is shown in Fig. 2.19, and a detailed experimental layout is shown in Appendix A2. The output from a Titanium-sapphire oscillator (KMLabs Collegiate, 500 mW, 5 nJ, 92 MHz) is split into four beams by a Fourier beam-shaper. These four beams are then imaged using a 4-F imaging system to an ultrafast pulse-shaper. The diffraction based pulse-shaper is used to alter the temporal and spectral characteristics of the beams, which are then focussed and overlapped at sample (again using 4-F imaging geometry). The generated signal then co-propagates along with the local oscillator into a spectrometer (IsoPlane 320, 1200 g/mm, 785 blaze, 0.15 nm resolution) where it is detected using spectral interferometry.

The following sub-sections provide more details about the various components and explain how they are used and optimized.

2.4.1 *Oscillator*

The pulsed laser source used in these experiments is a mode-locked Titanium-sapphire (Ti:Sapp) oscillator. Ti:Sapp oscillators are an effective tool to study ultrafast dynamics in QWs due to their relative simplicity, stability and high rep rate (compared with amplified systems). The oscillator used in this experiment is a KMLabs Collegiate that is supplied as a kit. It is assembled (using standard optical mounts) directly on a breadboard bolted to the optical table, which makes it very adaptable and easily maintained. The ‘Collegiate’ is capable of producing pulses with bandwidths of ~20 nm up to ~95 nm, which (when transform limited and cen-

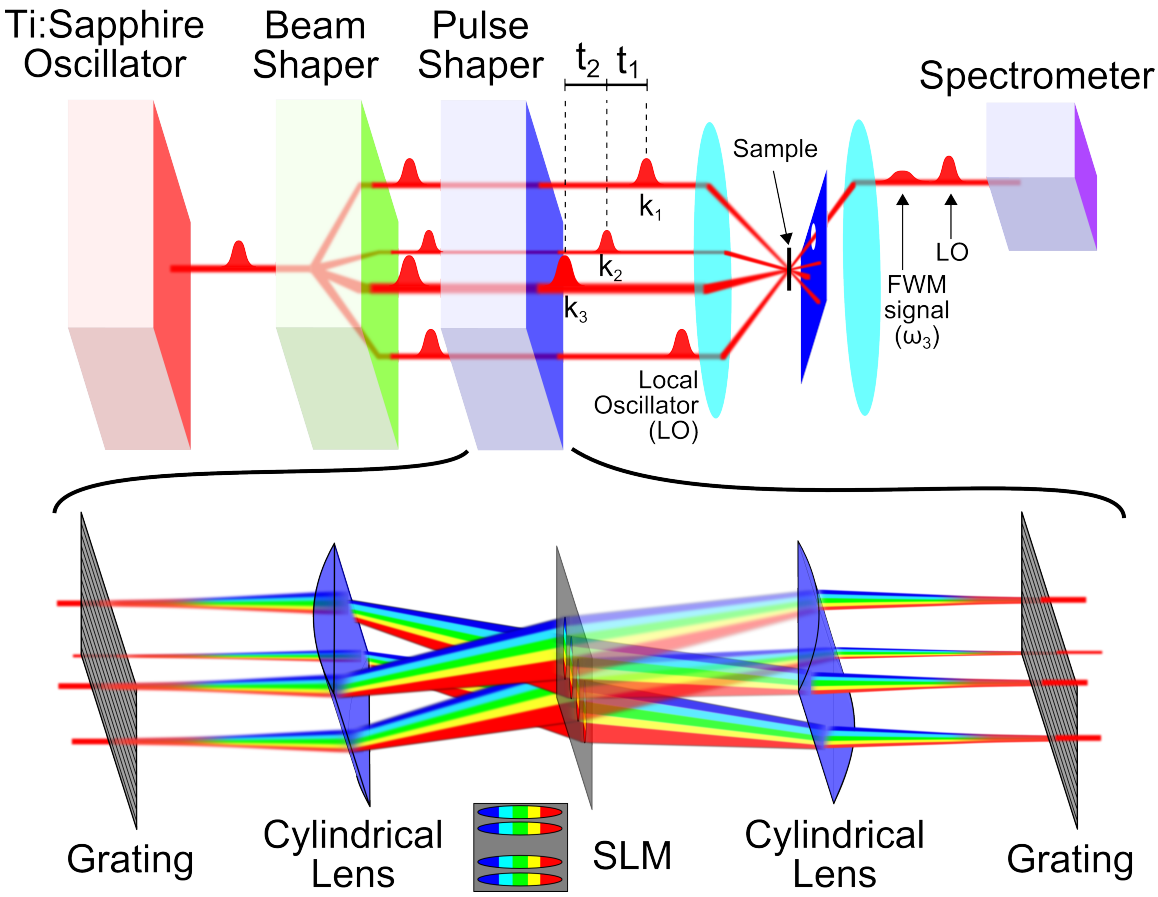

Figure 2.19: A block diagram of the CMDS experiment, with a detail of the pulse-shaper. The pulse-shaper is depicted in transmission geometry for simplicity, but is actually used in reflection geometry in the experiment. Similarly, the sample is also typically studied in reflection geometry, though transission geomety is also possible. A detailed diagram of the CMDS apparatus is provided in Appendix A2.

tred at 800 nm) supports pulses from ~50 fs down to ~10 fs. The center of the pulse spectrum is tunable from 760 nm to 830 nm. For the experiments in this thesis, the oscillator is set to ~35 nm bandwidth (transform limited pulse duration of 30 fs) to match the ideal pulse-shaper bandwidth (explained in more detail in section 2.4.3).

The Collegiate cavity is designed such that the Ti:Sapp crystal is between the phase compensation prisms and the output coupler. In this design, the final pass through the crystal is not phase compensated by the prisms, leading to imperfectly compressed pulses due to self-phase modulation and quadratic phase accumulated in the crystal. To compensate for this additional spectral phase, a prism compressor is placed after the oscillator in a double pass configuration [120]. This prism compressor is also used to pre-compensate for the spectral phase accumulated by passing through the rest of the optics in the experiment, which delivers optimally compressed pulses at the sample position. Fine tuning of the compression of the individual excitation beams is accomplished using the pulse-shaper, and described in Section 2.4.5.

2.4.2 *Beam Shaping*

A Fourier beam shaper based on a spatial light modulator is used to split the oscillator output into four beams in the box geometry. This is accomplished in the following way: an f=200 cm lens focuses the beam to a ~800 um spot on the SLM surface. A 2D phase pattern is applied to the SLM which splits the incoming beam into four beams in a rotated box geometry. These beams are then collimated using an f=75 cm lens.

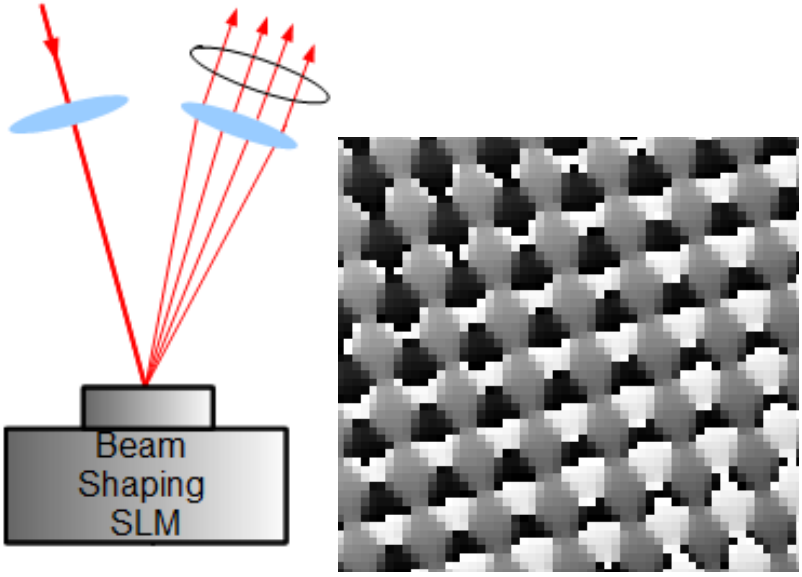

(a) (b)

Figure 2.20: (a) diagram of the Fourier beam shaper. (b) A typical spatial phase pattern for a four beam output.

The phase pattern is generated in the following way. First, a 2D map ($I(x,y)$) is generated with the desired beam geometry. A 2D Fourier transform is then applied to convert 2D real space map into an inverse space representation of the beam geometry: $\hat{I}(k_x,k_y)$. The angle (phase) of $\hat{I}(k_x,k_y)$ is then scaled to match the SLM pixel size, and sent to the SLM.

The phase pattern on the SLM modifies the incident beam in the following way. The incoming beam has an ideally flat phase-front when it reaches the lens in front of the beam shaping SLM. This lens performs a Fourier transform of the real-space laser profile, imaging the inverse space beam exactly to the surface of the SLM. The phase pattern on the SLM then modifies the wavevectors of the incident beam so that the reflected beam travels out with a modified angular dependence. The second lens then performs another Fourier transform returning the beam to 'real' space. The wavevectors that were imprinted onto the incoming beam are thereby returned to the 'real' space pattern of the desired beam geometry ($I(x,y)$). The resulting beam pattern generally closely resembles the input beam parameters. The number of beams, beam geometry, and relative power can all be precisely controlled using the beam shaper in this way.

The major benefit of using a beam shaper (instead of, for instance, a diffractive optic element or a spatial filter) is the beam geometry can be easily tailored to the needs of the experiment. In the CMDS experiments presented here, the box geometry is ideal, but for higher order experiments, other geometries are required. With this beam shaper switching between them is straight forward and instantaneous. Furthermore, the beam shaper can also be used to control the power and size of the beam which can be useful in certain situations.

While SLM based Fourier beam shaping is quite flexible and powerful, it is not without limitations. In addition to the desired beams, additional 'ghost' beams are generated because of the pixelated nature of the SLM. These 'ghost' beams can be thought of as higher diffraction orders (like the second order diffraction off of a linear grating), or diffraction in the opposite direction (like the m=-1 diffraction from a linear grating). Some of the power from the input beam also remains in the zero-order undiffracted beam. Altogether, the diffraction efficiency into the four beam box pattern is around 60% for this beam shaper.

2.4.3 *Pulse-shaping*

The beams generated by the beam shaper are imaged to a pulse-shaper based around a second, identical 2D SLM. The pulse-shaper is a powerful tool to manipulate the temporal and spectral properties of ultrafast pulses. This section will discuss the basic concepts of pulse-shaping and how it is used in this CMDS experiment.

2.4.3.1 *Pulse shaping principles*

A pulse-shaper is a tool that can be used to adjust the temporal and spectral characteristics of an ultrafast pulse. Devices which directly light as a function of time (be they mechanically or electrically) are limited to time scales in the ps-ns region, and are therefore useless in directly modifying the temporal characteristics of fs pulses. They can be used to precisely modify the temporal characteristics of fs pulses by exploiting the Fourier transform relationship between the pulse's spectrum and its temporal profile. By adjusting the spectral phase, the temporal shape of the pulse can be changed: it can be stretched, compressed, split into multiple pulses and/or shifted in time.

An ideal fs pulse can be thought of as a continuum of spectral components which add together constructively at one point in time and destructively everywhere else. The variation of the phase across the spectrum is called the spectral phase. The shortest period of constructive interference will occur when the spectral phase is constant (i.e. it doesn't change across the spectrum). A pulse with constant spectral phase is said to be bandwidth limited or transform limited. If the spectral phase is altered, the period of time in which there is constructive interference of the spectral

components changes shape and may be shifted in time. For example, by applying a spectral phase that varies linearly with frequency, the pulse can be shifted in time. This is equivalent to the well known Fourier-shift theorem [121]: a spectral phase gradient in one domain leads to a shift in the Fourier domain, which can be proven as follows. $E(\nu)$ is the pulse electric field in the frequency domain, $\hat{E}(t)$ is the electric field in the time domain, and the two are related by a Fourier transform: $\hat{E}(t) = \mathfrak{F}^{-1}[E(\nu)]$ and $\mathfrak{F}[\hat{E}(t)] = E(\nu)$. If we shift the electric field envelope by an amount t_0, then the Fourier transform of $\hat{E}(t)$ is:

$$\mathfrak{F}^{-1}[\hat{E}(t-t_0)] = \frac{1}{\sqrt{2\pi}} \int_{-\infty}^{\infty} dt\, \hat{E}(t-t_0) e^{i\nu t} \tag{2.31}$$

If we let $u = t - t_0$, then $t = u + t_0$ and $du = dt$. If we then substitute these into Eq. 2.31, we get:

$$\begin{aligned} \mathfrak{F}^{-1}[\hat{E}(t-t_0)] &= \frac{1}{\sqrt{2\pi}} \int_{-\infty}^{\infty} du\, \hat{E}(u) e^{i\nu(u+t_0)} \\ &= \frac{e^{i\nu t_0}}{\sqrt{2\pi}} \int_{-\infty}^{\infty} du\, \hat{E}(u) e^{i\nu u} \\ &= e^{i\nu t_0} \mathfrak{F}^{-1} \hat{E}(u) \\ &= e^{i\nu t_0} E(\nu) \end{aligned} \tag{2.32}$$

Thus the amount of phase applied to the pulse for a given time delay is then given by

$$\Phi = \nu t_0 \tag{2.33}$$

Pulse-shapers can therefore be used to shift fs pulses in time simply by applying a phase gradient that is linear with spectral frequency according to Eq. 2.34, where t_0 is the time delay applied, $\Delta\phi$ is the change in phase for a given frequency step $\Delta\nu$.

$$t_0 = \frac{\Delta\phi}{\Delta\nu} \tag{2.34}$$

A non-linear spectral phase will lead to different parts of the pulse spectrum interfering constructively at different points in time, and subsequently leads to an elongation of the duration of the pulse. Such non-linear spectral phase arises naturally in optical experiments as a result of dispersion in glass and dielectric/metal mirrors. In dispersive materials, the index of refraction depends on the wavelength of light. Thus, even though all the spectral components travel through the same

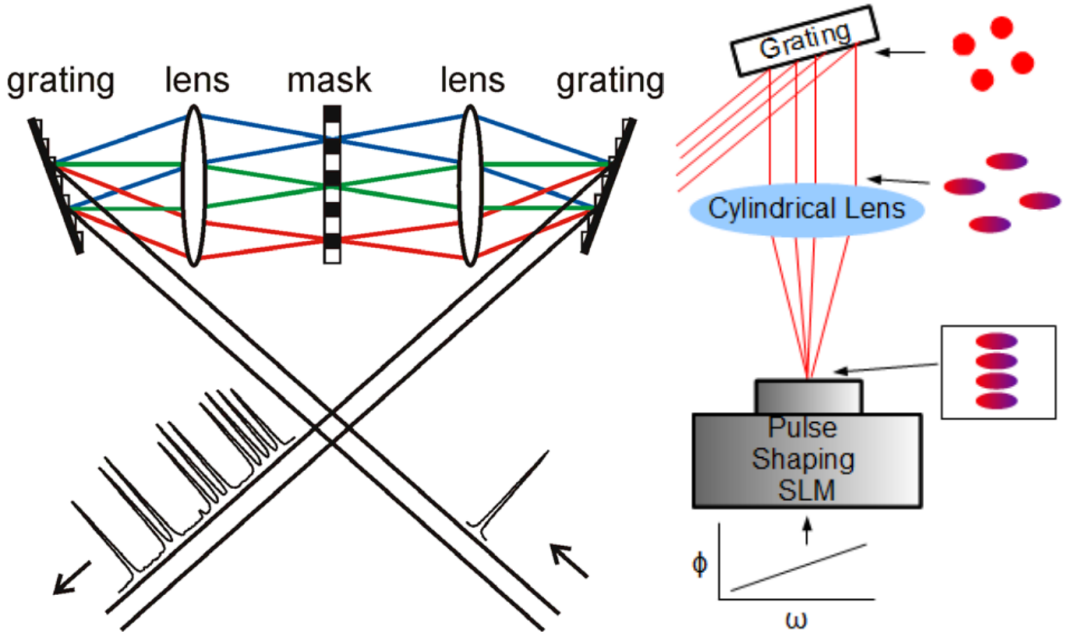

(a) (b)

Figure 2.21: (a) Transmission geometry pulse-shaper. Reprinted with permission from Ref. [122]. (b) Reflection geometry four-beam pulse-shaper as used in the CMDS experiment.

physical thickness of material (L), the optical path length (L^O) depends on wavelength:

$$L^O(\lambda) = n(\lambda) \times L \tag{2.35}$$

After passing though a dispersive optic, a phase delay set by the spectral dependence of the index of refraction (the material dispersion) will be applied to the pulse spectrum. If the material dispersion is non-linear, this phase delay will appear in the form of a quadratic (or higher order) spectral phase. pulse-shapers can be used to compensate for this accumulated higher order spectral phase and produce fully compressed, transform limited pulses at the sample.

2.4.3.2 *Experimental implementation*

This section will describe how pulse-shapers are generally implemented experimentally. A pulse-shaper typically consists of three main parts. First, a dispersive optical element such as a prism or a grating which disperses the beam. Second, a 1-dimensional focusing element (such as a cylindrical lens (CL) or a cylindrical mirror (CM)) that focuses the beams along spectrally dispersed axis. Finally there is an optical element that can precisely adjust the phase of the beam (such as an SLM).

The CL/CM is placed exactly one focal length from both the grating/prism and from the SLM. Each of the spectral components of the pulse is focused to a different point along the width of the SLM. The phase of a particular spectral component can

therefore be adjusted by changing the voltage applied to the SLM pixel it is incident upon.

In transmission geometry pulse-shapers (Fig. 2.21a), which use transmissive SLMs to shift the spectral phase, an identical set of optics (CL/CM and grating/prism) is needed re-compress and re-collimate the beam after passing through the SLM. Reflection geometry pulse-shapers (Fig. 2.21b) use reflective SLMs or microelectromechanical (MEMS) devices. In this geometry, the beam is reflected back though the same optics which re-collimate the beam and re-compress the pulse. The SLM can then be angled slightly up or down, so the shaped, reflected beam can be picked off from the incoming beam.

2D reflective SLMs can be used to shape multiple beams simultaneously (as shown in Fig. 2.21b). The pulse-shaper used in the apparatus described in this thesis is configured for four or five beams. The rotated box geometry allows each of the beams to be spectrally dispersed and focused across a different vertical region of the SLM surface. This allows each of the beams to be shaped simultaneously by applying separate spectral phase patterns to each region.

2.4.3.3 *Diffraction based pulse shaping and spectral amplitude shaping*

A 2D SLM also allows the implementation of diffraction based pulse shaping [61]: instead of angling the SLM down to pick off the shaped beams, a vertical phase grating pattern[18] is applied as shown in Fig. 2.22a. This vertical pattern is combined with horizontal phase masks which shape the spectral phase (Fig. 2.22c,d). The un-diffracted light simply reflects straight back along the incoming path, but the first order of diffraction can be picked-off. This has a number of important advantages. First, this reduces the prevalence of replica pulses (more on them later in this section) [61]. Second, the beams can be 'turned off' at will at the pulse-shaper which is useful in alignment and in experiments that involve only one or two beams. Third, using the depth of the diffraction pattern, the spectral amplitude the pulses can be modified.

A vertical sawtooth phase pattern with 2π depth maximizes the pulse energy diffracted into the first spatial order, and is used when no spectral shaping is to be employed. By reducing the depth of the phase grating, the amount of pulse energy diffracted into the first order can be reduced, as shown in Fig. 2.22b. The depth of the grating can be adjusted as a function of wavelength or frequency using spectral amplitude masks such as the ones in Fig. 2.22e. The varying diffraction efficiency across the spectrum generates diffracted beams with narrowed spectra, as shown in Fig. 2.22f, for example.

This can then be used to 'tune' the excitation spectra. The frequency is not actually shifted, but by reducing one side of the spectrum to zero, the central frequency of the shaped spectrum is shifted and the spectral width is reduced. Importantly,

18 This grating can also be equivalently thought of as a vertical phase gradient which is phase wrapped.

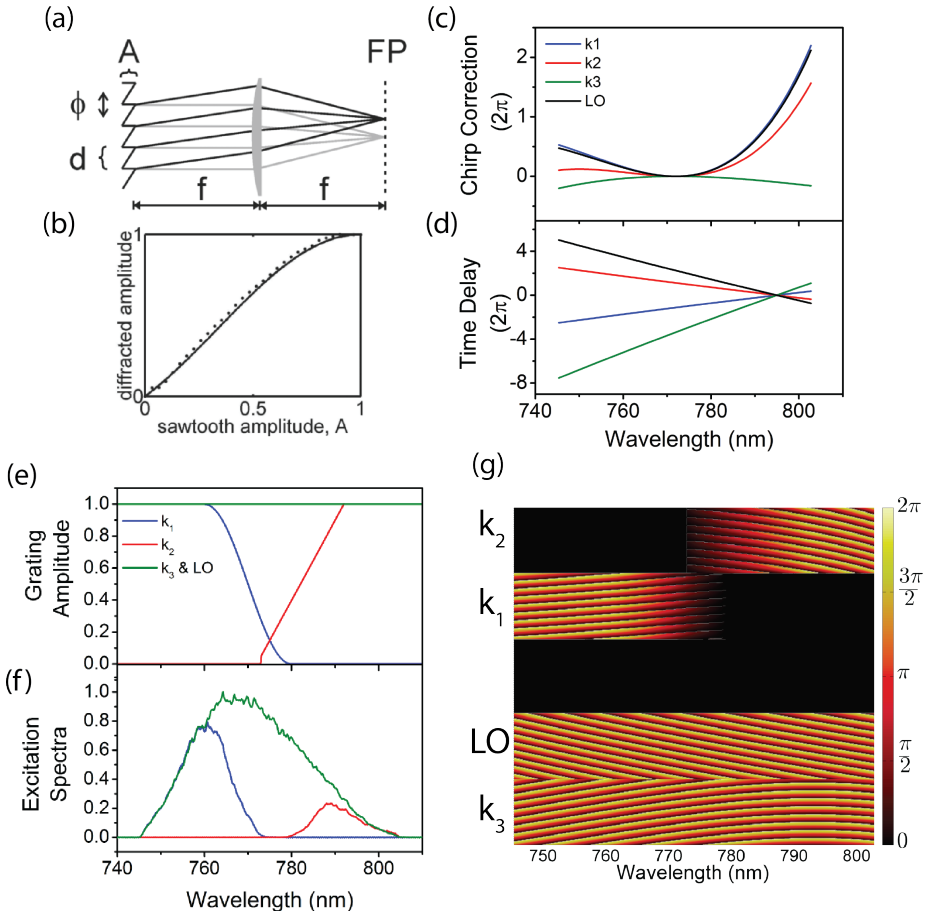

Figure 2.22: The vertical sawtooth pattern (a) used in diffraction based pulse-shaping. (b) Diffraction efficiency can be reduced by reducing the amplitude of the sawtooth. The spectral spectral phase masks in (c) and (d) are used to compress and delay the pulse, respectively. The spectral amplitude masks in (e) are used to modulate the depth of the vertical phase grating as a function of wavelength. The spectral amplitude masks in (e) are used to generate the pulse spectra shown in (f). The complete 2D phase mask in (g) combines the spectral phase masks in (c) and (d) with the spectral amplitude masks in (e). The diagram in (a) and the plot in (b) are reprinted with permission from Ref. [61].

the spectral amplitude can be shaped smoothly so that sharp spectral edges can be avoided. Sharp spectral edges lead to long temporal tails which reduce the temporal resolution of the experiment. The spectral 'tuning range' is limited by the incident laser bandwidth and/or the pulse-shaper bandwidth (i.e. the spectral width across the SLM).

Reducing the spectral width will inherently also increase the duration of the pulse due to the Fourier transform relationship between the pulse duration and the spectral width. By applying a phase correction that leads to a flat spectral phase, the unshaped pulse will be transform limited and have a flat phase. The spectral amplitude and phase can be adjusted independently, so narrowing the spectral amplitude will leave the spectral phase unaffected. The narrowed pulse will therefore retain a flat phase. This is to say, that even though narrowing the spectrum will increase the temporal pulse duration, it will still be compressed and can still be independently

shifted in time through the application of a linear spectral phase gradient. This independent control of the spectral phase and amplitude therefore results in the ability to spectrally tune the beams while still achieving transform limited pulses with controllable delays. Moreover, all of these aspects can be independently controlled for each beam. All this shaping is accomplished by generating phase patterns and sending them to the SLM, so aside from the liquid crystals in the SLM there are no moving parts.

Importantly, the pulses in the different beams are therefore intrinsically phase locked. This is true even when spectral amplitude shaping has been applied so that the pulses have no spectral overlap, they initially came from the same ultrafast pulse so they have a definite phase relationship which does not change shot-to-shot. This represents an important advantage over other methods for generating pulses resonant with different transitions (such as pairs of optical parametric amplifiers for example), which are not intrinsically phase stabilized, and in many cases cannot be actively stabilized either.

2.4.4 *Delaying Pulses in a Rotating Frame*

One additional benefit of using a pulse-shaper to apply the pulse delays is that they can be delayed in a rotating frame, which can vastly reduce the sampling requirements of the experiment.

In a typical 1Q spectrum in a non-rotating frame, the resulting complex signal is given by:

$$E_{sig}^{Non-Rot}(t_1) = E_s(t_1)[e^{i2\pi\nu t_1} + C.C.] \tag{2.36}$$

The phase of $E_{sig}^{Non-Rot}$ will oscillate with a period (T) given by $T = 1/\nu$, where ν is the optical frequency of the transition. For a transition at ~1.5 eV this results in a full phase rotation about every 4 fs. To avoid aliasing, the sampling as a function of t_1 must be less than this value, so step sizes of under 2 fs are typically required.

Using the pulse-shaper, we can reduce this requirement by applying the delays to the pulses in a rotating frame, which can be understood as follows. As established earlier, a delay relative to a particular point in time is equivalent to a linear phase gradient. An increasing delay can therefore be thought of as a steepening of the spectral phase gradient. As the gradient steepens, it must do so while keeping a particular frequency constant. This non-changing frequency is called the carrier frequency (ν_{CF}). When delays are applied using a translation stage or a prism pair, ν_{CF}=0.

On the other hand, when we apply a phase gradient to the pulse spectrum via an SLM, we have the freedom to choose any ν_{CF}. Typically ν_{CF} is picked so that it is within the laser spectrum and near (but not overlapping) the frequency of the

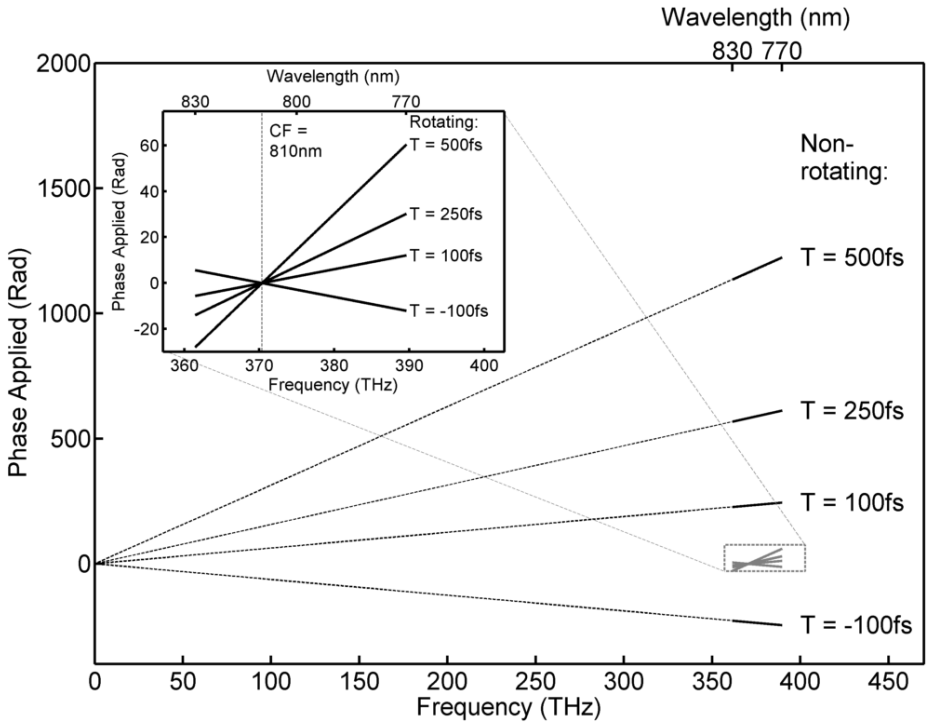

Figure 2.23: Number of phase rotations applied in non-rotating and rotating frame detection during a coherence scan. Rotating frame vastly reduces sampling requirements.

transitions of interest in the sample (ν_{sig}). By using $\nu_{CF} \approx \nu_{sig}$ instead of ν_{CF}=0 we significantly reduce the amount of phase accumulated in the signal for a given delay and hence significantly increase the period of phase oscillations of the FWM signal as a function of t_1. A graphical depiction of the amount of phase accumulated in a scan in the rotating ($\nu_{CF} = 810\,\text{nm} \approx 370\,\text{THz}$) and non-rotating ($\nu_{CF} = 0\,\text{THz}$) frames is shown in Fig. 2.23. This illustrates the significant improvement garnered by applying delays in a rotating frame. In a non-rotating frame experiment, a delay of 500 fs accumulates a total phase of 1200 rad (~190 optical cycles) at 390 THz, whereas a delay of 500 fs in the rotating frame accumulates just 60 rad (~10 optical cycles).

The relaxed sampling requirements for delays applied in the rotating frame can also be understood by looking at the expression for the complex signal in the rotating frame:

$$E_{sig}^{Rot}(t_1) = E_s(t_1)[e^{i2\pi(\nu_{CF}-\nu)t_1} + C.C.] \tag{2.37}$$

When the pulses are delayed in the rotating frame, the signal phase evolution is set by the difference between the detection frequency and the CF ($\nu - \nu_{CF}$). This difference is typically less than 0.1 eV or 24 THz. Sampling rates of about 20 fs will now suffice. These relaxed sampling requirements lead to an order of magnitude reduction in experiment time, which is particularly important for semiconductor

nanostructures, which typically have very long coherence times. This improvement also makes systematic 3D-spectroscopic studies more feasible.

2D 1Q Spectra collected using the rotating frame are centred around the CF in the E_1 direction. Signals with E_1 values below CF will appear as negative signals, while those with signals above CF will appear as positive signals. The absolute E_1 values can be calculated by simply adding on the CF to the E_1 axis. The final E_1 axis is then given by

$$E_1 = h\left(\overline{\nu}_{rot} + \nu_{CF}\right) \tag{2.38}$$

where $\overline{\nu}_{rot}$ is the frequency of phase oscillations in the measured signal. Precise measurement of the E_1 position of peaks depends on both a precisely known CF and good phase mapping of the SLM. Therefore, careful calibration of the pulse-shaper is important for dependable E_1 values.

2.4.5 *Pulse Compression*

As alluded to above, without any phase-compensation, pulses arrive at the sample with some higher order spectral phase originating in the Ti:sapph crystal in the laser and accumulated as the beams pass through the various optics used throughout the experiment. The majority of the phase is quadratic (linear chirp), and is compensated by optimizing the prism compressor (i.e. the distance between the prisms and the amount the prism is inserted into the beam).

The four beams pass through different amounts of glass in the pulse-shaper, so they cannot be all optimized simultaneously [63]. Also, the prism compressor cannot be used to compensate for spectral phase that is higher order than quadratic. For these two reasons, individual phase corrections must be applied to each of the beams. This phase is corrected by applying quadratic, cubic, and quartic spectral phase functions using a trial and error approach (discussed in detail in 2.5.1). Typically, the majority of the phase correction is quadratic. The cubic and quartic terms are quite small, and are typically the same for all four beams, as it is mostly generated in the Ti:Sapph crystal [27], rather than in the optics in the experiment.

2.4.6 *Heterodyne Detection*

The key experimental difference for CMDS that leads to the various enhancements over other FWM techniques is that the full complex signal needs to be measured. To measure the signal phase, the FWM signal is detected using spectral interferometry in what is a form of heterodyne detection.

A diagram depicting spectral interferometry is shown in Fig. 2.24a. A reference pulse (the LO) is spatially overlapped with the FWM signal and the two co-propagate into the spectrometer where they interfere to form a spectral interferogram. The

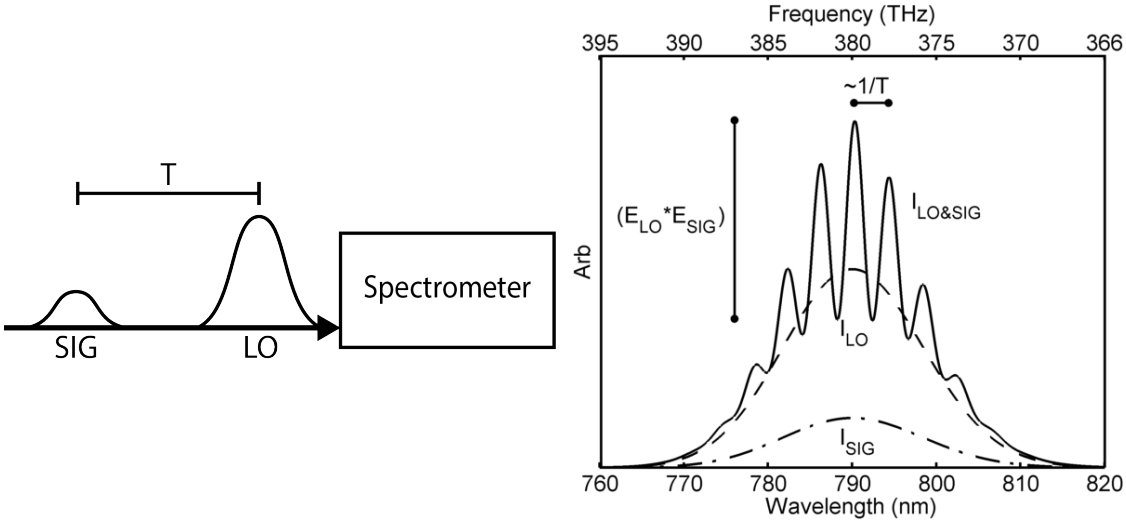

(a) (b)

Figure 2.24: (a) Diagram of heterodyne detection using spectral interferometry. (b) Spectral interferogram of signal and LO. The amplitude of the fringes is proportional to the product of the electric fields of the signal and LO, and fringe spacing is inversely proportional to the delay between the signal and LO.

signal is thus detected as interference fringes across the top of the LO spectrum as shown in Fig. 2.24b. The spacing of the spectral fringes is the inverse of the time delay between the signal and the reference. For this reason, the local oscillator is typically delayed such that it arrives at the sample ~1 ps before the excitation beams to optimize the fringe visibility.

The fringe amplitude is proportional to the product of the electric field of the signal and LO ($E_s E_{LO}$). The amplitude of the detected signal can therefore be amplified significantly by increasing the power of the local oscillator beam. This allows the detection of much weaker signals, orders of magnitude weaker than in FWM experiments. The fact that heterodyne detection measures E instead of E^2 (as in non-interferometric detection) also improves the sensitivity of the experiment.

2.4.7 *Phase-Cycling*

The detected interferogram is not, however, only a measure of the interference between the signal and the local oscillator. Any stray coherent light that co-propagates into the spectrometer will generate spectral fringes. This includes scatter from the three excitation beams, either at the sample or earlier in the experiment, as well as back-surface reflections from optics and coherent photoluminescence from the sample. The LO and all of these sources will generate non-interferometric background signals as well, which must be removed. To make matters worse, all of the stray light sources can interfere with one another and generate fringes with a variety

of different spacings. The full range of contributions to the measured signal are represented in Eq. 2.39 [123].

$$S \propto \left| E_{LO} e^{i\phi_{LO}(\omega)} + E_{SIG} e^{i\phi_{SIG}(\omega)} + \sum_{n=1,2,3} E_n e^{i\phi_n(\omega)} \right|^2 \tag{2.39}$$

Equation 2.39 can be expanded into Eq. 2.40.

$$\begin{aligned} S \propto & E_{LO}^2 + E_{SIG}^2 + \sum_{n=1,2,3} E_n^2 \\ & + 2E_{LO}E_{SIG}\cos(\phi_{LO} - \phi_{SIG}) \\ & + 2\sum_{n=1,2,3} E_{LO}E_n\cos(\phi_{LO} - \phi_n) \\ & + 2\sum_{n=1,2,3} E_{SIG}E_n\cos(\phi_{SIG} - \phi_n) \\ & + \sum_{n=1,2,3}\sum_{m=1,2,3}^{m\neq n} E_m E_n \cos(\phi_m - \phi_n) \end{aligned} \tag{2.40}$$

The first three terms in the top line represent the non-interfering spectra of the LO, the signal and the excitation beams. The second line is the term we would like to measure, the interference of the LO and the signal. The third and fourth lines represent the interference of the excitation beams with the LO and the signal respectively. The final term is the interference of the excitation beams with one another.

To get rid of all these components and isolate just the second line, a process called phase cycling is employed. Phase cycling exploits the fact that the interference of the signal and the LO will uniquely depend on the phase of all the excitation beams and the local oscillator. All the other signal components depend on only one, two or three of the beams. As a result, by recording spectral interferograms in which the excitation beams and the LO have different combinations of either 0 or π phase offsets, all the components that don't depend on the phase of all four beams can be eliminated.

In all, this takes 8 interferograms with the sets of phases listed in Table 2.1. These interferograms can then be combined using Eq. 2.41 to eliminate all the components in Eq. 2.40 except for the interference between the signal and the LO.

$$\begin{aligned} E_{SIG} \propto S_{SIG} = & [(S2 - S1) - (S4 - S3)] \\ & - [(S6 - S5) - (S8 - S7)] \\ = & \, 16E_{LO}E_{SIG}\cos(\phi_{LO} - \phi_{SIG}) \end{aligned} \tag{2.41}$$

PHASE CYCLE STEP	k_1	k_2	k_3	LO
S1	0	0	0	0
S2	π	0	0	0
S3	0	π	0	0
S4	π	π	0	0
S5	0	0	0	π
S6	π	0	0	π
S7	0	π	0	π
S8	π	π	0	π

Table 2.1: 8-step phase-cycling procedure

An example of the 8 spectral interferograms that make a single point are shown in Fig. 2.25. The resulting S_{SIG} interferogram (at the bottom of Fig. 2.25, labelled 'signal') contains only the interference between the signal and the reference beam. This process can add a significant amount of data acquisition time - each delay data point requires the collection of 8 spectra. However, S1-S8 each contain a signal contribution, so there is also an $8\times$ amplification of the amplitude of S_{SIG} compared with the non-phase cycled signal. This amplification of S_{SIG} offsets the extra data acquisition time. After phase cycling, the signal is now (ideally) background free.

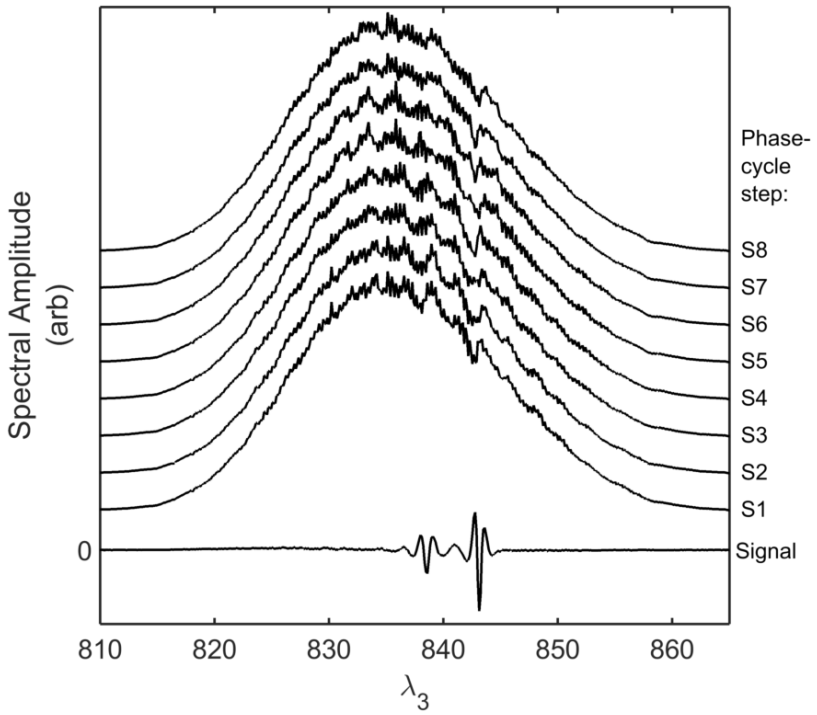

Figure 2.25: Eight spectra recorded for phase-cycling, and resulting phase-cycled interferogram for a double quantum well sample.

2.4.8 *Experimental stability*

The successful implementation of phase cycling relies on experimental stability. Any phase or amplitude drift between phase cycling steps result in imperfect scatter subtraction and/or imperfect background subtraction. In our case, this is the main way that noise is introduced in 2D and 3D spectra. The experiment must also remain phase stable for the duration of the 2D or 3D scan. Phase variations during scans can lead to peak spreading and additional peaks along the Fourier transformed frequency directions (E_1 and E_2).

In this pulse-shaper based CMDS experiment, the phase is stabilized passively and great care is taken to ensure uncorrelated sources of noise are avoided. Where possible, pedestal mounts are used, the entire experiment is enclosed in a metal box and all equipment with moving parts is removed from the table (including the cryostat expander, section 2.4.9). The limiting factor for the stability is now mostly the thermal stability in the lab.

The effects of the remaining phase/amplitude noise and wandering can be reduced by experimental optimization and averaging the acquired data at the spectral level (repeating the acquisition of each spectrum in the phase cycling process), at the S_{SIG} level (repeating the acquisition of each full set of phase cycles) and at the scan level (repeating the same scan multiple times). The ideal averaging depends on the intensity of the signal being measured, but we have found that generally the best results are achieved by minimizing the number of point averages. Instead, the scan is repeated several times and the resulting 2D spectra are averaged. This provides an improved SNR by better removing artifacts due to laser scatter and access to uncertainty statistics on the spectra not available otherwise.

2.4.9 *Vibration Isolated Cryostat*

Recirculating cryostats are convenient in that they can run stably for long periods of time without necessitating expensive liquid helium. The downside is that they typically have significant vibrations at the sample, which spread across the optical table. In this experiment we use a vibration isolated cryostat which is mechanically decoupled from the table. This is a key element of what makes the experiment so stable: there are no moving parts attached to the optical table.

In a typical recirculating cryostat, a compressor supplies helium gas at 300 psi via hoses to an expander where it expands and cools. The attached cold finger then transfers that cooling power to the sample. In a typical design, there is a direct mechanical connection between the expander and the sample mount which, along with cooling power, transmits the large amplitude vibrations (10's to 100's of micrometers) from the expander to the sample.

In the vibration isolated version (Advanced Research Systems, Inc. Model: DE204N-DMX-20), the sample mount is mechanically decoupled from the expander. In an additional step, a helium exchange gas allows the transmission of the cooling power to the sample chamber. The expander is mounted to a support arm which sits directly on the floor rather than on the optical table. The bottom half of the cryostat (which contains the sample) is mounted to the table. Matching translation stages allow coordinated x/y adjustments of the sample chamber and the expander. The depth of the exchange gas allows ± 1 cm of movement of the bottom half of the cryostat without necessitating also moving the expander. The movable, home-built expander support arm also allows removal of the cryostat from the table and access to the samples.

When using cryostats which are not vibration isolated, the limiting factor in the achievable signal to noise is the movement of the cryostat during the data acquisition. This movement leads to slight variations in the phase and amplitude of the detected interferograms. With the vibration isolated cryostat, this limitation is removed and the stability of the experiment is improved significantly, allowing for longer scans and detection of weaker signals.

2.4.10 *Limitations of the SLM based CMDS experiment*

Though there are clearly many advantages to pulse-shaper based CMDS, there are also some drawbacks, which make it less useful for certain types of experiments. The main drawback to using the pulse-shaper for beam delays is the so-called time-window effect which stems from the pixelation of the SLM. This pixelation leads to additional pulses before and after the main pulse, called replica pulses. Thankfully, these replicas are not efficiently diffracted down into the first vertical order, so they do not affect the dynamics measured. They do, however, take energy away from the 'main' pulse causing a delay dependent modulation of the pulse intensity [61, 124, 125].

As the applied delays increase, eventually the full phase range across the SLM exceeds the 2π phase that can be applied with the SLM. To increase the range of the SLM, phase wraps are applied, creating a saw-tooth pattern, which is shown in Fig. 2.26a. As the applied phase gradients get steeper still, more and more phase wraps must be used, and the phase-step from pixel to pixel increases. As the spacing between phase wraps approaches the resolution of the pulse-shaper,the diffraction efficiency into the intended beam drops while the diffraction efficiency into the replicas increases.

This has two important consequences. First, the pulse energy changes continuously as a function of delay. This is often called the time-window, and takes the form of the Gaussian-sinc window shown in Fig. 2.26b. Second, the delay range is limited to ± 5 ps (for the parameters used here) before the delayed pulse energy

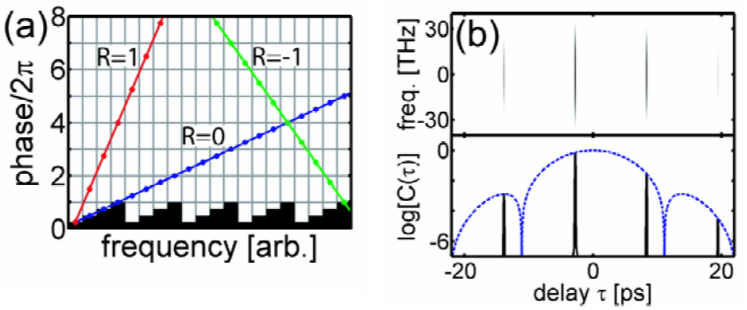

Figure 2.26: (a) Phase-wraps in a sawtooth pattern on a SLM. (b) Gaussian-sinc window. Both are adapted with permission from Ref. [122].

has reduced to a point where the signal fully disappears. These two taken together limit what types of details can be extracted from this experiment. For instance, many semiconductor nanostructures have dephasing times that are greater than 10 ps [46]. Such a dephasing time cannot be reliably measured with this type of experiment, and therefore homogeneous linewidths will be over-estimated.

A second drawback of pulse-shaping is spatio temporal coupling. The diffraction limited spectral focal spot in the pulse-shaper causes the horizontal (ideally purely spectral) axis of the SLM to also shift the beam spatially [126]. The shift is actually initially angular, which the cylindrical lens turns it into a spatial shift. The amount the beam shifts is small - on the order of 100 um/ps of delay. The overlap at the sample remains unchanged, even with these relatively large spatial shifts (0.5 mm at the maximum delay) because the experiment is setup in 4-f imaging geometry [127]. This shift does cause a change in the wave-vector of the excitation beam and the overlap between the generated FWM signal and the LO. This shifting overlap causes additional delay dependent signal modulations, though they are less pronounced than those coming from pixelation(as long as care is taken that no irises or optical mounts clip the beams).

2.5 Experimental procedures

This section will discuss the experimental procedures that are used in aligning and calibrating the experimental apparatus and then the procedures for running CMDS experiments.

2.5.1 *Alignment and Calibration*

For reliable performance, the CMDS experiment requires alignment and calibration before each experimental run. These processes are relatively straight-forward. This section will describe the alignment and calibration procedure.

A. The oscillator is optimized for desired spectrum based on sample and experiment to be conducted.

B. The beam-shaper zero order beam (or with a constant phase pattern applied to the SLM so it is effectively just a mirror) is aligned so that it passes through a series of alignment irises. This guarantees the box beam pattern will be aligned axially and centred on all of the imaging optics.

C. The vertical grating on the pulse shaping SLM is turned 'on' with no phase correction or delay applied, and a 100 μm thick beta barium borate (BBO) non-linear crystal at the sample position. The prism compressor can then be optimized by maximizing the second-harmonic signal. This provides a coarse pulse compression which then must be optimized for each beam later in the calibration procedure.

D. The vertical arrangement of the beams must then be mapped out on the SLM surface. All four beams in the box geometry are turned 'on' at the beam shaper. A single period of the vertical grating is scanned across the SLM from top to bottom. The vertical beam pattern is mapped out based on the integrated spectral intensity. This also is a check that all four or five beams are on the SLM, and that there is no overlap of the beams (which leads to cross-talk between beams and imperfect cancellation of unwanted signals in phase cycling). The boundaries of the SLM regions that represent the different beams are set based on this measurement.

E. Using the regions measured in the previous step, the spectral mapping of each beam is performed by scanning a narrow (typically 1 pixel wide) grating pattern across the region while measuring the resulting spectrum, which is a sharp peak. This peak is fit, and the center of the fit is taken to be the central frequency at that pixel. The resulting pixel number vs frequency data is fit to a linear function, which is used when spectral amplitude and phase shaping is performed while running the experiment.

F. The BBO crystal is placed back in the experiment at the sample position, and the pulses are compressed using an iterative series of cross-correlations between the different beams. In a typical cross-correlation FROG measurement, a pulse with a well defined and known pulse shape is scanned across an unknown pulse and the spectrum of the mixing signal is measured as a function of delay. The temporal electric field can then be accurately extracted using an iterative algorithm. In our case, neither of the pulses are well known. In this case, the exact electric field variation cannot be unambiguously extracted from a single cross-correlation. To get around this, we do a series of cross correlations with different combinations of first quadratic and then cubic/quartic phase until the cross correlation is the expected transform limited width. In

theory, this could lead to non-transform limited pulses that have cancelling electric fields such that the cross correlation appears to be transform limited. To confirm that this is not the case, cross correlations with different combinations of beams are performed, and the quadratic, cubic and quartic corrections to each beam are adjusted until all of the cross-correlations are transform limited. In practice, most of the phase correction is quadratic, so it can be done consistently and relatively quickly with a trial and error approach. Shorter pulses with more complicated corrections would probably benefit from a more involved, systematic approach.

G. The arrival time of the pulses in the different beams will be slightly different. These delay offsets must also be measured and corrected. The delay offsets for the excitation beams can be corrected using the cross correlations, but the local oscillator cannot. During the experiment, a 4 mm thick neutral density filter with an optical density of 4 is placed in the local oscillator beam to reduce its power such that it is comparable with that of the signal. In addition to reducing the power, this filter also delays the LO relative to the other beams. To measure exactly how much it is delayed, a FWM signal with a well defined temporal profile is required. For this, a laser dye (IR785) is placed at the sample position. The three excitation beams are all overlapped temporally, which generates a coherence spike signal. The broad signal from the laser dye roughly reproduces the laser spectrum and leads to a temporal shape that matches the excitation pulses. The delay between the local oscillator and the signal can then be measured by scanning the three excitation pulses temporally relative to the LO. The dye may not have a perfectly instantaneous response, so there may be some inaccuracy in this calibration. However, this inaccuracy will only impact the real peak-shapes, not the amplitude peak-shapes.

H. Phasing: If the real part of the signal is required, the relative phase of the excitation beams relative to the local oscillator must be determined. This has not been conducted for any of the results reported in this thesis.

2.5.2 *Typical Scan parameters*

Scan parameters (beam powers, scan range, sampling rate) change depending on the sample and scan type, and vary across the experiments presented in this thesis. Typical scan parameters are shown in table 2.2, but specific parameters for each set of experimental data are listed in Appendix A1.

As alluded to in section 2.4.10, typical single transition coherence and population lifetimes times for QW excitons exceed the range of delays accessible by this experiment. For that reason, the delay ranges are usually set to the maximum achievable delays: 5 ps. Coherent superpositions of excitons have much shorter de-coherence times, which are limited by the exciton inhomogeneous linewidth (in both in t_1 and

Scan	t_1 Range, Step	t_2 Range, Step
1Q	5 ps, 20 fs	
0Q		5 ps, 20 fs
2Q	2 ps, 20 fs	
1Q-CS	1 ps, 20 fs	
0Q-CS	2 ps, 20 fs	
1Q-3D	5 ps, 20 fs	5 ps, 20 fs

Table 2.2: Typical parameters used in CMDS experiments

t_2) to about 0.5 to 1 ps. Due to the rotating frame detection, sampling requirements are relatively low, and do not change much on the type of scan, except 2Q scans which must be conducted at twice the sampling rate of 1Q and 0Q scans.

As evidenced by the results in Chapter 7, beam powers are very important in the detected exciton dynamics. A range of different powers are used throughout the results presented in this thesis. While some of the original work had to be conducted at high powers (>3 mW per beam or 1.8×10^{11} photons·cm^{-2}·pulse^{-1}) most of the rest is conducted at less than 200 μW per beam (8×10^9 photons·cm^{-2}·pulse^{-1}/beam) below which 5th order signals are expected to play little to no part [54].

2.5.3 *Data Processing*

A series of manipulations must be performed to the recorded data before it can be presented as a 2D spectrum. This section describes the key elements of the analysis process for a 1Q 2D spectrum. The scripts used in data analysis can be found on the Swinburne ultrafast spectroscopy group website.[19]

Figure 2.27a shows the acquired $\mathbf{E}(t_1,E_3/\lambda_3)$ data for a scan of t_1 after phase-cycling. The signal as well as some scatter (which was not fully removed by phase cycling) are present in these interferograms. The data is then transformed into $\mathbf{E}(t_1,t_3)$ using an inverse fast-Fourier transform (iFFT) as a function of E_3, the result of which is shown in Fig. 2.27b. In this form scatter and spectral amplitude instabilities are separable from the FWM signal, as most scatter signals appear at t_3 values that are shorter than the FWM signal. As the recorded data has no imaginary component, the fast-Fourier transform produces two mirrored temporal patterns. Using the functions delineated by the red lines in Fig. 2.27b, one half of the data is thrown away, and most of the scatter signals are windowed out.

An FFT along t_3 returns the data to the $\mathbf{E}(t_1,E_3/\lambda_3)$ domain (as shown in Fig. 2.27c). This data is now free of scatter signals and artifacts due to experimental instabilities. An additional phase gradient is added to the signal phase to account

19 http://www.swinburne.edu.au/engineering/caous/ultrafast/publications/CMDS_Scripts.zip

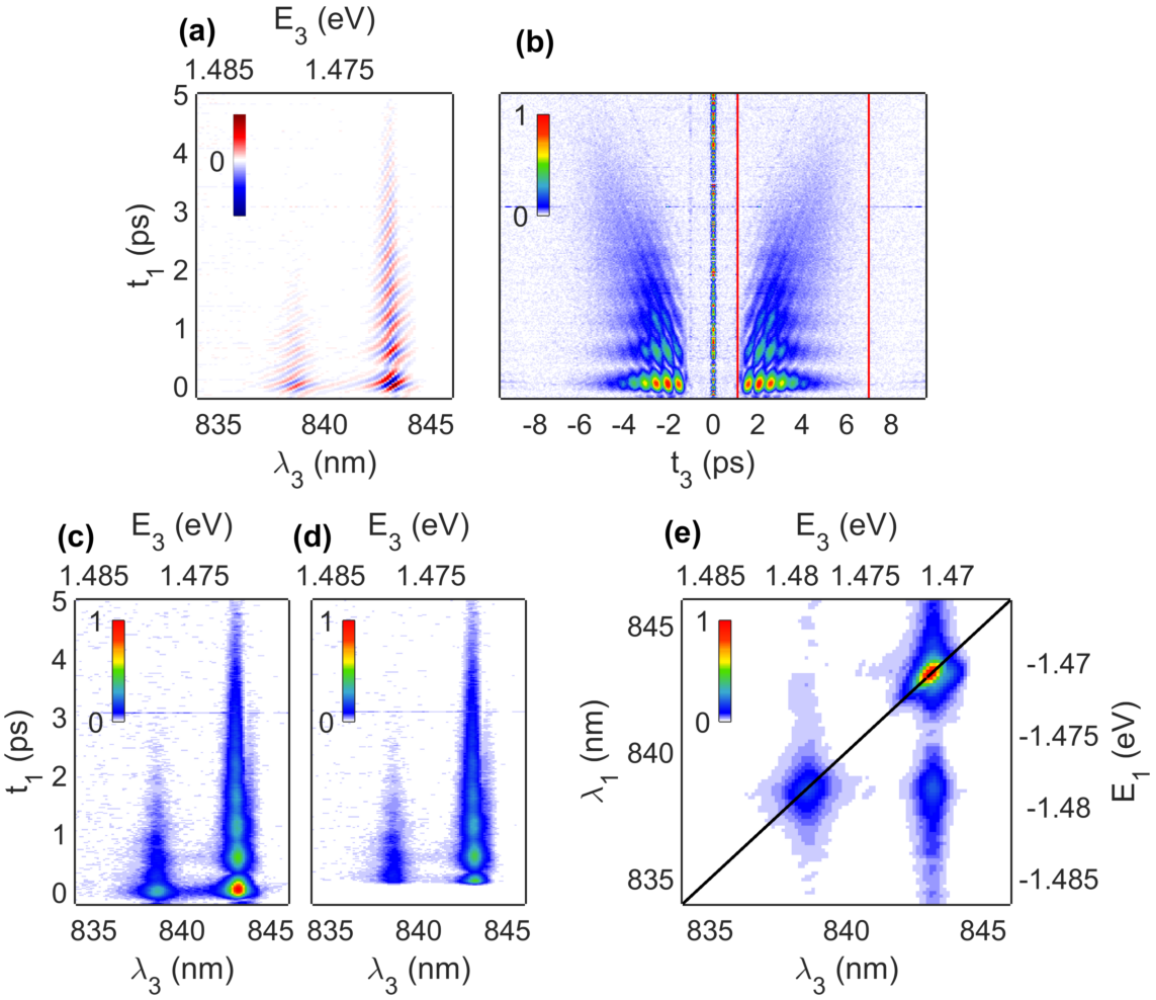

Figure 2.27: Stages of data analysis. First, the collected interferograms in (a) are fourier transformed into (t_1, t_3) and windowed (b) and then fourier transformed back into the (t_1,λ_3). This is windowed along t_1 to remove pulse overlap before being Fourier transormed along t_1 to generate the 2D spectrum which is usually presented as (E_1,E_3).

for the measured time delay between the signal and the LO (typically 1.5 ps). The phase correction (Φ_{C1})is given by:

$$\Phi_{C1}(E_3) = \frac{(E_3 - E_{CF})}{h} t_{LO} \tag{2.42}$$

t_{LO} is constant for the 1Q scan, so the correction Φ_{C1} does not depend on t_1. This correction could equivalently be applied in the time domain by shifting the zero point of the time axis to amount for t_{LO}.

An error function window is applied to remove the coherent artifact generated by pulse overlap at t_1=0 across all E_3 values (as shown in Fig. 2.27d). Details of these can be found in the appendix. A final FFT is then applied along t_1 to generate the 2D spectrum (Fig. 2.27e). The E_1 axis is calculated taking into account the carrier frequency used in the rotating frame (details in the appendix).

2Q 2D, 0Q 2D and 1Q 3D spectra require an additional phase rotation step, because the timing of the signal shifts with respect to the LO. This shift occurs because in all three of these types of scans, the timing of the third pulse (k_1 in 2Q 2D, k_3 in 0Q 2D and 1Q 3D) changes with respect to the LO. To account for the changing arrival time of the third pulse relative to the LO over the course of the scan, the following additional phase correction is applied to the signal for 2Q spectra:

$$\Phi_{C2}(E_3, t_{2Q}) = \frac{(E_3 - E_{CF})}{\hbar} t_{2Q} \tag{2.43}$$

and for 0Q and 3D spectra:

$$\Phi_{C2}(E_3, t_2) = \frac{(E_3 - E_{CF})}{\hbar} t_2 \tag{2.44}$$

3D spectra also require an additional FFT and pulse overlap windowing along the second scanned time domain (t_2). Otherwise, all the data processing steps are the same as 1Q described above.

2.6 Photoluminescence Excitation Spectroscopy with a pulse-shaper

In a typical photoluminescence (PL) experiment, a sample is excited by a light source with photon energy higher than its relevant optical transitions, while photoluminescence is detected by a spectrometer. In many samples, the PL spectrum is very sensitive to the excitation frequency [128], so recording spectra at multiple excitation frequencies is important for proper interpretation. Taken one step further, if the photoluminescence can be recorded while the excitation frequency is scanned smoothly, an excitation spectrum can then be collected. This technique (called photoluminescence excitation spectroscopy or PLE) has been a very valuable technique for spectroscopists since at least the 1960's [129], and is still in wide use today [130, 131].

PLE is typically implemented in one of two different ways: 1. using a tunable CW laser [132], or 2. using a broadband coherent or incoherent source (such as a lamp) with a monochromator [129]. Both implementations have advantages and disadvantages. The laser must tune smoothly, and be stable both in spectrum and power. Stabilized, tunable CW laser sources can produce excitation linwidths below 10 MHz (<0.00004 meV) [133–135]. The monochromator approach is more involved technically and is limited to light sources that are broad enough to cover the spectral range of interest. The light source must also be free of structure which can complicate interpretation if they overlap the spectral features of the sample. Conventional commercial monochromators can achieve spectral resolution in the

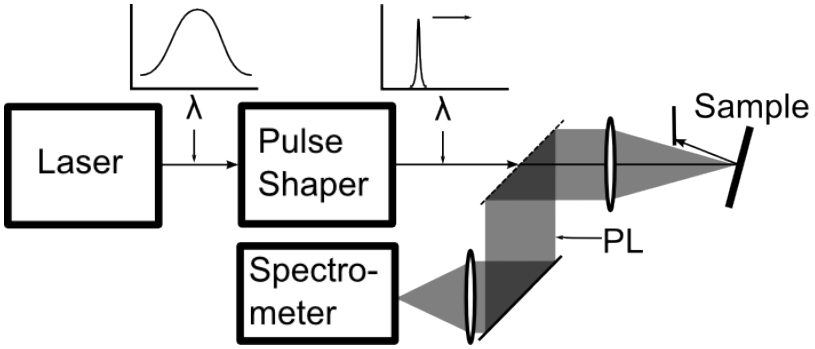

Figure 2.28: A diagram of the PLE setup using a pulse-shaper

~0.07 meV to ~0.2 meV range [136, 137], which is markedly worse than the spectral linewidth achievable with lasers.

We have demonstrated a relatively simple alternative, using a pulse-shaper capable of spectral amplitude shaping, a diagram of which is shown in Fig. 2.28. In this approach, the pulse-shaper is used like a monochromator to take narrow lines (<1 meV) from a broadband fs laser spectrum. Pulse-shapers are well suited to this task: they are repeatable, stable and fast, with no moving parts. In recent years pulse-shapers have been used for a wide variety of experiments, and are becoming more commonplace in ultrafast spectroscopy labs [138–141]. Pulse-shaper based PLE could easily be incorporated alongside many of these techniques without significant experimental changes.

In our implementation of PLE, we use the same pulse-shaper as in the CMDS experiment. Only a few minimal changes to the experiment must be made to switch from CMDS to PLE measurements: two irises are closed to block unused excitation beams, and two others are opened to allow more efficient collection of the PL signal. This allows us to conduct PLE immediately before or after CMDS experiments, and on the same sample position.

The experiment is conducted in much the same way as the spectral calibration of the pulse-shaper (section 2.5.1, item E). All but one of the beams are turned 'off' at the pulse-shaper (meaning no vertical grating is applied so they miss the pick-off mirror). A 1-4 pixel wide vertical grating is scanned horizontally across the region of the SLM upon which the excitation beam is incident. The grating is scanned in 1-4 pixel steps, and the PL spectrum is recorded for each position of the grating on the SLM.

Some stray light from the excitation beam (both before and after it is narrowed) is also recorded by the spectrometer, which can be significant. Because the experiment is quite stable, the unshaped scatter can be removed by taking a background spectrum with all the beams 'off'. The stray light from the narrowed excitation beam mostly originates from the sample itself, and cannot be as easily removed, so accurate PL at the excitation frequency is not recorded.

A typical PLE spectrum is shown in Fig. 2.29a, which illustrates the quality of the PLE data that can be recorded with this pulse-shaper. A typical spectrum of the

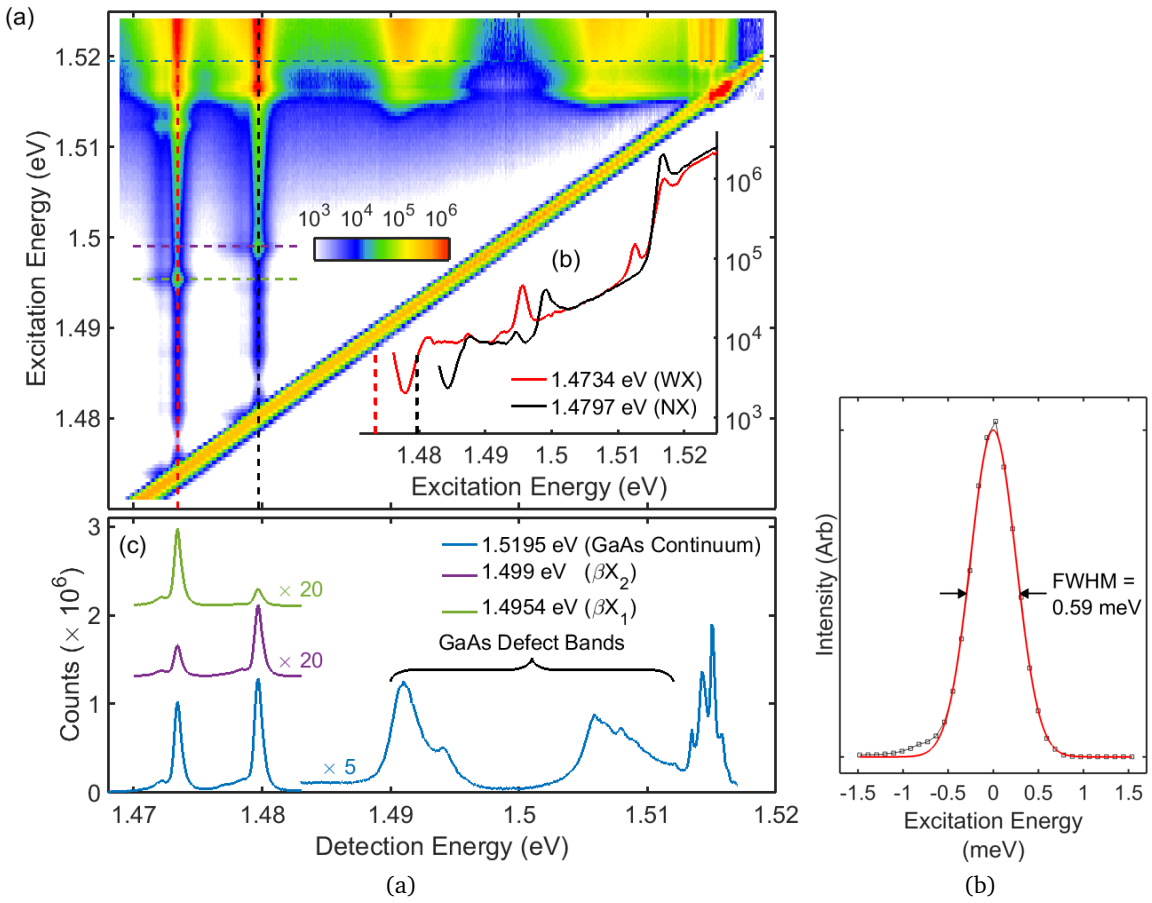

Figure 2.29: (a) A PLE scan of an InGaAs double-QW, including some slices along the excitation and emission directions. A full description of this data is provided in Section 6.3.1.(b) Typical spectrum of the excitation beam. The excitation spectral resolution is limited by the pulse-shaper resolution to 0.59 meV FWHM.

excitation beam is shown in Fig. 2.29. A Gaussian fit to the excitation spectrum shows an excitation resolution of 0.59 meV FWHM, which is typical of the entire scan range. This excitation resolution is not as good as the resolution achieved with monochromator (~0.1 meV) or tunable CW (<1 μeV) sources. The excitation resolution of the pulse-shaper is limited by the size of the focal spot from the cylindrical lens on the SLM surface, and the period of the grating used to disperse the beams [124]. The resolution could be improved by using a shorter focal length cylindrical lens and/or increasing the number of grooves per mm of the grating. These changes would come at the expense of other attributes of the pulse-shaper, including the range of photon energies that can be scanned in a PLE experiment. The improvement in resolution would be in the range of a factor of ×2 to a factor of ×4, which would lead to a resolution comparable to monochromator based PLE experiments, but still much worse than achievable with tunable CW lasers.

One other drawback to this approach is that the range of excitation wavelengths that can be scanned by the pulse shaper is limited by the laser bandwidth. The source (an oscillator in this case) is tunable, and the grating in the pulse shaper can be rotated to access different spectral ranges, so a wide spectral range can be

accessed. However, connecting scans across the pulse shaper from different spectral ranges would not be feasible in most cases, so the spectral range achievable in a single scan is smaller than the what could be accessed using a monochromater, OPA or tunable CW laser. However, for the purposes of our studies on QWs, the resolution and scan range (~65 nm) provided by the pulse shaper are typically more than sufficient. The linewidths of the excitonic features we are interested in are ~1 meV or larger. We cannot necessarily record precise absorption energies or linewidths, but we can still clearly distinguish the excitonic resonances from one another. Furthermore, the benefits of the of this pulse-shaper based approach (such as stability, repeatability and speed) and its integration into the CMDS experimental apparatus make it a very useful complementary technique.

2.7 Summary

In this chapter we have presented the FWM concepts important for an understanding of CMDS. We have introduced CMDS, and discussed how it can be enhanced by the use of spectral shaping for pathway selection. Finally, we have described the CMDS experiment that was established at Swinburne as part of this PhD project. The following experimental results chapters will show that this newly established apparatus and experimental approach can be used to study a range of new coherent effects in semiconductor QWs.

3

COHERENT DYNAMICS IN SEMICONDUCTOR QWS: BACKGROUND

This chapter covers some of the fundamental concepts relevant to the investigations of semiconductor QWs that are presented in subsequent chapters. We will first examine the well understood physics that leads to the linear optical response in Section 3.1. In Section 3.2, we will then delve into the coherent non-linear response of excitons in QWs, exploring the important concepts of dephasing and decoherence (3.2.1, 3.2.2), quantum beats (3.2.3) and many-body effects (3.2.4). Finally, in section 3.2.5 we will briefly cover what investigations have been conducted using coherent multidimensional spectroscopy (CMDS) to study the coherent response of excitons in QWs.

3.1 Fundamental concepts and linear optical response

The electronic structure of single atoms are characterized by a series of discrete energies which are solutions to the Schrödinger equation including the Coulomb interaction between negatively charged electrons and positively charged nucleus. When two atoms are covalently bonded, the electrons are shared and each atomic level splits into two discrete levels. As the number of covalently bonded atoms increases, the number of levels increases and the spacing between the split levels decreases until eventually the once discrete states of the atoms become bands in the limit of a quasi-infinite crystal [142].

The electronic characteristics of the bands can be calculated based on the interatomic distances in the crystal, which vary as function of the direction of the real space vector relative to the crystal lattice vectors. For the large number of atoms in semiconductor lattices, it is more convenient to determine and discuss these properties in momentum space (k-space or reciprocal-space) rather the real-space, in which the energy of the bands are represented as a function of the momentum, defined with respect to the reciprocal-space lattice. In this basis, the different directions of crystal symmetry can be defined. The bands are usually represented as 1D energy/momentum dispersion relations between the different symmetry points, which denoted by different symbols (Γ, X, Λ, etc.) as shown in Fig. 3.1. From these dispersion relations, the effective mass (m^*) of the electron can be calculated, which

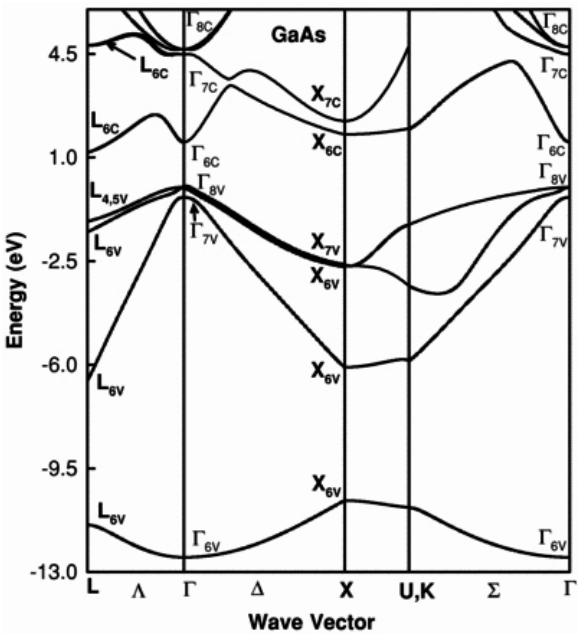

Figure 3.1: Dispersion relations for different bands in GaAs. Reprinted with permission from Ref. [143].

relates to how the electrons in different bands respond to the application of force. m^* is inversely proportional to the curvature of the bands [142].

In equilibrium, the bands are filled up to a certain level, while higher bands remain empty. The lowest empty band is called the conduction band while the highest filled band is called the valence bands. The gap separating the highest point of the valence band from the lowest point of the conduction band is called the bandgap. The bandgap energy corresponds to the amount of energy required to promote an electron from the valence band to the conduction band. If that gap is small enough that some electrons can be thermally promoted into the empty band, then the crystal will act as a semiconductor. In typical semiconductors, the bandgap ranges from 10's of meV up to a few eV [142].

When the lowest point in the conduction band and the highest point of the valence band occur at the same point in momentum space, the semiconductor is said to have a direct band gap. In this configuration, the radiative relaxation of an electron from the conduction band is allowed (since no change of momentum is required), so the material will absorb and emit light. In the alternative configuration, where the conduction band minimum and valence band maximum occur at a different momenta, the transition does not conserve momentum and is no longer allowed. Indirect gap semiconductors can still emit some light if some other interaction (for instance, the absorption of a lattice vibration) accounts for the momentum difference of the bands. Inter-band absorption (i.e. promotion of an electron from the valence band to the conduction band) can still occur without momentum change, but requires a photon energy larger than the bangap energy. The excited electron in the conduction band is far from the conduction band minimum and relaxes down

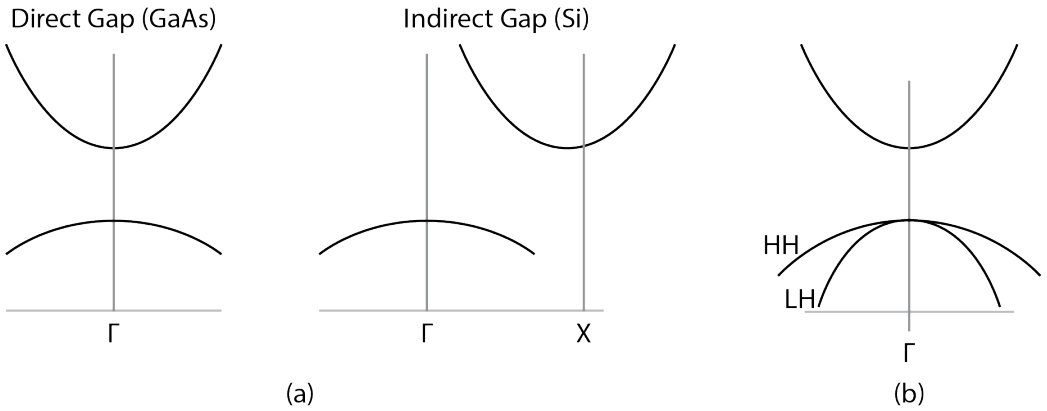

Figure 3.2: (a) Band structures with direct and indirect gaps. Γ and X represent points of symmetry in the k-space representation of the crystal. (b) In the GaAs bandstructure, the highest energy valence band is split into heavy-hole (HH, $m_j = \pm 3/2$) and light-hole (LH, $m_j = \pm 1/2$) bands. The HH and LH bands are degenerate at the Γ point.

to the bottom of the conduction band much faster than radiative relaxation into the valence band. For these reasons, indirect semiconductors are efficient absorbers, but weak emitters compared with direct bandgap semiconductors.

Semiconductors can be made of crystals of a single atom (such as Si), or a combination of two (or more) different atoms. Compound semiconductors are very useful as the optical and electronic properties can be controlled by which pairs of materials are used [142]. These properties can also be tailored by changing the stoichiometry of the constituent components. The most well studied binary semiconductors involve a pairing of a group III element (In, Al, Ga) with a group V element (N, As). Of these III/V semiconductors, Gallium Arsenide (GaAs) based compounds are the most common. They exhibit a direct band gap and can be grown precisely and with high purity. The bandgap can also be easily controlled by replacing Ga atoms with Al (In) atoms to increase (decrease) the bandgap.

Like atomic states, semiconductor bands are characterized by a quantized angular momentum, which depends on the magnetic quantum number (m_j). The highest energy valence band is split into two bands, one for $m_j = \pm 3/2$ electrons and $m_j = \pm 1/2$ electrons.[1] These bands are labelled heavy-hole (HH) and light-hole (LH), respectively, in reference to their different effective masses. A cartoon depicting the HH and LH bands can be seen in Fig. 3.2b. At zero momentum (i.e. at the Γ point) the HH and LH bands are typically degenerate due to lattice symmetry, but for higher momentum the bands separate.

1 There are actually three bands. The HH and LH correspond to the J=3/2 case, but there is also a band for J=1/2, which is called the split-off band [142]. For our purposes the split-off band is ignored because it is energetically offset by a few hundred meV from the HH and LH bands.

3.1.1 *Electrons, holes and excitons*

When an electron is promoted from the valence band to the conduction band, an empty state appears in the valence band. We call this missing electron a 'hole', which acts like a particle with a positive charge[2]. Like electrons, due to the interacting nature of semiconductor crystal we cannot view the hole as belonging to one atom in particular, but rather delocalized across multiple lattice sites.

When an electron is excited from the valence band to the conduction band, the electron and hole (which are initially overlapped in real and momentum space) have a Coulomb attraction, leads to the formation of a stable bound state. This bound state is a hydrogen like quasi-particle called an exciton, and has an energy just below the bandgap energy. The difference between the bandgap energy and the exciton energy is called the exciton binding energy. In general, excitons come in two different types - Frenkel type excitons which are confined to a single unit cell, or Wannier type excitons which are delocalized over a number of atoms [142]. Frenkel excitons are tightly bound (exhibit large binding energies) and typically appear in molecular systems, while Wannier excitons are weakly bound (exhibit low binding energies, ~4.6 meV in GaAs) and appear in solid state systems. The optical properties of semiconductors and semiconductor nanostructures are dominated by excitonic effects at low temperatures, as excitons are typically the stable excited state configuration with the lowest energy [46, 142]. Exciton recombination also has a much larger dipole moment than free-carrier recombination (in most cases) because the significant spatial overlap of the electron and hole.

3.1.2 *Phonons*

In addition to electronic excitations, semiconductor lattices support vibrational excitations in the form of coordinated motion of the nuclei [46, 142]. Due to the well-defined crystal structure, these vibrations take the form of sharp, quantized modes which can be treated quantum mechanically as a quasi-particle called a phonon. In semiconductors, phonons can be split into two general categories, acoustic (in which all the atoms in a single unit cell move in phase) and optical (in which atoms in a single unit cell move out of phase). Optical phonons amount to an oscillating dipole, and can therefore interact with photons. Optical phonons typically have larger energy than acoustic phonons (40 meV in GaAs) [142].

Phonons can be further separated based on the direction of the propagation relative to the motion of the nuclei. Longitudinal (transverse) modes involve motion of the nuclei parallel (perpendicular) to direction of the phonon propagation. Longitudinal and transverse modes can be either acoustic or optical. Furthermore, the

2 In reality the motion of the hole is actually valence band electrons moving to fill the empty valence band states, (and thereby moving the empty states), but the characterizing this as motion of a single hole rather than a number of electrons is significantly simpler.

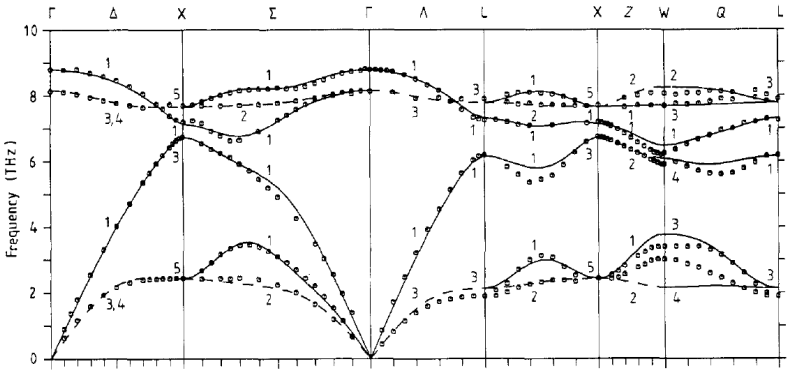

Figure 3.3: GaAs phonon dispersion curves. Reprinted with permission from Ref. [144]

energy of the phonon depends on the direction of propagation relative to the orientation of the lattice. As a result, phonon dispersion curves can be generated which are very similar to the electron and hole dispersion curves in Fig. 3.2. An example phonon dispersion curve is shown in Fig. 3.3. Another important difference between acoustic and optical phonons is that acoustic phonons go to E=0 at k=0, while optical phonons do not[3]. The equilibrium population of phonon modes depends on the temperature of the lattice; at low temperature very few modes are populated, and acoustic phonons dominate because they can have very low energies. Because phonons can have a finite momentum, they can combine with photons to activate transitions that otherwise wouldn't conserve momentum. Phonons can also scatter with other quasi-particles or be generated by the interaction of a quasi-particle with the lattice. Phonons therefore play an important role in the electronic and excitonic properties of semiconductors.

3.1.3 *Heterostructure*

A very useful aspect of semiconductor materials is that crystals made up of different compounds can be grown on top of one another to form a variety of interesting multi-layer thin-films called heterostructures. For example, materials with different band gaps grown one on top of the other will form a step like potential. In some cases, important characteristics of the heterostructure depend on the alignment of the bands, which is characterized by a value called the band offset (QC) [142]. QC is defined as the percentage of the difference in band gaps that appears in the conduction band:

$$QC = \frac{\Delta E_c}{\Delta E_c + \Delta E_v} \tag{3.1}$$

3 Alternatively, we could say that the optical phonons can be stationary, but acoustic phonons must have some non-zero momentum.

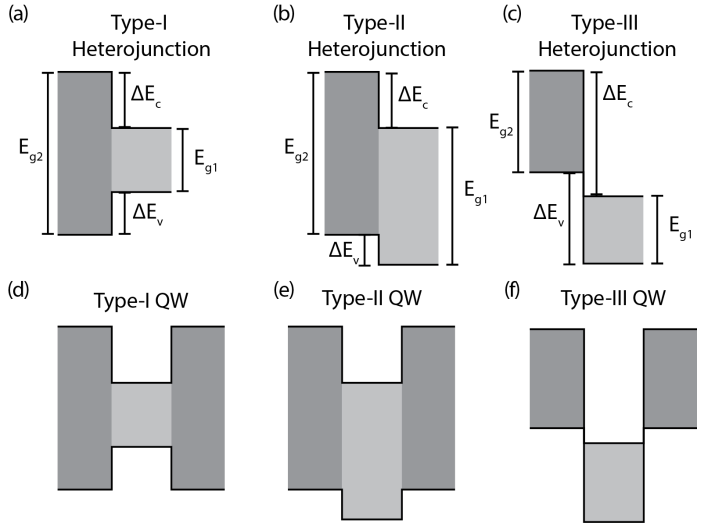

Figure 3.4: Type-I and Type-II heterostructures.

$$E_{g2} - E_{g1} = \Delta E_c + \Delta E_v \tag{3.2}$$

In general, three different types of alignments can appear for heterostructures depending on the band offset. In type-I heterostructures (Fig. 3.4a), the lowest energy conduction band and the highest valence band appear in the same material. In type-II heterostructures (Fig. 3.4b), the highest valence band and lowest conduction band levels appear in different layers. Type-III heterostructures (Fig. 3.4c) are the same as type-II, except that the lowest conduction band level appears below the highest valence band level. These different configurations result in a range of different optical and electrical properties.

3.1.4 *Exciton Confinement*

The semiconductor heterostructure that we will be studying in this thesis are called quantum wells (QWs). QWs are heterostructures consisting of a thin layer of one semiconductor material sandwiched between two layers of higher bandgap materials. If the width of the lower bandgap material approaches the exciton Bohr radius (~12 nm), discrete levels form in the QW, due to the confinement of the exciton in one direction [46, 142]. This confinement of the exciton has a number of important consequences:

A. The QW transition energy increases with the degree of confinement (decreasing QW width).

B. The exciton binding energy increases as the size of the exciton Bohr radius decreases.

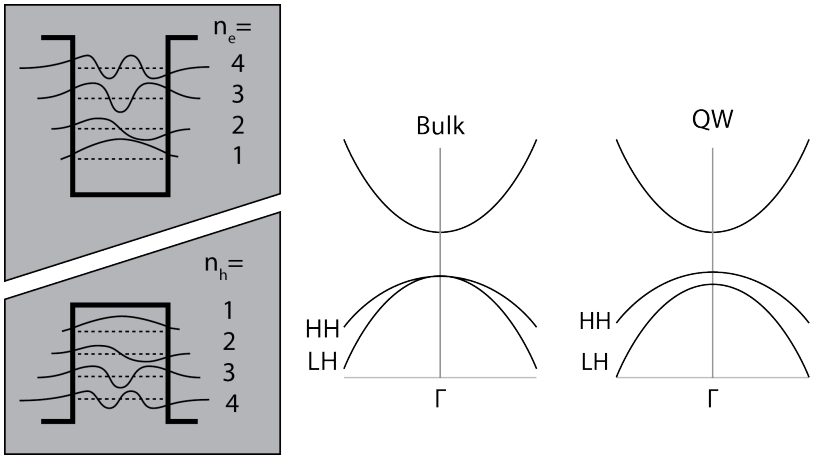

Figure 3.5: Example of wavefunctions in a QW, and band splitting of the HH and LH valence bands due to confinement.

c. The degeneracy of the HH and LH bands is lifted as the confinement shifts the bands by differing amounts due to their differing effective masses. In most cases, the HH band is the highest energy valence band in confined systems.

The optical response of QWs is dominated by excitonic effects, even more than in bulk semiconductors because of the higher binding energies. Generally speaking, there are two main types of QW systems: in which the electron and hole are confined in the same layer (type-I, Fig. 3.4c) or different layers (type-II, Fig. 3.4d)[4]. Most of the experiments in this thesis involve type-I systems, but some discussion of type-II excitons is included in Section 6.1.

Type-I QW structures consist of two potential wells - one for electrons and one for holes. The form of the solutions of the Schrödinger equation for the square potentials shown in Fig. 3.5 are well known, and commonly used during introductory quantum mechanics courses. Confinement of the electron wavefunction leads to a series of quantized approximately sinusoidal solutions of increasing order. Because the potential is not infinitely tall, the wavefunction penetrates slightly into the barrier, decaying exponentially. The exciton transition energy for the electron and hole QW states 'e' and 'h' ($E^X_{e,h}$) is then the difference between the energy of the electron (E_{n_e}) and hole (E_{n_h}) states less the exciton binding energy E_{BE}.

$$E^X_{e,h} = (E_{n_e} - E_{n_h}) - E_{BE} \tag{3.3}$$

3.1.5 *Growth Techniques*

Semiconductor QW nanostructures are realized experimentally through epitaxial growth techniques in which layers of material are deposited (grown) on a substrate.

4 Type-III QW structures can also be made, but this case does not appear in this thesis so it will not be discussed here.

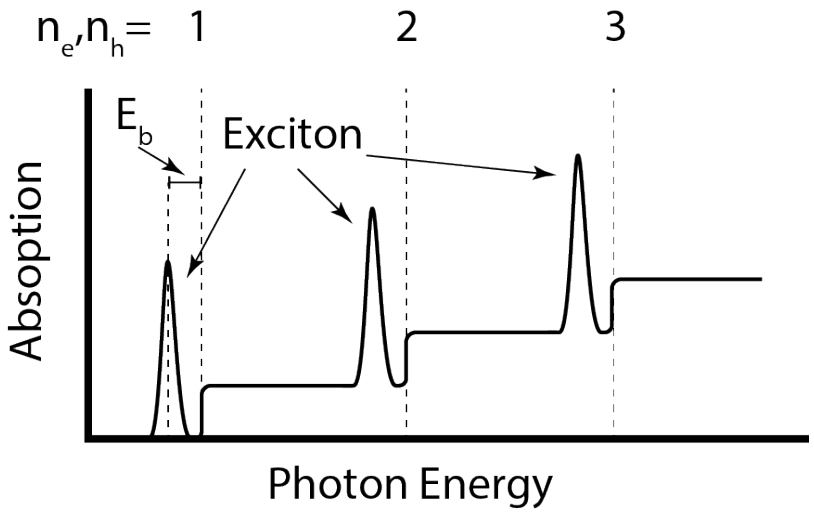

Figure 3.6: Absorption spectrum of a QW (1D confinement).

The two most common techniques used to make semiconductor QWs are molecular beam epitaxy (MBE) and metal organic chemical vapour deposition (MOCVD). In MBE, the individual constituent materials are evaporated under high vacuum and then allowed to condense on the substrate [145]. The sources of the the intended constituents are offset from one another so that they don't bond until they have reached the substrate and begun to cool to the substrate temperature. The substrate is also heated so that the atoms can find the lowest energy configuration on the surface. Thus, this technique results in single crystal growth and very uniform surfaces with sharp interfaces, controllable down to monolayer precision.

In MOCVD, gasses of molecules containing the desired constituent materials (called precursor gasses) are injected into a reactor, where they react with molecules already on the sample surface [146]. The reactions are designed so that the precursor gasses decompose on the surface and the unwanted parts of the molecules detach from the substrate and can be vented out of the reactor. The intended atoms carried to the substrate by the precursor gas bond with the atoms already on the substrate and form crystalline or polycrystalline films.

Both techniques can be used to grow samples with sub-nm precision, and both have strengths and weaknesses. MBE generates higher quality interfaces which, as we will see in the following sections, has very important implications for the optical and non-linear properties of the resulting nanostructure. MOCVD, however, has much higher throughput and does not require ultra-high vacuum, so it is used much more commonly in the manufacture of devices. The lateral (in-plane) characteristics of the interface roughness and range of defect inclusions in MBE and MOCVD grown samples are also different [147].

3.1.6 *QW Linear optical and electronic properties*

In a QW, the carriers are confined in one direction but unconfined in the other two (which is called 1D confinement). The states in the two unconfined directions are not quantized, so the solutions shown in Fig. 3.6 aren't really discrete[5]. Put another way, the carriers in the QW retain some in-plane momentum which is not quantized in the unconfined directions. To understand how this affects the optical properties, we can look at the density of states (the quantity of states at a particular carrier energy) for 0D (no confinement) and 1D confinement [142].

$$D^{0D}(E) = \frac{V}{2\pi^2}\frac{2m^*}{\hbar^2}E^{1/2} \tag{3.4}$$

$$D^{1D}(E) = \frac{A}{2\pi}\frac{2m^*}{\hbar^2} \tag{3.5}$$

The density of states for 0D (1D) confinement is dependent on $E^{1/2}$, (independent of E). As a result, the free-carrier absorption spectrum in QWs is a series of step functions, with the absorption increasing suddenly as the energy for each n is surpassed and an additional level is added. Absorption from the exciton resonance appears just below each of the steps, separated by E_{BE}.

After the excitons or free-carriers are created, they rapidly funnel down towards the 0-momentum state and the lowest confined band in the QW. This relaxation is mediated by carrier-carrier and/or carrier-phonon scattering. Because of the efficiency of this relaxation, many of the higher lying transitions do not strongly emit, even if they have reasonably large transition dipole moments. Unlike absorption, the emission from QWs is dominated by recombination of excitons with 0 momentum, and mostly from the lowest band. The zero-momentum excitons also have the largest dipole moment and subsequently the largest absorption strength.

The dipole moment of a transition is proportional to overlap integral of the electron ($\psi^e(z)$) and hole ($\psi^h(z)$) wavefunctions. In the case of QW transitions, the dipole moment (d) for transition between the valence band level n_h and the conduction band level n_e is proportional to the integral of the wavefunctions in the growth direction (z) [148]:

$$d_{n_e,n_h} \propto \int \psi^{h*}_{n_h}(z)\,\psi^{e}_{n_e}(z)\delta z \tag{3.6}$$

5 Confinement in the remaining directions can be used to create quantum wires (2D confinement) and quantum dots (3D confinement). 3D confinement does lead to discrete states. The results and discussion in this thesis are limited to 1D confined structures so the details of confinement beyond 1D will not be discussed in detail.

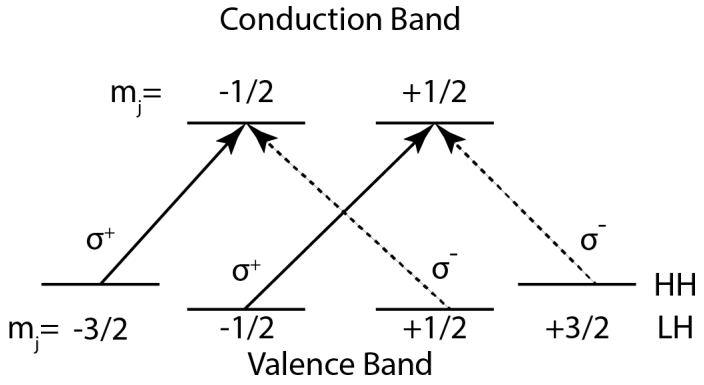

Figure 3.7: Polarization selection rules for optical transitions in semiconductor QWs. The valence band states depicted here are actually the electron states. The hole states will have an opposite m_j.

where $\psi^e_{n_e}(z)$ and $\psi^h_{n_h}(z)$ are the electron and hole wavefunctions in the confined direction (respectively). The largest overlap integrals appear when $n_h = n_e$, as the valence band and conduction band wavefunctions have a very similar z-dependence in most cases. The solutions to an infinite square well have even parity for odd values of n and odd parity for even values of n. Symmetry considerations require that the overlap of solutions with different parity (one odd, one even) will always be zero. For that reason transitions including an even n_h and an odd n_e (and vice versa) are forbidden. If $n_h \neq n_e$ but both wavefunctions have the same parity, the transition is allowed, but the overlap integral is smaller than for $n_h = n_e$, thereby reducing the dipole moment. For asymmetric potentials the parity of the wavefunctions can become ill defined so the previously parity forbidden transitions can become weakly allowed. For this reason, parity forbidden transitions can be detected experimentally in some cases.

Absorption or emission of a photon constitutes a change of ± 1 unit of angular momentum. To conserve angular momentum, the associated valence and conduction band states must have angular momentum with a difference of ± 1. This leads to only one allowed exciton transition involving each valence band state, as shown in the diagram in Fig. 3.7 (σ^+ (σ^-) indicate a right (left) polarized photon). Thus, the optically allowed excitons have a total $m_j = \pm 1$, which can be separately addressed based on the polarization direction of circularly polarized light. The spin of an electron in a LH exciton is the opposite of the spin of an electron in a HH exciton when they are both excited by the same circular polarization. Linear polarization can be expressed as a linear combination of σ^+ and σ^- circularly polarized light, so all the possible transitions in Fig. 3.7 can be excited by linearly polarized light [142].

In the absence of disorder, the linewidth of an exciton transition is limited by the pure decoherence time (T_2^*) and the exciton lifetime (T_1). The resulting homoge-

neous distribution has a Lorentzian shape with a width ($\Gamma^{(H)}$) set by the dephasing time (T_2):

$$\Gamma^{(H)} = \frac{2\hbar}{T_2} \tag{3.7}$$

Where T_2 is limited by both T_2^* and T_1.

$$\frac{1}{T_2} = \frac{1}{2T_1} + \frac{1}{T_2^*} \tag{3.8}$$

T_2^* and T_1 can be understood as follows. If we start with an ensemble of degenerate states, then T_2^* is the time it takes for an initially coherent ensemble of excitons generated by a laser pulse to lose there set phase relationship due to random phase breaking interactions. In QWs, these random interactions take the form of scattering with other carriers, phonons, defects and interface features [46]. Importantly, these interactions must be elastic, so that the phase of the oscillations of the exciton stays the same, but its phase does not. T_1, on the other hand is limited by inelastic interactions - those interactions in which the energy of the exciton is changed. Examples of inelastic interactions that occur in QWs include radiative decay of the exciton, non-radiative relaxation of the exciton into a lower energy state, or a change in kinetic energy due to absorption or emission of a phonon [46].

In unconfined semiconductors, T_1 is strongly dependent on the types of defects and their concentrations, as well as the electron-hole wavefunction overlap. In GaAs based QWs, on the other hand, T_1 is dependent mostly on the well width, and is typically in the 100's to 1000's of ps range [46]. GaAs based QWs have T_2^* which are typically on the order of 10's of ps (but as we will see in Sections 3.2.1 and 3.2.2 they depend heavily on the excitation conditions and the temperature). Thus, for semiconductor QWs, T_1 is generally much larger than T_2^*, therefore T_2^* effectively defines $\Gamma^{(H)}$. A more detailed description of the interactions that lead to decoherence and therefore shorten T_2^* and T_2 in semiconductor QWs are discussed in Sections 3.2.1 and 3.2.2.

3.1.7 *Disorder and exciton localization*

Even the best epitaxial growth techniques cannot create perfect atomically flat material interfaces. Non-uniform growth rates lead to local hills and valleys, interface roughness, and monolayer islands or terraces. Disorder can also arise in form of fluctuation of the alloy composition at the material interfaces (particularly prevalent in ternary alloys). Even layer thickness fluctuations of a single monolayer lead to significant and measurable shifts of the exciton transition energy which is extremely sensitive to the confinement potential. In high quality samples with large,

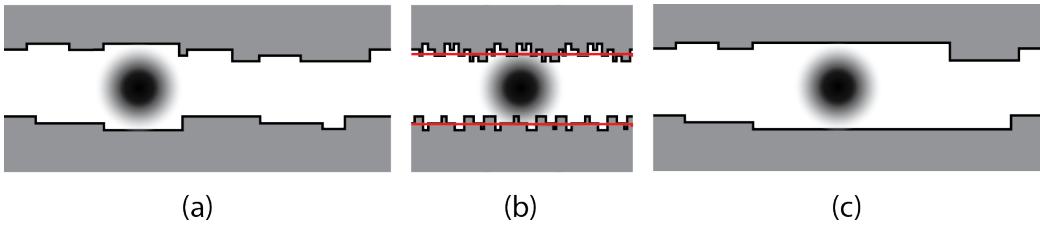

Figure 3.8: Different length scales of disorder. (a) $\ll \alpha_X$ (b) $\approx \alpha_X$ (c) $\gg \alpha_X$. The exciton in (a) sees an effective potential averaged over the disorder within its Bohr radius, represented by the red lines.

almost perfectly flat terraces, monolayer fluctuations can even be spectrally separated and the precise well-width identified [149]. In the same paper, they identified some fluctuations of the emission energy within these flat terraces which were less than the shift expected for single monolayers. The presence of these shifts revealed that even in such apparently atomically flat regions some disorder remains.

The lateral size of the disorder is also very important in predicting the exciton's optical properties. Monolayer islands with lateral dimensions similar to the exciton Bohr radius (α_X) represent an additional confinement of the exciton in the x/y plane (Fig. 3.8a), which further shifts the exciton transition energy. Roughness which is small compared with α_X (Fig. 3.8b), does not confine the exciton in plane. Instead, the exciton experiences an effective potential which is an average of all the different widths within α_X (represented by the red lines in Fig. 3.8b). Finally, roughness which is very large compared with α_X results in large areas with nearly degenerate exciton energies, and discrete energy levels due to the monolayer fluctuations in high quality, narrow QWs (Fig. 3.8c).

The interface roughness can be coarsely controlled by changing the growth parameters (such as growth speed or substrate temperature), or by including growth interruptions of ~10-90 s, which lead to the generation of monolayer islands of increasing size. Loosely speaking, the longer growth interruption applied, the larger the resulting islands become as the atoms are given time to relax into the lowest energy configuration [149–151].

Static disorder causes some important modifications of the optical properties of QWs. First, the lateral size of the roughness is typically much smaller than the spatial resolution of optical experiments, so many different well widths are excited simultaneously. These optical measurements therefore represent an ensemble measurement encompassing a large range of well widths, resulting in additional broadening of the exciton line. For monolayer fluctuations that have a lateral size much larger than α_X, the structural broadening is inhomogeneous, since (in principle) we can consider each exciton to inhabit a QW with a well-defined width and a linewidth limited homogeneous broadening. This is the way that static disorder is typically considered in QWs, and results in a stochastic broadening of the exciton line. The resulting exciton line-shape is a convolution of the dephasing limited homogeneous linewidth with the Gaussian disorder induced broadening. This line-

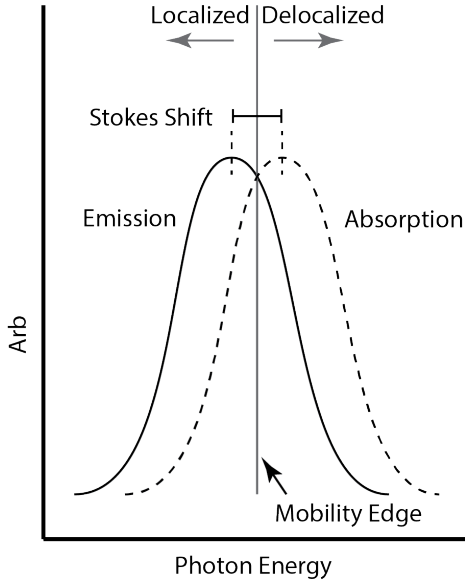

Figure 3.9: Spectral characteristics of localization in QWs. The stokes shift, and localized and delocalized excitons separated by a mobility edge.

shape is commonly referred to as a Voigt line-shape. For the MBE (MOCVD) grown GaAs based QW samples studied in this thesis, structural disorder typically results in linewidths of ~0.5-2 meV (~3-5 meV).

Another important effect of disorder, is excitons in the narrower region (the higher energy side of the inhomogeneous distribution) can relax into the wider regions of the QW through the emission of a phonon or inelastic scattering with another exciton. For QWs with broad inhomogeneous distributions and certain types of disorder, this results in a shift of the emission spectrum to lower energy with respect to the absorption line (as shown in Fig. 3.9). This shift is often called a Stokes shift. The inhomogeneous distribution of excitonic states is therefore typically interpreted in the following way [152, 153]: the low energy side of the distribution is made up of localized states - excitons trapped in a monolayer island. The high energy side of the inhomogeneous distribution consists mostly of excitons which are not trapped in monolayer islands. The two types of states are separated by a line in the middle of the distribution which is called the mobility edge. The sharpness of the mobility edge, and the size of the Stokes shift depend on the number and distribution of the lower energy islands as well as the excitation density and the well width.

In this view, separately measuring the properties of delocalized and localized excitons is possible by looking at the high and low energy side of the inhomogeneous line, respectively. For example, studies have shown that the delocalized excitons are affected by collisional dephasing at lower densities than localized states [154] and that the homogeneous linewidth is typically larger for delocalized excitons [153, 155].

Webb et al [156] presented a differing view of how disorder manifests spectrally. In this work and several others [157–159], they reported a QW sample that simulta-

neously exhibits free polarization decay and photon echo signal, suggesting simultaneous homogeneous and inhomogeneously broadened character. To reconcile these surprising results they suggest that the photon echo signal belongs to localized excitons while the free polarization decay belongs to delocalized excitonic state. This is a surprising result because the delocalized and localized excitons have nearly identical emission energies, contradicting (or going beyond) the mobility edge interpretation given above, which would predict the two types of excitonic states to have separate emission energies. Interestingly, in agreement with the interpretation given above, the localized and delocalized excitons appeared to have different density dependence, with the delocalized excitons only appearing at high power. Such spectrally overlapped localized and delocalized exciton states have also been reported by Ashkinadze et al [160] based on modulation of resonantly excited excitons in GaAs/AlGaAs QWs, and by Erland et al [161], who determined that a multi-exponential decay of a FWM signal came from sub-populations of localized and delocalized excitons.

However, this interpretation - the existence of spectrally overlapped delocalized states - is not widely accepted, and a detailed understanding of what leads to the appearance of the apparently delocalized state at high power is still lacking [162]. Correlation of these properties with detailed, nm scale measurements of layer topography would be very enlightening, but unfortunately such measurements are difficult to realize. It is also hard to know which of these views of disorder to apply to MOCVD samples because most of the studies of disorder focus on MBE grown samples which likely have very different lateral disorder distributions and because there are not many nm scale measurements of MOCVD grown samples.

Finally, it is worth noting that excitons can dephase due to scattering off disorder, though the details of how the topography induces scattering is not clear [163–166]. One intuitive way that scattering can occur is through the relaxation of the exciton from one region of the well into an energetically favourable one.

3.1.8 *Defects*

Semiconductors can also have defects in the crystal structure, which come in the form of point defects (e.g. incorporation of an unintended atom, or a missing atom) and longer range dislocations of the crystal structure. Point defects can be donors (has an extra electron) or an acceptors (extra hole). Excitons can be bound to a defect site (localization of the electron and hole at the defect), or lead to recombination of a free electron (hole) with an acceptor (donor) defect. In GaAs, defects are typically shallow[6] and can be identified in photoluminescence experiments as peaks just below the material bandgap energy or as a red shift of the band edge. Dislocations, unlike point defects, do not typically have optically allowed transitions,

6 Deep defects can occur in GaAs and other materials and can modify properties, but for the purposes of this thesis, only shallow defects are discussed.

but instead function as non-radiative relaxation centres in which the energy of the electronic excitation is dissipated into the lattice [142].

Even in the highest quality epitaxial layers defects still occur. Deposited GaAs layers, for example, have been studied in great detail using photoluminescence and PLE spectroscopy, and it has emerged that the most common defects are interstitial or substituted carbon [128, 167, 168]. Carbon defects in GaAs have a well known emission profile at low temperature: a range of defects occur just below the bandgap (from 1.510 eV to 1.515 eV), as well as two broad, strong peaks at 1.490 eV and 1.493 eV [128, 167, 168].

Controlled incorporation of defects also allows for doping of the semiconductor such that there are some carriers in the conduction band (n-type) or holes in the valence band (p-type) at equilibrium. Doped semiconductors are incredibly important for opto-electronic devices, such as PIN diodes, and therefore their electronic and linear optical response have been studied in great detail. However, most of the fundamental studies of the coherent response of excitons have been limited to nominally intrinsic (undoped) materials [142].

3.1.9 *Lattice mismatch and strain*

Differences in the lattice constants of the materials which make up semiconductor heterostructures (often called lattice mismatch) can lead to the incorporation of strain which can affect the optical and electronic properties of the resulting structure [142, 169, 170]. If the lattice mismatch is small and the layers are thin, the strain results in a static deformation of the crystal structure. If the lattice mismatch is large and/or both layers are thick, the interface can relax in the form of dislocations (missing bonds). In the static deformation regime, lattice mismatch induced strain reduces the symmetry of the crystal lattice, which has important consequences for the optical properties [142]. Crystal deformation shifts the bands, and changes the band gaps according to the deformation potential, which is an intrinsic material property. Additionally, (depending on orientation of the lattice relative to the growth direction) the HH and LH bands are shifted in opposite directions due to spin-orbit coupling of the holes. This can have important consequences in certain heterostructures. For example, in GaAs/InGaAs QWs with certain well-widths and low indium content, strain can lead to a potential profile which is type-II for light holes and type-I for heavy holes [169, 170].

Depending on the growth direction and the types atoms in the lattice, strain can induce an internal electric field which can modify the shape of the potential well in QW structures. This deformation can lead to effects such as ill-defined wavefunction parity, the quantum confined stark effect, and drastically extended exciton radiative recombination lifetimes [171].

Lattice mismatch induced dislocations are important as well, but less easily identified in optical experiments. The deformation of the crystal and subsequent strain are reduced, but defects are introduced. These defects can act as traps for electrons or holes which prevent them from recombining radiatively. Instead they will eventually relax via non-radiative processes (which can also be provided by the defects themselves) [171].

To avoid lattice mismatch a select few material systems (such as GaAs/AlGaAs) have been used extensively. However, if strain could be tolerated, a much larger range of materials would become available for use in heterostructures. For this reason, there is considerable interest in understanding the effects of strain and mitigating those which are detrimental to the resulting quality of the resulting heterostructures [172].

3.2 Coherent response

An ultrafast laser pulse incident on a semiconductor QW and resonant with the excitonic transition energy will excite a coherent ensemble of excitons which then scatter off other excitons, free-carriers, phonons, defects and/or structural disorder. At low temperature ($T < 20K$) the coherent ensemble dephases (due to inhomogeneous linewidth) and decoheres (due to random phase breaking interactions) over the first couple of picoseconds, then relaxes through radiative and non-radiative processes back into equilibrium over the following 100's to 1000's of ps[46]. FWM and successive techniques such as six-wave mixing and CMDS are capable of measuring exciton dynamics through this first coherent stage. This section will provide a brief overview of what coherent experiments have been performed on excitons in QWs and what they have taught us about the physical underpinnings of the coherent response of the system. More specifically, it will show how it has emerged that the coherent response of excitons QWs is fundamentally dependent on many-body interactions and is therefore a good template for studying many-body phenomena[162].

3.2.1 *Decoherence induced by phonons*

In QWs at low temperature, decoherence of the macroscopic polarization induced by the first pulse occurs over a number of ps. At the low excitation limit, the dominant physical mechanism for the decoherence is elastic (interactions that contribute to T_2^*) and inelastic scattering (interactions that contribute to T_1) with phonons. The inelastic scattering mechanisms include emission of a phonon due to cooling of excitons not generated at k=0 and migration of excitons to an energetically favourable monolayer island. The processes involving absorption of a phonon are also possible, but less likely at low temperature when very few phonon modes are thermally pop-

ulated. Elastic scattering in which phonons stochastically change the phase of the polarization but do not change its energy - also contribute to decoherence [46].

The role of phonon induced decoherence can be studied using temperature dependent FWM and absorption experiments. Absorption experiments cannot separate homogeneous and inhomogeneous broadening, and are therefore intrinsically difficult to extract the information we want (especially at low temperature where the inhomogeneous linewidth is typically much larger than the homogeneous linewidth). For that reason, direct measurement of the decoherence time with FWM is more easily interpreted, and can elucidate the role of acoustic phonons (which contribute more than optical phonons at low temperature) [46, 173, 174]. Several experiments have been conducted, showing the expected linear dependence on temperature for acoustic phonons [174], and a more complex exponential dependence for optical phonons [173]. The fits to temperature dependent experimental dephasing rates do not go to zero when extrapolated to 0 K. This is due to the additional contribution of decoherence due to interface roughness, defects and the exciton radiative lifetime [46, 162].

3.2.2 *Decoherence due to carrier-carrier interactions*

Collisional decoherence due to exciton-exciton and exciton-free carrier scattering can be measured with FWM or linear techniques as a function of excitation density. FWM is better suited as it can be used to isolate the homogeneous linewidth. Several experiments have been conducted, and experimentally demonstrated that (particularly for large densities) the homogeneous exciton linewidth broadens linearly with increasing intensity. Interestingly, it was also shown that the scattering of excitons with free-carriers caused a linear increase of the homogeneous linewidth which was $8\times$ greater than that produced by the same density of excitons [46, 175].

It should be noted that the deconvolution of exciton-exciton scattering and phonon scattering is not straightforward. Typically it involves measuring the exciton homogeneous linewidth as a function of both excitation density and temperature, and then extrapolating to 0-excitation and/or 0 K [46, 173]. However, the validity of extrapolation of the linewidth to 0-excitation density has been questioned as it requires that the excitation induced decoherence can be fully deconvolved from the single exciton response [43, 176, 177]. This is not necessarily the case, because (as we will see in section 3.2.4) exciton-exciton many-body interactions and correlations are now known to be significant contributors to the FWM signal, and are not easily deconvolved from the single exciton response [43, 176].

3.2.3 *Quantum-beats*

When multiple exciton transitions are simultaneously excited, quantum beats (QB) can sometimes be detected. QBs occur when multiple quantum pathways interfere in a single quantum system, resulting in oscillations of the FWM signal as a function of t_1 and/or t_3, which match the energy separation of the excitonic transitions. A requirement for the presence of QBs is that the two transitions to be part of the same quantum system, so the detection of QBs is often taken as evidence that the transitions are coupled[7]. QBs have been detected for a range of different exciton transitions in QWs, including coupling of HH and LH excitons [179, 180], excitons localized in different monolayer islands [24, 33, 44], localized and delocalized excitons [181], excitons in a coupled double QW [32, 76, 182], type-I and type-II excitons [183, 184].

QBs were usually interpreted as indicating that the two transitions cannot be described as two separate (uncoupled) two level systems, but instead as a three level system with a shared ground state [44, 46]. Unfortunately, (as detailed in Fig. 2.11) population transfer, coherent superpositions, ground state bleach and excited state absorption pathways can all interfere with single transition pathways to generate QBs. For this reason, the detection of QBs is not by itself enough to unambiguously identify the coupling pathway or underlying mechanisms.

Multidimensional spectroscopy represents a notable expansion of FWM capabilities in this regard. First, through detection of the phase, the QBs generated via the coherent superposition pathway can be isolated by scanning the second time delay. Second, the detection of the signal phase also helps to separate the QBs from fluctuations in the signal due to noise. The phase of the QBs varies systematically as the delays between the pulses change, while the phase of the noise varies randomly. QBs are therefore more easily identified and separated from noise when the signal is Fourier transformed, even when the beat amplitude is near the noise floor. Finally (as indicated in Fig. 2.7), the inclusion of phase information in CMDS removes the ambiguity in the energetic direction of the coupling. Put another way, QBs tell us what the magnitude of the energy difference of two coupled states A and B is ($|E_A - E_B|$), while CMDS gives us both E_A and E_B directly. The improvements listed in this paragraph are a large part of what makes the experiments in the following chapters possible.

Subsequent FWM experiments [49, 185] and (in recent times) multidimensional spectroscopy studies [53, 54, 81] have been used to understand how the many-body effects described in the following section contribute to QBs and coupling of distinct states.

7 For detection at a single wavelength, polarization interference (PI) can be mistaken for QBs (interference of the emitted signal in the far field, instead of interfering quantum pathways in the sample). However, QBs have in phase oscillations across the entire ensemble while the phase of the PI oscillations changes by π. QB and PI can therefore be easily separated in spectrally resolved four-wave mixing (FWM) experiments [178].

3.2.4 *Many-body Effects*

Inorganic crystalline semiconductors are ordered arrangements of atoms whose behaviour is dictated by a semi-infinite number of covalently bonded atoms interacting through Coulomb forces over semi-infinite distances. This fundamentally many-body system is therefore an interesting platform for studying many-body interactions of delocalized electronic excitations [186].

The prevalence of many-body effects in QWs was first hinted at by two beam FWM experiments. The basic theory of FWM (as presented in section 2.1.1) tells us that we should only see signal when the conjugate pulse arrives first (which is typically considered to be a positive delay). However, a wide range of two beam FWM experiments demonstrated negative delay signal that was nearly as strong as the positive delay signal [31, 186]. Furthermore, time-resolved two beam FWM experiments showed an unexpected delayed signal rise even for positive delays and homogeneously broadened QWs [187]. The consensus formed that these anomalous signals were a result of many-body interactions [43, 186]. Several different many-body effects have been investigated: local field effects (LFE) [31], excitation induced dephasing (EID) [176], excitation induced shift (EIS) [79] and multiparticle correlations (e.g. biexcitons) [180].

LFE, EID and EIS are in many ways very similar effects, in that they involve the generation of signals through spatial modulation of the different material properties. Therefore, they cannot be easily separated experimentally. Furthermore, though this section focuses on the negative delay signals, these many-body effects also contribute to signals when t_1 and t_2 are positive, where they are inherently convolved with the single exciton response. For this reason, understanding these many-body effects is crucial in the proper interpretation of FWM and CMDS experimental results.

3.2.4.1 *Local field effects*

Local field effects occur because of the coherent re-emission of photons by a macroscopic polarization which was generated by a laser pulse [43][8]. Each pulse that is incident on the sample creates a macroscopic polarization with the wave-vector of the incident pulse, which then decays according to the inverse of its inhomogeneous linewidth. While the macroscopic polarization still exists it is continuously emitting radiation with same wave vector as the incident pulse. This polarization can then act as a source for signal in the phase matched direction instead of the original pulse. Since the polarization lasts for much longer than the ultrafast pulse, this second field can a produce a signal in which the interaction involving the second

8 LFE does not necessarily require coherent re-emission of a photon, just that there is some remaining polarization from previous pulses that can act as sources even after the pulses have disappeared. However, thinking of LFE as coherent re-emission is more intuitive. Furthermore, the effect of the non-radiating polarizations is also suppressed by dielectric screening.

pulse occurs after the first (conjugate) pulse even for negative delays far beyond the excitation pulse widths.

3.2.4.2 *Excitation induced decoherence*

Although it wasn't recognized as such at first [63, 175], excitation induced decoherence of excitons is also a many-body effect, and can be used to explain the presence of signal for negative delays [43, 162, 186]. EID is a many-body effect in that the collective action of many exciton-exciton interactions serve to shorten the dephasing time and increase the linewidth. In addition to modifying the signal in the positive delays, EID was found as a possible source of negative delay signal [176, 177]. A physical explanation of how EID can generate signal in the negative pulse ordering[9] can be more intuitively provided considering a three pulse FWM experiment, detected in the $-k_1 + k_2 + k_3$ direction, with the $k_2 \rightarrow k_3 \rightarrow k_1$ pulse-ordering.

The first pulse incident on the sample (k_2) generates a macroscopic polarization. k_3 and k_1 then produce a population grating. This population grating leads to a spatially varying decoherence rate due to EID, which modulates the decoherence of the macroscopic polarization left over from the first pulse. This leads to a sort of 'decoherence grating' in which the areas of constructive interference between the second and third pulse decohere rapidly, and the areas of destructive interference decohere slowly. As a result, the wave-vector dependence of the second two pulses will be imprinted on the macroscopic polarization from the first pulse, and some portion of the emitted signal is diffracted into the $-k_1 + k_2 + k_3$ direction. The strength of this signal is proportional to the strength of the EID. Put another way this effect can be thought of as the scattering of the coherence generated by k_2 off of the population created by k_3 and k_1 [43].

3.2.4.3 *Excitation induced shift*

Like EID, EIS is a many body effect that results from exciton-exciton interactions and therefore depends on density. It was first identified in spectrally resolved transient transmission experiments, where it manifested as a spectral shift of splitting of the exciton line [188, 189]. Later, it was recognized that EIS could be considered as a source for FWM signals [43, 79]. In the same work the authors demonstrated that peak shapes in FWM and transient transmission experiments could be accurately predicted by modified Bloch equations (a modified form of the equation in section 2.1.1) with phenomenological inclusion of an EIS parameter that scales with the exciton population. Physically, EIS can be explained as a modification of the exciton binding energy due to excitation induced screening of the electron-hole Coulomb attraction [188].

A semi-physical explanation of how EIS can generate signals is very similar to the explanation for EID [43, 63]. The population grating generated by k_3 and k_1

9 EID can also generate signals for 'positive' delays.

leads to spatially periodic modulations of the center of the exciton spectrum, and subsequently the susceptibility. Like the 'decoherence grating' induced by EID, the 'susceptibility grating' from EIS imprints the wave-vector dependences of k_1 and k_3 onto the polarization, which then emits photons into the $-k_1 + k_2 + k_3$ direction. Less intuitively, EIS also leads to a mixing of the real and imaginary parts of the susceptibility which changes the real peak shapes in 2D spectra from absorptive to dispersive. This peak shape change has been detected experimentally in both cross-peaks (CPs) and diagonal peaks (DPs) [53, 54].

3.2.4.4 *Multi-particle correlations*

LFE, EID and EIS are usually considered phenomenological modifications to a mean-field interpretation. A more complete physical description of the coherent response would also include higher order multi-particle correlations. Such correlations can be included by expanding the system density matrix to include additional states, and (though they cannot be solved analytically) the resulting differential equations can be solved numerically depending on how large the system is and what effects are included. A detailed understanding of how these correlations contribute to the FWM signal and affect the single exciton response is unfortunately still lacking. In that vein, a variety of experiments that isolate signals resulting from correlations of four or more particles have been conducted in recent years [86, 190, 191]. These preliminary experimental results will be the subject of the following paragraphs. While it is clear from these results that multi-particle correlations are present in QWs, it remains to be shown what role they play and how important they are in the single exciton response.

Beyond excitons, the next level of complexity in multi-particle correlations are biexcitons, which is a bound quasi-particle made up of two excitons (two holes and two electrons). Bound biexcitons in GaAs have a binding energy of 1-2 meV, and therefore appear in spectra as shoulders at slightly lower energy than the 1-exciton transition [192]. It has been shown that unbound four particle correlations also appear. The lack of binding energy means that they occur at the same energy as the single exciton resonance, so they cannot be as easily detected using linear techniques. 2-quantum (2Q) 2D spectroscopy has proven to be a very effective tool for studying these four particle correlations, since they can be separated along the 2Q axis [86, 191].

If we leave the exciton quasi-particle basis and return to electron/hole particle basis, we can view biexcitons as the correlated motion of four charged particles in a potential well. In a simple view, this can explain how signals are generated in the negative delays. Two photons excite a four particle quadrupolar motion, which oscillates at the sum of the two exciton frequencies [63]. Although the quadrupolar motion represents oscillating charges, symmetry of the correlation means that the charge motion cancels and there is no net dipole. The four-particle motion

can therefore not directly emit photons. The third pulse then perturbs this motion, inducing some net charge oscillation. The oscillation of charges implies a dipole moment and therefore the perturbed four particle motion emits signal photons. This four-particle picture provides an explanation for the observation of 2-exciton correlations in QWs which appear in experiments with negative delays[63].

If we take a step back again and remember that these oscillations are not actually occurring in a 'vacuum', but rather spread out across a large number of lattice sites, we see that the physical details of this motion are dependent on the real space characteristics of the lattice. The real space motion of two- or four-particle correlations is therefore far from intuitive. This illustrates the difficulty of a true many-body treatment of excitons including multi-particle correlations [63].

Still, recent work has gone into measuring and understanding the dynamics of biexcitons, including identifying which biexcitonic pathways contribute to third order signals [191], measuring binding energies [96], understanding how biexcitons interact with excitonic pathways [86] and how biexcitons contribute to coupling of distant excitonic states [73]. Other experiments have used six-wave mixing to investigate correlations beyond four particles, (such as triexcitons and six particle correlations) and shown that they also affect the single exciton response [190, 191]. Finally, stepping away from FWM momentarily, a very stable pump-probe experiment and 2D spectroscopy were recently used to identify a new quasi-particle to which the authors gave the name 'dropleton'. They use a novel analysis protocol in which the fundamentally classical measurement is projected onto a basis made up of coherent states, and demonstrate stable correlations of up to 6 electron hole pairs [193]. Beyond identification of these signals, many of the details of these multi-particle correlations (such as their prevalence and how they contribute to measured single exciton dynamics) remain to be explored.

Viewing the coherent response of excitons in QWs as a many-body system including multi-particle correlations beyond excitons is a more complete physical way of looking at the system. Based on the recent experiments, these multi-particle correlations clearly can be generated in QWs and contribute in experiments measuring coherent exciton dynamics. However, the fundamental understanding and computational tools required to incorporate multi-particle correlations into the mean field theory are lacking. Care must therefore be taken in reconciling FWM and CMDS experiments with theory because multi-particle correlations clearly exist (based on the experiments detailed in the previous paragraphs), and may play a non-trivial role which is not captured in typical mean-field interpretations. Furthermore, extending experiments beyond these preliminary investigations is an important next step. It would be particularly useful to find a way to experimentally deconvolve the multi-particle response from the single-exciton response.

3.2.5 *Multidimensional spectroscopy to study coherent effects in QWs*

Because of the enhancement of the capabilities over standard FWM, CMDS is a likely candidate for future investigations into many-particle correlations and many-body effects in semiconductor QWs, and for clearing up some of the ambiguity discussed in the previous section. Over the last decade a range of 2D spectroscopy experiments into QW excitons have been conducted, and have been focussed on replicating or extending previous FWM experiments. These experiments have served to both characterize the capabilities of 2D spectroscopy and to exploit them to incrementally extend our understanding of QW exciton dynamics.

Since the first report in 2005 [56, 194], nearly all of the investigations into coherent effects in QWs using multidimensional spectroscopy have been conducted by two groups. The Cundiff group has been using 2D spectroscopy to investigate many-body effects. Their general approach has been to use numerical simulations involving phenomenological incorporation of EIS, EID and LFE to understand the peak shapes and presence of CPs in 1-quantum (1Q) and 2Q 2D spectra [53, 54, 80, 81, 195]. They also demonstrated that 0Q coherence could be used to explore coherent-superpositions [50], detected exciton-trion coupling in a polar CdTe QW [82], demonstrated photo-current detected 2D spectroscopy [69], and measured the coherent linewidth of a QW grown on a (110) substrate [196]. In addition to this single-QW work, they have also performed two investigations into coupling of double QWs, (which will be discussed in more depth in the following chapter) [54, 197].

The Nelson group has focused on studying multi-particle correlations using third, fifth and seventh order experiments [191]. As described in the previous section, they were able to identify 6-particle correlations and learn many things about bound and unbound biexcitons.

Two other investigations have recently been added by other groups. Paul et al reported some basic characteristics of a modulation doped single QW using 2D spectroscopy techniques [198]. Glinka et al investigated the in-plane coupling of excitons localized to different monolayer islands in a narrow single QW, and similar to the FWM mixing experiments described in section 3.2.3 demonstrated that nonlocal coupling of excitons can be relatively strong in QWs [199].

Many of the experiments listed in the previous paragraphs have focused (in one way or another) on technique development. They have developed and characterized the capabilities of 2D spectroscopy of QWs, and shown its extensive potential. Beyond technique development, these experiments have also led to incremental improvements in our understanding of the coherent response of excitons in QWs in part by repeating experiments conducted previously using FWM techniques. Finally, some important extensions of FWM have been recently demonstrated, particularly by looking at the 2Q response.

We are approaching a point at which the capabilities of CMDS are well understood and characterized, and the analysis tools we have available (such as peak shape analysis) are well defined. We are therefore now ready to extend experiments in new directions not previously possible using FWM, with the goal of continuing to unravel the complex many-body interactions that dominate the coherent exciton response in QWs.

4

INTER-WELL COHERENCE AND PATHWAY-SELECTION IN DOUBLE QUANTUM WELLS

The study of inter-well coherences in asymmetric double quantum wells (DQWs) is a good demonstration of how pathway selection can be useful. In particular, we will show that it can effectively isolate coherent inter-well interactions in the case where the barrier between the wells is wide enough that there is essentially no hybridization of the wavefunctions. In this chapter, 1-quantum (1Q) 2D and 3D spectroscopy with and without pathway-selection are used to study inter-well coherences in two separate DQW systems. Section 4.1 presents a brief literature review of coherent dynamics in DQWs, and provides the motivation for the work presented in this chapter, which can be split into two categories: technique development and understanding coherent inter-well interactions in DQWs. Section 4.2 expands on Section 2.3, and presents a more detailed description of the benefits of pathway selection using spectrally shaped pulses. Sections 4.3 and 4.4 present experimental results on GaAs/AlGaAs and InGaAs/GaAs DQWs, respectively. The some of the discussion in Section 2.3 and some of the results in Section 4.3 were published in 2014 [95].

4.1 Motivation

4.1.1 *Motivation 1: Technique development*

Evidence of coherent coupling of excitons in biological light harvesting complexes (LHCs) was recently demonstrated experimentally using 2D spectroscopy [6, 200]. These original results have set into motion a large number of experimental and theoretical studies, with coherences now observed in several different types of LHCs [5, 8, 9, 97, 98, 200, 201]. The interpretation of these results are still controversial, and whether the observed coherent effects are important to the function of photosynthesis still remains to be determined. Still, it is a phenomenon that merits further examination because it has been suggested that the coherences may be responsible for the surprisingly fast and efficient funnelling of charges from the antennas to the reaction centres. If this effect could be understood in LHCs, it could perhaps be used in the design of more efficient light harvesting technologies.

Some challenges in interpreting these results come from experimental limitations of 2D spectroscopy. All of the 2D spectroscopy experiments previously reported use broadband excitation pulses which simultaneously excite a wide range of pathways. As most of what is of interest are coherent interactions, many of those pathways do not provide useful information but do obscure the signal of interest. By using pulses tuned to two different transitions, the coherence pathway can be selectively excited and all other pathways suppressed.

Some previous experiments have used this approach to study the LHC PC645. These experiments utilized pulses from two different OPAs tuned to two different transition energies to isolate the coherent superposition signals [10, 97, 98, 201]. They were able to use the selectivity to develop a much clearer picture of the electronic structure of PC645. They were, however, also unable to perform 2D spectroscopy because the outputs from the OPAs lacked the phase stability required to measure the signal phase. An extension of this selective approach to coherent multidimensional spectroscopy (CMDS) by also collecting the signal phase would be advantageous, as the peak-shape and line-shape analysis tools in CMDS are very powerful.

However, LHCs are not the best sample for demonstrating such a technique due to their broad spectra and short dephasing times. They also have very complex electronic structures including ground and excited state vibrational manifolds as well as multiple overlapping electronic states. For the purposes of demonstrating the pathway selective CMDS technique, it would be preferable to use a 'simpler' sample. DQWs are a good option because they exhibit discrete excitonic levels and sharp phonon lines instead of broad vibrational manifolds. The exciton transition energies can be controlled by changing the width of the wells, and the amount of interaction between the wells can also be controlled by changing the width of the barrier between the wells. While the types of excitons in QWs are completely different from those in LHCs, the success of the technique in studying QWs may signal that pathway selective CMDS could be useful in studying other systems (including LHCs) as well.

4.1.2 *Motivation 2: Mechanism of coherent inter-well interactions in wide barrier DQWs*

Over the past three decades, continued effort has been put into understanding the physics underpinning inter-well excitonic interactions in DQWs, multiple-QWs (MQWs) and QW superlattices [32, 46, 202, 203]. Understanding these interactions is important for devices, such as superlattice lasers [202], quantum cascade lasers [2] electro-absorption modulators [204] and resonant tunnelling diodes [3]. In addition to these device applications, double quantum-wells provide a very nice template for studying fundamental quantum mechanical phenomena. With modern deposition techniques such as molecular beam epitaxy (MBE) and metal organic

chemical vapour deposition (MOCVD), many aspects of the structure (such as barrier height, well and barrier widths, doping concentrations) can be very precisely controlled. This makes for a template in which coupling strength, environmental factors and spectral markers can be designed to suit the experiment.

The DQW potential profiles have confined conduction band and valence band states with wavefunctions that are straight forward to calculate numerically. As with many semiconductor nanostructures, DQWs exhibit strong interactions with electromagnetic fields and sharp, excitonic resonances. These resonances provide convenient spectral markers which can be used to precisely identify where in the heterostructure the exciton is located. MBE and MOCVD growth techniques produce QWs with very little structural disorder and hence very little inhomogeneous broadening, which typically lead to excitonic resonances which are easily separable even in the presence of the structural disorder.

For this reason, there have been many investigations into coherent interactions in DQW structures. However, most of the investigations have focussed on DQW samples in which the barriers are narrow and/or low, so that there is significant hybridization of the wavefunctions. In this situation, states are better considered as eigenstates of the full DQW structure rather than individual states. As a result, differentiating between coupling due to a shared ground state and excited state coupling is more difficult. To study the phenomena of coherent superpositions of spatially separated states, we must investigate DQWs with wide enough barriers that there is very little wavefunction hybridization.

The dynamics of coherent inter-well interactions were first studied using FWM spectroscopy. Leo et al [32, 205] showed that coherent inter-well interactions can also be detected as quantum beats (QBs) in pump-probe and four-wave mixing (FWM) measurements. The interpretation of these QBs, however, was limited by ambiguity in the assignment of the quantum pathways generating the signals. The QB spectroscopy of inter-well coupling was mostly limited to DQWs with narrow barriers (in which strong QBs could be resolved), so little insight was gained into coherent inter-well coupling in the excited state.

Quantum beats from a DQW structure indicate the presence of charge oscillations from one well to another. In strongly coupled wells (i.e. with narrow barriers) these beats can have a large amplitude so the charge oscillations can generate emission at the energy difference between the coupled transitions (typically in the low THz range) [32]. It was shown that the THz emission could be coherently controlled in double pulse experiments [106]. The emission of THz radiation relies on the coherent inter-well charge oscillations, so spectroscopic studies of the THz emission from DQWs when excited by fs pulses can be used to study inter-well coupling [206]. However, the long wavelength of the THz emission intrinsically produces emission over a long a period of time, so some inter-well dynamics which appear on a much shorter time scale cannot be temporally resolved. Furthermore, these experiments typically focussed on the narrow barrier DQWs where charge oscillations can be

more readily observed. For wider barrier wells, the less efficient tunnelling of carriers through the barrier results in a much weaker THz emission [46].

Some fundamental insight has been gained during the development of devices in which coherent inter-well interactions play a crucial role. For example, the quantum cascade laser (QCL), first demonstrated in 1994 by Faust et al [2], relies on inter-well coherence to rapidly repopulate the lasing state. Studies of QCLs using ultrafast spectroscopic techniques has led to an improved understanding of rapid coherent charge/energy transfer. In particular, studies have focused on the regime where the barriers are narrow and there is strong inter-well coupling, which is most relevant to the function of the devices [207, 208].

More recently, several CMDS experiments have been conducted on DQWs with wide barriers [54, 76, 77, 182]. The first of which was published in 2009 by Li et al [197], in which 2D 1Q spectra were reported for DQWs with two different barrier widths (1.7 nm and 10 nm). The 2D spectrum of the sample with the 1.7 nm barrier demonstrated a grid pattern of cross-peaks (CPs) and diagonal-peaks (DPs) showing that the two transitions in each well (heavy-hole; HH and light-hole; LH) were strongly coupled to the two transitions in the other well. The wavefunctions were significantly hybridized because the barrier was quite narrow, so the excitons could not be considered to be localized to a particular well, but rather extended across the entire DQW. More interestingly in the context of coherent superposition of spatially separated states, the 1Q 2D spectrum for the 10 nm barrier sample appeared to show at least one inter-well CP. Unfortunately, conclusive identification of the excitonic states associated with the CPs was prevented by the lack of spectral separation of the transition energies. Specifically, the separation of the lowest energy HH exciton transition in each well was comparable to the the separation of the HH and LH exciton transitions in the wide-well. As a result, the authors were unable to determine whether the ostensibly inter-well CP was not a result of intra-well interactions between HH and LH excitons in the same well. This work also demonstrated that simply identifying CPs a 2D spectrum cannot be used to directly discern coupling mechanisms or pathways. In particular, identifying coherent superpositions was not possible with a 1Q 2D spectrum alone.

Earlier work in the ultrafast spectroscopy group at Swinburne used a non-interferometric, phase-retrieval CMDS technique to study a DQW sample (similar to the one in Section 4.3, but with a narrower, 4 nm barrier) [76, 77, 182]. The FWM signal was collected as a function of both t_1 and t_2, and a phase retrieval algorithm was used to generate a 3D spectrum. Two above diagonal inter-well CPs were identified in the analysis of the 3D spectrum. This work demonstrated the usefulness of 3D spectroscopy in isolating signals resulting from coherent superpositions. However, the lack of heterodyne detection meant that the sensitivity of the technique was lower than other CMDS experiments, and consequently much higher beam powers were used. This higher excitation density lead to more rapid dephasing of the excitons

in the wide-well (the well with the lower exciton transition energy) and prevented detection of below-diagonal CPs at the emission energies of the wide-well excitons.

Most recently, Nardin et al [54] reported results including a set of CMDS spectra for an InGaAs/GaAs DQW. This DQW ostensibly has a somewhat simpler electronic structure compared with the previously discussed DQWs. It has only one bright transition per well because the LH bands are not confined in the potential. This simpler electronic structure meant that they were able to avoid the ambiguity in peak assignments that were evident in the previously discussed paper by Li et al [197]. The 1Q and 2-quantum (2Q) spectra showed clear inter-well CPs the latter indicating that the coupling was coherent in nature. Notably absent, however was the inter-well coherent superposition CP in the 0-quantum (0Q) 2D spectrum. These results were reproduced by phenomenological inclusion of excitation induced dephasing and shift (EID and EIS) in simulated spectra. Their simulations reproduce the 1Q and 2Q CPs and absence of 0Q CPs by introducing a lack of symmetry of the ground to one-exciton transition and the one-exciton to two-exciton transitions. This lack of symmetry (which they use as a proxy for many-body effects: excitation induced shift and excitation induced dephasing) results in imperfect cancellation of overlapping signal pathways (including CPs), breaking the symmetry of the transitions. Though this argument makes sense in a description of quantum pathways, it does not directly describe the physical coupling mechanism. The results reported in Ref. [54] are discussed in more detail in Section 4.4.1. Experiments on this same sample were conducted at Swinburne, and are reported later in this chapter (Section 4.4).

In studying the interactions in DQWs our ultimate goals is understanding the inter-well coupling mechanisms when the barrier is wide enough that the excitons can be considered to be spatially separated. In working towards this goal, we must first find a way to detect the coherent superposition CP (CS-CP) consistently and with good signal to noise. In this chapter, we will show that we can do so through the use of pathway selective CMDS. Beyond this first step, by measuring the amplitude of the CS-CP in the InGaAs/GaAs DQW in Section 4.4, we show that the 0Q is much larger amplitude than predicted by the simulations in Ref. [54] for the same sample. We then suggest that many-body induced coupling cannot alone explain the observations in this sample (at least in how it is currently implemented).

4.2 Pathway selection in 1Q and 0Q spectra

Pathway selection with spectrally tuned pulses was introduced previously in Section 2.3. This section will cover how it can be applied specifically to the 1Q and 0Q 2D and 3D spectra.

In principle pathway selection with shaped pulses can be used to isolate a wide variety of pathways. We consider a simple system, consisting of a ground state,

two singly-excited states with corresponding doubly-excited states and one doubly-excited mixed state (as shown in Fig. 4.1). All the available $\chi^{(3)}$ quantum pathways for this type of sample are depicted in Fig. 2.12. As described in Section 2.2.1.1, the pathways in this diagram can be constructed by following the arrows from the bottom of the diagram to the top. The pathways are grouped in pairs of signals that will cancel in the absence of interactions, and the blocks are coloured based on where they appear in 1Q and 0Q spectra. The strings of four color-coded 1's and 2's indicate the different pulse sequence allow each pathway. The first number indicates the transition in which the first interaction takes place (and therefore the E_1 energy of the peak associated with that pathway in a 1Q spectrum). Similarly, the second and third numbers indicate the transition in which the second and third interactions take place. The final number indicates the transition from which the FWM signal is emitted (and therefore the the E_3 energy of the peak associated with that pathway in 1Q and 0Q spectra). The first three numbers in the sequence thus indicate the spectral shaping that can be used to excite each pathway. For example, the 2211 sequence can be used to isolate below diagonal CPs resulting from population pathways and the 1111 sequence isolates only the pathways that occur along the diagonal at the transition energy corresponding to transition 1. The 2121 and 1212 pulse sequences can be used to isolate signals resulting from coherent superpositions of excited states. The full Feynman diagrams for these pathways are shown in Fig. 4.2. The 1212 and 2121 pulse sequences lead to only two pathways each (one SE-like and one ESA-like), both of which involve a coherent superposition of 1 and 2 during t_2. It is worth noting that all population pathways are suppressed when the first two pulses are not resonant with any of the same transitions (as in the 12XX, or 21XX pulse sequences). Only pathways that involve a coherent superposition of 1 and 2 will generate signal. This is true regardless of which transitions the third pulse is resonant with. This suppression of all of the 1122 and 2211 pathways removes the ambiguity in the 1Q CPs. The 1212 sequence generates two 'uphill' or 'above-diagonal' CPs, while 2121 generates two 'downhill' or 'below-diagonal' CPs.

Using a broadband third pulse is therefore preferable, as it will result in improved time resolution in the waiting time without introducing any additional signal pathways.

Applying pathway selection to 0Q 2D spectra was first suggested by Yang et al [50], in which 0Q spectra with spectrally tuned pulses were simulated. Our work (which makes up much of the results in Section 4.3) published in 2014 was the first experimental demonstration of such an approach [95]. The use of pathway selection in 0Q 2D spectra to study molecular systems was also recently experimentally demonstrated in 2015 by Senlik et al [67]. Although there are no other pathways overlapped with the coherent-superposition cross-peak (CS-CP) in 0Q spectra, there are still several benefits to using pathway selection. The suppression of population signals can actually be quite important because the $E_2=0$ population signals can be orders of magnitude stronger than the coherence signals. The population peaks can,

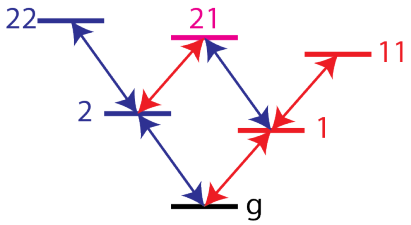

Figure 4.1: Cartoon of a six-level system including a ground state (g), two excited states (1, 2), two doubly excited states involving excitons of the same type (11, 22), and one involving a mixed exciton (21).

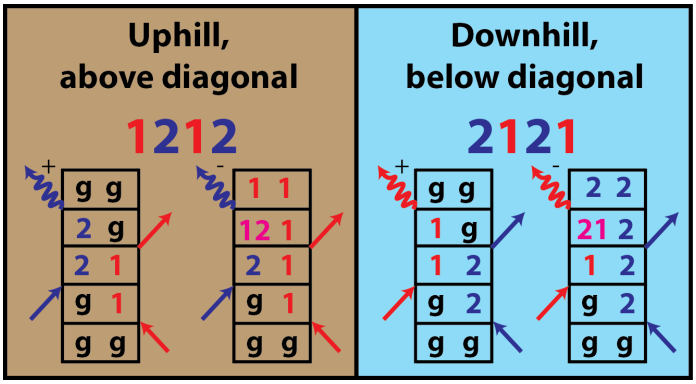

Figure 4.2: Uphill and downhill pulse sequences that isolate interwell coherent superpositions.

therefore obscure the CS-CPs through generation of noise which spreads across all E_1 and E_2 values which share the same emission energy and in the form of long tails along E_2. This can be clearly seen in simulated and measured 0Q spectra in Yang et al [50], and in some of the 0Q spectra presented in Chapters 6 and 7 in this thesis. These long tails and scatter can interfere with or obscure the coherence signals, so suppression of the population pathways can be beneficial in the detection of coherence CPs in 0Q spectra.

Excited state coherent superpositions (which otherwise require a full 3D spectrum to separate from population pathways) can be isolated using either 1Q or 0Q 2D spectroscopy with pathway selection. In this way, the data acquisition time can be shortened by up to a factor of 100. This more rapid data acquisition provides two important benefits. First, it can improve the signal-to-noise ratio by limiting the amount of phase and amplitude drift of the excitation pulses [67]. Second, it also allows systematic studies of other factors, such excitation density, polarization or temperature. Systematic studies of these factors are un-feasible using 3D spectroscopy which can take up to days to acquire.

The main way that we use pathway-selection in this thesis is in the elimination of ambiguity in the assignment of CPs and the removal of 'unwanted' signals (which is to say signals that are not pertinent to the topics/phenomena we are investigating). It was recently demonstrated that removing overlapping signals allows the extraction of quantitative details of the system Hamiltonian [209]. This was accomplished through a series of experiments which isolate different pathways in double-walled nanotubes using spectral amplitude shaping in a pulse-shaper. Pathway selection

can be helpful in other ways as well. For instance, intense signals, (even those that don't directly overlap CPs) can obscure CPs, either through extended tails or by increasing the noise floor across the entire spectrum. As the following sections show, pathway-selection can alleviate both of these problems. The improved SNR also allows us to resolve the peak-shapes of the CS-CPs. Peak shape analysis is a powerful part of CMDS, so being able to use it to study the coherent superpositions is an important benefit. Finally, pathway-selective and broadband CMDS spectra can be conducted consecutively, with no changes to the optical setup, which allows the results to be compared quantitatively.

The improved signal-to-noise ratio (SNR) of the CS-CPs in the pathway selective experiment is due to three different factors. First, the scan range required to collect the entire decay of the signal in both t_1 and t_2 is shortened considerably in the pathway selective experiment, so the acquisition times are shorter. The shortening of the scan ranges is due to the more rapid dephasing of the inter-well CS-CPs compared with the population pathways. The faster acquisition limits the amount of noise incorporated into the spectrum from phase drift and laser power instability [67]. Second, the DPs can naturally have long tails that can obscure the CS-CPs. The removal of the DPs, can therefore help reveal the CPs.

The third improvement in the SNR comes from the reduced spectral leakage from the stronger population signals. Spectral leakage is a type of artefact that appears in discrete Fourier transforms, due to windowing of the time domain data [210, 211]. The finite sampling range of the data results in some spreading of the power from the main peak to other points in the spectrum when a Fourier transform is applied. The amount of spectral leakage and where it appears depends on the details of the window function. For example, a square window function results in the least overall spectral leakage, but it appears across all frequencies as periodic modulations. On the other hand, a Gaussian window function produces more spectral leakage, but it occurs at frequencies near the signal [210]. Importantly, the amplitude of the spectral leakage is also proportional to the signal from which it is 'leaking' [211].

In 2D and 3D spectroscopy spectral leakage is introduced when the Fourier transform(s) are applied to the data which is recorded in the time domain. There are effectively three different ways that spectral leakage is introduced. First, spectral leakage can appear if the t_1 or t_2 delays are not scanned out to large enough delays that the full decay of the signal is recorded. This is effectively a rectangular windowing function, and results in periodic side-lobes that extend out in frequency from the actual peak [210]. Second, to remove the signal at pulse overlap, we must apply an additional time window. For this windowing, we do not use a rectangular function, but rather an error function with a width equal to the pulse overlap. This type of window function, results in less well-resolved side-lobes, but an overall increase in the background [210]. Third, as described in Section 2.4.10, the intensity of a pulse which is delayed using the pulse-shaper depends on the delay that is applied. This delay dependent pulse intensity is also effectively a time-window on

the signal as a function of t_1 and t_2, which has a sinc^2-Gaussian shape. This type of time window results in a spreading of the main peak rather than producing periodic side-lobes [210].

The spectral leakage from a particular peak 'P' at $(E_1, E_3)=(\epsilon_1, \epsilon_3)$ produces spectral leakage along E_1 at $E_3=\epsilon_3$, which is proportional to the amplitude of P. In this way, the background for all peaks for which $E_3=\epsilon_3$ will be increased. This can be problematic when the amplitude of the spectral leakage from DPs is comparable with the amplitude of the CPs that share the same emission energy. The spectral leakage actually interferes with the CP signals, which can change the sign or shape of the CP. Spectral leakage appears along the E_2 direction in the same way. Since this background is proportional to the amplitude of the strongest peak at a given ϵ_3, the removal of the DPs can result in a significant reduction in the background noise and effectively an improvement in the SNR.

One challenge of this approach is that in order to completely separate a specific pathway, the spectral separation of the transitions must be large enough to allow the pulses enough spectral bandwidth (and hence short enough duration) to resolve the coherent dynamics. In some cases (the partially overlapped A and B exciton transitions in monolayer MoS_2 for example [212]), these requirements cannot be accommodated. However, as Section 4.4 will show, pathway selection can still be helpful even when perfect spectral separation is not possible. Though the population pathways are not completely removed, they are suppressed enough relative to the coherent superposition pathways that the latter can be clearly observed. In the end, it becomes a problem of finding the right balance between temporal resolution and spectral selectivity (not spectral resolution) that allows the pertinent information to be extracted. Where this balance falls depends on the sample being studied, but the adaptability of this SLM based CMDS setup allows it to easily be tuned to match a wide variety of sample requirements.

In this section we have explained how pathway-selection in 1Q and 0Q 2D spectra is useful for detecting very weak signals (eg. those from coherent-superpositions) that are otherwise obscured by other much stronger contributions from population pathways. As described in the previous section, studying coherent-superpositions of excitons localized in separate QWs represents exactly this sort of a challenge. As a result, this is a good first application of coherence-specific pathway-selection in CMDS, which is demonstrated on two different DQW samples in Sections 4.3 and 4.4.

4.3 Inter-well coherence in GaAs/AlGaAs DQWs

In this section, results are presented from CMDS and pathway selective CMDS (PS-CMDS) experiments on a single AlGaAs/GaAs DQW. These results, which were published in Optics Express in 2014 [95], are both a proof of principle for coherence

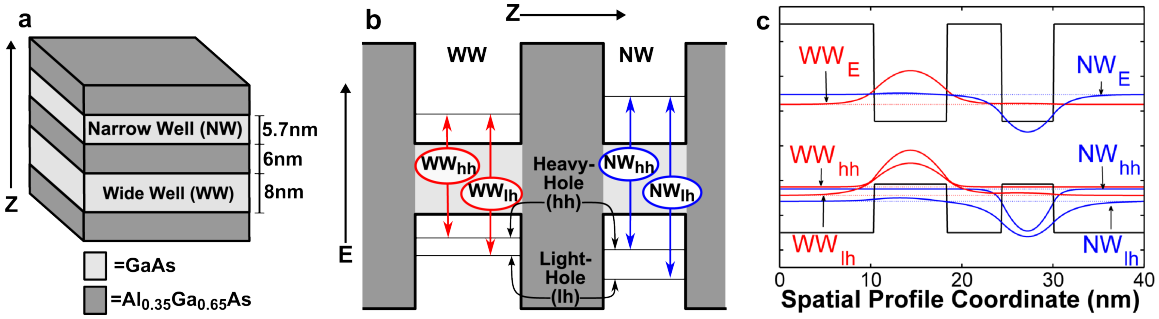

Figure 4.3: (a) A diagram of the layered AlGaAs/GaAs DQW. (b) 1D valence and conduction band potential profiles, along with the four lowest energy exciton resonances. (c) Electron and hole wavefunctions calculated from the 1D shrödinger equation, show very little hybridization.

specific PS-CMDS, and also a first study of excitonic coherence in a regime in which it is not well understood. The procedures and results developed in this section lay the foundation for the experiments performed in Section 4.4 and the following chapters.

4.3.1 *GaAs/AlGaAs DQW Sample*

The $Al_{0.35}Ga_{0.65}As/GaAs$[1] sample studied in this section is part of a set that have been studied previously and is the subject of several publications [76, 77, 182]. A diagram of the sample is shown in Fig. 4.3a. The sample was gown using metal-organic chemical vapour deposition (MOCVD) and consists of two layers of GaAs (the wells) sandwiched between layers of AlGaAs (the barriers). The wells are asymmetric (one well is 5.7 nm thick, the other is 8 nm thick) to set the exciton resonances so that the two QWs can be separated spectrally. The wells are separated by a 6 nm thick AlGaAs barrier. A cartoon of the 1D potential profiles of the sample is presented in Fig. 4.3b, along with the two lowest energy exciton transitions in each well. There is a HH and a LH exciton transition in each well. These transitions involve the hole states (WW_{hh}, WW_{lh} and NW_{hh}, NW_{lh}), and the electron states (WW_E, NW_E) in the same well. The two lowest energy conduction-band and four highest energy valence-band eigenstates for these profiles were calculated by solving the 1D time-independent Schrödinger equation (TISE) for the potential profiles shown in Fig. 4.3b. To find the allowed solutions to the 1D TISE, we use the Numerov algorithm and shooting method. A brief description of these methods are provided in Appendix A3, and full details of this calculation can be found in Refs. [76, 77, 182].

The calculated wavefunctions (presented in Fig. 4.3c) qualitatively show very little hybridization across the DQW structure, and appear to be localized to one well or the other. To quantitatively assess the degree of localization, the probability of

1 All AlGaAs/GaAs DQW samples which are studied in this thesis are $Al_{0.35}Ga_{0.65}As/GaAs$. The subscripts are dropped subsequently for the sake of simplicity.

Wavefunction	Wide Well	Narrow Well
WW_{E}	99.86%	0.14%
NW_{E}	0.30%	99.70%
WW_{hh}	100.00%	0.00%
WW_{lh}	99.80%	0.20%
NW_{hh}	0.00%	100.00%
WW_{lh}	1.40%	98.60%

Table 4.1: Calculation of the degree of localization of the electron and hole wavefunctions in the AlGaAs/GaAs DQW. Details of calculation are provided in the text.

finding the electron or hole in a given well is calculated by splitting the wavefunctions at the center of the barrier and then integrating the square of the part of the wavefunction that appears in each well. These probabilities (shown in Table 4.1) agree with the qualitative assessment of good localization in the wells, with <0.1% of the probability amplitude outside the given well. It is important to note, however, that these calculations are for the individual carriers. A more useful and accurate approach would be to calculate the actual exciton wavefunctions and include the Coulomb interactions. This would be much more involved and computationally intensive, and is beyond the scope of this work.

4.3.2 *Broadband CMDS results*

We first examine this DQW sample using traditional CMDS with three identical broadband[2] pulses in the rephasing ordering. The laser spectrum is tuned so it is roughly centred on the NW_{hh} transition (770 nm, 1.61 eV). The spectral width is tuned so that it covers all four of the exciton transitions shown in Fig. 4.3b with appreciable spectral intensity. The excitation spectrum used for the broadband experiments is the green curve (labelled 'k_3/LO') in Fig. 4.8b. This spectral width results in ~45 fs transform limited pulses. These experiments were performed at 20 K in a recirculating cryostat, and all the beams are co-linearly polarized. All scan parameters used in this experiment (and the rest of the measurements in this chapter) can be found in Table A1.1 in Appendix A1.

For the data reported in this section, each beam has an average power of ~3 mW, and a focal spot size of 150 μm, giving a photon density of $7 \times 10^{11}\,cm^{-2}$ photons per pulse. Although this excitation density should be at a level to generate a predominately $\chi^{(3)}$ response, recent results from Nardin et al. [54] and results in the following chapters show that even at these excitation levels, excitation induced effects are still important. Furthermore, some $\chi^{(5)}$ response is potentially generated in the detection direction. The higher photon densities in this experi-

2 The term 'broadband' can be ambiguous. In this thesis it is used to indicate that the laser output is not spectrally shaped by the pulse-shaper.

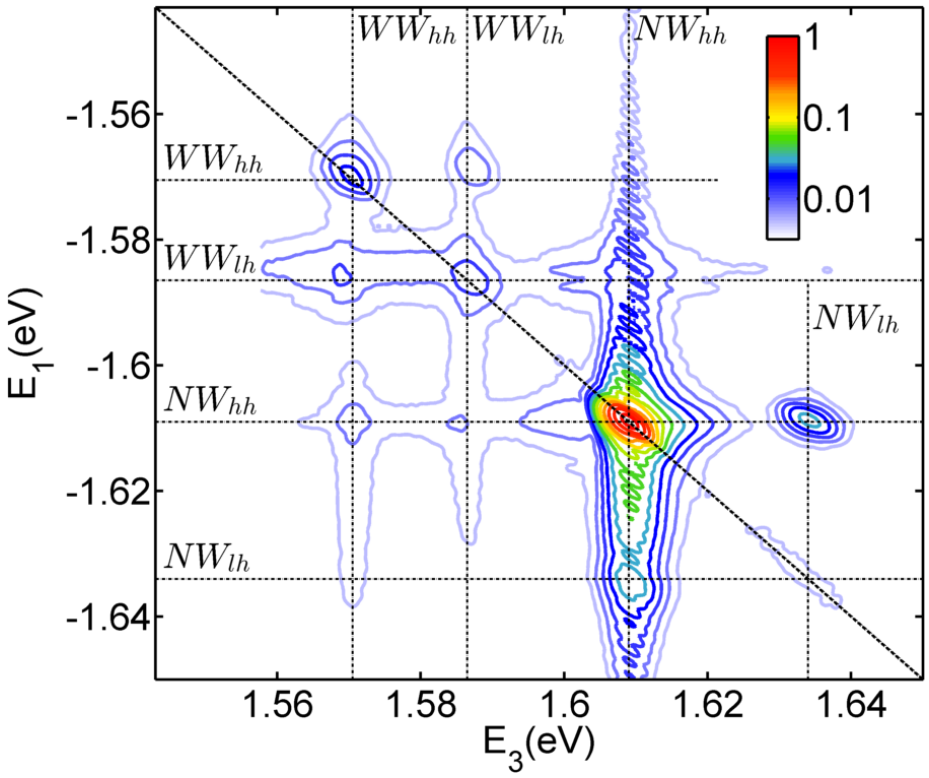

Figure 4.4: A 1-quantum 2D spectrum collected for the AlGaAs/GaAs DQW using broadband excitation, with $t_2 = 0$ and logarithmic color scaling spanning more than two orders of magnitude. t_1 was scanned 0 to 2000 fs in 10 fs steps.

ment were needed because several experimental optimizations had not yet been introduced. First, a less sensitive CCD (Garry3000 from Ames Photonics) was used with an Oriel Instruments 77480 spectrometer for detection of the signal. Second, a standard recirculating cryostat (Cryomech ST10SCTK) was used for sample cooling, which generated significant sample vibrations. These two factors reduced the overall sensitivity and stability of the experiment.

The absolute value of the rephasing part of the 1Q 2D spectrum is presented in Fig. 4.4. A wide variety of features are evident in this spectrum. First, we see DPs for three of the four excitonic transitions (WW_{hh},WW_{lh} and NW_{hh}). The NW_{lh} is visible just above the noise floor, but is not shown in this figure because of how the contours are drawn. The NW_{hh} is much stronger, and is in fact by far the most intense peak in the spectrum, due to its large oscillator strength and position near the peak of the excitation spectrum. This peak and too a lesser degree the WW_{hh} and WW_{lh} DPs show clear indications of inhomogeneous broadening through a tilt along the diagonal (indicated by the black line). As described in the previous chapter, inhomogeneous broadening is expected for QW excitons and largely arises from well width fluctuations.

There are also a number of CPs evident in the spectrum. The four strongest CPs occur between the HH and LH transitions within the same well, and occur both above and below the diagonal. These HH-LH CPs show a tilt along the diagonal,

which is indicative of correlated inhomogeneous broadening, and will be discussed in more depth in section 4.3.4. [3]

The CPs of interest in this spectrum are those that appear with absorption in one well and emission from the other. These are the CPs which we call inter-well CPs or inter-well CPs. There are indications of three inter-well CPs evident in this spectrum. However, there are several factors that make identification, assignment and interpretation of these peaks difficult. First, the identification of these peaks is hampered by their low signal compared with the intense DPs. The noise level across the spectrum is set by the strongest peak at that energy. As a result, the inter-well CPs suffer from noise generated by the much larger DPs. Secondly, the tails from the DPs extend out and in some cases overlap the inter-well CPs. Third, there is a broad free-carrier continuum in the wide-well that appears at the same position in the spectrum as the inter-well CPs and helps to obscure these peaks. The free-carrier continuum peaks can be identified as peaks elongated along E_1 with $E_3 = 1.565\,\text{eV}$ (WW_{hh} emission) and $E_3 = 1.582\,\text{eV}$ (WW_{lh} emission) which appear only at the lowest contour level. Finally, both population pathways (GSB, ESA, and PT) and coherence pathways can lead to signals that overlap in the 2D spectrum, so precise identification of the origin of the signals from this 2D peak is impossible.

The coherent superposition signal can in principle be isolated in a 1Q 3D spectrum. To this end, a 3D spectrum was collected with the same pulse-ordering and excitation conditions as the 1Q 2D dataset from Fig. 4.4. As in the 1Q 2D spectrum, t_1 was scanned 0 to 2000 fs in 10 fs steps. t_2 was scanned 0 to 900 fs in 15 fs steps. Displaying 3D spectra in illuminating ways is a challenge, especially when the pertinent information spans several orders of magnitude, and the noise floor varies across the spectrum. In the following paragraphs we will discuss four different ways to represent the data in the 3D spectrum:

1. Plot the entire dataset in 3D as a series of isosurfaces at different levels.
2. Integrate the spectrum along the E_1 axis so it can be presented as a 0Q spectrum.
3. Plot 2D slices extracted of the 3D spectrum
4. Break the dataset up into regions and plot each region of the dataset at the isosurface that best matches the amplitude of the data within.

The most complete way to display the 3D dataset is by plotting it along isosurfaces. Figure 4.5 shows the 3D spectrum plotted along three different isosurfaces.

3 The presence of (NW_{lh},NW_{hh}) and (NW_{hh},NW_{lh}) CPs which are significantly stronger than the NW_{lh} DP can be explained in the following way. The NW_{lh} DP amplitude is the product of four interactions at the NW_{lh} transition energy, while the CP amplitude is the product of two interactions at the NW_{lh} transition energy and two at the NW_{hh} transition. The NW_{hh} transition has a much higher dipole moment and there is more spectral intensity in the excitation pulses at the NW_{hh} transition energy than at NW_{lh} transition energy. As a result, the two interactions at the NW_{hh} transition energy significantly amplify the CP compared with the NW_{lh} DP.

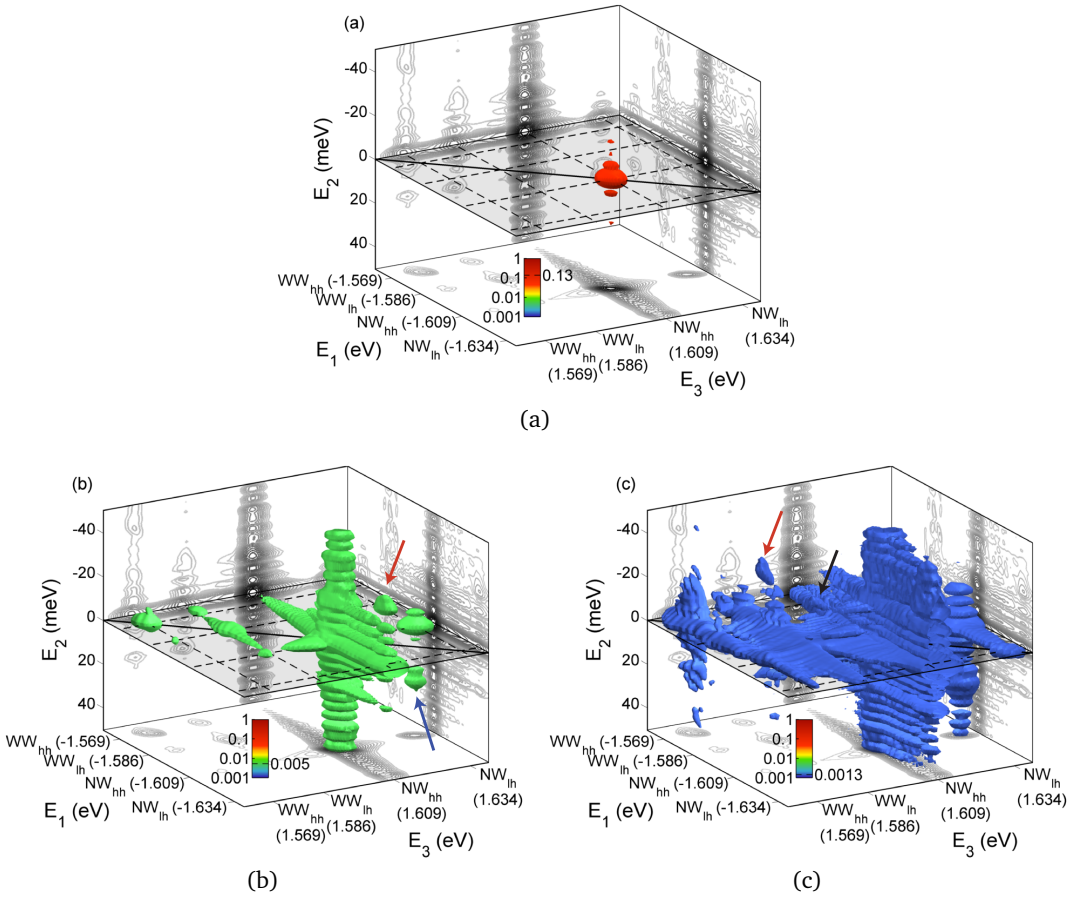

Figure 4.5: The broadband 3D spectrum of the GaAs/AlGaAs DQW plotted as a single isosurface at three signal amplitudes (which are normalized to the maximum amplitude in the 3D spectrum): (a) 0.13, (b) 0.005, and (c) 0.0013. These are the same amplitudes as the isosurfaces plotted for the various regions in Fig. 4.7a.

Each isosurface reveals a different set of signals, while obscuring others. The isosurface in Fig. 4.5a is plotted at the highest of the three levels of (0.13). It shows shape of the strongest peak, the NW_{hh} DP at E_2=0. Fig. 4.5b is plotted more than an order of magnitude lower than Fig. 4.5a, and shows a range of additional peaks. The WW_{hh} and WW_{lh} DPs and several intra-well CPs generated by population pathways can be seen in the E_2=0 plane. Two coherence peaks can also be seen in this plot (as indicated by the arrows) away from E_2=0 meV (specifically, in the $E_2 = E_3$-E_1 plane). The peak indicated by the red arrow is a coherent superposition CP in which the first pulse excites a NW_{lh} exciton and the second pulse excited a NW_{hh} exciton. The peak indicated by the blue arrow is the opposite: first pulse excites the NW_{hh} and the second pulse excites the NW_{lh}. The NW_{hh} DP is now hidden by the increased noise and streaking along E_2 which comes mostly from the fact that the full decay along t_2 was not detected. As a result, the delay range acts like a rectangular window function in the time domain. The rectangular window leads to sharp edges and significant spectral spreading (also called spectral leakage) along the E_2 axis [210, 211].

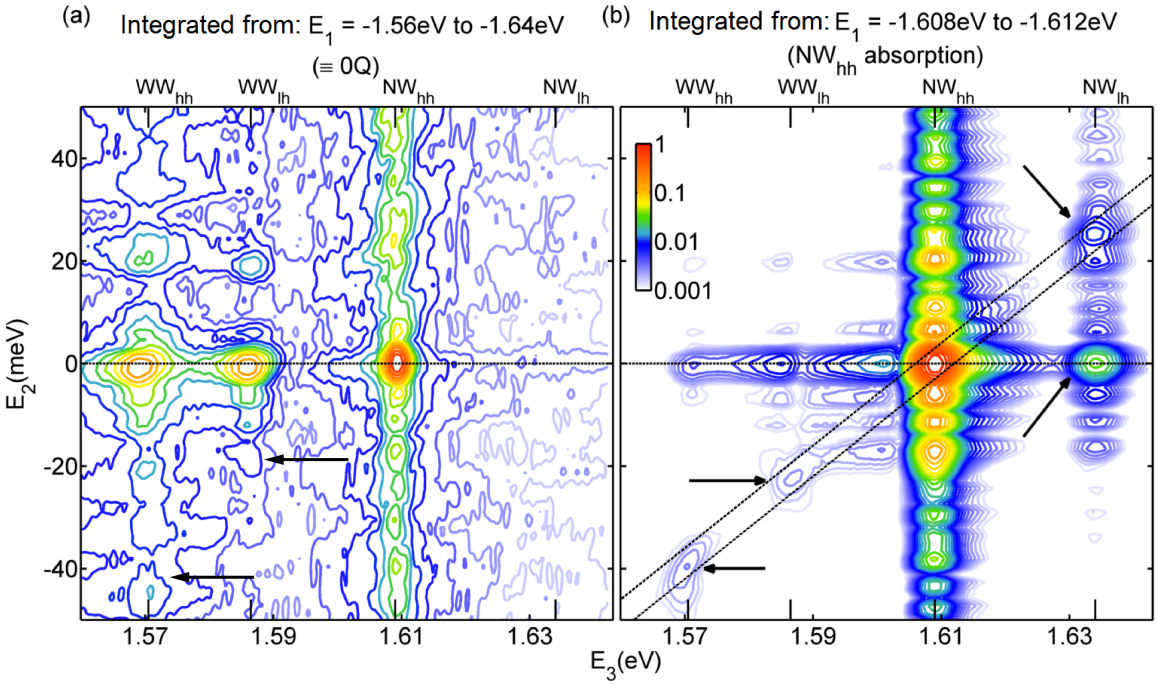

Figure 4.6: (a) a 0Q projection of the 3D spectrum and (b) a slice through the 3D spectrum at E_1 = NW_{hh}. CS-CPs (indicated by arrows) hidden in the noise in (a), but visible in (b) - demonstrating the benefits of looking at slices instead of projections.

The final isosurface in Fig. 4.5c is plotted two orders of magnitude below the isosurface in Fig. 4.5a to highlight two inter-well coherent superposition peaks (indicated by the arrows). The (NW_{hh}, WW_{hh}) coherent superposition peak is indicated by the red arrow. The (NW_{hh}, WW_{lh}) coherent superposition peak is indicated by the black arrow. At this isosurface level, all the other signals in the spectrum (i.e. population pathways and intra-well pathways) cannot be clearly resolved. In some cases they are hidden by spectral leakage along the E_2 or E_1 directions. The tails of multiple peaks overlap at this low isosurface level such that the separate peaks can no longer be resolved. The ability to resolve these incredibly weak inter-well interactions even in the presence of much stronger contributions illustrates the power of separating signals along the third energy axis.

Coherent superposition signals can also be isolated with a 2D, 0Q spectrum, which can be extracted from a full 3D spectrum by projecting it onto the (E_3,E_2) plane. Figure 4.6a shows a 0Q spectrum extracted from the 3D spectrum. Because the noise is proportional to the strongest signal at a particular absorption and emission energy, The CS-CPs resolved in the Fig. 4.5c would appear at the positions indicated by the arrows. In this representation of the data, the coherent superposition signals cannot be identified. This is due to the increase in the noise floor when we integrate across the entire 3D spectrum. In projecting the spectrum onto the (E_3,E_2) plane, we are integrating all of the noise at every E_1 value, including the spectral leakage that appears at E_2 values above and below the strong DPs. As a result, the projection has a higher noise floor than the 3D data.

2D slices through the 3D spectrum can also be used to present a smaller subset of the 3D data. By integrating a smaller range of the 3D spectrum, the noise floor remains roughly the same as that of the 3D spectrum, thus avoiding the amplification of the noise we saw in the projected 0Q spectrum in Fig. 4.6a. By using slices, CS-CPs can be more clearly identified since the E_1, E_2 and E_3 values for the peak are all known (which is not the case in 0Q spectra where only E_2 and E_3 are known). Furthermore, peaks that have the same E_2 and E_3 energies (i.e. those that overlap on the 0Q spectrum), but have different E_1 values can be separated by taking slices at different E_1 values. The same process can be conducted by slicing the spectrum along either of the other two energy dimensions, as well.

For example, Fig. 4.6b shows a slice through the 3D spectrum at the absorption energy which corresponds to the NW_{hh}. The slice is created by integrating the 3D spectrum along the E_1 direction from $E_1 = -1.608$ eV to $E_1 = -1.612$ eV. Coherence peaks with the right combinations of E_1, E_2 and E_3 can be identified as peaks which appear in-between the two diagonal lines. These lines correspond to the $E_2 = E_3 - 1.608$ eV and $E_2 = E_3 - 1.612$ eV covering the full width of the NW_{hh} transition. The spacing of the lines therefore corresponds to the width of the slice in E_1. In this slice, four additional peaks (marked by the black arrows) can now be identified, which were hidden in the fully integrated 0Q spectrum. The two inter-well coherence peaks appear in the bottom left part of the frame at $(E_1,E_2,E_3) = (NW_{hh},WW_{lh}\text{-}NW_{hh} = -20\text{ meV},WW_{lh})$ and $(NW_{hh},WW_{hh}\text{-}NW_{hh} = -40\text{ meV},WW_{hh})$.

We can also now observe two CPs at $E_3 = 1.632$ eV (the NW_{lh} emission energy): $(NW_{hh},0\text{ meV},WW_{hh})$ and one at $(NW_{hh},NW_{hh}\text{-}NW_{lh} = 24\text{ meV},NW_{lh})$. The latter of the two is the coherent superposition CP that involves the first pulse exciting the NW_{hh} and the second pulse exciting the NW_{lh}. The peak at $E_2 = 0$ is a CP corresponding to population interactions between NW_{hh} and NW_{lh}. This peak is referred to as a CP because it occurs at $E_3 \neq -E_1$ (specifically, $E_3 = NW_{lh} = 1.623$ eV, $E_1 = NW_{hh} = -1.610$ eV).

A fourth way to present the depth of information encapsulated in this 3D spectrum, is to plot all of the different peaks on different isosurface level. The 3D spectrum has therefore been re-plotted in Fig. 4.7a, with each spectral region plotted along one of the three levels from Fig. 4.5 that best matches the strength of the signal in that region. This way, the wide range of different signals present can all be simultaneously presented.

The region with inter-well coherent superposition peaks (the below diagonal region) is plotted in Fig. 4.7b. It is clear that these two peaks are indeed in the right place to be the CS-CPs corresponding to $(NW_{hh}, WW_{hh}\text{-}NW_{hh} = 40\text{ meV}, WW_{hh})$ and $(NW_{hh}, WW_{lh}\text{-}NW_{hh} = 20\text{ meV}, WW_{lh})$. Their are two other CS-CPs that could occur in this region: $(NW_{lh}, WW_{hh}\text{-}NW_{lh} = 62\text{ meV}, WW_{hh})$ and $(NW_{hh}, WW_{lh}\text{-}NW_{hh} = 54\text{ meV}, WW_{lh})$. These peaks, however, are not observed. The two peaks that have been resolved in Fig. 4.7b are quite noisy, meaning, very little analysis is possible beyond simply identifying the peaks.

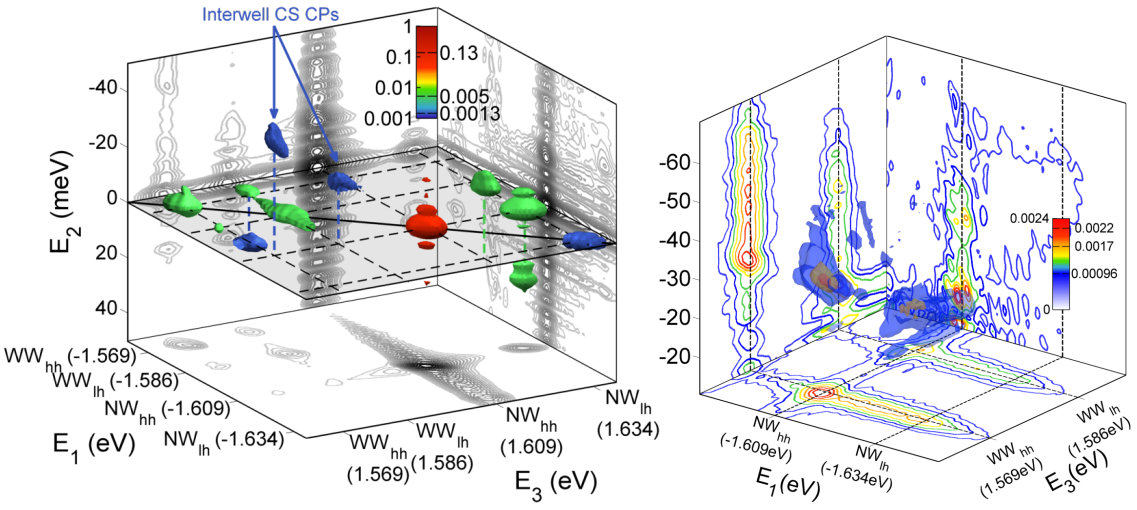

(a) (b)

Figure 4.7: (a) A 1-quantum 3D spectrum collected for the AlGaAs/GaAs DQW using broadband excitation, with different isosurfaces for different peaks for reasons described in the text. (b) The portion of the 3D spectrum where we see inter-well CS-CPs, normalized to the most intense point of the NW_{hh}-WW_{hh} CS-CP. Isosurfaces drawn at the levels indicated on the colorbar.

4.3.3 *Pathway-selective CMDS results*

To do any additional study of the inter-well coherent superpositions beyond simply identifying them, the SNR on the CS-CPs must be improved. To do this, we use pathway selection with a coherence-specific pulse ordering. This pulse ordering allows only coherent-superposition pathways and suppresses all population pathways (as described in the sections 4.2 and 2.3). In the results presented here, spectral amplitude masks are applied to k_1 and k_2 such that the k_1 excitation spectrum is resonant only with the NW exciton transitions and the k_2 excitation spectrum is only resonant with the WW exciton transitions[4]. The spectral amplitude masks used are shown in Fig. 4.8a. The spectrally shaped excitation spectra and the broadband FWM signal at ($t_1 = t_2 = 0$ fs) is shown in Fig. 4.8b. Fig. 4.8c shows the Fourier transforms of the spectra in Fig. 4.8b, assuming a flat spectral phase, matching the expected excitation pulses.

Coherence-specific PS-CMDS 2D and 3D spectra are presented in Fig. 4.9a and Fig. 4.9b, respectively. The scan ranges and step sizes are given in the figure caption. The beams are co-linearly polarized. As expected, the 2D spectrum in Fig. 4.9a is very different from the spectrum recorded using broadband excitation (Fig. 4.4). First, there are no DPs, and the only CPs that are resolved are the ones that appear at the expected positions for inter-well CPs. The two inter-well CPs which were missing in Fig. 4.4 and Fig. 4.7b (i.e. CPs in which $E_1 = NW_{lh}$)are also now clearly

4 In principle, the spectral masks could be switched such that k_1 is only resonant with the WW transitions and k_2 is only resonant with the NW transitions (which would isolate the above diagonal 1Q CPs), but this experiment has not been performed on the current sample.

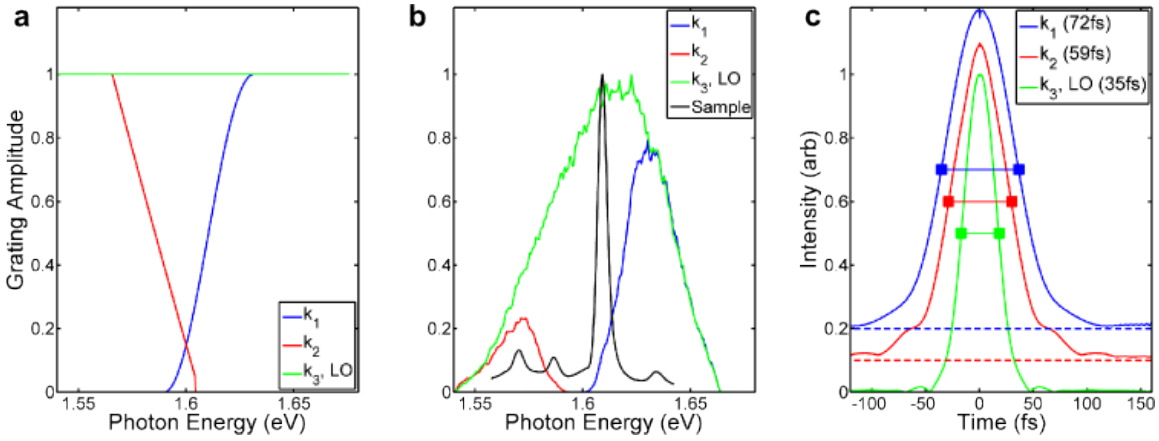

Figure 4.8: (a) spectral amplitude masks, (b) resulting spectra and (c) pulse shapes (Fourier transform of the spectra in (b)) used in the coherence-specific CMDS experiment. t_1 was scanned 0 to 2000 fs in 10 fs steps. t_2 was scanned 0 to 405 fs in 15 fs steps.

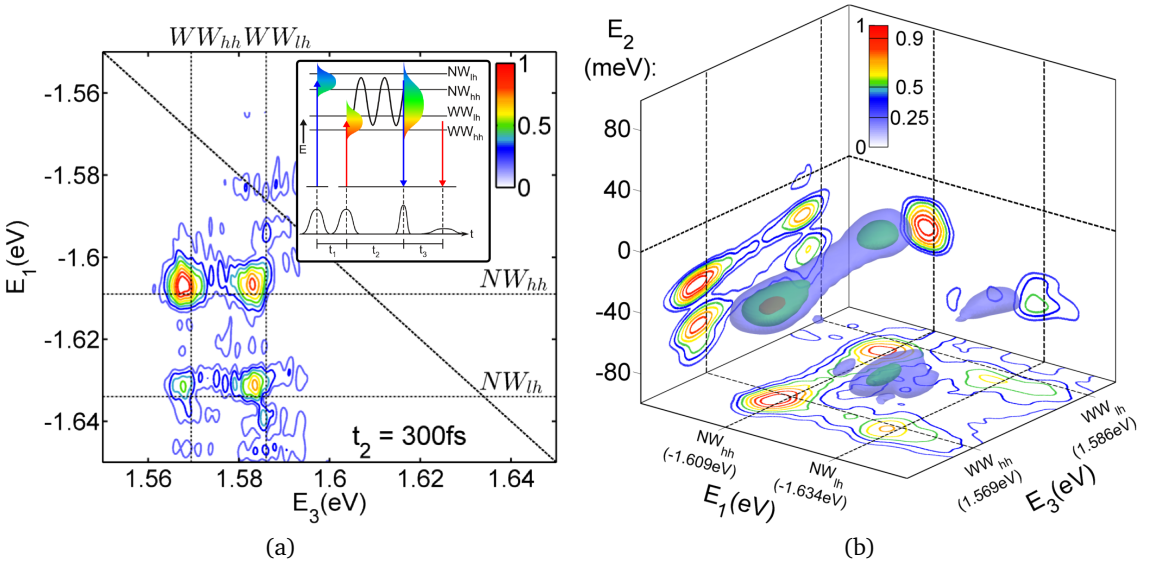

Figure 4.9: (a) A 1-quantum 2D spectrum at t_2 = 300 fs using the pulse ordering shown in the inset and in 4.8. (b) A 1-quantum 3D spectrum using the same pulse ordering as in (a). Analysis provided in the text.

resolved. This is consistent with the expectation that all population pathways are suppressed with this pulse ordering.

There is a slight shift of all four CS-CPs from the expected location compared with the peaks in Fig. 4.4. The peaks are shifted in both E_1 and E_3. The origin of this shift is not clear. One possible explanation for this shift is that there is an excitation induced shift of the peaks in the broadband spectra caused by the slightly broader (and therefore more intense) excitation pulses.

In principle signals with this pulse ordering could only result from coherent superpositions, but a single 2D spectrum does not definitively confirm this. Two factors could lead to the generation of population pathways. First, poorly compressed pulses could lead to temporal overlap of k_2 and the broadband k_3 and thereby allow signals from the $k_1 \rightarrow k_3 \rightarrow k_2$ pulse ordering, in which CPs generated by popula-

tion pathways are allowed where they overlap. Second, if there is some overlap of the k_1 and k_2 excitation spectra, some population pathways could be allowed. The spectra in Fig. 4.8b show no overlap, and we have nearly transform limited pulses based the measured cross-correlations (not shown), so we presuppose near complete suppression of population pathways. We can confirm that the CPs are indeed generated by coherent-superposition pathways and that population pathways are suppressed by collecting a 3D spectrum.

A coherence specific pathway-selective 3D spectrum is presented in Fig. 4.9b. All four of the coherence peaks have E_2 energies equal to the difference of the coupled transitions ($E_2 = E_3 - E_1$), confirming that they are indeed CS peaks. More importantly, there is no signal at $E_2 = 0$, which confirms that all population processes are suppressed as intended. The resulting peaks are well-isolated in all three frequency directions, and have significantly improved SNR compared with the same peaks measured using broadband pulses in Fig. 4.7b. The cleaner peaks allow us to determine the linewidths along the three energy directions and analyse the CS-CP peak-shapes in the following sections.

4.3.4 *Peak-Shape analysis*

As described in Section 2.2.1.1, a lot of useful information can be gleaned by analysing peak-shapes and linewidths of CMDS signals. The peaks from the broadband and pathway-selective 3D spectra can now be isolated in the three different frequency dimensions, and individually projected onto any of the three 2D frequency planes. Before looking at the 2D line-shapes, we will first give a brief recap of the 1D line-shapes of excitonic transitions in QWs, described previously in Ch. 3.

QW exciton emission and absorption line-shapes are broadened by both homogeneous and inhomogeneous effects. Homogeneous broadening comes in the form of random interactions that reduce the degree of coherence (such as exciton-exciton and exciton-phonon scattering). Inhomogeneous broadening is caused by well-width fluctuations across the sample, which shift the central energy of the homogeneous excitonic line by changing the degree of confinement. The variation of well-widths is typically a Normal distribution, which leads to a Gaussian line-shape. The homogeneous broadening is dissipative and therefore leads to a Lorentzian line-shape. The full excitonic line-shape is therefore a convolution of the Lorentzian (homogeneous) a Gaussian (inhomogeneous) lines, which is what is called a Voigt line-shape. In QWs at low temperature ($<10\,K$), inhomogeneous broadening is typically the larger of the two types of broadening, so the line-shapes are typically more Gaussian.

Inhomogeneous and homogeneous broadening also lead to different peak-shapes in 1Q 2D spectroscopy. Inhomogeneously broadened transitions have DP peak-shapes which are tilted along the diagonal. The diagonal width of the peak is the inhomoge-

neous linewidth, while the cross-diagonal linewidth is the homogeneous linewidth. Simulations have previously shown that CPs which are tilted along the diagonal are indicative of correlated inhomogeneous broadening [77], while round peak-shapes are indicative of uncorrelated inhomogeneous broadening. As in the linear case, we can parametrize the 2D line-shape using a convolution of a Gaussian and Lorentzian distributions. The inhomogeneous component of the linewidth can now be approximated by a bivariate distribution, in which the two independent variables (E_3 and E_1 in this case) are partially or completely correlated. The correlation, however, does not extend to the homogeneous component of the linewidth, which is limited by the coherence decay. The CP can therefore be represented as a convolution of the 2D homogeneous (uncorrelated) and inhomogeneous (correlated or uncorrelated) distributions:

$$S_{ih}(E_3, E_1) = exp\left(-\frac{1}{2(1-p_{ab}^2)}\left[\frac{(E_3-\mu_b)^2}{(\Gamma_b^{(ih)})^2} + \frac{(E_1-\mu_a)^2}{(\Gamma_a^{(ih)})^2} - \frac{2p_{ab}(E_3-\mu_b)(E_1-\mu_a)}{\Gamma_b^{(ih)}\Gamma_a^{(ih)}}\right]\right) \tag{4.1.1}$$

$$S_h(E_3, E_1) = \frac{1}{4pi()^2}\frac{\Gamma_b^{(h)}}{(E_3-\mu_b)^2+(\Gamma_b^{(h)})^2}\cdot\frac{\Gamma_a^{(h)}}{(E_1-\mu_a)^2+(\Gamma_a^{(h)})^2} \tag{4.1.2}$$

$$S(E_3, E_1) = S_{ih}(E_3, E_1) * S_h(E_3, E_1) \tag{4.1.3}$$

for a CP between transitions 'A' and 'B' with inhomogeneous (homogeneous) linewidths $\Gamma_A^{(ih)}$ ($\Gamma_A^{(h)}$) and $\Gamma_B^{(ih)}$ ($\Gamma_B^{(h)}$) centred at μ_A and μ_B, and with a degree of correlation (p_{AB}) which varies from perfect correlation (p_{ab} = 1) to no correlation (p_{AB} = 0) to anti-correlation (p_{AB} = -1). This labelling applies for peaks where the first pulse excites transition a, and emission comes from transition b.

CP peak-shapes are calculated from Eq. 4.1.3 for a range of different input parameters in Fig. 4.10. The top row shows the correlated inhomogeneous function (Eq. 4.1.1), the middle row shows the homogeneous function (Eq. 4.1.2) and the bottom row shows the convolution of the two functions (Eq. 4.1.3). The peak-shapes for transitions with various degrees of correlation can be seen in the first four columns going from perfect correlation in Fig. 4.10(a,h,o) to no correlation in Fig. 4.10(d,k,r). If the transitions have different inhomogeneous linewidths ($\Gamma_a^{(ih)} \neq \Gamma_b^{(ih)}$) then the resulting peak is tilted away from the diagonal line (as shown in Fig. 4.10e,l,s). A combination of imperfect correlation and $\Gamma_a^{(ih)} \neq \Gamma_b^{(ih)}$ leads to a both a tilting of the peak away from the diagonal and a broadening of the peak (as shown in Fig. 4.10f,m,t). Finally, the peak shape for an increase of the $\Gamma_a^{(h)}$ and $\Gamma_b^{(h)}$ (homogeneous broadening) is shown in Fig. 4.10f,m,t.

The peak-shape in Fig. 4.10u is similar to the peak shape in Fig. 4.10p, so differentiating between increased homogeneous broadening and decreased correlation

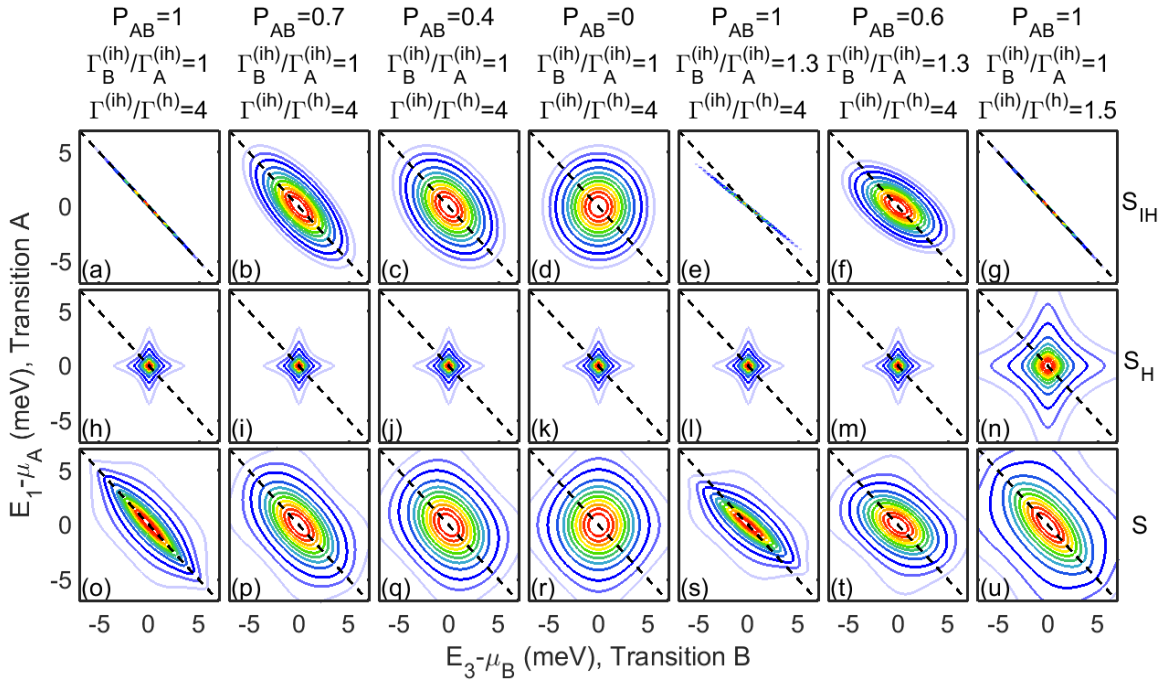

Figure 4.10: Simulated 2D (E_3, E_1) CP peakshapes using Eq. 4.1. The top row (a-g) is the inhomogeneous part (Eq. 4.1.1). The middle row (h-n) is the homogeneous part (Eq. 4.1.2), the bottom row is the full linewidth including both homogeneous and inhomogeneous contributions. Some of the parameters used in each column are shown above the top row. For all the plots, $\Gamma_B^{(ih)} = 2\,\text{meV}$. For all except (g), (n) and (u), $\Gamma_A^{(h)} = \Gamma_B^{(h)} = 0.5\,\text{meV}$.

is not necessarily straightforward. However, it should be possible with accurate measurements of homogeneous linewidth from the cross-diagonal widths of the associated DPs. Furthermore, with sufficient SNR we should also be able to separate the two possibilities by analysing the peak-shapes in more detail. The peak shape in Fig. 4.10u is characterized by diagonal and cross-diagonal slices which have a somewhat more Lorentzian character while the diagonal and cross-diagonal slices in Fig. 4.10p have a more Gaussian character.

In the limit of no correlation ($p_{ab} = 0$), Eq. 4.1.1 becomes simply a bivariate distribution with widths along E_1 and E_3 set by the inhomogeneous linewidths of the corresponding excitons. This distribution is aligned along E_1 and E_3 instead of the diagonal. If the inhomogeneous linewidths are equal, this results in a round peak (as in Fig. 4.10d). This results in a 2D peak-shape (including both homogeneous and inhomogeneous contributions) with no tilt.

E_1 vs E_3 projections for three selected peaks from the broadband spectrum 3D spectrum are presented in Fig. 4.11. The NW_{hh} DP, the (E_1, E_2, E_3) = (NW_{hh}, -26 meV , NW_{lh}) CS-CP and the (NW_{lh}, 26 meV, NW_{hh}) CS-CP are presented in 4.11. The NW_{hh} DP (like the same peak in the broadband 2D spectrum) has an elliptical shape with the major axis tilted such that it is aligned with the diagonal line. As has been mentioned previously, this peak shape is indicative of inhomogeneous broadening, and the diagonal (cross-diagonal) linewidth is the inhomogeneous (homogeneous) linewidth.

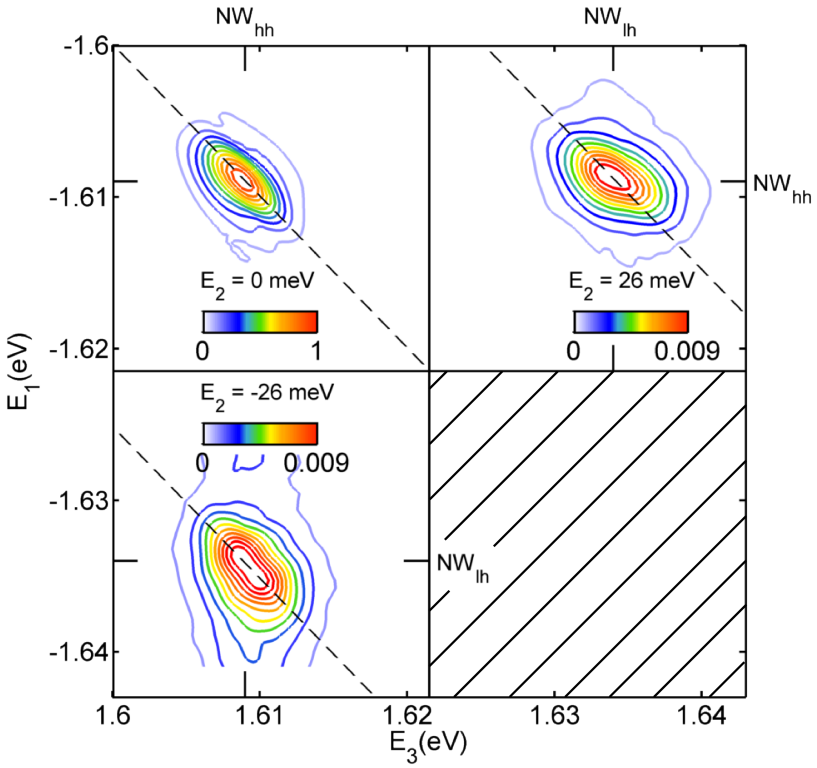

Figure 4.11: E_1 vs E_3 peakshapes for the NW_{hh} DP and the CS-CPs associated with HH-LH interactions. All three peaks show a tilt along the diagonal. The CS-CP tilt towards the diagonal indicates correlated broadening. The fact that the tilt is not exactly along the diagonal stems from the different inhomogeneous linewidths of the NW_{hh} and NW_{lh} excitons.

The intra-well coherence peaks in Fig. 4.11b-c are also tilted towards the diagonal. The $E_1 = E_3 - E_2$ line is also drawn in this figure as a guide to show that the peaks are not tilted exactly along the diagonal. The above diagonal CS-CP is tilted slightly towards being aligned with E_1, while the above diagonal CS-CP is slightly tilted towards being aligned with E_3. This shift away from a tilt exactly along the diagonal results from differences in how heavy- and LH excitons are affected by the well-width fluctuations. LH excitons have previously been shown to have broader inhomogeneous distributions for the same amount of well-width fluctuations [213, 214]. This broadening of the LH line leads to tilting of the intra-well CS-CP and is also consistent with the measured inhomogeneous linewidths of the HH and LH DPs (which can be found in Table 4.2). The degree of correlation of the CPs can be determined by measuring the cross-diagonal width of the CP, and then comparing it to the sum of the homogeneous linewidth of the two coupled transitions. We cannot perform this comparison here, since we were unable to determine the homogeneous linewidth of the NW_{lh} exciton transition. Furthermore, the delay range limitations of this experiment prevent us from accurately determining the NW_{hh} exciton homogeneous linewidth.

Still, the ability to identify correlated broadening is a useful tool for studying coupling of different transitions. Though experiments have previously shown that LH

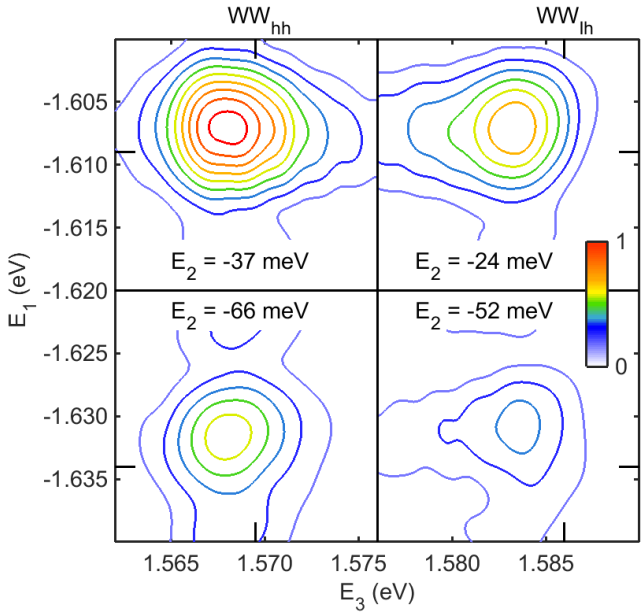

Figure 4.12: The 3D inter-well CS-CPs from Fig. 4.9b individually projected onto the E_1 vs E_3 plane. The lack of tilt shows that the inhomogeneous broadening of the coupled transitions is uncorrelated. The label indicates the center of each peak along E_2.

and HH excitons have correlated inhomogeneous broadening, this method of measurement (isolating 3D spectral peaks and projecting them onto 2D axes) provides much clearer evidence of the correlation of the LH and HH excitons than previous 1D FWM based techniques. These techniques relied on fitting decays along t_1 or t_2 to extract the decay of oscillations (quantum beats) on top of an exponential decay. If the decay of the beats was longer than the inhomogeneous dephasing time of the other transition involved in the coupling, then the inhomogeneous broadening must be correlated. Furthermore, we have shown that the coherence pathways also demonstrate correlated inhomogeneous broadening. This result could not be determined in previous 1D FWM experiments as the coherence pathways could not be separated from population pathways.

The inter-well CS-CPs from the pathway selective 3D spectrum are presented in Fig. 4.12. Unlike the intra-well CS-CPs, the inter-well CS-CPs clearly demonstrate peak-shapes aligned along E_1 and E_3, with no tilt towards the diagonal. This shape is indicative of completely uncorrelated inhomogeneous broadening, which is consistent with excitons localized in separate QWs. The dominant type of static disorder (well-width fluctuations) is not expected to be correlated between the wells. This is also consistent with wavefunctions that have very little hybridization across the DQW structure, as hybridization would induce some correlation of the inhomogeneous broadening, even in the case of uncorrelated well-width fluctuations.

The CS-CPs can also be projected onto the (E_3, E_2) and (E_1, E_2) planes. 2D peak-shapes for these projections have not been studied in detail, so we will first consider what peak-shapes to expect in specific circumstances. We will start with the simplest case, in which we ignore inhomogeneous broadening ($\Gamma^{(\mathrm{ih})} \ll \Gamma^{(\mathrm{h})}$). Assuming

	Γ_1 (meV)	Γ_2 (meV)	Γ_3 (meV)	ϵ_1 (eV) ±0.5 meV	ϵ_2 (eV) ±0.5 meV	ϵ_3 (eV) ±0.5 meV	$\tilde{A}^{(P)}$ (arb)	$A^{(P)}$ (arb)
WW_{hh}	8.3±0.9	7.1±1.7	7.2±0.4	-1.568	0.000	1.570	1.4±0.1	14±3
WW_{lh}	7.4±1.7	5.7±1.4	7.1±0.4	-1.586	0.000	1.587	1.5±0.5	4±1
NW_{hh}	4.5±0.2	5.8±1.1	4.9±0.2	-1.608	0.000	1.609	100±10	100±11
NW_{lh}	10.4±5.4	6.3±1.3	8.6±0.7	-1.634	0.000	1.635	0.4±0.1	1.2±0.4
(NW_{lh}, NW_{hh})	7.7±1.7	7.1±0.9	6.1±1.1	-1.634	-0.026	1.609	1.1±0.4	6±2
(NW_{hh}, WW_{hh})	10.1±1.3	22.6±1.4	7.1±1.4	-1.608	-0.041	1.570	0.2±0.1	0.7±0.3
(NW_{hh}, WW_{lh})	9.4±2.1	10.4±2.0	10.3±2.3	-1.608	-0.020	1.588	0.2±0.1	0.3±0.1
(NW_{hh}, WW_{hh})	9.0±0.3	17.7±0.2	7.5±0.3	-1.607	-0.037	1.568	0.04±0.01	1.2±0.3
(NW_{hh}, WW_{lh})	9.2±0.3	17.3±0.1	6.3±0.5	-1.607	-0.024	1.583	0.03±0.01	0.8±0.3
(NW_{lh}, WW_{lh})	11.6±0.4	20.2±0.6	6.4±0.5	-1.632	-0.050	1.584	0.02±0.01	0.2±0.1
(NW_{lh}, WW_{hh})	11.6±0.6	17.9±0.4	6.8±0.4	-1.632	-0.065	1.568	0.03±0.01	0.3±0.2

Table 4.2: Tabulated data includeing linewidths uncorrected and corrected peak amplitudes from pathway-selective and broadband 3D spectra.

there are no additional dephasing processes that affect the coherent superpositions of excited states and no correlated fluctuations, the dephasing time for a coherent superposition of excited states A and B (T_{CS-AB}) as a function of t_2 is given by:

$$\frac{1}{T_{CS-AB}} = \frac{1}{T_A} + \frac{1}{T_B} \tag{4.2}$$

where T_A and T_B are the dephasing times of the ground-state to excited-state coherence for states 'A' and 'B', respectively. Thus, the E_2 linewidth should be the sum of the homogeneous linewidths of the coupled transitions [215]. We expect the (E_3, E_2) and (E_1, E_2) projections to have peak-shapes which are aligned with E_2, (and not tilted on an angle) because the homogeneously broadened transitions can freely explore the entire range of energies within the distribution, so we can't know precisely which value it can have. As a result, all of the transition energies in one state can couple to all of the energies in the other transition so there is no correlation between E_2 and E_1 or E_3.

A 3D CS-CP for two homogeneously broadened transitions with no additional dephasing of the excited state coherent superposition is given by Eq. 4.3. Projections of a 3D peak calculated using Eq. 4.3 onto the three different 2D axes is shown in Fig. 4.13a-c.

$$S(E1,E2,E3) = \frac{(\Gamma_B^{(h)})^2}{2\pi\cdot((E_3-\mu_B)^2+(\Gamma_B^{(h)})^2)}\cdot\frac{(\Gamma_A^{(h)})^2}{2\pi\cdot((E_1+\mu_A)^2+(\Gamma_A^{(h)})^2)}\cdot \frac{(\Gamma_A^{(h)}+\Gamma_B^{(h)})^2}{2\pi\cdot((E_2-(\mu_A-\mu_B)^2+(\Gamma_A^{(h)}+\Gamma_B^{(h)})^2)} \tag{4.3}$$

Considering inhomogeneous broadening complicates the prediction of peak-shapes. Based on the arguments above for E_1 vs E_3 peak-shapes, we might initially expect peak-shapes with no tilt for uncorrelated inhomogeneous broadening. However, some basic simulated peak-shapes will show that the opposite is true: uncorrelated inhomogeneous broadening leads to tilted peak-shapes in (E_3, E_2) and (E_1, E_2) projections of CS-CPs. To explain how we simulate the inhomogeneously broadened 3D CS-CPs, we again consider the 1D linewidths. As described at the beginning of the section, the line-shape of a transition with both homogeneous and inhomogeneous broadening can be calculated by the convolution of a Lorentzian function with a width equal to the homogeneous linewidth and a Gaussian function with a width equal to the inhomogeneous linewidth. If the inhomogeneous linewidth is larger than the homogeneous width, this line-shape can also be approximated in the following way. We can define an array $\vec{R}$ of length M which is randomly sampled from a Normal distribution centred at 0 with a standard deviation of 1.

$$R \sim N(0,1) \tag{4.4}$$

This random, Normally distributed array can be used to approximate the inhomogeneous broadening distribution:

$$\vec{S}^{(IH)} = \vec{R} \cdot \Gamma^{(IH)} + \mu^{(IH)} \tag{4.5}$$

where $\mu^{(IH)}$ is the center of the inhomogeneous distribution. The full linewidth of the transition can then be approximated by summing over M Lorentzian functions whose center values are defined by the random normal distribution from Eq. 4.5:

$$S(E) = \sum_{1}^{M} \frac{\Gamma^{(h)}}{(E - (\vec{R}(M) \cdot \Gamma^{(IH)} + \mu^{(IH)})^2 + (\Gamma^{(h)})^2} \tag{4.6}$$

This is not an exact match for the convolution of the homogeneous and inhomogeneous distributions, but it is comparable. We can use this same approach to generate a 3D peak with both homogeneous and inhomogeneous broadening. We define two arrays ($\vec{R}_A$ and $\vec{R}_B$) of length M which are separately sampled randomly from a Normal distribution centred at 0 with a variance of 1:

$$\vec{R}_A \sim N(0,1) \tag{4.7.1}$$
$$\vec{R}_B \sim N(0,1) \tag{4.7.2}$$

If there is no correlation of the inhomogeneous broadening, the distribution of the inhomogeneous broadening along E_1 and E_3 are approximated based on the

randomly sampled variables. In the case of correlated inhomogeneous broadening, so both distributions use the same Normally sampled random variable R_A.

$$\vec{S}_A^{(IH)} = \vec{R}_A \cdot \Gamma_A^{(IH)} + \mu_A^{(IH)} \tag{4.8.1}$$

$$\vec{S}_B^{(IH)} = \begin{cases} \vec{R_A} \cdot \Gamma_B^{(IH)} + \mu_B^{(IH)} & \text{(Correlated)} \\ \vec{R}_B \cdot \Gamma_B^{(IH)} + \mu_B^{(IH)} & \text{(Uncorrelated)} \end{cases} \tag{4.8.2}$$

Where $\Gamma_A^{(IH)}$ is the inhomogeneous broadening of the transition excited by the first pulse, and $\Gamma_B^{(IH)}$ is the inhomogeneous broadening of the transition from which the signal is emitted. As in the 1D case, we then sum over a total of M 3D Lorentzian peaks which are each calculated using Eq. 4.3. The calculation of each Lorentzian peak uses a different value from the randomly distributed inhomogeneous distributions from Eq. 4.8 as the center of the peak along E_3 and E_1 and the difference between $S_A^{(IH)}$ and $S_B^{(IH)}$ as the center of the peak along E_2.

$$\begin{aligned} S(E1, E2, E3) = \sum_1^M & \frac{(\Gamma_B^{(h)})^2}{2\pi \cdot ((E_3 - \vec{S}_B^{(IH)}(M))^2 + (\Gamma_B^{(h)})^2)} \cdot \\ & \frac{(\Gamma_A^{(h)})^2}{2\pi \cdot ((E_1 + \vec{S}_A^{(IH)}(M))^2 + (\Gamma_A^{(h)})^2)} \cdot \\ & \frac{(\Gamma_A^{(h)} + \Gamma_B^{(h)})^2}{2\pi \cdot ((E_2 - (\vec{S}_A^{(IH)}(M) - S_B^{(IH)}(M))^2 + (\Gamma_A^{(h)} + \Gamma_B^{(h)})^2)} \end{aligned} \tag{4.9}$$

Eq. 4.9 can then be used to calculate 3D peak-shapes with and without correlated inhomogeneous broadening. Projections of the 3D peak onto the three 2D axes for correlated and uncorrelated broadening can be seen in Fig. 4.13d-f and Fig. 4.13g-i, respectively. For these calculations we have used the following parameters: M = 10,000, $\Gamma_{A,B}^{ih} = 8\,\text{meV}$, $\Gamma_{A,B}^{h} = 2\,\text{meV}$.

When the inhomogeneous broadening is uncorrelated (Fig. 4.13g-i), we can clearly see that the projections of the calculated peak along E_1 vs E_2 and E_3 vs E_2 are tilted. This can be understood in the following way: for each E_1, E_3 can span the entire range of inhomogeneous widths. The centre of the resulting peak along E_2 can vary by Γ^{IH} for a given E_1. As E_1 is shifted, the center of the distribution along E_2 also shifts, which results in a correlation of E_1 and E_2 and therefore a tilt of the peak. This same argument can be made for the E_3 vs E_2 peak-shape. Since the E_1 and E_3 values are no longer correlated (i.e. they come from different normal distributions), their difference will vary. The full width of the peak along E_2 is the sum of the inhomogeneous linewidths of the two transitions, and is therefore larger than the linewidths in E_1 or E_3.

For correlated broadening, we observe no tilt of the E_3 vs E_2 peaks or the E_1 vs E_2 peaks. This narrowing along E_2 and lack of tilt can be understood qualitatively

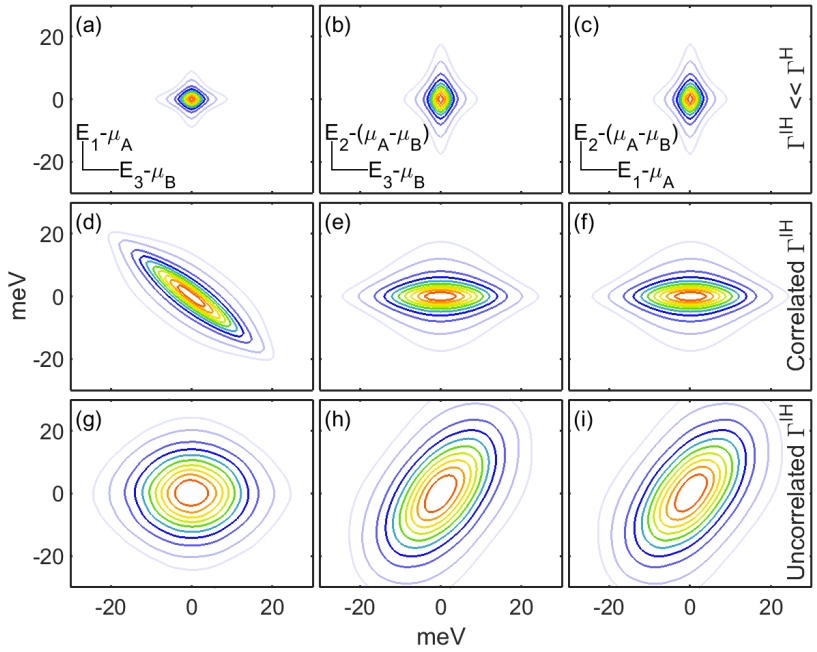

Figure 4.13: Projections of simulated 3D peak-shapes (a)-(c) neglecting inhomogeneous broadening, and for (d)-(f) correlated and (g)-(i) uncorrelated broadening inhomogeneously broadened transitions. Projections are (E_3,E_1) for (a)/(d)/(g), (E_3,E_2) for (b)/(e)/(h), and (E_1,E_2) for (c)/(f)/(i).

in the following way: regardless of which E_1 is chosen, the difference between the E_1 and E_3 remains constant, and therefore so does the center of the distribution along E_2. Even in the presence of inhomogeneous broadening the linewidth along E_2 is smaller than the widths along E_1 or E_3, and in the case of perfect correlation the width along E_2 is limited by the sum of the homogeneous linewidths of the two coupled transitions. Based on the obvious differences in the projections of these simulated peak-shapes, we should be able to clearly identify different types of broadening (i.e. homogeneous, correlated inhomogeneous, and uncorrelated inhomogeneous) in experimental data.

Projections of the seven experimentally measured peaks (4 inter-well CS-CPs, 2 intra-well CS-CPs and the NW_{hh} DP, which are the same peaks from Fig. 4.11 and Fig. 4.12) are shown in Fig. 4.14. The DP and the intra-well peaks are plotted in Fig. 4.14a-b, and the inter-well peaks are plotted in Fig. 4.14c-f.

The intra-well CS-CPs have linewidths along E_2 which are roughly equal to their linewidths along E_1 and E_3. The peak-shapes of the intra-well CS-CPs are aligned roughly along the E_2 axis (i.e. there is no tilt). The simulations for correlated inhomogeneous broadening predicted a linewidth along E_2 which was narrower than the linewidths along E_3 and E_1. These intra-well peaks therefore somewhat broader along E_2 than predicted by the simulations, but clearly also narrower than predicted for uncorrelated broadening (which predicts a linewidth along E_2 which is the sum of the linewidths along E_1 and E_3).

Furthermore, the resolution in E_2 is limited by the t_2 scan range, and the measured E_2 linewidths in Table 4.2 are roughly at the resolution limit based on the

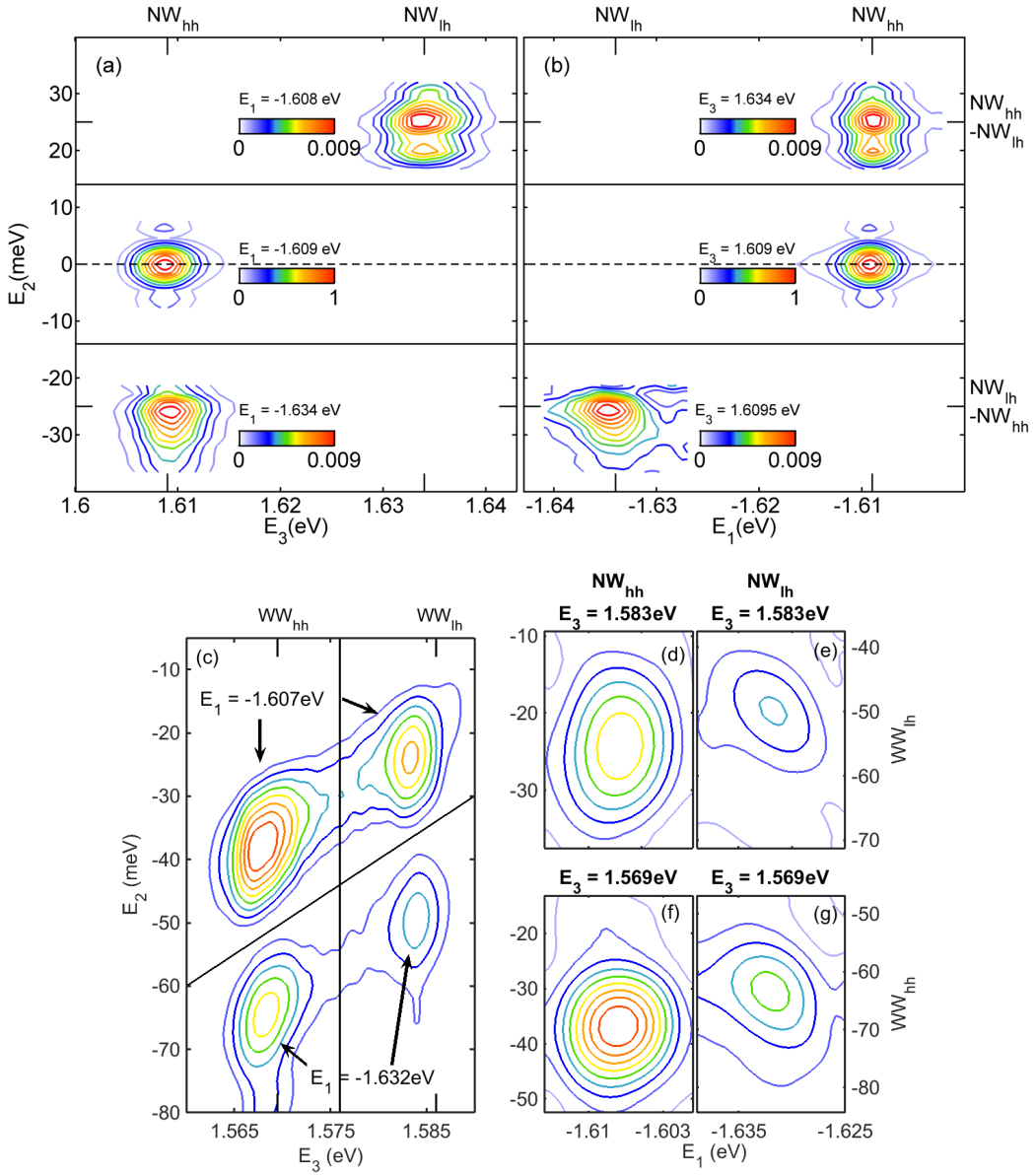

Figure 4.14: Projections of the NW_{hh} DP and the intra-well (NW_{hh}, NW_{lh}) CS-CPs onto the (a) E_3 vs. E_2 and (b) E_1 vs. E_2 planes. The centre of each peak along E_1 and E_3 are labeled. (c-g) show projections of the inter-well peaks from the pathway selective 3D spectral along the (c) E_3 vs. E_2 and (d-f) E_1 vs. E_2 planes.

scan range used. We therefore assume that these linewidths are resolution limited.[5] For comparison, the projections of the NW_{hh} DP are shown as well. The linewidth of the DP along E_2 (5.8 meV) is only marginally smaller than the linewidths of the intra-well CS-CPs (7.1 meV and 8.0 meV) along E_2. This is further confirmation that all of these linewidths are resolution limited, as the DP linewidth should be limited by the population lifetime, and as a result should have a significantly smaller linewidth than the CS-CPs.

5 The scan range used in this experiment (t_2=0 to 900 fs) is not the maximum scan range achievable with the pulse-shaper. This explains (in part) why E_2 linewidths of peaks in the 3D spectra presented in subsequent chapters are narrower. The modulations along E_2 are due to the spectral leakage caused by the limited t_2 scan range.

The fact that the width of the intra-well CS-CPs along E_2 is smaller than the sum of their widths along E_1 and E_3, and that they have no appreciable tilt is mostly consistent with the peak-shape predicted in Fig. 4.13d-f for correlated inhomogeneous broadening. The slightly broader than expected widths of the peaks along E_2 are likely caused by the limited E_2 resolution.

Figure 4.14c-g show the 2D projections of the inter-well CS-CPs (which demonstrate uncorrelated inhomogeneous broadening in the E_1 vs E_3 projections). We do observe some tilt (most notably in the E_3 vs E_2 projections of the CS-CPs emitting in the WW_{hh}). The linewidth of the CS-CPs projected onto the E_2 (i.e. the 1D width in the E_2 direction) are shown in Table 4.2, and are consistent with the sum of the inhomogeneous linewidths of the coupled transitions for all the inter-well CS-CPs (which we expect for uncorrelated broadening). However, the *2D* peak-shapes are broader along E_2 compared with what we expect based on the simulated 2D peak-shapes.

Broadening induced by the scan range cannot explain this discrepancy, as the entire decay of the signal is captured in the scan data. To understand the discrepancy between the simulated and measured E_1 vs E_3 and E_1 vs E_2 projections, we consider the assumption built into the simulations that there aren't any additional dephasing processes that effect the excited state coherent superposition (in t_2) compared to the ground-excited state coherent superposition (in t_1). This assumption may not be correct for two reasons. First, in t_1 (where we measure the dephasing of the ground-excited state), only one pulse has arrived at the sample. In t_2 (where we measure the dephasing of the ground-excited state), two pulses have arrived. This represents a significant increase in the number of carriers in the sample, which could lead to an increase in dephasing due to carrier-carrier scattering in t_2 compared with t_1. Second, the coherent superposition in t_2 may have a larger in-plane and out-of plane size than the sum of the two ground to excited state coherent superpositions. This larger in-plane size could lead to a larger scattering cross-section and therefore more interactions with other carriers and phonons. The increased interaction cross-section would thereby shorten the decoherence time of the coherent superposition and increase the E_2 linewidth.

To summarize: for uncorrelated inhomogeneous broadening, we expect that CS-CPs projected onto the E_3 vs E_2 and E_1 vs E_2 planes will have tilted peak-shapes. On the other hand, we expect projections of CS-CPs with correlated inhomogeneous broadening to have peak-shapes without no tilt, a linewidth along the E_1 (E_3) directions equal to $\Gamma_A^{(ih)}$ ($\Gamma_B^{(ih)}$) and a linewidth along the E_2 direction equal to $\Gamma_A^{(h)} + \Gamma_B^{(h)}$. The projections of the experimentally detected intra-well CS-CPs (in which the inhomogeneous broadening is correlated) have peak-shapes which are consistent with the expected peak-shapes, though experimental limitations prevent us from accurately measuring some linewidths. However, the projections of some of the experimentally detected inter-well CS-CPs (which have uncorrelated inhomogeneous broadening) have peak-shapes which are also qualitatively consistent with

the simulations. The projections onto E_3 vs E_2 and E_1 vs E_2 reveal linwidths along E_2 which are larger than predicted by the simulations. This suggests that there are additional dephasing processes that affect the excited state coherent superposition more than the ground-excited state coherent superposition.

4.3.5 *Quantitative Analysis*

One benefit of pulse-shaper based CMDS is that pathway-selection and broadband spectra can be collected contiguously, with no changes to the optical setup because the only difference is the spectral phase pattern sent to the pulse shaping SLM. The PS-CMDS and CMDS signals can therefore be compared quantitatively, allowing us access to the relative contributions of different signal pathways.

The excitation spectra used to collect the pathway selective and broadband 3D spectra are necessarily different. The measured signal amplitudes are dependent on the spectral intensity of the excitation pulse at the energy transition of the transition involved in each interaction. To quantitatively compare the signals, the different spectral intensity in the excitation pulses must be taken into account. The normalized signal $A^{(P)}$ (i.e. the signal we would measure if the excitation spectra were flat) can be calculated as using the following equations.

$$A^{(P)} = \frac{\tilde{A}^{(P)}}{\eta^{(P)}} \tag{4.10}$$

$$\eta^{(P)} = \sqrt{I^{(-k_1)}(\epsilon_1^{(P)}) \cdot I^{(k_2)}(\epsilon_2^{(P)}) \cdot I^{(k_3)}(\epsilon_3^{(P)}) \cdot I^{(LO)}(\epsilon_{sig}^{(P)})} \tag{4.11}$$

where $\tilde{A}^{(P)}$ is the measured amplitude for a signal P, and $\eta^{(P)}$ is a normalization factor. $\eta^{(P)}$ is calculated based on the spectral intensity of the excitation pulses at the transition frequencies for each of the interactions that are involved in the pathway for peak P. A justification for Eq. 4.10 and Eq. 4.11 can be found in Appendix A4.

Using Eq. 4.10 we can compare different amplitudes within the same 3D spectrum. We can also compare different 3D spectra as long as certain criteria are met:

1. The 3D spectra must be collected consecutively with no changes to the optical setup
2. The acquisition parameters (eg. CCD integration time) and delay sampling (both t_1 and t_2) must be the same for the different 3D spectra.
3. The excitation spectra used in both 3D spectra must be measured in such a way that they can be quantitatively compared (i.e. they must all also be recorded using the same acquisition parameters).

Using the pulse-shaper based CMDS experiment, these requirements can all be satisfied. The acquisition of the 3D and PS-3D spectra were done in this way, so we

can compare the CS-CPs in the pathway selective 3D spectrum with the CS-CPs and population pathways in the broadband 3D spectrum.

$\tilde{A}^{(P)}$ is determined for all of the peaks in both 3D spectra by integrating the entire peak. Integrating the peak is necessary to account for the different dynamics of the various pathways. Two different pathways with the same strengths, but different decay rates as a function of t_1 or t_2 will still produce the same $\tilde{A}^{(P)}$ when integrated, even though they will have different peak-shapes and peak heights. $A^{(P)}$ is then calculated based on the measured excitation spectra.

The $I_0(\epsilon)$ factors are determined by extracting the spectral intensity at ϵ from the excitation spectrum I_0. For simplicity, the spectral intensity is assumed to be flat across the width of each transition, and $I_0(\epsilon)$ is calculated using the average spectral intensity across the transition width. We then include the variation of the spectral intensity across the transition as an additional source of uncertainty in error analysis.

In an ideal experiment with delta function pulses and infinitely broad spectra, this correction would be unnecessary, which is why many CMDS experiments use spectral widths which are broad compared to the spectral spacing of the transitions of interest. In this experiment, however, we cannot use pulses broad enough to be adequately spectrally flat across all transitions due restrictions of the pulse-shaper and the nature of the pathway selective experiment.

The corrected and uncorrected peak amplitudes for all of the PS-CMDS CS-CPs as well as the DPs and selected CS-CPs from the broadband CMDS 3D spectrum can be found in Table 4.2. The (NW_{hh},WW_{hh}) and (NW_{hh},WW_{lh}) CS-CPs (which are the only two peaks that appear in both spectra) are about 2$\times$ higher amplitude in the PS-CMDS spectrum. Two factors are likely working together to cause this increased signal. First, there are much fewer free-carriers (which have been shown to reduce decoherence lifetimes) generated in the PS-CMDS experiment. Second, this correction assumes that all of the signals have the same $\mathbf{E}^3$ dependence on the pulse electric field amplitude (and therefore on the excitation density). We show in Chapter 7 that the intra-well signals follow a roughly $\mathbf{E}^3$ dependence on excitation density while the inter-well signals follow a clearly sub-$\mathbf{E}^3$ dependence. As a result, the corrected values in Table 4.2 overstate the strength of the inter-well coherent superposition signals because they implicitly assume an $\mathbf{E}^3$ dependence on the excitation density.

Still, these should amount to relatively small errors as the excitation density does not change much. Furthermore, the delay range of all of the signals are limited in a similar way, so the error there is also not going to be huge. Therefore, this is a still a useful tool for getting a ball park estimate on the relative strength of pathways whose strength vary by orders of magnitude.

By combining CMDS and PS-CMDS the overall dynamic range of the experiment is improved considerably. The amplitude of the uncorrected peaks detected vary by almost four orders of magnitude in electric field amplitude, or eight orders of

magnitude in intensity. Combining this large dynamic range with the ability to quantitatively compare individual signal pathways results in a powerful tool for quantitatively studying weak quantum-effects.

4.4 Inter-well coherence in InGaAs/GaAs DQW

In this section, broadband and pathway-selective CMDS spectra will be presented to study inter-well coherence in an $In_{0.05}Ga_{0.95}As$[6] DQW structure. The sample studied is a different piece of the same sample used in Nardin et al [54]. The results presented here using broadband excitation are consistent with the results presented in the previous study. The CMDS results presented in Ref. [54] utilized translation stages to control the delays and active phase stabilization. The consistency of our results with a well-established CMDS apparatus[7] (which employs very different delay methods) is an additional confirmation that the experimental apparatus and processes established as part of this PhD project are sound.

Results in the section also show that when pathway-selection is employed, inter-well 0Q coherence signals (which are otherwise hidden) can be resolved. These results show that pathway-selection can be useful even in samples in which the spacing of electronic transitions is very small compared with the transition linewidth. Both above- and below-diagonal coherence peaks can be detected with different pulse sequences. We observe CS-CP peak-shapes that are broader than expected along both E_1 and E_2. This may suggest that different exciton sub-populations contribute to the CS-CPs and population pathways. We compare the amplitude of the CS-CPs (relative to the amplitude of the population signals in a 0Q spectra) to the values predicted by the simulations in Ref. [54], and find that they are not consistent. We suggest that the coupling is therefore not entirely due to many-body interactions, and my include two-body coupling of WW and NW excitons.

4.4.1 *Previous studies on this sample*

The most recent report on coherent coupling in DQWs was published by Nardin et al [54] in 2014. In this experiment, an InGaAs DQW was studied using 1Q, 0Q and 2Q 2D spectroscopy. A diagram of the DQW potential and electron and hole wavefunctions are shown in Fig. 4.15a (reproduced from Ref. [54]). The calculated electron wavefunctions show some hybridization, but the HHs are well localized. The LHs are confined in the GaAs barriers due to strain, so there are only two direct single-exciton transitions, one in each QW[8]. The electronic structure shown in Fig.

6 All of the InGaAs samples reported in the rest of this thesis are $In_{0.05}Ga_{0.95}As$. For simplicity, the percentages are sometimes omitted.

7 The CMDS experiment at JILA was one of the first used to study QWs [56, 194], and has been used for many experiments since [50, 53, 81, 82, 193, 197, 216–218].

8 As chapter 6 will show, there are actually a range of other transitions in this sample, but the nonlinear response in the spectral range studied in Ref. [54] and in this chapter is dominated by these two exciton transitions.

4.15b (also reproduced from Ref. [54]) shows two single-exciton states (WW-X and NW-X) and three two-exciton states (WW-2X,NW-2X, Mixed-NW/WW-2X). The full origin of the six level system is described in the Supplementary Information from Ref. [54], but it can be briefly understood as follows. As described in Section 2.2.1.1, two two-level systems can be reformulated as a four-level system (4LS). This is done for both WW-X and NW-X, to generate two 4LS's. These two 4LS's can then be reformulated into a 16-level system (16LS). However, only 11 of the 16 states in the 16LS can contribute to the signal (the other 5 states involve 3 or 4 particle states, which cannot be involved in any of the 1Q or 2Q spectra). Five of these 11 are actually duplicates of other states. As a result, for the purposes of the experiment, the 16LS reduces to the 6LS shown in Fig. 4.15a.

The presence of signal from the mixed two-exciton state implies some type of coherent coupling of the two single-exciton transitions. The dotted lines below the transitions indicate that some characteristic of the X-2X transition is different from the GS-X transition (eg. the transition energies or dephasing rates).

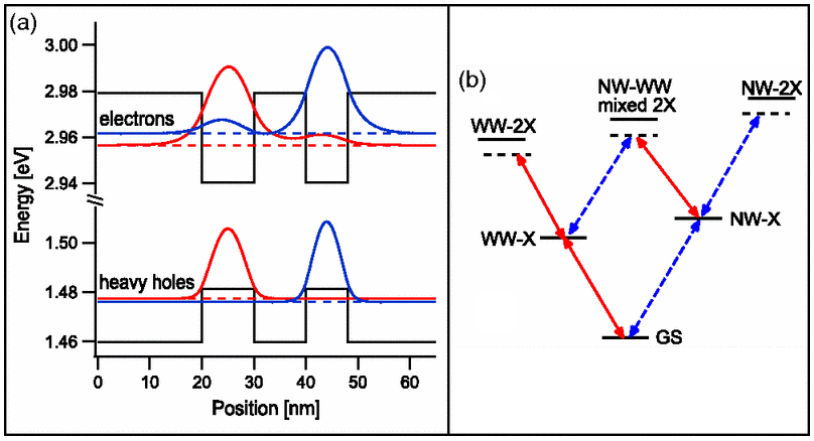

Figure 4.15: Sample diagram and level scheme for the InGaAs DQW sample. Reprinted with permission from Ref. [54].

The results of experiments and simulations from Ref. [54] are shown in Fig. 4.16. The 1Q spectra in Fig. 4.16a,b (experimental) and Fig. 4.16e,f (simulations) show the absolute value and real parts of the 1Q spectrum. The two DPs have inhomogeneously broadened peak-shapes tilted along the diagonal. The real part of the DPs have absorptive cross-diagonal line-shapes. There is an obvious below diagonal CP with absorption in NW-X and emission from WW-X, showing there is some kind of inter-well coupling. The real part of the CP is dispersive, in contrast with the DPs. Based on previous work on single and multi-QWs, the dispersive real line-shape indicates that many-body effects are present and play a role in the generation of the CP [53]. However, in Ref. [53], they observed dispersive line-shapes for both DPs and CPs, in contrast with the results in Ref. [54] (and Fig. 4.16).

The 0Q spectra in Fig. 4.16c,g shows the two peaks at $E_2 = 0$, corresponding to the population pathways for WW-X and NW-X. No CPs are resolved, which suggests

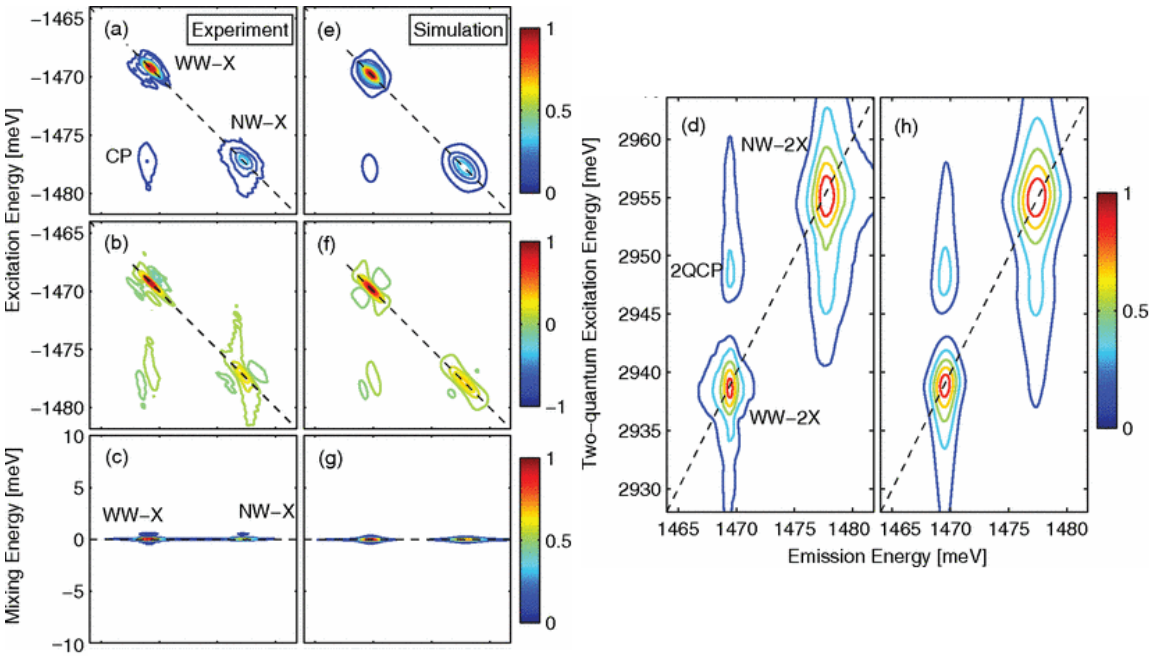

Figure 4.16: 1Q, 0Q and 2Q 2D spectra for the InGaAs DQW recorded at JILA. Reprinted with permission from Ref. [54].

that the coherent-superposition pathway is not present, or the signal is too far below the signal from the strong population pathways to be detected.

The 2Q spectra show the two DPs corresponding to signals from (E_3, E_{2Q}) = (WW-X, WW-2X) and (NW-X, NW-2X) pathways. There is also a clear CP which corresponds to (WW-X, WW-X+NW-X), which is one of the places we expect to see signals from the Mixed-NW/WW-2X state. The existence of this CP therefore confirms that excitation into the mixed two exciton state is possible, and therefore that the two transitions are coherently coupled.

Simulations were conducted to understand the underlying mechanism responsible for the coupling. The third order polarization was calculated for the six level system shown in Fig. 4.15b. To simulate the coupling between the wells, they introduced two differences between the G-X and the X-2X transitions: 1. different dephasing rates (we will refer to this as $\Delta\gamma$) and 2. different transition energies (we will refer to this as ΔE_M). When certain $\Delta\gamma$ and ΔE_M are introduced, the simulations generated 1Q and 2Q 2D spectra with below diagonal CPs, and a dispersive cross-diagonal line-shape in the real part of the 1Q CP. There are a total of 23 free parameters in the simulations, which were constrained by 25 different parameters extracted from the experimental data. Using the constraints from the experimental data they used a manual fitting approach to find $\Delta\gamma$ and ΔE_M which produce simulated spectra that best match the experimental results. They find that a non-zero ΔE_M is required to reproduce the dispersive line-shape of the real part of the 1Q CP. They find that $\Delta E_M = 0.15$ meV provides the best match of simulation and experiment for the line-shape of the real part of the 1Q CP. They further find that non-zero $\Delta\gamma$ and non-zero ΔE_M are required to produce the 2Q DPs.

They attribute these shifts to many-body effects: non-zero $\Delta\gamma$ is due to excitation induced dephasing (EID) and non-zero ΔE_M is due to excitation induced shift (EIS). However, this phenomenological method of including these effects is actually not directly related to the physical source of EID and EIS generated signals, which is population dependent dephasing and population dependent transition energies. However, other types of coupling could lead to non-zero $\Delta\gamma$ and non-zero ΔE_M. For example, a simple two-body coupling (for instance due to hybridization of the electron wavefunctions) might also introduce a shift of X-2X relative to g-X.

4.4.2 *Broadband and pathway selective CMDS Results*

A puzzling aspect of the results presented in Ref. [54] is the missing 0Q CS-CP. In this section, our goal is to discern whether the CS-CP signal pathway is present, and what the amplitude of the CS-CPs are relative to others. We use the same approach we used on the AlGaAs DQW (Section 4.3) to isolate and investigate this signal pathway. This sample presents new challenges, as the WW-X and NW-X transitions are energetically less separated than the AlGaAs transitions, making it more difficult to fully isolate the coherence pathways.

We first performed broadband 1Q, 2Q and 0Q spectroscopy to ensure that we could reproduce the results in Ref. [54] (and in Fig. 4.16).[9] The resulting 1Q and 2Q broadband spectra collected at Swinburne are presented in Fig. 4.18. The results are mostly qualitatively consistent with those in Ref. [54], with a few discrepancies. First, the cross-diagonal linewidth of the DPs is larger in our results, due to the limited scan range of the pulse-shaper. The ratio of 1Q DP intensities is different, but can be explained by the spectral intensity which is weighted towards NW-X in Ref. [54], and roughly even in ours.

Instead of a typical 0Q spectrum we performed a full rephasing 3D spectrum to look for the CS CPs. A pseudo-0Q spectrum is generated by projecting the 3D spectrum onto the E_3 vs E_2 plane, and is presented in Fig. 4.18b. From this projection, there is clearly no peaks at (E_3, E_2) = (WW-X, -10 meV) and (NW-X, 10 meV) (where we expect to see CS-CPs). Even if we examine slices of the 3D spectrum (not shown) there is no indication of a CS-CP. The lack of a CS-CP is, again, consistent with previous investigations of this sample.

In the previous section, signals that were undetectable with broadband excitation were revealed using coherence-specific pathway-selective spectroscopy. Similarly, it is unlikely that the CS pathway in this InGaAs DQW is completely forbidden, but rather just too weak to be detected. Thus, the coherence-specific pathway selective approach could potentially reveal the 0Q coherence in these DQWs. To that end two coherence-specific pathway-selective 3D spectra were recorded contiguously with the broadband spectrum. One spectrum used a pulse sequence that isolated the

9 The pertinent experimental parameters can be found in Table A1.1 in Appendix A1

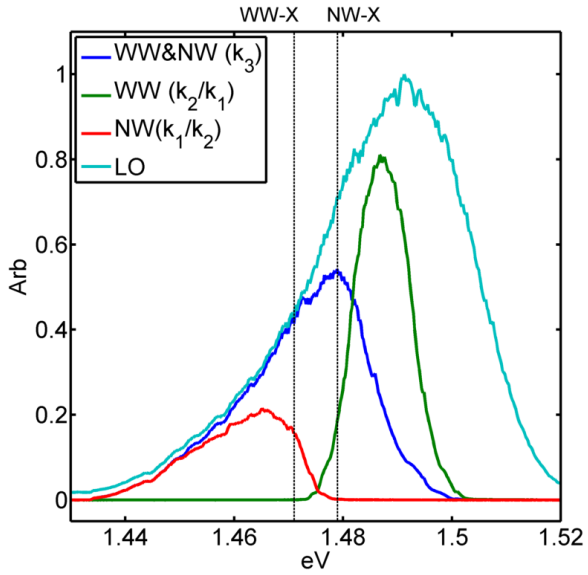

Figure 4.17: Laser spectra for interwell broadband and pathway selective CMDS experiments on the InGaAs DQW.

below-diagonal CS-CP (k_1 only resonant with NW-X, k_2 only resonant with WW-X - the 2121 pulse sequence in Fig. 4.2) and the other spectrum used a pulse sequence that isolated the above-diagonal CS-CP (k_1 only resonant with WW-X, k_2 only resonant with NW-X - the 1212 pulse sequence in Fig. 4.2). The excitation spectra used to collect the spectra are shown in Fig. 4.17. Because the transitions are so closely spaced, the coherence signal is not entirely isolated. As a result, the 2D 1Q spectrum (with coherence-specific spectral shaping) includes some peaks from population pathways which may overlap the peaks from the coherence pathways. In a 3D spectrum, however, these contributions can easily be windowed out as they occur at different E_2 values.

The two pathway selective 3D spectra can be seen in Fig. 4.19a and Fig. 4.19b. Clearly, there are still significant contributions from population pathways, as the strongest signals appear at $E_2 = 0$. There are also well defined and isolated CS-CPs centred at the expected E_1,E_2 and E_3 values for the given pulse orderings, which can be clearly separated from the population contributions.

As in the previous section, these peaks can now be isolated in 3D frequency space and analysed. The slices in Fig. 4.20c-f illustrate this by showing that the CPs appear along the $E_2 = E_3 + E_1$ line (angled dotted line) for the $E_{3/1}$ of the given slice. The peak-shapes in Fig. 4.20a and Fig. 4.20b are not tilted, which indicates that there is no correlation of the broadening between the two wells (which is consistent with the 1Q spectrum in Fig. 4.18).

The FWHM of CS-CPs from the pathway selective spectra, the population pathway CP (Pop-CP) and the DPs from the broadband spectrum are shown in Table 4.3. The CS-CPs and the Pop-CP are projected onto each of the three energy axes and then fit with a Gaussian function. To characterize the inhomogeneous width of the transitions, a slice is taken of the BB 3D spectrum along the $E_3 = -E_1$ diagonal line at E_2

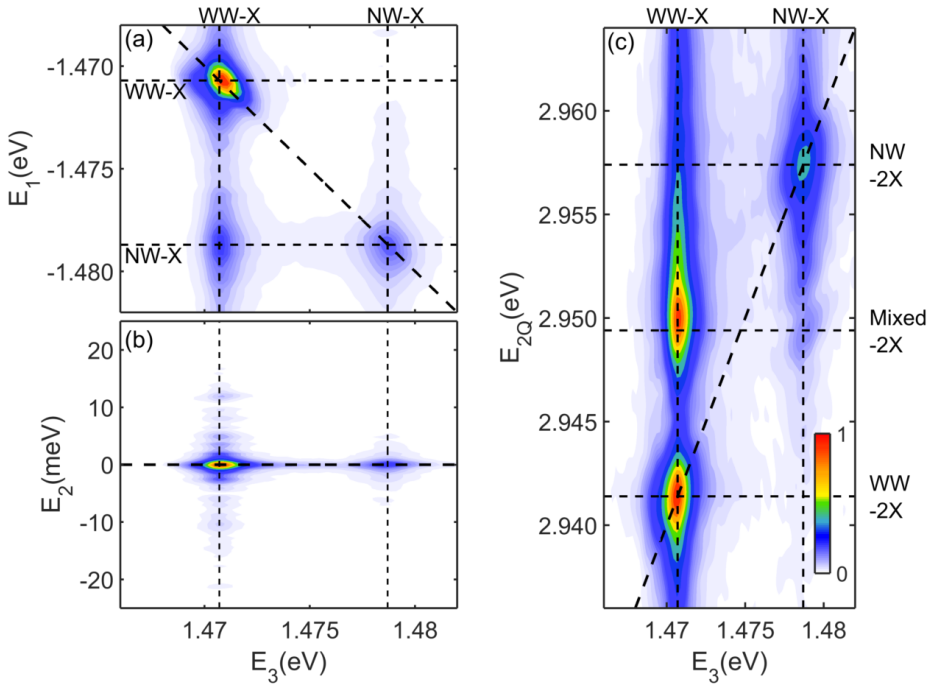

Figure 4.18: Broadband 2D spectra for the InGaAs DQW recorded using the CMDS apparatus at Swinburne. (a) 1Q (b) 0Q and (c) 2Q spectra when exciting only the two QW excitons.

$= 0$. Gaussian functions are then fit to each of the DPs along the diagonal slice. The width of each peak along the diagonal is labelled D in Table 4.3. A cross-diagonal slice is then taken at the peak of each of the DPs and fit to a Lorentzian function to characterize the homogeneous linewidth of each transitions[10]. The cross-diagonal linewidth is labelled XD in Table 4.3.

The E_3 width of the CS-CPs and the Pop-CP all match the inhomogeneous width of the DP that shares the same emission energy. All the CPs have E_1 widths which are larger than the DPs that share the same E_1 energy: Pop-CP and CS-CP_1 both have larger widths along E_1 than the inhomogeneous width of the NW-X DP (1.1 meV). The difference between the E_1 widths of CS-CP_2 and WW-X is even more striking: the CS-CP_2 width along E_1 is ~3× larger than WW-X (0.7 meV). This is a surprising result, because the Feynman diagrams for the CS-CPs (shown in Fig. 4.21a,c) are each identical to the diagrams for the DP with the same absorption energy (shown in Fig. 4.21b,d, respectively) up to the second interaction. The CS-CPs and DPs should therefore experience the same dephasing as a function of t_1 (and hence have the same E_1 width).

As has been noted several times previously in this thesis, the experimental delay limitations can cause an artificial increase in linewidths along E_1 and E_2. This, however, cannot account for the discrepancy between the CS-CPs and DPs because the achievable delay range is equal for both broadband and pathway selective experiments. Furthermore, if the excitation of additional carriers in the BB spectra were involved, then we would expect the opposite effect (i.e. CPs narrower along E_1 than

10 As the delay range in this experiment is limited, the homogeneous linewidths represent an upper bound only.

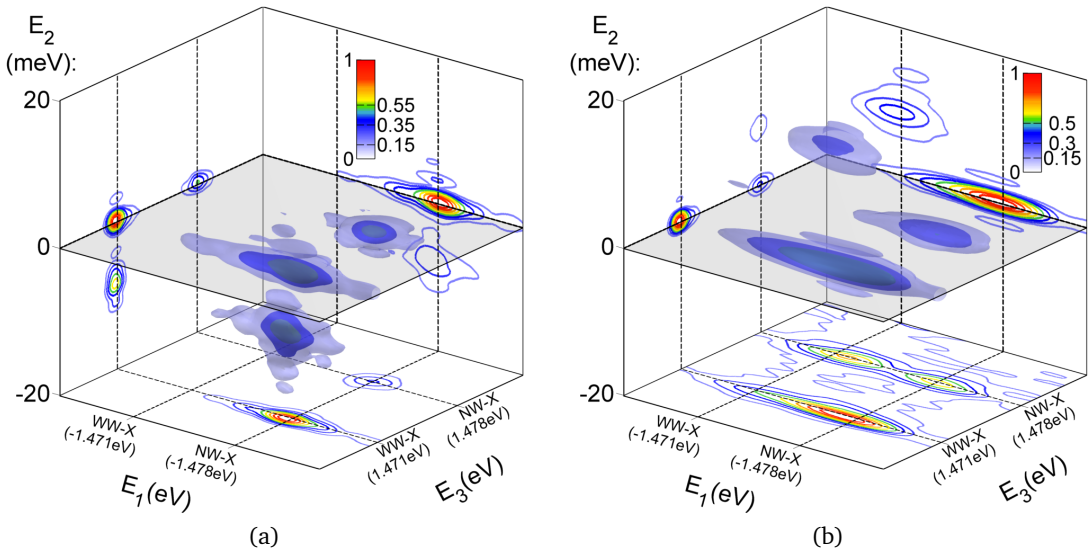

Figure 4.19: Coherence-specific, pathway-selective 3D spectra for 2121 (a) and 1212 (b) sequences, showing some population signals at $E_2 = 0$ as well as the CS-CP.

3D Spectrum	Peak	E_1 (meV) ±0.1	E_2 (meV) ±0.1	E_3 (meV) ±0.1	D (meV) ±0.1	XD (meV) ±0.1
Broadband	WW DP				0.8	0.5
Broadband	NW DP				1.1	1.1
Broadband	Pop-CP	1.5	1.1	0.7		
2121	CS-CP_1	1.3	2.3	0.7		
1212	CS-CP_2	2.3	1.7	1.2		

Table 4.3: Peak-widths (FWHM) measured for several peaks from the three different 3D spectra. The diagonal (D) and cross-diagonal (XD) linewidths are measured for the two DPs in the broadband spectrum. For the three CPs, the 3D peaks are projected onto each axis and then fit with a Gaussian function. CS-CP_1 refers to the below diagonal CS-CP with $E_2 \approx -10$ meV. CS-CP_2 refers to the above diagonal CS-CP with $E_2 \approx 10$ meV.

the DP at the same E_1). Another possibility is that different exciton sub-populations contribute to the different signals. We see evidence for multiple sub-populations in Ch. 7, and suggest that they may be related to inter-well CS-CPs in a different DQW sample. We postulate in Ch. 7 that the sub-population predominately responsible for inter-well interactions is a delocalized state, which also has a much larger homogeneous linewidth. This larger homogeneous linewidth would be consistent with the broadening of the E_1 widths of the CS-CPs here.

We also observe no tilt of the peak-shapes of the E_1 vs E_2 and E_3 vs E_2 projections of the CS-CPs(shown in Fig. 4.20c-f). Given that these transitions are inhomogeneously broadened and uncorrelated, we would expect there to be some tilt of these peak-shapes. Although we were able to resolve this in the previous sample (Section 4.3.4), those peaks were also significantly broader along E_2 than was expected in the absence of enhanced dephasing of the excited state coherence compared with ground-excited state coherences. The linewidths of the transitions in the InGaAs

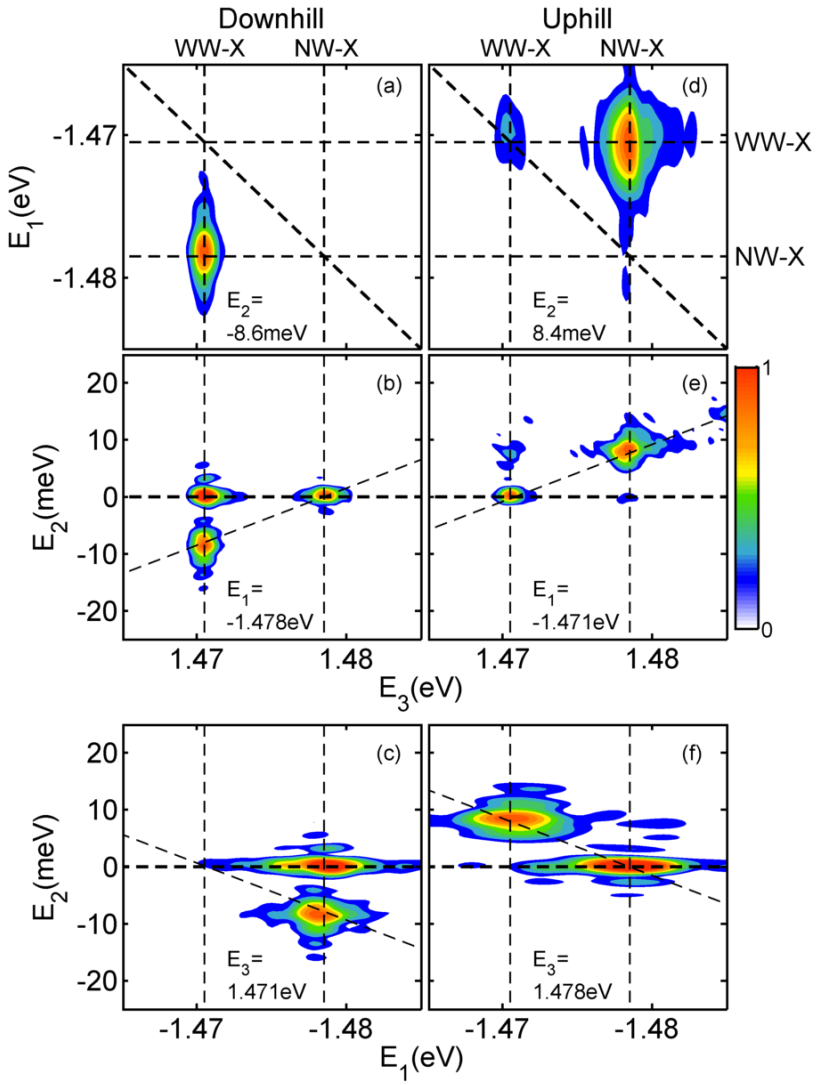

Figure 4.20: The two inter-well CS-CPs for the InGaAs/GaAs DQW projected onto the (a),(b): (E_3,E_1), (c),(d): (E_3,E_2) and (e),(f): (E_3,E_2) planes for the (a,c,e) below diagonal (2121) and (b,d,f) above diagonal (1212) pulse orderings.

DQW are much smaller than the linewidths in the previous section, so a tilt of the peak would be more difficult to resolve as we approach the spectral resolution in the different domains.

The simulations reported in Ref. [54] predicted amplitudes of the 0Q CS-CPs for this sample[11], but they were unable to compare them to experimental values because no 0Q CS-CPs were detected experimentally. Now that we have been able to detect the CS-CPs, we can compare the CS-CP amplitude to the amplitude of the peaks in the simulated spectra, and determine whether they are consistent. The ratio of the amplitude of each CS-CP to the amplitude of the population peak that shares the same emission energy is shown in Table 4.4 for the simulations and for the peaks we have detected experimentally. Experimental amplitudes were corrected for the differences in the excitation spectra according to the technique

11 The CS-CP amplitudes are not reported in Ref. [54] but were provided to us by the authors.

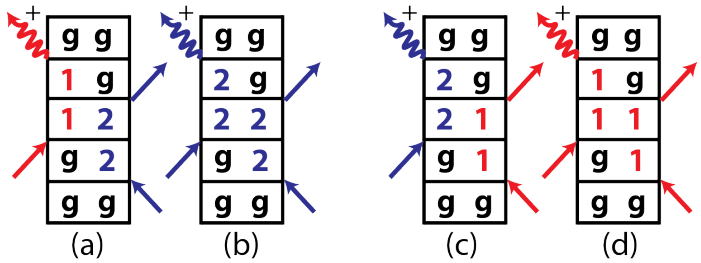

Figure 4.21: Feynman diagrams for the downhill (a) and uphill (c) CS pathways. (b) and (d) are the pathways for the DP with the eivalent E_1 to (a) and (c) respectively. Although these pairs of diagrams are identical up to the second interaction, the CS-CPs show much broader peaks along E_1 (indicating shorter dephasing time), broader even than the inhomogeneous linewidth of the associated DP.

	A_{sim} / A_{sim}	$\tilde{A}^{(P)}$ / $\tilde{A}^{(P)}$	$A^{(P)}$ / $A^{(P)}$	$\tilde{A}^P/A_{Sim}$ / $\tilde{A}^P/A_{Sim}$	A^P/A_{Sim} / A^P/A_{Sim}
$CS-CP_1/WW-X$	0.004	0.020±0.004	0.080±0.020	4.6	19.2
$CS-CP_2/NW-X$	0.013	0.050±0.016	0.290±0.101	3.8	21.9

Table 4.4: The ratio of the amplitudes of the CS-CP and population peaks which share the same emission energy in a 0Q spectrum. A_{sim} are the values extracted from the simulations used in Ref. [54]. $\tilde{A}^P$ are the as measured values from the experimental results here. A^P are the measured values corrected for the different amplitudes of the laser spectra. $\tilde{A}^P$ and A^P represent an upper and lower bound on the CS-CP amplitude, respectively. The ratio of the measured amplitudes and the simulated amplitdes ($\tilde{A}^P/A_{Sim}$ and A^P/A_{Sim}) show that the measured values are not consistent with the simulations. The measured peak amplitues are comparable with the background noise in the BB 3D spectrum.

in Section 4.3.5. Both corrected and uncorrected amplitudes are reported in Table 4.4.

The amplitudes measured in this experiment are much larger than those predicted by the simulations. The uncorrected amplitudes are roughly a factor of four larger than the simulations, and the corrected amplitudes are a factor of 20 larger. As discussed in Section 4.3.5, the correction for the electric field amplitude assumes that the signals scale with $\mathbf{E}^3$. Like the previous sample, experiments in Ch. 7 will show that the inter-well CS-CPs follow a sub-$\mathbf{E}^3$ dependence on excitation density. The corrected amplitudes shown therefore overestimate A^P. Still, using $\tilde{A}^P$ as a lower bound and A^P as an upper bound, we can conclude that the experiment and simulations are not consistent, and that the measured CS-CPs have larger amplitudes than predicted by the simulations.

We interpret this discrepancy in the following way. The simulations in Ref. [54] used differences between the GS-X and the X-2X transitions as a way of introducing many-body effects phenomenologically. As a reminder, the physical origins of coupling due to many-body effects can be thought of in the following way[12]. A dephasing-grating or a shift-grating (which are caused by spatial variations of EID and EIS, respectively) imprints the wave-vector of one signal onto others. Specifi-

12 This described in more detail in Section 3.2.4

cally applied to inter-well coupling, this involves populations in one well creating a shift or dephasing grating in the other well through many-body interactions between the wells.

As we noted previously, the way $\Delta\gamma$ and ΔE_M are introduced is not explicitly related to EID and EIS (which are density dependent dephasing and density dependent transition energies, respectively). Furthermore, the differences between the G-X and X-2X transitions could also come from two-body coupling between WW-X and NW-X. In that vein, the larger CS-CP amplitude might suggest that the two-body coupling was underestimated in the simulations. Future simulations will aim at understanding the interplay between the two-body coupling and the many-body coupling by including the many-body coupling in a more physical (but still phenomenological) way. Many-body coupling will be introduced as density dependent dephasing rates and transition energies in the system Hamiltonian.

To summarize, in this section we have presented 1Q, 2Q and 0Q spectra for an InGaAs DQW sample using broadband excitation that are consistent with previously published 2D spectra on the same sample. This is a useful result in its own right, CMDS is an emerging technique which has many different experimental implementations, and establishing consistency across a range of different experiments is crucial in the pursuit of reliable and repeatable results, especially given the wide range of unexpected and interesting phenomena which are being investigated.

By spectrally shaping the excitation pulses we were able to detect the inter-well coherent superposition signal that remained elusive in broadband 2D spectroscopy. From the isolated peaks, we were able to compare the strength of the CS-CP signal to the predicted value from the simulations reported in Ref. [54]. We found that the simulations under-estimates the CS-CP amplitude by between a factor of 4 and a factor of 20.

These results also show that even when signal pathways cannot be perfectly isolated due to closely spaced transitions, excited state coherent-superposition signals can be enhanced relative to everything else by selecting pathways using spectral shaping. These results emphasize that pathway selection could be useful in other material systems in which transitions are closely spaced or overlapping, such as 2D materials [212, 219], nano-platelets [215, 220], quantum dots [221], bacterial light-harvesting complex 2 [9], and other biological light harvesting complexes [6, 8, 97, 200].

4.5 Comparison of AlGaAs and InGaAs results and summary

The two DQW samples investigated in this chapter are similar in some ways, but different in others. The AlGaAs sample has a narrower (6 nm vs 10 nm) barrier which is also much higher ($\sim$280 meV vs $\sim$60 meV). The lower potential barrier in the InGaAs/GaAs sample means that the wavefunctions penetrate much further

into the GaAs barriers, which leads to more significant hybridization of the electron wavefunctions, even though the barrier is thicker. The AlGaAs (InGaAs) sample is grown by MOCVD (MBE), so the InGaAs/GaAs DQW has cleaner interfaces, and the GaAs/AlGaAs DQW has exciton lines which exhibit increased inhomogeneous broadening. The larger inhomogeneous broadening in the GaAs/AlGaAs DQW also allows us to more easily identify correlated and uncorrelated broadening in the E_3 vs E_2 and E_1 vs E_2 peak-shapes of CS-CPs.

InAs and GaAs are not lattice matched so InGaAs layers experience strain. For low indium content the strain does not cause dislocations or lattice/interface defects, but instead leads to a uniform deformation of the lattice. The most notable difference this creates is that it removes the degeneracy of the HH and LH bands, and shifts the energy the LHs such that they are no longer confined in the DQW. AlAs and GaAs on the other hand are nearly perfectly lattice matched so the layers remain unstrained. It is not clear whether this difference plays much of a role in understanding inter-well coupling, but it does have important consequences for the overall electronic structure of the InGaAs/GaAs QW sample, which will be discussed in more detail in the following chapter.

Finally, in the GaAs/AlGaAs sample, an AlGaAs layer forms the barrier between the wells. AlGaAs is a ternary compound which are known to be more prone to defects than binary layers [222]. On the other hand, the barrier in the InGaAs/GaAs sample is just GaAs, a binary compound which can be grown very cleanly. The levels of impurities are much higher in barriers made of composite materials, so the actual confinement may be much less than expected for the AlGaAs sample. As impurity driven tunneling is one of the suggested mechanisms for tunneling in QWs [222], this could explain the relatively large inter-well CS-CPs in the GaAs/AlGaAs sample even when the wavefunctions are well localized in separate wells. Whether impurity driven changes to the potential could allow coherent interactions is not as clear.

Given all of these differences between the samples, there are quite a few similarities in the results. We might be able to use to these similarities understand what aspects of the experimental results are sample specific and which are more general. The first similarity is that the inter-well coherent superpositions generate CPs which show no tilt and therefore no correlation of the inhomogeneity. Second, the coherent superpositions are significantly weaker than the diagonal pathways. One important difference between the results for the two samples is that in the InGaAs sample, the $E_2 = 0$ inter-well CP (Pop-CP) is very strong compared with the CS-CP. In the results for the GaAs/AlGaAs sample, on the other hand, the $E_2 = 0$ CP and the CS-CP have similar amplitudes. A speculative explanation for the differences in these samples is that the InGaAs/GaAs sample is coupled through through the ground state due to wavefunction hybridization while the GaAs/AlGaAs sample (which has very little wavefunction hybridization) is coupled in the excited state.

In both of these samples, the E_1 vs E_2 and E_3 vs E_2 peak-shapes are broader along E_2 than we expect based on the simulations in Section 4.3.4. Although some of the

CS-CPs in the AlGaAs sample qualitatively matched the amount of tilt (lack of tilt) expected for inter-well (intra-well) peaks, the peak widths were all larger than expected. The disparity for intra-well CS-CPs is caused by the t_2 scan range. The scan did not go out far enough in t_2 to collect the entire population decay or dephasing of the excited state coherent superpositions. This reduced scan range resulted in broadening and spectral leakage along E_2. However, for the inter-well CS-CPs, the widths are far from experimentally limited and the full decay is captured within the t_2 scan range used. The CS-CP dephasing time is therefore clearly shorter than we would have expected given the linewidths of the individual exciton transitions. Similarly, the inter-well CS-CPs in the InGaAs samples are much broader along E_2 than we would expect based on the inhomogeneous linewidth of the coupled excitons. The measured CS-CP dephasing times, however are in the range where we are unable to definitively determine whether they are limited by the experiment. However, for the E_1 and E_3 widths of these peaks we would expect to see some tilting of the peaks. The fact that we don't could also indicate a faster than expected CS dephasing.

We hypothesize that this more rapid dephasing could be caused by excitation induced effects, and that the excited state CS in t_2 are more sensitive to exciton-exciton interactions or free-carrier-exciton interactions than the ground-excited state coherences. The excitation density dependence in Ch. 7 also seems to support this view, though a repeat of these exact experiments at low powers would be necessary to show it definitively. We have several other experiments planned to test this hypothesis, which will be discussed in Ch. 8.

Finally, we we showed that the amplitude of the 0Q CS-CP in the InGaAs/GaAs sample is inconsistent with the simulations previously reported for this sample. Using these new constraints to improve the simulations will be the subject of future work.

5

PATHWAY-SELECTIVE TWO-QUANTUM COHERENCE

Some of the motivation for developing coherent multidimensional spectroscopy (CMDS) for electronic transitions is related to to the success of multidimensional nuclear magnetic resonance (NMR) spectroscopy, which is a technique that is in many ways conceptually similar to CMDS [223, 224]. In particular, triple-resonance NMR has been very successful in resolving the structure of complex molecules (including proteins) by selectively exciting spins of different nuclear species in a controlled order [15, 21, 225, 226]. In this chapter, we will demonstrate the deterministic and selective excitation of mixed two-exciton states, in which the order of excitation is defined. This is an important step towards an excitonic equivalent of triple-resonance NMR. The first section will describe some of the key concepts required to understand triple-resonance NMR, and then we will describe how an analogous technique for excitons can be useful, and how it can be realized in our SLM based CMDS experiment.

5.1 Triple-resonance NMR

NMR is a technique that uses radio-frequency (RF) radiation to investigate nuclear spins [14]. In 1D NMR experiments, a sample is placed in a strong magnetic field (10 T) and excited by an RF pulse, which creates a macroscopic nuclear spin polarization. This spin polarization then emits RF radiation which is detected in the time domain and then Fourier transformed into the frequency domain. The resonant frequency of the emitted radiation depends on the nuclear species, the magnetic field amplitude and the electronic environment of the nuclear spin. The electronic environment of the spin in turn depends on what atoms are bonded to the nucleus (as shown in Fig. 5.1), so NMR is intrinsically sensitive to the molecular structure.

In multidimensional NMR [14], multiple RF pulses are used to generate a nonlinear signal, and dynamics are explored by scanning the time delays between the pulses. Multidimensional spectra are then generated by Fourier transforming the collected data along one or more of the scanned delays. In the simplest case (autocorrelation spectroscopy, also called COSY) this results in an absorption-emission correlation map similar to a 1-quantum (1Q) spectrum, as described in Ch. 1. Interactions that involve only a single type of nucleus in a specific bonding environment

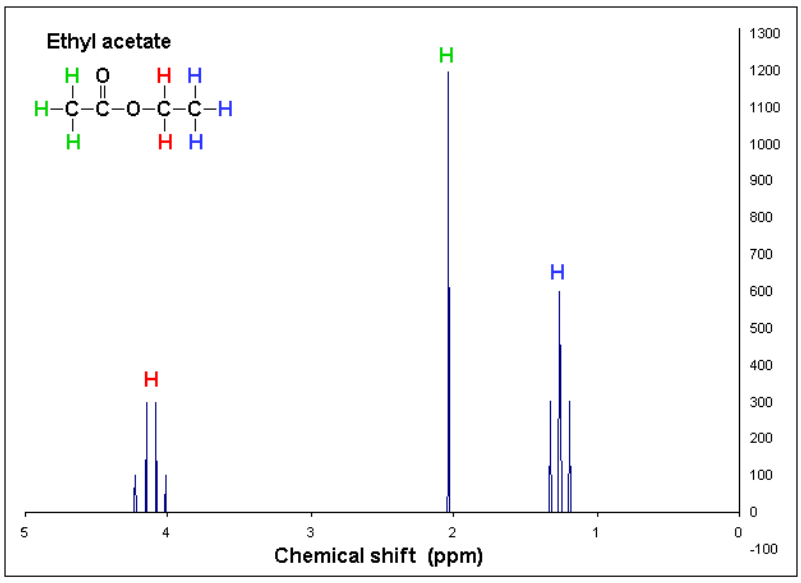

Figure 5.1: An example NMR H spectrum for Ethyl Acetate. The H nuclei bonded in different arrangements (as indicated by the different colored H's in the inset) have different resonances. Reproduced from Ref. [227].

will appear as peaks along the diagonal (i.e. diagonal-peaks; DPs). The spin coherence can be transferred between nuclei that are close to one another and/or share a bond. Transfer of the spin from one nucleus to another will appear in the 2D spectrum as a cross-peak (CP). Basic information about the structure can then be determined by observing where the CPs occur. If the RF pulses are only resonant with a particular nuclear species (this is often called homonuclear NMR), then all of the DPs and CPs will involve the same type nucleus in different bonding environment. In homonuclear NMR, the directly observed structural information is mostly limited to the species being excited, and some a priori knowledge is required to work out the structure of larger molecules.

A different category of experiments are called heteronuclear experiments [228–230], in which some pulses are resonant with one species of nucleus (e.g. H) and others are resonant with a different species (e.g. N). This can be thought of as a sort of CP specific approach in that the modulations in the time domain(s) that are scanned are at a different frequency than the emission frequency [228]. The benefit of this approach is that H nuclei which are bonded to N in different environments can be clearly separated based on which CPs appear in the 2D or 3D spectra. Heteronuclear NMR can be conducted using pulse orderings in which CPs appear due to spatial proximity of the nuclei, or through bonds between nuclei.

Heteronuclear NMR can be extended to include pulses separately resonant with three different nuclei (H, N and C), in what is typically called heteronuclear triple-resonance NMR, or simply triple-resonance NMR [225, 226]. This approach is often conducted in 3D, such that each of the three resulting frequency axes represents a different species of nucleus (H, N, C). Correlations between the H, N and C nuclei in different electronic environment can therefore be observed. H, N and C are some of

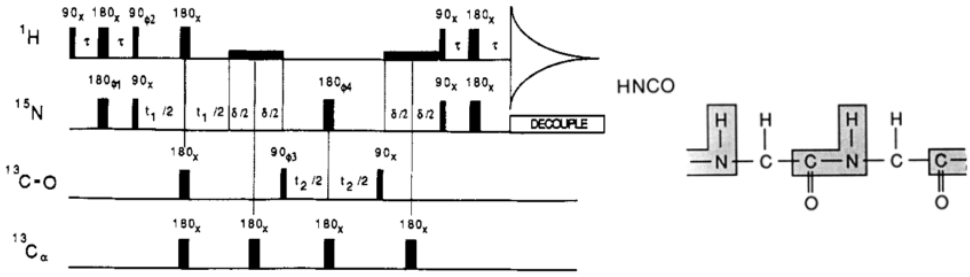

Figure 5.2: The plot on the left shows an example of a pulse sequence used in a heteronuclear NMR experiment. The horizontal axis represents time flowing left to right. The black rectangles indicate RF pulses and the horizontal lines represent the nuclei with which the pulses are resonant. This pulse sequence (called HNCO) can isolate signals from the arrangement of C, N, and H shown on the right. Adapted with permission from Ref. [225].

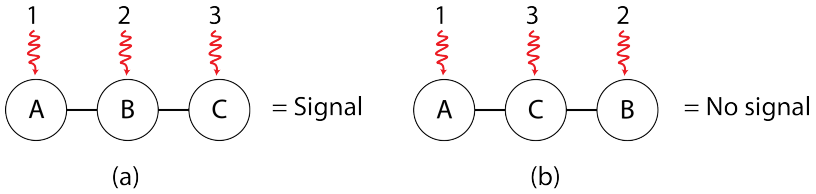

Figure 5.3: An illustration of how mutli-quantum triple-resonance NMR can be used to separate signals from the same atoms bonded in different configurations. If the A $\rightarrow$ B $\rightarrow$ C excitation pulse sequence is used, then the "molecule" in (a) will result in signal while the "molecule" in (b) will not.

the most common constituent elements of proteins, so the ability to observe their spin correlations is incredibly powerful, and is a key part of the use of NMR to determine protein structure [15].

Different pulse sequences have been devised to investigate H, N and C bonded in specific arrangements. An example is given in Fig. 5.2, (reproduced from Ref. [225]), which shows a HNCA pulse sequence along with the arrangements of C, N and H it is sensitive to. Combining the selectivity of triple-resonance NMR with the ability to resolve CPs along three frequency axes in 3D spectra has proven to be incredibly powerful. This basic approach has been expanded out to many (up to thousands of pulses) to identify large complexes. Protein structure can then be determined by combining a series of several triple-resonance NMR experiments with well developed calculations [231].

Some of the pulse sequences used in triple-resonance experiments involve multiple-quantum spin coherences as a means to determine what spins are connected directly through bonds [14, 226, 229]. The utility of selective excitation of multi-quantum coherences can be understood using the following example: the pulses sequentially excite spins of three different nuclei - A, B, C - which are bonded as shown in the cartoon in Fig. 5.3. If we excite a 3-quantum coherence in the A $\rightarrow$ B $\rightarrow$ C order, then the "molecule" in Fig. 5.3a will generate a signal, while the molecule in Fig. 5.3b will not. If we are investigating a larger molecule, we can therefore use the selectively excited 3-quantum coherences to isolate signals

from nuclei bonded to the complex in Fig. 5.3a, while suppressing those from the complex in Fig. 5.3b even though they both consist of the same three nuclei. Selectively excited multi-quantum coherences can be integrated as part of a larger pulse sequence to eliminate signals that don't involve a particular arrangement of nuclei, in what is referred to as multi-quantum filtering [14]. Thus, the ability to selectively excite these multi-quantum coherences in different orders is very useful for determining the structure of large complexes. It is important to note that a key component of this selective approach is deterministically exciting the multi-quantum coherences in a particular order.

Clearly, the selective excitation of multi-quantum coherences in heteronuclear NMR experiments is powerful, so an exploration of similar approaches in the optical regime would appear to be advantageous [232]. There are, however, many differences between NMR and CMDS that make applying this type of approach to electronic transitions more challenging. First, the non-linearity of materials is much weaker at optical frequencies than at microwave frequencies, so the extension to large numbers of pulses at is not feasible. Experiments are typically only conducted up to 5^{th}-order [63, 68, 190, 191](though at least one 7^{th}-order experiment has been reported [63, 191]). In 5^{th}-order experiments, only coherences up to 3-quantum can be directly observed, which limits the degree of filtering that can be applied.

Another challenge, is that to achieve selectivity we must generate pulses which are resonant only with different transitions. At optical frequencies, generation of non-overlapping excitation spectra while also maintaining the phase stability required to perform CMDS is not straight forward (as described in Ch. 2 and Ch. 4). Furthermore, multi-quantum spectroscopy requires an even more stable apparatus than 1Q spectroscopy due to the increased frequency of the signal phase oscillations as a function of the scanned delay (i.e. t_{2Q} in 2-quantum (2Q) spectroscopy).

These challenges notwithstanding, some of the heteronuclear and multi-quantum NMR methodologies could be useful at optical frequencies to study excitonic systems. For example, in systems where excitonic states are predominately localized to different parts of a complex, a technique similar to the one described in Fig. 5.3 could be used to infer the spatial layout of the states in the complex. Multi-quantum coherences could be used to determine which states are indirectly coupled (i.e. not directly coupled to one another, but both coupled to a third state). Extrapolating from this, we could also investigate how electronic couplings between states extend across the complex by determining which states can be combined into a 3Q-coherence and in which order.

Selective excitation of multi-quantum coherences could also be used as a filter to isolate specific signals in mixed samples (like the cartoon shown in Fig. 5.4). In this example, the sample is made up of three different complexes (A, B and C), which exist in a sample in several different combinations - A, B, C, AB, BC, AC and ABC. If CMDS with broadband excitation is used to study this sample, the signal would

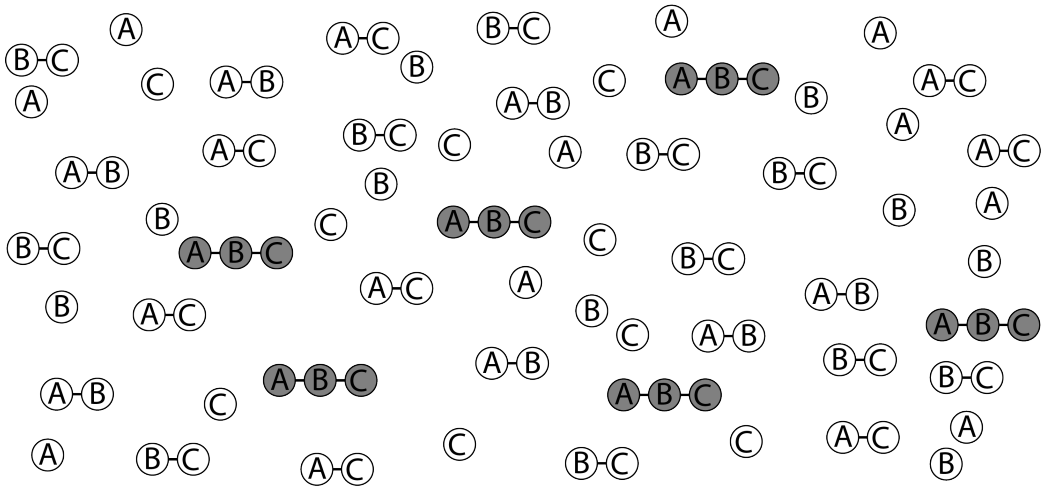

Figure 5.4: Multi-quantum filtering in excitonic systems. A mixed sample made up of complexes with three excitonic states in a variety of different configurations: A, B, C, AB, BC, AC and ABC. In a broadband 3Q experiment the signal from the singles and pairs will dominate. However, if we use a selective 3Q experiment, we could excite only the ABC configuration.

be dominated by signals from the single complexes. A signal involving a selective 3-quantum coherence made up of A, B, and C could be used to isolate signal from just the ABC complexes, while suppressing signal from the singles and pairs.

Pulse-shaper based CMDS can alleviate some of the challenges in realizing selective multi-quantum spectroscopy. First, as demonstrated in Ch. 4, we can use spectral amplitude shaping to produce sequences of pulses that are each resonant with different transitions. Second, the intrinsic phase stability allows us to perform 2Q spectroscopy, while delaying pulses in a rotating frame allows us to sample in much larger steps. 3Q-coherences in 5^{th} order experiments will also benefit from stability and rotating frame delays. Finally, because of the controllable beam shaper and pulse-shaper, the experiment can easily be reconfigured to perform 5^{th} order experiments. Indeed, a similar apparatus was previously used for 5^{th} and 7^{th} order experiments experiments (which are required for direct detection 3Q and 4Q coherences, respectively) using non-selective broadband excitation [63, 191]. However, because these experiments used non-selective excitation, they were unable to benefit from the concepts borrowed from heteronuclear NMR, and focused mostly on correlations of excitons of the same transition.

In this chapter, we present proof of principle results showing that spectral shaping can be used to selectively excite mixed 2Q-coherences in 2Q 2D spectroscopy. We also show that the order in which the mixed 2Q-coherence is excited can be controlled, which is a key part of what makes the selection and filtering processes in NMR possible. This represents an important step towards selective excitation of higher order excitonic multi-quantum coherences.

The first section will describe how pulses tuned to specific transitions can be used to isolate signals from mixed two-exciton coherences. The following section then presents results in which the signal for a mixed two exciton state made up of a

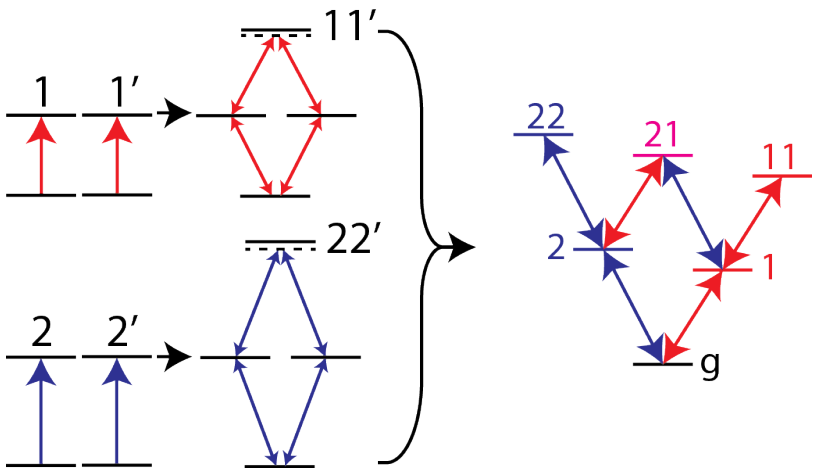

Figure 5.5: Two pairs of identical 2LS's can be recast as a pair of four 4LS's or a single six-level system involving two 1-exciton states and three 2-exciton states. In the 6LS, the mixed two exciton state can be accessed via either 1-exciton state, but not directly from the ground state.

quantum well exciton and a barrier exciton is isolated. We show that in addition to isolating the mixed signals and removing the single transition peaks, the signals involving the free-carrier continuum can also be suppressed. Excitonic peaks which otherwise are hidden behind strong free-carrier peaks are thereby revealed, and quantitative analysis of amplitudes and peak shapes is made possible.

5.2 Pathway selection in two-quantum coherence pulse ordering

As described in Section 2.2, we can reformulate a system of four 2-level systems (2LS's) into a pair of 4 level systems (4LSs) or a 6 level system (6LS) like the one shown in Fig. 5.5. Depending on which of the 2LS's are coupled, this 6LS can collapse back down into either two 4LS or into four 2LS's. If 1 and 1' are not coupled to 2 and 2', then the 6LS collapses back down to a pair of 4LS's, and all of the pathways that involve the 21 state cancel. Thus, presence of signals involving this 21 state confirm that the 6LS cannot be represented as a pair of 4LS's, and that 1 and 2 are coherently coupled in some way [54].

As described in Section 2.2.1.3, 2Q 2D spectra allow us to directly detect signals from these two-exciton states (21, 11, and 22) which we cannot not directly identify in 1Q or 0-quantum (0Q) spectra. Furthermore, pathways that involve 21 appear as CPs (at $E_{2Q}=\epsilon_1+\epsilon_2$, where ϵ_1 and ϵ_2 are the transition energies of states 1 and 2, respectively), while signals involving 11 and 22 appear as DPs (at $E_{2Q}=2\cdot\epsilon_1$ and $E_{2Q}=2\cdot\epsilon_2$, respectively). Signals involving these three different two-exciton states can therefore be clearly separated in 2Q 2D spectra. As a result, the detection of a CP in a 2Q spectrum at $E_{2Q}=\epsilon_1+\epsilon_2$ must involve the 21 state, and therefore indicates that the two associated transitions are coupled and cannot be represented as separate 4LS's.

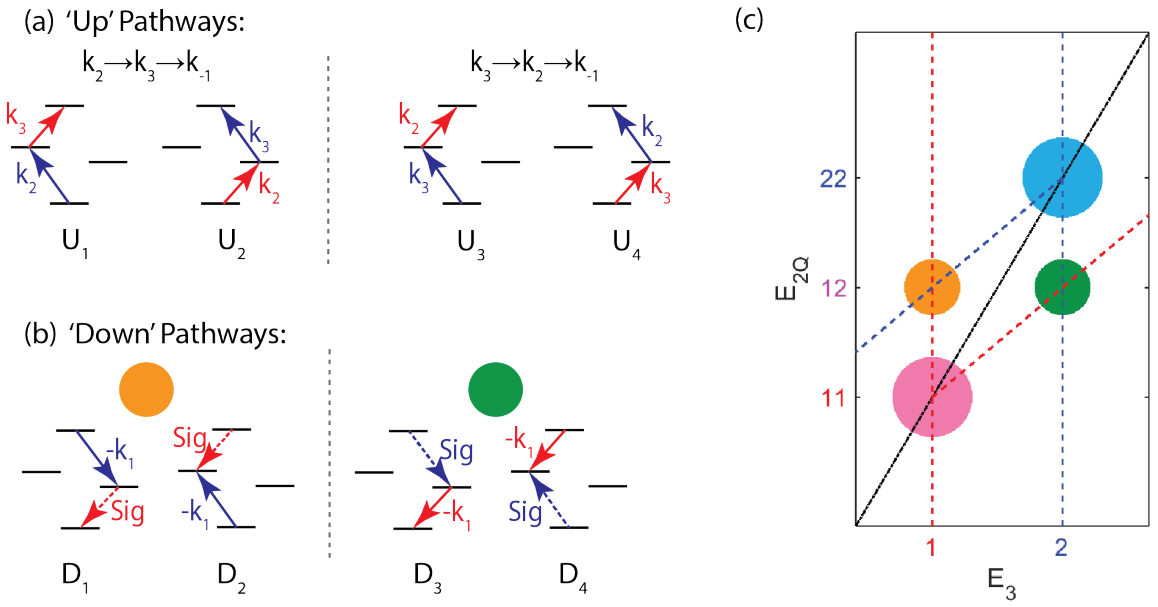

Figure 5.6: Pathways that involve the mixed 2Q coherence state must go 'up' via one of the four pathways shown in (a). Once in the mixed-2Q coherence the signal can go 'down' any of the four different ways shown in (b). The 'down' pathways can be separated spectrally, so the signals involved appear at different points in the 2Q spectrum, as indicated by the colored circles in (b) and in the cartoon 2Q spectrum in (c).

If 1 is not coupled to 1' and 2 is not coupled to 2', then each of the 4LS's collapse back into two 2LS's, and there are no longer any 11 or 22 states. In the context of FWM, 1 and 1', (or 2 and 2') indicate two separate but indistinguishable states within the ensemble excited by the pulse. If there are interactions between 2LS's then 1 and 1' (or 2 and 2') are coupled in some way, so the system is coherently coupled and the two pairs of 2LS's (1, 1' and 2, 2') can each be described as a 4LS. As a result, if we measure signal from pathways involving 11 and 22 (which we can do in a 2Q 2D spectrum), then there must be interactions within the ensemble excited by the laser.

The interaction pathways that involve the 21 state (and therefore lead to 2Q CPs) can be split into two parts: 'up' (first two pulses) and 'down' (third pulse and signal). In the 'up' portion, the first two pulses each interact with different transitions to generate a mixed 2-quantum coherence (a coherence of the 2-exciton state with the ground state). The mixed 2-quantum coherence (2Q-coherence) then evolves at the sum of the two single exciton transition energies. In the 'down' part, the third pulse interacts with the 2Q-coherence to produce a signal and return the system to a population state.

As shown in Fig. 5.6a, there are a total of four 'up' pathways that can generate a mixed 2Q coherence, which are labelled U_1-U_4. All four are excited if the broadband excitation is used and $t_1=0$. U_1 and U_2 are identical to U_3 and U_4 (except for the order in which the k_2 and k_3 pulses interact) and experimentally indistinguishable as long as k_2 and k_3 are identical. As shown in Fig. 5.6b there are also four 'down' pathways, which have been labelled D_1-D_4. These are split into two pairs, which

appear at different positions in the 2D 2Q spectrum (as indicated by the coloured circles in Fig. 5.6c).

Each of the 'down' pathways can be paired with any of the 'up' pathways, so at each of CP positions in the 2Q 2D spectrum a total of $2\times4=8$ pathways can lead to a signal. When broadband excitation spectra are used and $t_1=0$, these 8 pathways cannot be further separated. However, we can limit some of the possible 'up' pathways using spectral amplitude shaping of the first two excitation pulses so that they are each resonant with different transitions. If we shape the spectra of k_2 and k_3 so that they are only resonant with states 1 and 2 respectively, then only 'up' pathways U_2 and U_3 will be allowed. If we are interested in separating out signals that go up via a particular single exciton state, this is not very useful alone, because U_2 goes up via state 1 and U_3 goes up via state 2. However, if we increase t_1 so that k_2 and k_3 pulses have no temporal overlap, then we can eliminate either U_2 (if k_3 arrives first) or U_3 (if k_2 arrives first). Now, each of the CPs represent only one 'up' pathway and hence only two complete pathways.

By shaping the spectrum of the third pulse (k_1), we could eliminate either D_1 & D_2 or D_3 & D_4. There is no real reason to do so, however, because these pairs already appear at different E_3 values and are therefore separable even when the third pulse is resonant with both 1 and 2. For that reason, k_1 can be left broadband to improve the time resolution in the t_{2Q} scan without introducing any ambiguity in identifying the signal pathways responsible for the CPs. Leaving the third pulse broadband is also advantageous because it allows us to record signals that involve all four down pathways simultaneously (again, without introducing any additional ambiguity in identifying which pathways are involved).

Another benefit of shaping the spectral amplitude of the first two pulses so that they are not resonant with any of the same transitions, is that none of the pathways that involve either the 11 or the 22 states are allowed, even at $t_1=0$. As a result all of the DPs are suppressed. As we saw in the Ch. 4 removing strong DPs in 1Q spectra can lead to an improvement in the signal-to-noise ratio of the CPs, and reveal CPs that are otherwise hidden by tails of the DPs. This is also true in the case of 2Q spectra.

Finally, pathway selection with spectral amplitude shaping can also suppress pathways that are generated by interactions of the excitons with free-carriers and defect states. This is also important, as these defect and free-carrier features can often obscure excitonic peaks. The suppression of free-carrier and defect related peaks is explained in detail in Section 5.3.1.

5.3 Results and discussion

Broadband and pathway-selective 2Q 2D spectra are collected for the $In_{0.05}Ga_{0.95}As$ double quantum well (DQW) sample that has been discussed previously (Section

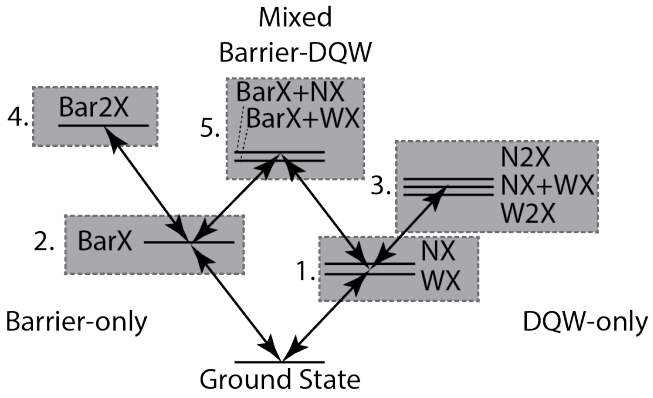

Figure 5.7: A system with three 1-exciton states and six 2-exciton states. The mixed BarX+NX and BarX+WX states can be accessed via the BarX or either of the DQW states. The grouping of the states is explained in the text.

4.4). There are three 'bright' exciton transitions in this DQW sample - one in each QW (labelled WX and NX in this chapter[1]), and one in the barrier (labelled BarX). Including all two-exciton states, this sample can be represented as a 10-level system (10LS). For the purposes of this discussion this 10LS can be represented in a fashion analogous to that of the 6LS in Fig. 5.5 by grouping some of the states together as shown in Fig. 5.7. The groupings in Fig. 5.7 can be understood as follows. The one exciton states are separated into two groups: DQW only ($\times$2, in box 1) and BarX only ($\times$1, in box 2). The two-exciton states can be separated into three groups: DQW only ($\times$3, in box 3), barrier only ($\times$1, in box 4) and mixed DQW-Barrier ($\times$2, in box 5). Spectral amplitude masks and pulse orderings were chosen to isolate signals resulting from mixed-two exciton states involving one exciton in the barrier and the other in the DQW (box 5). Both sets of 'up' pathways are isolated in two separate pathway-selective spectra (PS1 & PS2), and compared with the spectra generated with broadband excitation (BB).

The pulse sequence and excitation spectra used (along with the emission spectrum of the FWM signal $t_1 = t_{2Q} = 0$) are shown in Fig. 5.8a and Fig. 5.8b respectively. The spectral amplitude masks were applied to the pulses in three different configurations: BB, PS1 and PS2 (Fig. 5.8c,f,i). In BB pulse-sequence no spectral shaping is applied. In the PS1 (PS2) pulse-sequence, the first pulse is shaped to excite the DQW (barrier) and the second excites the barrier (DQW). No spectral amplitude masks were applied to the third pulse or LO, as shaping these does not add to the selectivity already provided by the spectrally resolved emission energy. For all three configurations $t_1 = 300$ fs. In the BB case all three of the two-exciton states are populated. Two 'up' pathways (U_3 and U_4) are allowed for each of the mixed to combine to form each of the mixed BarX - WX/NX two exciton states (as shown in Fig. 5.8d). In contrast, only one 'up' pathway populates each of mixed two-exciton states in PS1 and PS2. In PS1, only U_4-like 'up' pathways (i.e. path-

1 These transitions were labelled WW-X and NW-X, respectively, in the previous chapter for consistency with the notation used in previously published results.

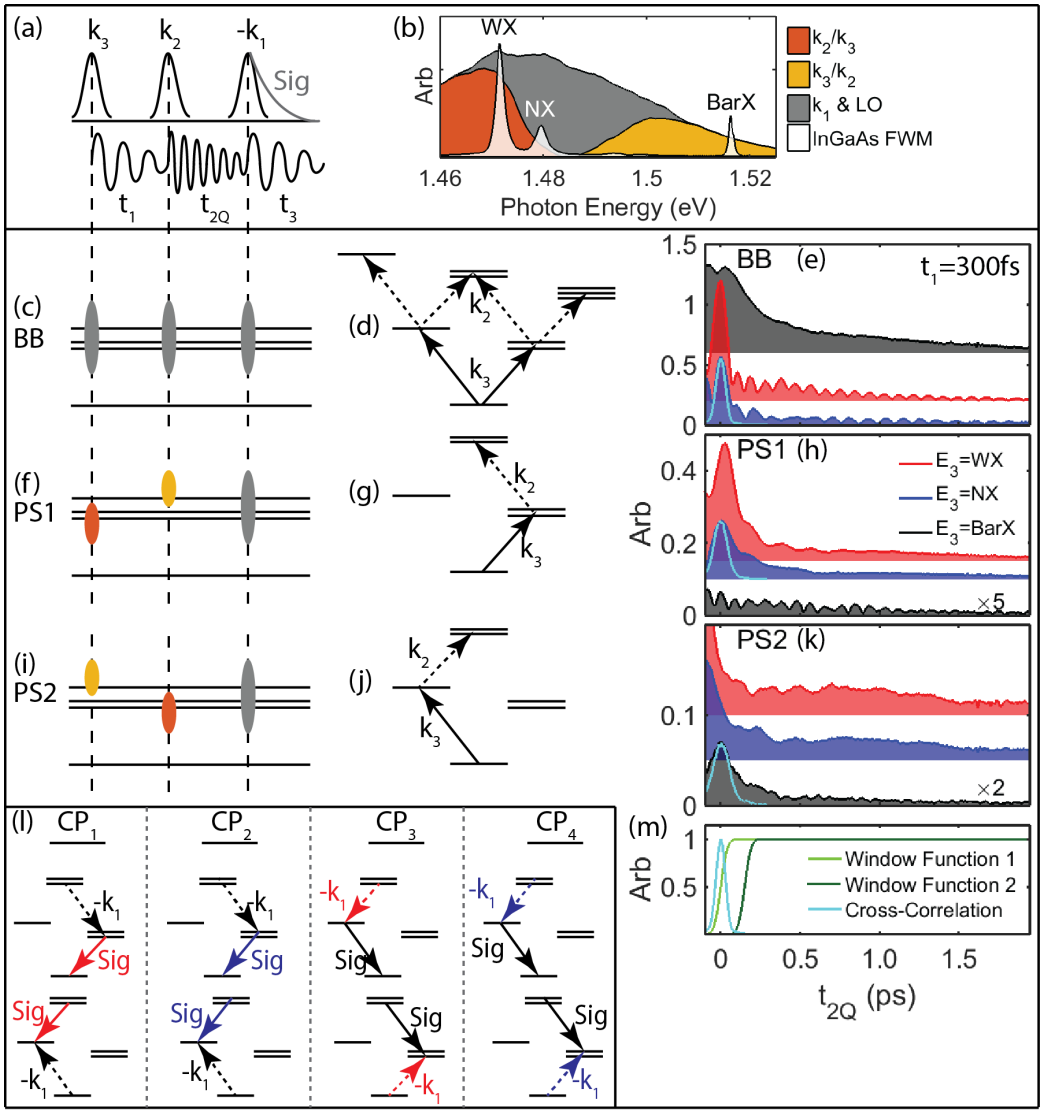

Figure 5.8: (a) 2Q pulse ordering. (b)excitation laser spectra and the DQW FWM response when $t_1 = t_{2Q} = 0$. (c), (f) and (i) show the BB, PS1 and PS2 pulse sequences. (d), (g) and (j) show the available 'up' pathways for each sequence. (e),(h),(k) show the 2Q signal as a function of t_{2Q} for emission from each single exciton transition for each sequence. The relavent pulse cross correlation measured using a BBO crystal is presented in light blue. (l) shows the two available 'down' pathways for each CP and emission energy. (m) shows the two window functions and the pulse cross correlation

ways in which the DQWs are excited first) are allowed, while in PS2, only U_3-like 'up' pathways (i.e. pathways in which BarX is excited first) are allowed. In both PS1 & PS2, none of the two-exciton states in box 3 or box 4 are populated.

The 2Q FWM signal as a function of t_{2Q} for the BB, PS1 and PS2 configurations is shown in Fig. 5.8e, Fig. 5.8h, and Fig. 5.8k, respectively, at the emission energy of the WX, NX and BarX transitions.[2] The BB DQW signals for E_3=WX (NX) shows oscillations with energy equal to the difference between BarX and WX (NX), indicating the interference of signals with $E_{2Q} = 2 \cdot WX$ ($2 \cdot NX$) and $E_{2Q} = BarX + WX$ (BarX + NX). The WX and NX emission energies in all three shaping configurations

2 The pertinent experimental parameters used in collecting this data can be found in Table A1.2 in Appendix A1

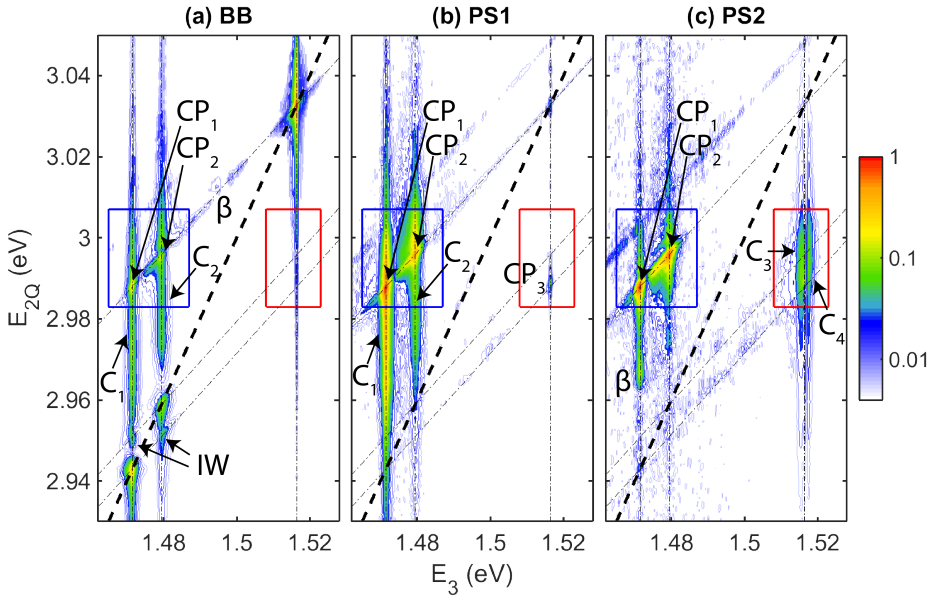

Figure 5.9: Broadband and pathway selective 2Q 2D spectra plotted on a logarithmic scale for the (a) BB, (b) PS1 and (c) PS2 pulse sequences. Window function 1 is used to remove pulse overlap effects before the Fourier transform along t_{2Q}.

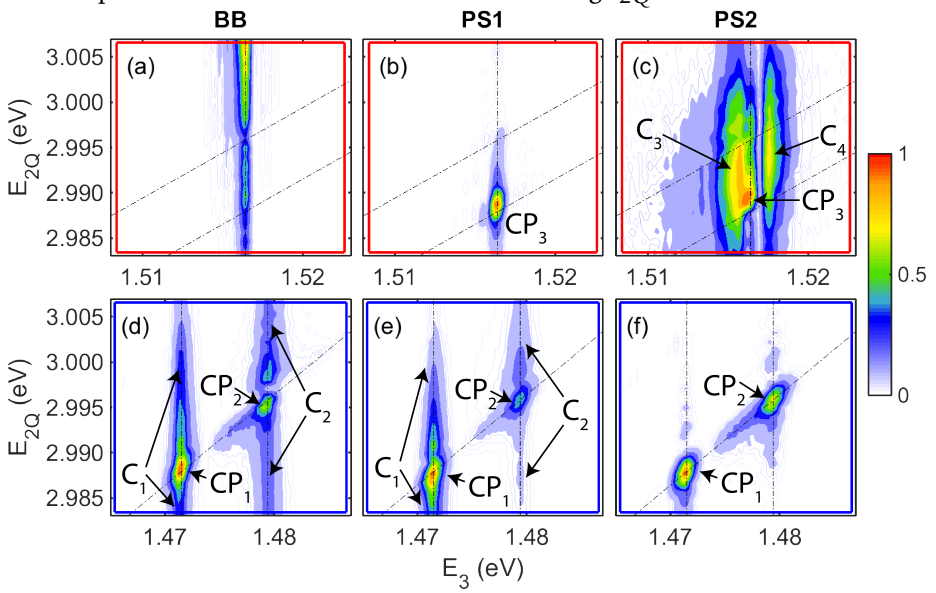

Figure 5.10: Zoomed view of CPs in Fig. 5.9. Colors are scaled linearly and normalized according to the highest value in each subplot. Windowed along t_{2Q} using window function 1.

involve the two 'down' pathways shown in Fig. 5.8l for CP_1 and CP_2, respectively. The BarX emission energy includes four 'down' pathways, but they can be separated into pairs after the data is Fourier transformed as a function of E_{2Q}.

At $t_{2Q} = 0$, both 2Q and non-rephasing ($k_3 \rightarrow -k_1 \rightarrow k_2$) signal pathways can be generated. When the rotating frame is used for delays, these signals can sometimes overlap in 2Q spectra. To isolate the 2Q signal, a time windowing function is typically applied to the data to remove the pulse overlap signal. Window Function 1 (shown in Fig. 5.8m) is the error function with a width equal to the measured cross-correlation width of pulses k_2 and k_1. This window function cuts off most of the non-rephasing signal without losing much 2Q signal.

Figure 5.9 shows BB, PS1, and PS2 2Q spectra which are Fourier transforms of the time domain data presented in Fig. 5.8e,h,k.[3] In these spectra, Window Function 1 was used to remove the pulse overlap signal before the Fourier transform was applied. The BB spectrum (Fig. 5.9a) shows three DPs (WX, NX, BarX) and several CPs. CPs involving a transition with energy ϵ include all peaks which share the same emission energy (vertical dashed lines), and peaks along the $E_{2Q} = E_3 + \epsilon$ line (angled dashed lines). We observe two CPs (labelled CP_1 and CP_2) with E_3 equal to WX and NX and E_{2Q} equal to the WX+BarX (NX+BarX) mixed two-exciton energies (close ups of CP_1 and CP_2 are shown in Fig. 5.10d). The inverse CPs (emitting in BarX with the same two-quantum energies) are missing, or hidden by contributions from the strong tail of the BarX DP. Close ups of the region where these CPs are expected, is shown in Fig. 5.10a. There may be slight dips in the tail of the BarX DP, but not clear enough to identify as CPs. We also observe NX-WX inter-well CPs (labelled 'IW') as well as interactions with the βX excitons which are described in Ch. 6 (labelled 'βX'). In this chapter, our focus is on WX-BarX & NX-BarX mixed two-exciton states, so the IW and βX peaks will be ignored.

In Fig. 5.9a and Fig. 5.10d, we observe two continua along E_{2Q}, which have emission in from WX and NX (labelled C_1 and C_2, respectively). These continua are generated by 2Q-coherences that involve one exciton and one unbound electron-hole pair (EHP). These exciton-EHP 2Q-coherences dephase very rapidly as a function of t_{2Q}, and hence are broad along E_{2Q}. The EHP in the 2Q coherence could be in the QW or in the barrier. The presence of the C_1 and C_2 continua is consistent with the time domain plots in Fig. 5.8e, which show a significant increase in emission from WX and NX at $t_{2Q} < 200$ fs. The pathways leading to these continua will be discussed in Section 5.3.1.

As expected, when the spectrally shaped pulse configurations (PS1 and PS2) are used, we observe significant changes in the resulting 2Q spectra. First, in both Fig. 5.9b and Fig. 5.9c the DPs disappear, but several CPs remain. In both PS1 and PS2, CP_1 and CP_2 below-diagonal CPs are observed, as in the BB configuration. We also now observe an above diagonal CP (labelled CP_3), which is clearly evident in Fig. 5.10b (the PS1 configuration). This peak is generated by the D_3 and D_4-like 'down' pathways shown in Fig. 5.8l for CP_3. We also observe what may be a very weak CP at E_{2Q}=NX+BarX and E_3=BarX, where we would expect to observe CP_4. CP_3 can also be observed in the Fig. 5.10c (the PS2 configuration), but it is partly hidden by two strong continua, which are labelled C_3 and C_4. C_3 and C_4 have emission energies below and above BarX, respectively, which correspond roughly to known emission energies of GaAs defects [128, 168, 233].

The C_1 and C_2 continua are observed in the PS1 configuration, but not in the PS2 configuration. Conversely, the C_3 and C_4 continua are clearly evident in the

3 The time domain data is presented in Fig. 5.8e,h,k as an absolute value for simplicity. Like all the other 2D spectra in this thesis, the complex valued time domain data is Fourier transformed to produce the 2D spectra in Fig. 5.9.

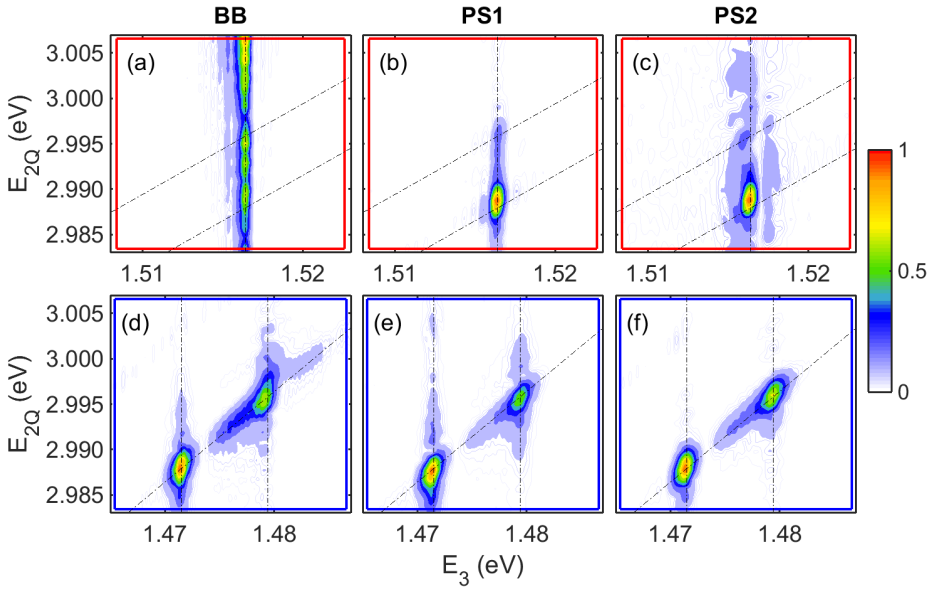

Figure 5.11: Same CPs as in Fig. 5.10, but windowed using window function 2 instead of window function 1, to supress free carrier-DQW exciton and defect-BarX interactions.

PS2 configuration but are completely suppressed in the PS1 configuration. This difference highlights the significance of being able to selectively isolate different 'up' pathways and points to an interesting application of selective 2Q spectroscopy which will be discussed in more depth later.

These results show that the PS1 and PS2 pulse sequences are functioning roughly the way we expect them to: DPs are suppressed, and the pathways that lead to CPs are further isolated. Unlike pathway selection in the 1Q pulse ordering, where each the coherence specific pulse ordering isolates either above diagonal or below diagonal CPs, pathway selection in 2Q generates both above diagonal and below diagonal CPs regardless of which transition is excited first. This difference stems from the fact that the E_{2Q} energy of a CP is not the energy of a single interaction but rather the sum of the energies of the first two light-matter interactions. Furthermore, the E_3 energy of a given pathway does not necessarily depend on the order of the first two interactions. Put another way, regardless of how the system gets into the mixed two-exciton state, it can in principle go down any of the available 'down' pathways.

Signals which dephase quickly can be removed from the 2D spectra by shifting the window function so that it removes more of the scanned signal before the data is Fourier transformed along t_{2Q}. To suppress the C_1, C_2, C_3 and C_4 continua, but leave the excitonic CPs unaffected, we shift the centre of the window function from $t_{2Q}=0$ fs to $t_{2Q}=100$ fs and then Fourier transform the windowed data as a function of t_{2Q}. This window function is shown in Fig. 5.8l as 'window function 2'. The use of window function 2 instead of window function 1 results in changes to the CPs as shown in Fig. 5.11. The two continua with $E_3=$WX and NX (C_1 and C_2) are now nearly completely suppressed in Fig. 5.11d,e (which correspond to BB and PS2 configurations, respectively). In Fig. 5.11c, we also observe a suppression of the C_3 and

C_4 defect related continua. While the CPs in Fig. 5.11b,f remain mostly unchanged, we can now clearly identify the CPs in Fig. 5.11c-e because the continua have been suppressed. The shape and position of CP_1 and CP_2 in Fig. 5.11d,e are now comparable with the same peaks in Figs. 5.10f. Similarly, the shape and position of CP_3 in Fig. 5.11c is now comparable to the shape and position of CP_3 in Fig. 5.10b. The similarity of the CPs in the different configurations is reasonable given that they share the same 2Q-coherence during t_{2Q}, (which determines the linewidth and position in E_{2Q}) and follow the same 'down' pathways (which determine the linewidth and position in E_3).

Although both of the excitonic CPs can now be clearly observed in the BB, PS1, and PS2 configurations, the CPs in which the continuum signals are intrinsically removed (Fig. 5.10b,f) still show far better contrast between the excitonic peak and the background than those in which the continua were suppressed by the window function (Fig. 5.11c-e). Furthermore, using the window to suppress the continuum can alter the peak shapes in some situations, so being able to avoid the use of window functions is advantageous.

The CP shapes in Fig. 5.10d-f and Fig. 5.11d-f are all tilted to some degree. In 1Q spectra (as we have discussed previously), CPs with a tilted peak shape are a result of correlated inhomogeneous broadening. In 2Q spectra, however, the tilt is *not* caused by correlated broadening but rather an inherent correlation of E_3 and E_{2Q} which can be observed when the E_{2Q} width is limited by the sum of the single exciton linewidths, and not by carrier-carrier scattering. This effect will be discussed in more detail in Section 7.3.1.

5.3.1 *Suppression of free-carrier and defect interactions*

In this section we will discuss the pathways that lead to the continua observed in the spectra in Fig. 5.9, and explain why different continua are suppressed in PS1 and PS2. Finally we will explain how this is advantageous and can be used to reveal exciton resonances.

We will start by considering the pathways responsible for the continua C_1 and C_2, which have emission WX and NX, respectively. The pathways that lead to C_1 and C_2 involve a 2-Quantum coherence involving an exciton (WX or NX, respectively) and an unbound electron hole pair (EHP) during t_{2Q}. The EHP can be in the free-carrier continuum of one of the QWs or in the free-carrier continuum in the barrier.

This 2Q coherence dephases very quickly for two reason. First, the continuum is by definition spectrally broad, so the different spectral components fall out of phase very quickly. Second, unlike excitons, carriers have a net charge and therefore interact strongly with other charged particles, so dephasing due to carrier-carrier interactions also contributes. Regardless of the exact origin of the dephasing, the 2Q-coherence of an exciton and an EHP dephases much faster than two-exciton

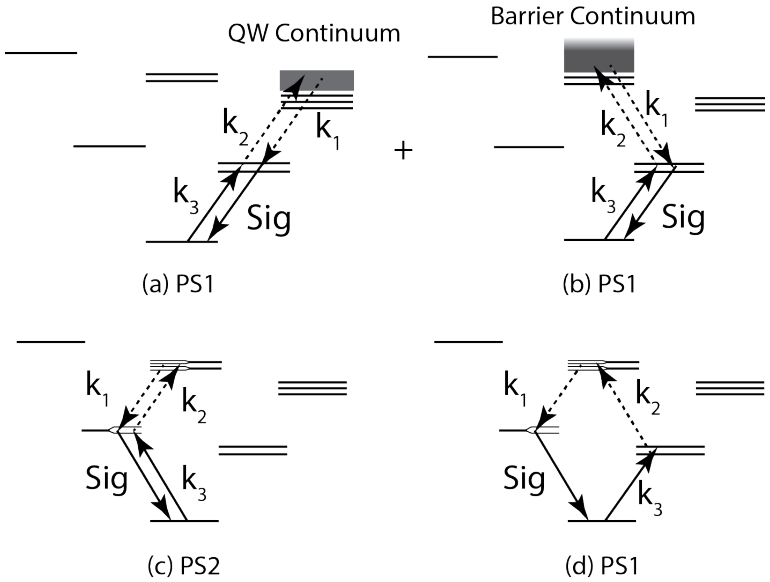

Figure 5.12: A graphical depiction of the pathways that lead to the continua in (a-b) Fig. 5.10d,e and (c) Fig. 5.10a,c. A full description of the pathways is provided in the text.

2Q-coherences. When the second and third pulse are overlapped temporally we can still get strong signal from pathways involving exciton-EHP 2Q-coherences. In a t_{2Q} scan we start from $t_{2Q}=0$, so there is some finite amount of time in which exciton-EHP 2Q-coherences will contribute strongly to the signal.

2Q-coherences of a QW exciton with an EHP in the QW and 2Q-coherences of a QW exciton and an EHP in the barrier both contribute to the C_1 and C_2 continua (as shown in Fig. 5.12a-b). The part of the C_1 (C_2) continuum that appears at values ofE_{2Q} lower than CP_1 (CP_2) are 2Q coherences of WX (NX) and EHPs in one of the QWs (as shown in Fig. 5.12a)[4]. The part of the C_1 (C_2) continuum that appears at values of E_{2Q} higher than CP_1 (CP_2) involves a 2Q coherence of WX (NX) and EHPs the barrier free-carrier continuum (as shown in Fig. 5.12b).

To generate a 2Q-coherence of an exciton and an EHP, one of the first two pulses must interact with an exciton state and the other with the free-carrier continuum. There are therefore two possible orderings for the 'up' part of the pathway: 1. The first pulse interacts with free-carrier continuum and the second pulse interacts with the exciton (we'll call this the EHP$\rightarrow$exciton ordering) or 2. the first pulse interacts with an exciton transition and the second pulse interacts with a EHP (we'll call this the exciton$\rightarrow$EHP ordering).

In order to form a 2Q-coherence, some macroscopic polarization generated by the first pulse must still be present when the second pulse arrives. The ground-EHP decoherence time is expected to be on the order of $\sim$50 fs [175], which is consistent with what we observe in the 1Q pulse ordering (not shown here). Both 'up' pathways involving EHPs are possible at $t_1=0$, but as t_1 increases, the EHP$\rightarrow$exciton

4 Intuitively we might assume that the exciton and EHP involved in the 2Q coherences are in the same well. We know, however, that the wells are coupled due to the presence of the inter-well CP, so in principle a 2Q-coherence of an exciton to an EHP in the other well is also possible.

ordering becomes much less likely, due to dephasing of the ground state to EHP coherence during t_1. In the experiments presented here, $t_1 = 300$ fs, so by the time the second pulse is incident upon the sample, any macroscopic polarization involving EHPs will have long since dephased. Any signal from the exciton-EHP 2Q-coherence must involve the exciton→EHP ordering, as evidenced by the experimental results in Fig. 5.10. Thus, when we use the PS2 pulse sequence, only a macroscopic polarization of excitons remains when the second pulse arrives. The second pulse is not resonant the free-carrier continuum, so only 2-quantum coherences involving two excitons are generated even at $t_{2Q} = 0$.

We will now consider the pathways that lead to C_3 and C_4 in Fig. 5.10c. The explanation for these continua involves defects instead of the EHPs, and is shown in Fig. 5.12c. The first pulse excites one of two defect states in the barrier which have a transition energy similar to BarX, which we will call $\mathrm{BarX^o}$. The second pulse excites one of the QW excitons, putting the system into a 2Q-coherence of a shallow defect in the barrier and a QW exciton. Because the defects are charged, this 2Q state dephases very quickly during t_{2Q}. The third pulse puts the system back into a single quantum coherence of the defect state and the ground state, and the signal is emitted from the defect state. It isn't clear, however, why C_3 and C_4 are suppressed in the PS1 configuration. In principle, the pathway in Fig. 5.12d could generate emission from the defects as well. One possible explanation for the suppression of the pathway in Fig. 5.12d is that the excitons very quickly decohere when they are close enough with defects to interact. As a result, the ground to QW exciton coherence in t_1 would decay quickly the pathway in Fig. 5.12d would be suppressed. To explore this possibility, we could perform a 3D experiment using the PS1 configuration in which t_1 is scanned as well t_{2Q}. We would then look for the appearance of signal from the pathway in Fig. 5.12d at a lower t_1.

The results presented here clearly show that the presence of C_1-C_4 depends on which configuration is used, so we can therefore control whether these continua appear in the 2Q spectrum through our choice of spectral shaping configuration and t_1. This ability to control whether the continuum contributes to the 2Q spectra could be quite useful, as the continua can obscure excitonic peaks. While window functions can be used to suppress 2Q signals from continua in data analysis, the ideal choice of window function is often not clear, and removing the continuum without affecting the signals of interest is not always possible. In particular, small changes in the length and shape of the function can affect precise peak positions and shapes due to the interference of the two signals. This is particularly problematic when the features of interest are spectrally broad and/or have an amplitude comparable to the that of the free-carrier signals. A better solution, then, would be to find a way of suppressing the free-carrier continuum in the way the experiment is conducted. The pathway-selective 2Q spectra do just that. By choosing one or the other 'up' pathways, the continuum is suppressed on one CP or the other. As demonstrated here, this can allow us access to weak excitonic signals that are otherwise

hidden underneath the stronger (though short lived) features from the free-carrier continuum.

5.3.2 *Quantitative comparison of cross-peak amplitudes*

Now that we have further isolated the mixed 2Q pathways, we could conceive of a more quantitative analysis of the signals embedded in these spectra. For instance, we could compare the amplitude of the CPs generated by the PS1, PS2 and BB sequences to test the premise that both 'up' pathways and both 'down' pathways are weighted equally. If the 'down' pathway is truly independent of the 'up' pathway, then we would expect the CPs in Fig. 5.9b and Fig. 5.9c to be of equal amplitude (assuming that the pathways have the same dynamics in t_1). This appears not to be the case - the above diagonal CP is much weaker than the below diagonal CPs. There are, however, four factors that affect the signal amplitudes and complicate direct quantitative comparisons:

1. The spectral amplitude of the third excitation beam and the LO are different for the CPs emitting at different energies.

2. Free-carrier continuum overlaps some of the peaks in some of the spectra. While they can be somewhat suppressed by the choice of window function, the continua still result in a larger background signal and noisier peaks.

3. The macroscopic polarization during t_1 will decay differently depending on which exciton is excited by the first pulse.

4. The CP amplitudes oscillate as a function of t_1 with a frequency equal to the energy of the first interaction, which is different for PS1 and PS2.

Item 1 can be dealt with by simply measuring the spectral intensity of excitation pulses and accounting for the differences as we did in Section 4.3.5. The free-carrier continua (item 2) can be reduced by carefully applying the windowing function. The decay of the macroscopic polarization (Item 3) can be readily measured and then corrected for, and only represents a small correction. The fourth item, however cannot be corrected for in the current experiment. The amplitude of the CPs depends on the relative phase of the first and second pulse, and therefore oscillates as a function of t_1. However, if we were to collect a 3D 2Q spectrum (by scanning t_1 and t_{2Q}) we would be able to account for this effect as we did in the 3D spectra in Section 4.3.5. The data here was only acquired for a single t_1, so it is not possible to apply this correction. Alternatively, we could also estimate this correction by calculating the phase differences between the coherences excited by the first pulse based on the frequency of the coherences and the t_1 used in the experiment. At optical frequencies such an estimate is difficult, but in the rotating frame it becomes possible. We have not attempted to calculate an estimate for this data.

5.4 Summary

In this chapter we have demonstrated that spectral shaping can be used in 2Q 2D spectroscopy to isolate mixed two-exciton coherences. We also found that different pulse orderings can suppress the broad E_{2Q} features created by rapidly dephasing coupling to free-carriers or defects, and thereby reveal the excitonic CPs hidden underneath. The ability to selectively excite specific two-exciton combinations in a deterministic order also represents a step towards the application to electronic transitions of some of the methodologies used extremely successfully in triple-resonance NMR. An extension of this selective approach to 5^{th} order signals and 3-particle correlations should be possible with the current experimental apparatus and work towards that goal is ongoing.

Recent investigations into multi-excitonic correlations have only just begun to scratch the surface, particularly when it comes to *mixed* multi-exciton correlations. The ability to selectively excite multiple particle correlations and explore their dynamics will allow us to better understand what role these play in the many-body dynamics of semiconductor QW systems and in what excitation regimes they are relevant. Finally, this approach is promising for exploring mixed multi-quantum correlations in other systems, such as light harvesting complexes [5, 201, 234], nano-platelets [215, 220] and monolayer materials[212, 235, 236].

6

DARK STATE COHERENT DYNAMICS AND INTERACTIONS BETWEEN QUANTUM WELL AND BARRIER STATES

In this chapter, we investigate interactions between barrier and QW excitons as well as the coherent dynamics of 'dark' exciton states in two $In_xGa_{1-x}As$ double quantum well (DQW) samples using photoluminescence excitation spectroscopy (PLE) and coherent multidimensional spectroscopy (CMDS). These states have dipole moments small enough that they are difficult to detect in linear experiments. They are also strongly coupled to bright exciton states in the QWs and the barrier. We exploit this coupling to study them via the cross-peaks (CPs) that appear in CMDS experiments for strongly coupled transitions. The population and coherent dynamics of these 'dark' states are studied in detail using 0-, 1-, and 2-quantum (0Q, 1Q, and 2Q 2D as well as 3D spectroscopy. The 3D spectrum reveals strong coherent interactions between these dark states and the bright QW states. In fact, the reason we are able to detect these states at all is because they are coherently coupled to the bright QW states.

We observe three types of dark states: 1. parity forbidden excitons in which the electron has even parity and the hole has odd parity (which are labelled as αX), 2. type-II light-hole (LH) excitons in which the hole is localized in the barrier and the electron in the QW, (which are labelled as $\beta X_{1,2}$), and 3. excitons which involve an electron in the barrier and a hole in the QW the nature of which is not yet fully understood (which are labelled as βX_{3-6}). These peak assignments are confirmed using evidence from PLE, 2D and 3D spectra as well as comparisons of the detected transition energies with wavefunction calculations. We show that the population lifetimes of all these dark states are not vanishingly short. Indeed, $\beta X_{1,2}$ appear to have population lifetimes at least as long as the bright, allowed QW excitons.

Even though these 'dark' states do not strongly emit or absorb light, they very likely play an important role in the relaxation of 3D bulk excitons and free carrier into the QW states. They also may play a role in the dynamics of the QW excitons themselves. The access to these dark states we have gained through their coupling to bright excitons will help us understand how significant a role they play, and allows us access to new exciton physics which is elusive using other optical techniques.

6.1 Background: barrier-QW interactions and type-II LH excitons

The dynamics of exciton and carrier relaxation/capture into QWs is a topic of fundamental interest, but is also important in design of devices like QW lasers and infrared detectors [237–239]. Due to carrier confinement in the QW, it is not surprising that carrier capture is best described through quantum mechanical rather than classical means. One way the quantum mechanical nature of the capture process is revealed is by the dependence of the capture rate on the width of the QW. This rate is found to exhibit oscillations as a function of well width [240, 241], which can be understood in the following way: the dominant mechanism for relaxation into the well is the emission of LO phonons. The efficiency will therefore be maximized when there is a QW level whose energy (E_{QW}) is an integer multiple of the LO phonon energy (E_{LO}) below the barrier exciton energy (E_{Bar}).

$$E_{QW} + nE_{LO} = E_{Bar} \tag{6.1}$$

As the well width increases, different QW levels come in and out of resonance, and so the capture efficiency oscillates. Furthermore, it was suggested that the carrier capture is ambipolar - meaning that the exciton is captured whole, rather than being split [241].

Coherent coupling of the barrier excitons and QW excitons, even when the energy difference is not resonant with the LO phonon is another key aspect of carrier capture which is clearly quantum mechanical. In PL and PLE experiments, Reynolds et al [242, 243] demonstrated that direct excitation of the barrier exciton led to enhanced emission from the QW exciton in InGaAs/GaAs DQW samples, which they suggested was caused by coherent coupling of the barrier and QW well excitons through wavefunction overlap. The wavefunctions were overlapped due to penetration of the QW exciton wavefunction into the barrier. Direct measurement of coherent coupling of barrier and QW excitons requires a technique that can directly measure coherent interactions of excitons, (such as CMDS). In this chapter, we find (based on the existence of CPs in 1Q, 0Q and 2Q spectra) that the barrier and QW excitons are indeed coherently coupled. We also find, however, that direct barrier-QW coherence is only part of the picture as a range of additional intermediate states are also detected and couple to both the QW and the barrier excitons.

Typically, excitons in heterostructures are separated into two categories: type-I and type-II. In type-I excitons (such as typical QW and GaAs bulk excitons) the carriers are overlapped spatially and localized in the same material (Fig. 6.1a). Type-II excitons involve carriers that are predominately localized to different layers in the heterostructure, and exist in a variety of contexts. A basic example is an exciton in a type-II heterojunction with a staggered gap (Fig. 6.1b), in which both the valence band and conduction bands of one material are lower than the other.

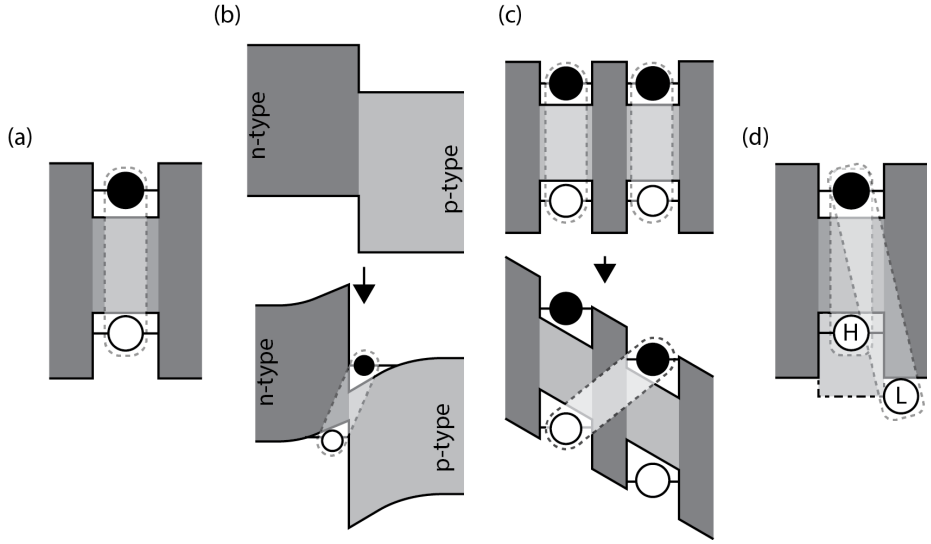

Figure 6.1: A cartoon illustrating type-I and several type-II exciton configurations. (a) Type-I, direct exciton transitions. (b) Type-II heterojunction between two layers with different dopings. (c) Type-II excitons in a CDQW. When a bias is applied along the growth direction the type-II inter-well exciton has the lowest energy. (d) In some InGaAs quantum wells the LH is type-II while the HH is type-I.

In doped samples, the alignment of carriers along the interface can modify the potential profile and generate pockets or barriers which can confine the carriers along the interface [244]. These single junction heterostructures are sometimes called type-II QWs.

Type-II excitons can also appear in coupled DQWs (CDQWs) when an electron predominantly localized in one well is bound to a hole localized in the other (Fig. 6.1c). Such inter-well type-II excitons appear most strongly when they are the lowest energy transition in the system. Such an arrangement can be achieved by the application of an external electric field along the growth direction. In this configuration, indirect excitons in high quality (defect free) CDQW samples can exhibit enormous lifetimes because there is very little overlap of the electron and hole wavefunctions and there is consequently a very small transition dipole moment [245, 246]. CDQW type-II excitons (also called spatially indirect excitons) have been used for a variety of fundamental experiments, including coherent in plane transport and in pursuit of Bose-Einstein condensation of excitons [247–250].

A third sort of type-II exciton (which is the type that we will be considering in this chapter) can arise in strained $In_xGa_{1-x}As$ QWs. For low indium content ($x<0.2$) the LHs are confined in the GaAs barrier rather than the $In_xGa_{1-x}As$ wells in a staggered gap configuration(as in Fig. 6.1d). What makes this system different than the typical type-II heterostructure is that the heavy-hole excitons are still type-I, so both type-I and type-II excitons can coexist simultaneously.

Type-II LH excitons were first considered in the 1980's by Marzin et al [169] and Pan et al [251], who recognized that strain induced splitting of the heavy-hole (HH) and LH bands could cause the LH valence band to shift below the GaAs valence

band. The nature of these states (i.e. type-II or type-I) was at first contentious [252–254]. The arguments for the type-II configuration relied on the results of wavefunction calculations which in turn relied on the band offset (QC) which was then (and still is now) not precisely known for $In_xGa_{1-x}As/GaAs$ systems. This controversy was settled by Moran et al [255], who presented direct experimental evidence confirming the type-II nature of the LH exciton in a $In_{0.11}Ga_{0.89}As/GaAs$ DQW. They showed that when the DQW is biased, the LH exciton transition energy is increased beyond that of the barrier exciton, confirming that it involves a carrier outside the QW. The identification of the LH transition was confirmed by polarization dependent photoluminescence spectroscopy. Type-II LH excitons were the subject of some fundamental interest (for instance, due to the tunability from type-I to type-II behaviour) into the 1990's and 2000's [256–259], though no applications for this phenomenon appeared.

More recently, it was suggested that the quantum beats between type-I HH excitons and the type-II LH excitons could be used to generate terahertz (THz) radiation [184]. It has been previously shown that coherent, tunable THz could be generated by coherent superpositions of HH and LH excitons in single uncoupled QWs which could be enhanced and tuned by applying an electric field along the growth direction [260]. It was also shown that the amplitude of the THz field is proportional to the distance over which the charges oscillate while in the coherent superposition [260]. As a coherent superposition evolves, it oscillates between each of the associated states with a frequency equal to the energy separation. For a coherent superposition of type-I HH excitons and type-II LH excitons this would constitute the hole 'hopping' into and out of the well, increasing the average spatial separation of the charges, which would in turn amplify the THz emission. Conversely, the same effect could be used to optically or electrically detect THz fields. Work by Kojima et al in 2012 [184] showed strong quantum beats of the type-I and type-II excitons using time resolved reflection pump-probe spectroscopy. However, as discussed previously, quantum beats in pump probe do not necessarily indicate coherent superpositions of excitons are excited as there are many pathways (including signals generated by many-body interactions) that can lead to the detection of oscillations.

In this chapter, we also present unambiguous evidence of coherent superpositions of type-I and type-II excitons, in two different samples, through the appearance of strong CPs away from $E_2=0$ in 3D spectra. In addition to the fundamental interest in better understanding the exciton dynamics (in which these type-II LH excitons clearly play a role) this strong long-lived coherent coupling shows that this arrangement is also promising for THz generation and detection.

We find a rich landscape of 'dark' states that couple to both the QW direct excitons and the barrier excitons. We also find that the barrier-direct exciton coupling is weak compared with their mutual coupling to the dark states. The presence of these additional states and the strong coupling both inside and outside the QW suggests

that there is more to the story of barrier to QW exciton interactions than a simple three level system. The following sections will describe these various excitonic states, how they are detected, and how the different detected signals are identified.

6.2 Sample and wavefunction calculations

Two InGaAs GaAs DQWs are studied in this chapter, and are given the labels sample A and sample B. Sample B is the same sample that was studied in Section 4.4, Chapter 5 and in Ref. [54], which has $In_{0.05}Ga_{0.95}As$ QWs and GaAs Barriers. The narrow well is 8 nm thick, the wide well is 10 nm thick and the barrier is 10 nm thick. Sample A is identical to sample B except that the barrier between the wells is 30 nm thick. Both samples are grown on (100) GaAs substrates. While both of these samples have been studies previously, the previous experiments have focused specifically on the lowest energy bright excitonic states, and (excepting the results presented in Chapter 5), broadband 2D spectroscopy simultaneously exciting the barrier, QW excitons and the dark states at intermediate energies has not been performed.

We first perform wave-function calculations for both InGaAs DQW samples. The goal of these calculations is not a precise determination of transition energies, but rather a qualitative exploration of what transitions we might see in these samples and a justification for peak assignments of the αX and βX type excitons.

The steady-state wavefunctions and associated energy levels are calculated by solving the 1D time-independent Schrödinger equation for the DQW structures using the Numerov/shooting method described in Appendix A3. Excitonic transition energies can then be calculated based on the energy separation of the hole and electron wavefunctions less the exciton binding energy. The main material parameters that are used to determine the energy levels are the GaAs bandgap (E_g^2), InGaAs bandgap (E_g^1), and the GaAs/InGaAs band offset (QC), electron and hole effective mass (m_e, m_{hh}, m_{lh}) and the QW exciton binding energy which varies by exciton transition (E_{BE}). The QW and barrier widths are used along with the material parameters to construct the double-well potential.

The calculated transition energies are very dependent on the degree of carrier confinement, so using the correct well-width to define the potential is crucial for accurate results. For large barrier widths the transition energies are nearly independent of barrier width, as the two QWs largely behave as separate, non-interacting single QWs. For small barrier widths (DQW sample B for example), penetration of the wavefunctions through the central barrier leads to an increased splitting of some of the transition energies (e.g. E_1 and E_2). The well and barrier widths were not directly measured, so we must assume that they are close to the nominal values.

The accuracy of the calculated transition energy also relies on the accuracy of the material parameters. Most of the pertinent material parameters are precisely

		$In_{0.05}Ga_{0.95}As$	GaAs
m_e^*	$(\cdot m_0)$	0.023	0.067
m_h^*	$(\cdot m_0)$	0.505	0.510
m_l^*	$(\cdot m_0)$	0.079	0.082
E_{g0}^1	(eV)	1.441	
E_g^2	(eV)		1.510
a_0	Å	5.67	5.65
C11	(GPa)	1202	1221
C12	(GPa)	560	566
dE_g/dp	$\cdot 10^{-6}$eV$\cdot$cm^{-2}/kg	11.4	11.5
b	(eV)	-1.99	-2
Δ_{SO}	(eV)	0.343	0.340

Table 6.1: InGaAs and GaAs parameters used in the wavefunction calculation. The E_g^1 is calculated including strain according to the method described in Ref. [170]. Material parameters are sourced from Refs. [170, 261].

known for GaAs, but some are not for strained $In_xGa_{1-x}As$, particularly in an indium concentration dependent form. Parameters which are not available in the concentration dependent form are instead typically interpolated linearly from the binaries (InAs and GaAs in this case) [170, 258, 261]. There are some parameters however, which cannot be interpolated. For example, $In_xGa_{1-x}As$ band offset (QC) for x = 0.05 has been reported to be from 0.46 all the way up to 0.75 [262–265]. It has been suggested that QC is sample dependent [253, 262], linearly dependent on indium content [266], has a more complicated dependence [267] or even that QC is independent of indium content [172, 263, 268, 269]. Taken together, most of these values tend to center around QC=0.6, including a recent review [261].

E_g^1 (the InGaAs bandgap) depends not only on the concentration of indium, but also what method and which material parameters (elastic constants and bandgap pressure dependence) are used when calculating strain induced shifts [170, 261]. Finally, though MBE grown samples have very precisely controllable thicknesses and stoichiometry, the resulting heterostructure may not perfectly match the nominal values. Well width variation of only a few monolayers, and indium variation of less than 0.5% will lead to energy shifts of several meV. The material parameters used in these calculations are shown in Table 6.1. E_g^1 for the strained InGaAs layer is calculated using the method described in Ref. [170].

This large number of input parameters which are not precisely known, make a multi-variate fit imprudent as it would likely produce unreliable results. Instead, we perform calculations across the range of reasonable values for indium content and QC, and then do a trial and error fit to determine the range of possible conduction and valence band bound states. The goal of these calculations is to determine what

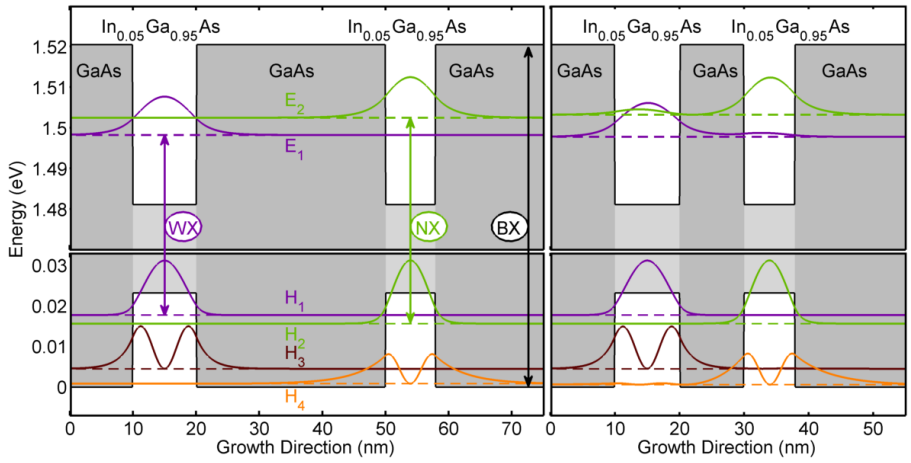

(a) Sample A (30 nm Barrier) (b) Sample B (10 nm Barrier)

Figure 6.2: Typical wavefunction calculated by solving the 1D Schrodinger equation for a the 1D potential shown. Sample A (a) and B (b) have similar solutions, but hybridization of the wavefunction leads to increased splitting of the E_1 and E_2 conduction band levels and H_3 and H_4 valence band, and additional penetration through the barrier.

types of exciton transitions might appear in this sample, and to justify the βX and αX peak assignments in the following experimental results sections.

6.2.1 *Exciton transitions in the InGaAs DQWs*

The specific transition energies shift across the parameter space, but the resulting wavefunctions remain qualitatively similar. Figure 6.2 shows a typical set of wavefunctions calculated for sample A (Fig. 6.2a) and B (Fig. 6.2b) using the the parameters shown in Table 6.1. There are a total of two bound conduction band wavefunctions (labelled E_1 and E_2) and four bound valence band wavefunctions, which correspond to the HH ($m_j = \pm\frac{3}{2}$) valence band (labelled H_1,H_2,H_3, and H_4).

The lattice constants of GaAs and InGaAs are not the same, which in $In_xGa_{1-x}As$/GaAs QWs introduces strain in the InGaAs layer which increases with x (indium content). For large indium content (x>0.2) relaxation of the strain causes dislocations in the InGaAs crystal. Thin layers in the low indium range (x<0.2), create an elastic deformation of the InGaAs layer with no lattice dislocations due to relaxation. This deformation can be separated into a two effects - a hydro-static component that results from compressive strain of the InGaAs layer in the lateral direction, and a uniaxial component due to tensile strain in the growth direction. The hydrostatic component produces a uniform shift of all of the valence bands together, while the uniaxial component reduces the symmetry of the crystal structure, thereby lifting the degeneracy of the HH and LH valence bands. The HH is shifted up (decreasing the HH-E_1/E_2 bandgap) while the LH is shifted down (increasing the LH-E_1/E_2 bandgap). When x<0.2, the InGaAs LH valence band can actually be shifted down below the GaAs valence band [169, 251, 254], leading to an inverted potential

(barriers become wells and wells become barriers). For the DQW samples here, the calculated InGaAs LH valence band is ~ 4 meV below the GaAs valence band in these samples, so the LHs are weakly confined in the barriers (GaAs layers) instead of the wells (InGaAs layers).

In addition to the states in the QW, there are also states in the conduction band (E_b) and valence band (H_b) of the GaAs barriers. Because of the lack of confinement and strain in the barriers, the GaAs LH and HH bands are degenerate, so we won't be able to differentiate between them spectrally.

This total of five[1] valence band states and three conduction band states lead to a total of three direct, parity allowed exciton transitions (shown in Fig. 6.3a). These include the two lowest energy transitions: H_1-E_1 and H_2-E_2 which we will call WX and NX because they are localized mostly to the wide-well and narrow-well respectively. As discussed in the previous chapter, there is some hybridization of the conduction band wavefunctions in Sample B. H_1 and H_2, however, are very much localized to one well or the other, so the resulting excitons are also expected to be mostly localized. The third and final direct parity allowed transition is the bulk GaAs exciton in the barrier H_b-E_b.

There are also two spatially direct, but parity forbidden transitions, one in each well: H_3-E_1 and H_4-E_2 (which are given the labels αX_1 and αX_2, respectively, and shown in Fig. 6.3b). Though they are optically forbidden, they may be accessed by other, non-radiative processes. Also, if the parity of the wavefunctions is not pure, they may become weakly allowed. These types of forbidden transitions have been detected in InGaAs QWs previously [251, 270–275].

If we now broaden our view to include spatially indirect excitons, there are several more to consider: four inter-well spatially indirect excitons (H_1-E_2, H_2-E_1, H_3-E_2, and H_4-E_1, shown in Fig. 6.3c) two excitons involving a hole in the barrier and an electron in the QW (H_b-E_1, and H_b-E_2, which will be given the labels βX_1 and βX_2[2], and are shown in Fig. 6.3d), and four excitons which involve a hole in the QW and an electron in the barrier (H_3-E_b,H_4-E_b,H_1-E_b,H_2-E_b, which will be given the labels βX_3-βX_6, respectively, and are shown in Fig. 6.3d). The four lowest energy barrier-QW exciton transitions ($\beta X_{1,2,5,6}$) have transition energies between 1.490 eV and 1.505 eV, though the ordering changes depending on the material parameters used in the wavefunction calculations. The final two ($\beta X_{3,4}$) have transition energies between 1.510 eV and 1.515 eV. It should be noted, that each of these βX could form along the inner or outer barrier of the QW, and from the experiments detailed here there is no way to unambiguously tell one from the other.

1 There are actually six, but two of the GaAs valence bands (the GaAs HH band and the GaAs LH band) are degenerate and experimentally indistinguishable.

2 H_b represents both the HHs and LHs in GaAs, which are indistinguishable here. For now, the $\beta X_{1,2}$ label are used to encompass both valence band states, though we expect most of the experimental signals involving H_b are the LH due to its confinement outside the QW.

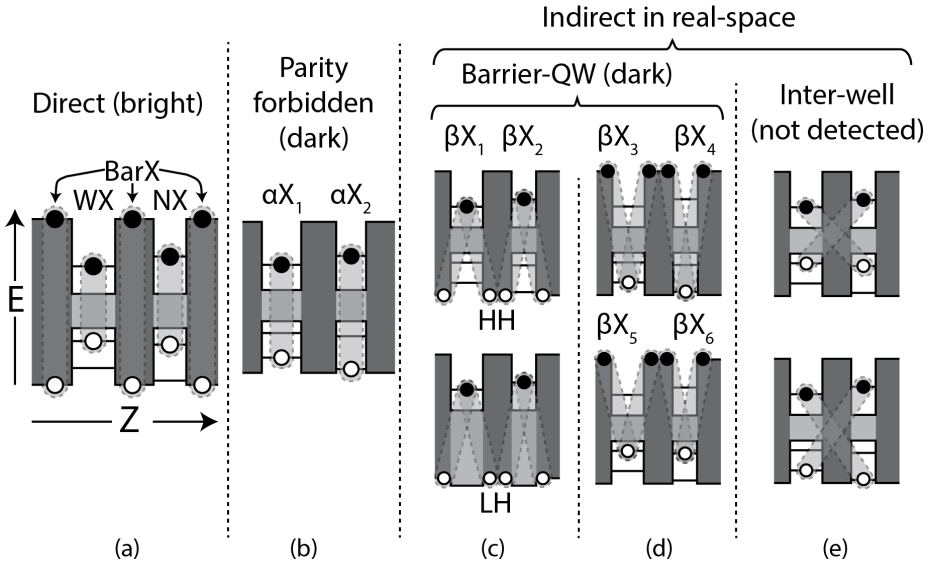

Figure 6.3: Excitons in the DQW samples studied in this chapter can be devided into three categories: direct bright excitons, direct dark parity forbidden excitons and indirect type-II like excitons where one carrier is localized predominately in the barrier and the other in the QW. The top cartoon shows what the exciton configuration looks like in the potential surface as a function of the growth direction. The lower cartoon shows what the configuration might look like in real space.

The following results will show that we detect $\alpha X_{1,2}$ and $\beta X_{1,2,3,4,6}$ in sample A and α_1 and $\beta_{1,2,6}$ in sample B, but do not detect the any of the inter-well spatially indirect excitons (H_1-E_2, H_2-E_1, H_3-E_2, and H_4-E_1) in either sample.

6.2.2 *Variation of the calculated exciton transition energies*

To identify the experimentally detected signals, we calculate transition energies using material constants across the reasonable parts of the parameter-space. We then determine the set of parameters most consistent with the experimental results. Calculated transition energies for both samples are presented in Fig. 6.4 as a function of QC as it is the most important parameter for predicting the order of βX type transitions, and is also the least well defined. Other parameters such as the $In_xGa_{1-x}As$ band gap (E_g^1) and the well widths shift most of the transition energies in the same direction, but changing QC moves conduction band type βX (e.g. E_1-H_b) and valence band type βX (e.g. E_b-H_1) transitions in opposite directions. The dashed lines denote the transition energies that correspond to signals detected in the various PLE and CMDS experiments presented in the following sections.

The clearest spectral markers to use as constraints in the calculations are the WX and NX transition energies. To get the appropriate energy separation, a slight modification of the nominal narrow well width is made (7.85 nm instead of 8 nm). This discrepancy is within the precision of the MBE machine used to grow the samples (and less than a single unit cell of $In_xGa_{1-x}As$ which is ~0.6 nm). Changing QC also changes the WX and NX transitions slightly, which we compensate for by adjusting

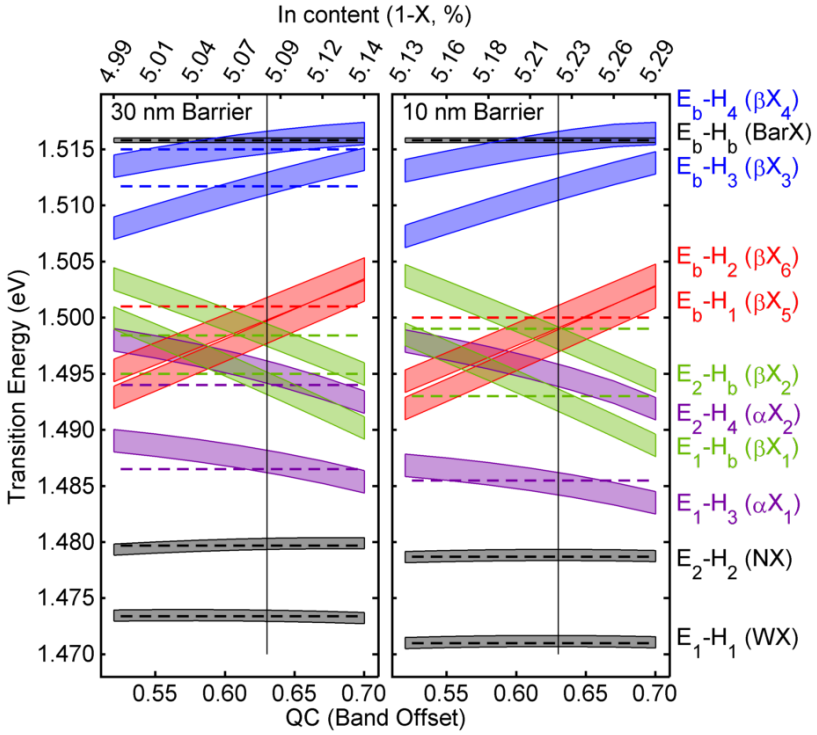

Figure 6.4: Transition energies of WX NX βX_{1-6} and αX_{1-2} as a function of the band offset (QC) for (a) sample A (30 nm barrier) and sample B (10 nm barrier). The wavefunctions are calculated by solving the Schrödinger equation for the QW potential using the Numerov method, and the width of the bars indicates the range of reasonable binding energies. The experimentally measured peak positions (dashed lines) line up with the calculated barrier/QW exciton energies, for most transitions in both samples for QC = 0.63 (vertical line).

the indium content (and hence E_g^1). The resulting variation in indium content (5.2% instead of the nominal 5%) is also within reasonable ranges for the MBE machine.

The binding energy (E_{BE}) for WX and NX was extracted from the PLE data from sample A (Fig. 6.5) by measuring the separation of the free carrier continuum from the exciton resonance. It was found to be 6.5±1 meV which is consistent with values found in the literature, which are typically around 7-8 meV [169, 267]. Though we are unable to experimentally measure the binding energy for sample B, we assume that it will be approximately the same as in sample A.

The binding energy of αX and βX transitions cannot be extracted from the PLE data for either sample, and there is little data in the literature on type-II excitons [258]. We assume that the βX binding energy would be lower than NX and WX, due to the delocalization and reduced confinement of the exciton. Intuitively, we might guess that the binding energy of the bulk GaAs 3D exciton might be a good lower bound on (E_{BE}), but calculations by Piao et al [258] showed that the binding energy could actually be even lower than that - down to ~3 meV.

The holes in $\alpha X_{1,2}$ (H_3 and H_4) are less confined than the holes in WX and NX (H_1 and H_2). In addition, the odd parity of $H_{3,4}$ means that the average displacement of the hole from its center of mass is larger than for $H_{1,2}$, which have even parity. These

two things (odd parity and reduced confinement) both lead to a slight increase in the average inter-particle separation (exciton Bohr radius). Since binding energy is inversely proportional to the exciton Bohr radius, this suggests that αX have a slightly lower binding energy than WX/NX. We expect the binding energy to still be larger than that of the bulk GaAs exciton, since the electron and hole are overlapped and both confined. The precise binding energy could be calculated based on the wavefunctions, but that is beyond the scope of this work.

To account for the indefinite binding energies, all of the calculated transition energies in Fig. 6.4 are plotted as bars with a width which indicates the range of reasonable binding energies (3-6 meV for βX, 5-6.5 meV for αX , 6-7 meV for NX and WX and 4-5 meV for BarX).

The calculations for the two samples use the same material and structural parameters, with the only exception being the indium content, which is slightly higher in sample B (as shown on the top axis). The calculated and experimentally detected (dashed lines) transition energies show good agreement around QC = 0.63, which is near the center of the range of previously reported values of QC for InGaAs/GaAs QWs with low indium content. It is encouraging that the calculations accurately capture the increased WX and NX energy difference due to increased coupling of E_1 and E_2 in sample B. The increased splitting of E_1-H_b and E_2-H_b is also reproduced.

It should be noted that these calculations do not take into account strain induced electric fields or permeation of indium across the GaAs/InGaAs interface - both of which could perturb the potential profile and shift the calculated energy levels. However, we expect that the changes would not be large enough to lead to different peak assignments. Also, the precise values of well width and indium content are not necessarily captured here, as they both can be adjusted interchangeably to get nearly the same set of transition energies. The constants used to calculate the strain induced band shifts could also account for the same variations in transition energy. However, the calculated levels are most sensitive to QC, particularly in the energetic ordering of the transitions. The changes induced by the well width, indium content and strain constants shift all of the transitions in the same way, whereas QC shifts the valence band and conduction band in opposite directions.

6.2.3 *Wavefunction overlap*

The relative magnitude of the transition dipole moment of the excitons (d_{n_e,n_h}) can be estimated by calculating the overlap of its constituent electron and hole wavefunctions ($\psi^e_{n_e}$ and $\psi^h_{n_h}$ respectively).

$$d_{n_e,n_h} \propto \int \psi^{h*}_{n_h}(z)\psi^e_{n_e}(z)\delta z \tag{6.2}$$

	H_1	H_2	H_3	H_4
E_1	0.9043	0.0060	0.0001	0.0170
	0.8688	**0.2534**	**0.0161**	**0.0636**
E_2	0.0095	0.8895	0.0050	0.0019
	0.2769	**0.8562**	**0.0819**	**0.0866**

Table 6.2: Wavefunction overlap integrals for all the QW wavefunctions in sample A (black) and sample B (red). Wavefunctions calculated using optimum QC and InGaAs content taken from Fig. 6.4.

Carrier/Exciton	DQW A	DQW B
$E_1/\beta X_1$	0.22	0.24
$E_2/\beta X_2$	0.33	0.28
$H_1/\beta X_5$	0.06	0.05
$H_2/\beta X_6$	0.09	0.09
$H_3/\beta X_3$	0.37	0.35
$H_4/\beta X_4$	0.73	0.67

Table 6.3: Probability of finding an electron or hole in the barrier for all calculated wavefunctions in both samples. Wavefunctions calculated using optimum QC and InGaAs content taken from Fig. 6.4.

Electron/hole overlaps for all combinations of the four valence and two conduction band wavefunctions are presented in Table 6.2. They are calculated using the wavefunctions that best fit with the experimental transition energies, (at QC = 0.63 in Fig. 6.4). WX and NX have dipole moments near one, indicating nearly perfect overlap of the electron and hole. Surprisingly, the spatially indirect inter-well excitons (E_2-H_3 and E_1-H_4) have higher overlap integrals than the direct but parity forbidden αX_1 and αX_2 (E_1-H_3 and E_2-H_4). This is in contradiction to the experimental results, in which $\alpha X_{1,2}$ (E_1-H_3 and E_2-H_4) are detected but E_2-H_3 and E_1-H_4 are not.

Imperfectly defined parity of the wavefunctions is a plausible explanation for this discrepancy: Parity forbidden excitons involve an electron and a hole which have an overlap integrals of 0, due to the symmetry of their wavefunctions. If one wavefunction has odd parity, and the other even, they will always integrate to zero. A less symmetric potential than the ones that are used for these calculations would increase the $\alpha X_{1,2}$ overlap integrals. Strain induced band bending or a strain induced internal electric field could induce a non-symmetric perturbation of the potential which would reduce the purity of the wavefunction parity. The previously forbidden exciton states could thereby be weakly allowed. The Numerov/shooting method used here to solve the 1D Schrödinger equation can be applied for an arbitrarily defined potential, so wavefunctions could be calculated for asymmetrically perturbed potentials. Realistic incorporation of strain into the DQW potentials could therefore be used to account for the discrepancy between the experiment and calculations (i.e. the detection of parity-forbidden excitons and lack of detection of inter-well spatially indirect excitons). This will be the subject of future work.

Calculating the overlap between barrier electrons (holes) and QW holes (electrons) is less straightforward. If we assume that the barrier electron/hole wavefunctions are mostly localized in the barrier[3], we can estimate the overlap integral of

3 This is not necessarily a good assumption as (for the GaAs HHs) there is nothing preventing the wavefunction of the GaAs electron/hole from extending into the InGaAs layer.

βXs by calculating the percentage of the QW wavefunctions that penetrate into the barrier. Using these pseudo-overlaps, we can compare the relative strengths of the exciton transitions that involve the same carrier in the barrier. For example, βX_1 (E_1 - H_b) can be compared with βX_2 (E_2 - H_b) because they both involve the same hole in the barrier valence band. Similarly, βX_{3-6} (E_b - H_{1-4}) can be compared with one another because they all involve an electron in the barrier conduction band. The wavefunctions of the H_b and E_b are certainly not identical, so $\beta X_{1,2}$ (E_{1-2} - H_b) cannot be directly compared with βX_{3-6} (E_b - H_{1-4}). However, just looking at the amount of the QW wavefunctions that is in the barriers (Table 6.3), we see that the βX excitons that are detected with strong signal in the 2D and 3D spectra are the ones with the highest values in Table 6.3.

6.3 Results from DQW Sample A (30 nm barrier)

6.3.1 *Photoluminescence excitation: Exciton relaxation pathways*

Photoluminescence excitation (PLE) spectroscopy can be used to identify transitions which do not generate efficient photoluminescence (PL), but relax to transitions which do. It can also be used investigate relaxation pathways, by correlating excitation and emission energies. However, it only tells us that there is an allowed relaxation pathway from the state associated with initial excitation to the state associated with the detected emission energies. PLE doesn't tell us anything about the relaxation rate or complete relaxation pathway.

PLE is a good candidate for detecting and identifying the 'dark' states. Both αX and βX have smaller electron/hole wavefunction overlap integrals than NX and WX, so they will have a lower dipole moment and a therefore longer radiative lifetimes. These long radiative lifetimes will then likely be outpaced by relaxation since one of the carriers is already in the well. It is thus expected that these αX or βX states show very weak PL emission (probably below the threshold for detection), but relax efficiently into WX and NX. We therefore expect an increase in emission from NX and WX when αX or βX is selectively excited.

PLE was conducted as described in section 2.6. A narrow sliver of the mode-locked laser bandwidth is used to excite the sample, while monitoring the PL. The photon energy of the excitation beam was scanned from 1.470 eV to 1.525 eV in steps of 0.4 meV using the pulse-shaper. The excitation power of the beam varies along with the laser spectrum from 4.9 μW at 1.516 eV to 27.6 μW at the peak (1.485 eV). The excitation power and spectrum at each point is recorded after each scan. A linear correction is then applied to normalize the PL according to the excitation power. [4]

4 To justify the use of a linear correction, a coarse power dependence of the PLE was conducted (not shown), which shows that the excitation power is low enough to avoid higher order signals.

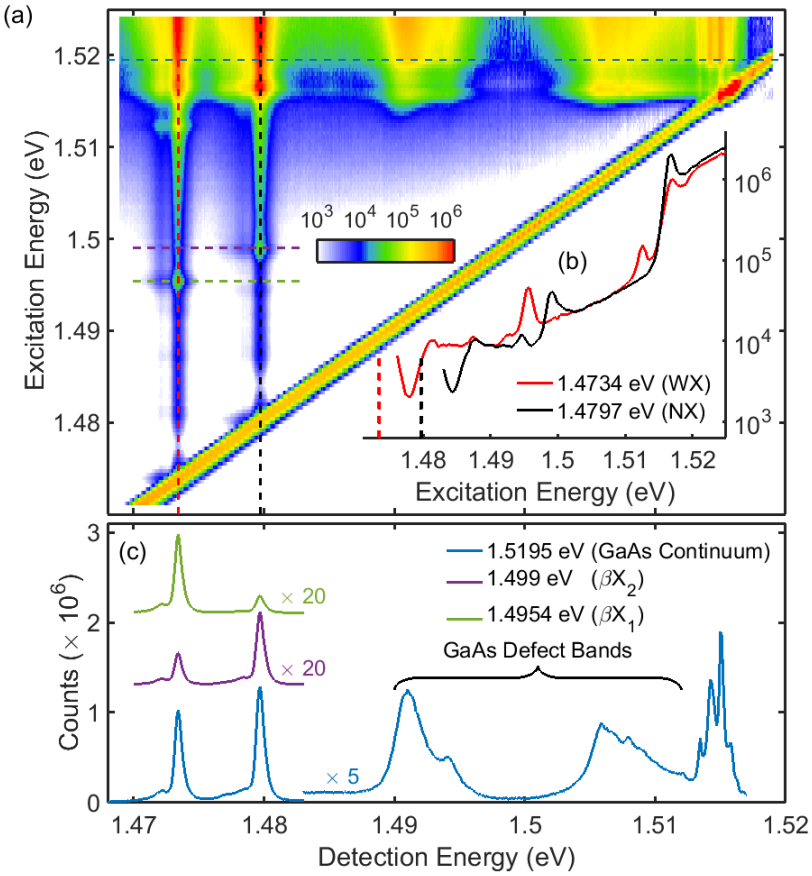

Figure 6.5: PLE on 30 nm barrier DQW. (a) shows the full 2D PLE spectrum which is discussed in detail in the text. Specific slices of the spectrum along the excitation (b) and detection (c) axes are presented as well.

A full 2D[5] PLE spectrum for sample A is shown in Fig. 6.5a. There is a great deal of information in this plot. First, there are two vertically elongated continua along the excitation axis at emission energies of 1.4734 eV and 1.4797 eV, which correspond to emission from WX and NX respectively. At each of these emission energies there are discrete peaks indicating excitation of excitonic features as well as underlying continua elongated along excitation axis, which correspond to the excitation of free-carriers in the QW or (above 1.52 eV) in the GaAs barrier. The excitons and free carriers relax into WX or NX states (depending on which well the original excitation was in) which then recombine radiatively to give us the emission signals at WX and NX transition energies. A detailed discussion of the excitonic features is more easily conducted when the excitation spectra are presented as slices at the WX and NX emission energies, which are shown in Fig. 6.5b.

Working from high to low energy (right to left), we see several peaks. First, there is the GaAs free carrier continuum from the beginning of the scan (1.53 eV) down to about 1.518 eV. This relaxes equally into both WX and NX. After a small dip, there is a distinct exciton resonance at 1.5158 eV (corresponding to the GaAs free

5 This is a linear measurement of PL as a function of the energy of the exciting photon, both measured in the frequency domain. It is fundamentally different from and not to be confused with 2D 1Q, 0Q or 2Q spectra in which the E_1, E_2 and E_{2Q} axes are generated by a Fourier transform of time delay data.

exciton) which relaxes into both QWs, but the emission from NX is nearly 3× larger. Two factors contribute to the enhanced emission from NX when the GaAs exciton is excited. First, the spectral separation of βX_4 and BarX is smaller than the excitation resolution in the experiment, so both features are likely contributing to this excitation peak. Second, the narrow well is closer to the surface of the DQW, so more of the excitation light has been absorbed before it gets to the wide well. Below the GaAs bandgap, there is a continuum which corresponds to the free carriers in each of the respective wells, as well as a few peaks.

At the WX detection energy there are two main peaks at 1.512 eV and 1.495 eV (corresponding to βX_3 and βX_1, respectively), and a weaker peak at 1.486 eV which corresponds to αX_1. There is no peak emitting in WX for excitation at NX, which suggests that there is very little tunneling between the wells. At the NX detection energy, there are two peaks at 1.498 eV and 1.494 eV, which correspond to βX_2 and αX_2. The above βX and αX peak assignments are justified because they appear in roughly the right spectral ranges, and they all relax into the appropriate QWs. Furthermore, there is no relaxation from βX_3, βX_1 or αX_1 (βX_2 or αX_2) into NX (WX) which is consistent with the lack of cross-barrier relaxation from NX to WX.

A complicating factor in conclusively identifying the βX transitions in this sample, is that they appear in spectral ranges where there is also emission from GaAs defects. These defect peaks can be seen in Fig. 6.5a as emission features for excitation above the GaAs bandgap and plotted in Fig. 6.5c which shows emission energy when the GaAs free carrier continuum is excited. The two defect peaks at 1.490 eV and 1.493 eV, as well as the complex structure of defect emission between 1.505 eV and 1.515 eV are well known carbon defects which appear in GaAs epilayers [128, 168]. Control experiments have shown that the concentration of defects (both relative and absolute) changes between MBE machine and even run to run. For this reason, defect emission cannot always be unambiguously identified or ruled out based on the spectral characteristics alone [233]. This makes it difficult to rule out defect related explanations for the peaks labelled as βX and αX.

That said, the excitation position and line-shape of the βX transitions (which can be seen in 6.5b) are very different from the detected defect peaks. These peaks are shifted to higher energy than the defect emission, and have much narrower lines. Though it is not uncommon to have some spectral separation of absorption and emission lines, a shift of 5 meV or greater is unlikely. These differences suggest that the βX and αX excitation peak cannot be accounted for by defects. A more complete discussion of why these defects can't explain most of the signals detected in the PLE and CMDS spectra is presented later in section 6.5.1.1.

The free-carrier continua (features elongated along the excitation axis with emission in WX and NX), provide further evidence that βX_1 and βX_2 involve a carrier in the barrier. The WX and NX continua are flat as a function of excitation energy below the βX_1 and βX_2 resonances (respectively). This is expected for free-carrier absorption in a QW, since the density of states is a step like function (as shown

in Fig. 3.6 and described in Section 3.1.6). Above the $\beta X_{1,2}$ resonances, the absorption begins to increase sharply with increasing photon energy. We expect this absorption dependence on photon energy for bulk semiconductors, which have a density of states which increases with photon energy. The photon energy is still well below the band gap so one of the generated carriers (the electron in this case) is still in the QW, while the other (the hole) is in the barrier.

6.3.2 *1Q/2D results*

Similar to PLE, 2D spectroscopy can be used to investigate 'dark' states through coupling to bright states. Unlike PLE, however, 2D spectroscopy can actually drive emission from these dark states in the form of diagonal-peaks (DPs) or above diagonal CPs. More importantly, using 2D spectroscopy, the femtosecond and picosecond dynamics of the excitons can be explored, and interaction pathways can be identified.

We first perform 2D 1Q spectroscopy using three identical broadband pulses, with spectra that cover the entire transition landscape detailed in section 6.2. The excitation density is 4.5×10^{10} photons$\times$cm^{-2} per pulse, and all the beams are collinearly polarized. The waiting time (t_2) is set to 0 fs, and t_1 is scanned from 0 to 5000 fs in 25 fs steps.[6]

A 2D spectrum is presented in Fig. 6.6. It is first important to note the logarithmic colour scale, spanning three orders of magnitude, which reveals the CPs even in the presence of much stronger DPs. This plot contains a great deal of information which will be dissected in the following paragraphs. There are three DPs corresponding to WX, NX and BarX, two much lower amplitude DPs corresponding to $\beta X_{1,2}$, and at least 18 CPs corresponding to interactions between WX, NX, BarX and the αX, and βX states.

We will first discuss the shape of the main three DPs. The WX and NX DPs are nearly resolution limited along the E_3 (emission) axis. They have oval peak-shapes with no elongation along the diagonal, which indicates that they have very little inhomogeneous broadening. The significant broadening of both the WX and NX DPs along E_1 (roughly twice the width of the same peak along E_3) is an artifact related to the scan range limitations of this particular experimental setup. Previous experiments on this sample using delay stage based 2D spectroscopy have shown that the width along E_1 is much lower than we report here, and that these states do actually contain some inhomogeneous broadening which cannot be resolved with this experiment [54]. The BarX DP has some complex structure in its emission, which can also be seen in the PLE emission. This structure is qualitatively consistent with emission from shallow defects which commonly occur in GaAs epilayers. The largest emission feature near the GaAs resonance in the 1Q spectrum is observed

6 The pertinent experimental parameters for this measurement (and the rest of the measurements in this chapter) can be found in Table A1.3 in Appendix A1

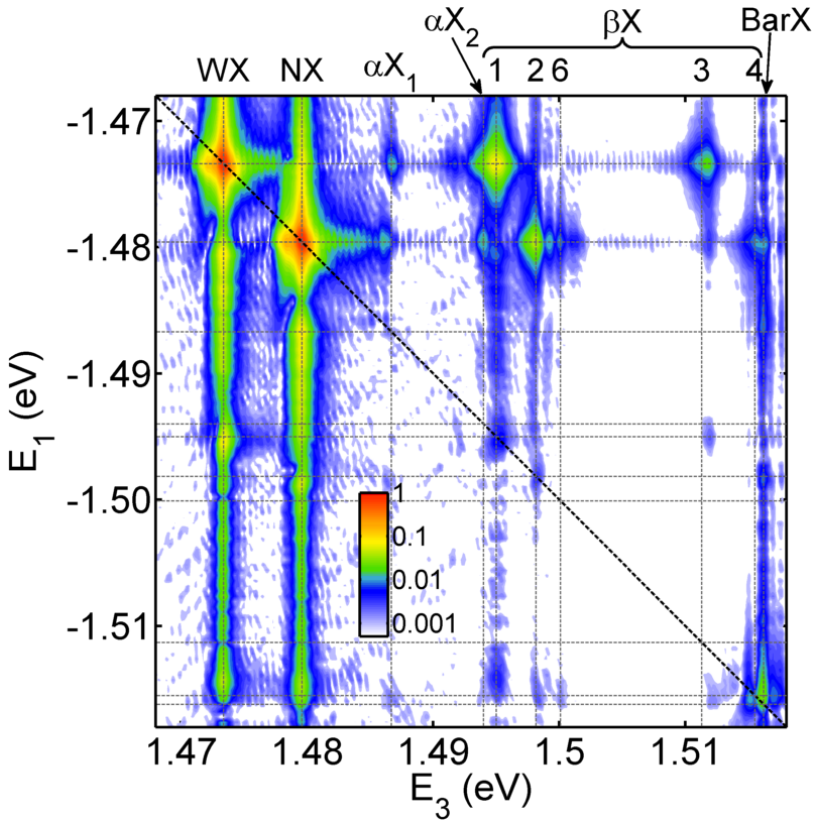

Figure 6.6: A typical 1Q 2D spectrum for sample A showing three strong DPs (WX, NX and BarX) as well as a wide variety of CPs indicating coupling of NX, WX and BarX to several βX and both αX states. Full analysis of the spectrum provided in the text. Plotted on a logarithmic colour scale spanning three orders of magnitude.

at the energy where we expect the GaAs free exciton. Along the E_1 axis, the BarX DP is again much broader than it's emission width due to the scan range limitations of the experimental apparatus. It is not immediately clear what the 'actual' E_1 line-shape is for this peak as the excitation spectrum used in previous experiments on this sample did not cover this transition. Like WX and NX, the βX_1 and βX_2 DPs also have oval line-shapes with narrow emission and somewhat broadened absorption.

Our attention now turns to the CPs. First, we see emission and absorption CPs coupling WX and NX to the same three βX transitions that appeared in the PLE data: βX_1 at 1.495 eV, βX_2 at 1.498 eV and βX_3 at 1.512 eV. As in the PLE data, the βX_1 and βX_3 are coupled only to WX while βX_2 is coupled only to NX. βX_4 can now be resolved as an additional peak emitting just below BarX, and there is a weak peak at 1.500 eV which might be βX_6. As expected based on the descriptions, βX_4 and βX_6 only show emission in NX. The presence of below diagonal CPs with E_1 = BarX indicate that the barrier is coupled to WX, NX, and βX_{1-4}.

Finally, we see CPs absorbing in WX (NX) with emission at 1.486 eV (1.494 eV) which is where we expect to find the parity forbidden αX_1 (αX_2). Like in the PLE, there also appears to be a CP coupling αX_1 to NX, but if we look closely we can see that it is actually red shifted by about 1 meV, and has somewhat broader emission. This feature occurs at low energy edge of the free-carrier continuum in the NW,

and only couples to NX. We therefore attribute this peak to free-carriers with no momentum. We do not typically expect to see emission from free-carriers, because they dephase quickly and efficiently form excitons.

The 1Q results are also consistent with αX and βX being 'dark' transitions. We see DPs for two of them, but they are two orders of magnitude weaker than the bright NX and WX DPs. The fact that the CPs are much stronger than the DPs is consistent with strong coupling of the 'dark' states to NX and WX. To illustrate why we expect this, we consider two states A and B with transition dipole moments $\mu_{1A} \ll \mu_{1B}$. The DPs for A and B scale with μ_A^4 and μ_B^4 respectively, while the CPs scale with $J \times \mu_{1A}^2 \times \mu 1B^2$ where J is a coupling parameter. In this way, the state B actually amplifies signals from state A in the form of CPs as long as J is not tiny (i.e. strong coupling). For example, if $\mu_{1B} = 10 \times \mu_{1A}$, and $J = 0.5$ the resulting AB CP is $50\times$ larger amplitude than the DP for state A.

Like the PLE results, the 1Q results and peak assignments are consistent with what we expect for the β_X and α_X states. They are coupled to the right transitions, there is no cross-barrier coupling and the coupling (as expected) appears to be quite strong. The pathway(s) leading to these CPs are still unclear. These CPs could be generated by GSB, ESA, coherent superpositions or population transfer pathways. The following section presents 0Q and 2Q spectra with the aim of trying determining what coherent coupling pathways are present.

6.3.3 *0Q/2D and 2Q/2D results*

Though the pathways are different, 2Q 2D spectroscopy provides an alternative method to detect excitonic coupling and is therefore a convenient way to expand upon some of the 1Q results. In the 2Q pulse ordering (in which the conjugate pulse, k_1 arrives last), signals whose phase evolves at twice the optical frequency of the laser during time t_{2Q} are detected. 2Q signals can either result from excitation of a one-exciton state with a transition energy equal to twice the laser photon energy or a two-exciton state consisting of two excitons each with a transition energy equal to one laser photon. In this DQW sample, there are no single exciton states at $\sim 2\times$ the energies of the single exciton signals, so all the signal in the 2Q pulse ordering correspond to excitation of two-exciton states[7]. CPs only appear when the first two pulses excite different transitions, and thereby excite a mixed two-quantum coherence. Such a 2Q CP can therefore only appear if the two excitons appear in the same quantum system, meaning that the system can be described as four level system instead of two separate two level systems. Presence of CPs therefore indicates the coherent nature of the coupling [54, 276].

A 2Q/2D spectrum for sample A is presented in Fig. 6.7a. t_1 was set to 0 fs and t_{2Q} was scanned from 0 to 2500 fs, with the same polarization and excitation den-

7 Biexciton signals can also be detected, but they are spectrally separated from the two-exciton signals.

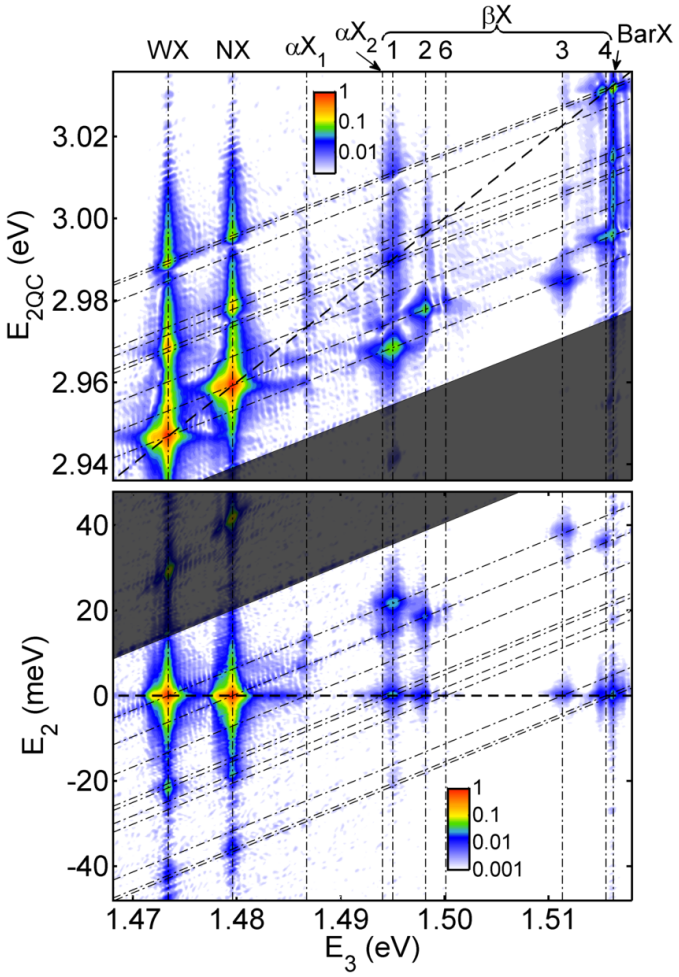

Figure 6.7: 2D spectra in 2Q (a) and 0Q (b) pulse orderings show that there is coherent coupling between the QWs, βX, αX and barrier excitons, and qualitatively. These spectra show coupling between the same sets of transitions which appear in the 1Q spectrum. The shaded regions indicate spectral areas in which artefacts appear due to reflections of real signals across the E=0 line in the rotating frame.

sity as was used in the 1Q spectrum. 2Q CPs involving two-exciton coherences are characterized by E_{2Q} that is the sum of the coupled transitions, and can therefore be identified as peaks which appear at E_{2Q} halfway between the two associated 2Q DPs. In addition to the $E_2=2E_3$ dashed line, the dash-dotted lines are added as a guide to identify the transitions associated with the CPs. CPs for a transition with energy ϵ include all peaks which share the same emission energy (vertical dash-dotted lines), and peaks along the $E_{2Q} = E_3 + \epsilon$ line (angled dashed-dotted lines).

This spectrum clearly shows CPs associated with the same pairs of transitions as the 1Q spectrum. We see (above and below diagonal) interactions between WX (NX) and βX_1, βX_3 and αX_1 (βX_2, βX_4 and αX_2). There is also perhaps a very weak peak below the βX_3 DP at $E_{2Q}= \beta X_3 + \beta X_1$. As before, there are only weak DPs for βX_1 and βX_2, and no cross-barrier coupling. We also see clear peaks related to the interaction of WX and NX with BarX, which are much more well resolved and intense than the interactions we saw in the 1Q pulse ordering.

As demonstrated in the previous chapter, 0Q scans can be used to differentiate between coherence and population pathways in the rephasing pulse ordering [50]. A 0Q scan was conducted in which t_1 was set to 0 fs and t_2 was scanned from 0 fs to 5000 fs, with the same excitation spectrum and excitation density as the 1Q scans. A typical 2D 0Q scan for this sample is presented in Fig. 6.7b. The population pathways appear along the E_2=0 line. There are population peaks for each of the transition energies in which we see significant emission in the 1Q spectrum, but the WX and NX peaks dominate.

A wide range of above diagonal coherence CPs appear as well. Coherence CPs for a transition with energy ϵ include all peaks which share the same emission energy (vertical dashed lines), and peaks along the $E_2 = E_3 - \epsilon$ line (angled dashed lines). Along the WX mixing line (the angled line which crosses $E_2 = 0$ at E_3 =WX) there are a total of three clearly defined CPs at $E_3 = \beta X_1$, βX_3, and a slightly weaker one at αX_1. These CPs represent the same sets of transitions we see coupled to WX in the 1Q and 2Q scans. Similarly, there are peaks along the NX mixing line at $E_3 = \beta X_2$, βX_4 and a very weak peak at αX_2.

The only below diagonal CPs which appear, are at WX and NX emission energies. WX to βX_1 and NX to βX_2 peaks are clearly there, but many of the others are either missing or buried in noise from the tails of the E_2=0 peaks. There are broad peaks at the appropriate E_2 energies to indicate coupling of WX and NX to BarX. However, both of these peaks are broad enough that it is not possible to separate βX_4 and BarX.

The regions in both Fig. 6.7a and Fig. 6.7b which are greyed out represent signals that appear either along the carrier frequency line, or on the opposite side, and are therefore taken to be artifacts. Though signals do appear here, they are reflections of real signals across the 0-frequency line in the rotating frame, caused by phase errors in the experiment, scatter and artifacts introduced in data analysis (such as windowing, FFT spectral leakage etc.)

The 0Q and 2Q spectra presented in this section are consistent with the PLE and 1Q results in that all of the same transition combinations that result in CPs in the 1Q spectrum in Fig. 6.6 also produce CPs in the 0Q and 2Q spectra. More importantly, these two spectra also show that there is coherent coupling of the same sets of transitions, and the 0Q results suggest that CP pathways involving coherent superpositions of NX/WX with $\beta X/\alpha X$ are nearly as strong as those involving populations (ESA/GSB).

6.3.4 *3D spectroscopy*

Using 3D electronic spectroscopy, we can more carefully analyse the coherences and CPs detected in the 1Q and 0Q 2D spectra by fully isolating all of the different contributions. Figure 6.8a shows a projection of the 3D spectrum onto the E_1 vs

E_3 plane, which is equivalent to a 1Q/2D spectrum. In Fig. 6.8b, the amplitude of four of the CPs is plotted as a function of t_2. As expected based on the presence of coherence peaks in the 0Q spectrum, clear oscillations can be seen in the phase and amplitude of each of the CPs. The depth of the oscillations (dipping almost to zero) suggest that the CPs are almost equal parts coherence and population pathways for short t_2. A signal made up of purely coherence pathways would lead to oscillations in CP phase but not in amplitude. A signal made up entirely of population pathways would lead to no oscillations (in phase or amplitude).

A superficial analysis of the frequency of the oscillations shows that they roughly match the energy separation of the coupled transitions. A more detailed analysis of these coherence and population signals can be conducted when a Fourier transform is applied along the t_2 axis to generate a full 3D spectrum. A depiction of the resulting 3D spectrum is shown in Fig. 6.8c. As in the previous chapter, the signals included in this spectrum span more than three orders of magnitude. To display all the information together, the different regions are rendered on different isosurface levels. In total, we detect 5 DPs, 13 population CPs and 15 coherence peaks. The full list of amplitudes of the various peaks is displayed in Table 6.4. In addition to well defined excitonic peaks, there are also free-carrier peaks which appear as two continua elongated along E_1 at $(E_2, E_3) = (0, \mathrm{WX})$ & $(0, \mathrm{NX})$ which make identification of some of the population CPs difficult as the CPs cannot be completely separated from the free-carrier continua.

A more useful display of some of this data is provided in Fig. 6.9, which focusses on the E_1 vs E_3 region that is sectioned out in Fig. 6.8a. Fig. 6.9a and 6.9b show slices of the 3D spectrum for signals where the first photon is absorbed in the WX and NX respectively. The red line shows where we expect to see coherences for this particular E_1 energy. The dotted horizontal lines show mixing energies where we expect to see coherences based on the peak locations in the 1Q spectrum. In Fig. 6.2a (6.2b), we detect coherence peaks for (in ascending order) αX_1, βX_1,βX_3 and BarX (αX_2, βX_2,βX_6,βX_4, and BarX). Each of these peaks appears along the red line and has an associated population CP at $E_2 = 0$, which is of comparable amplitude.

We can then plot the E_1 vs E_3 slices at the the E_2 energies in which we see coherence peak. These plots are shown in Fig. 6.9c through 6.9j. An E_1 vs E_3 at $E_2 = 0$ meV is presented in Fig. 6.9k, which shows the population CPs that exist for each of the coherence peaks. 6.9a-k taken together clearly show that the various coherence signals that we see appear at the appropriate E_1, E_3 and E_2 energies to be coherence signals between the direct QW excitons and the βX and αX. The usefulness of 3D spectroscopy in isolating signals can be seen particularly in frames 6.9c-f. The four peaks here are overlapped and not fully isolated in 6.9k. In the other frames they are much more well separated. This is particularly important for the $(E_1,E_3) = (\mathrm{NX},\alpha X_2)$ peak, which partially overlaps the WX free carrier continuum in 6.9k, but is quite isolated in 6.9f. In 6.9j, we see two overlapping coherence peaks $(E_1,E_3) = (\mathrm{NX},\beta X_4)$ and (NX,BarX).

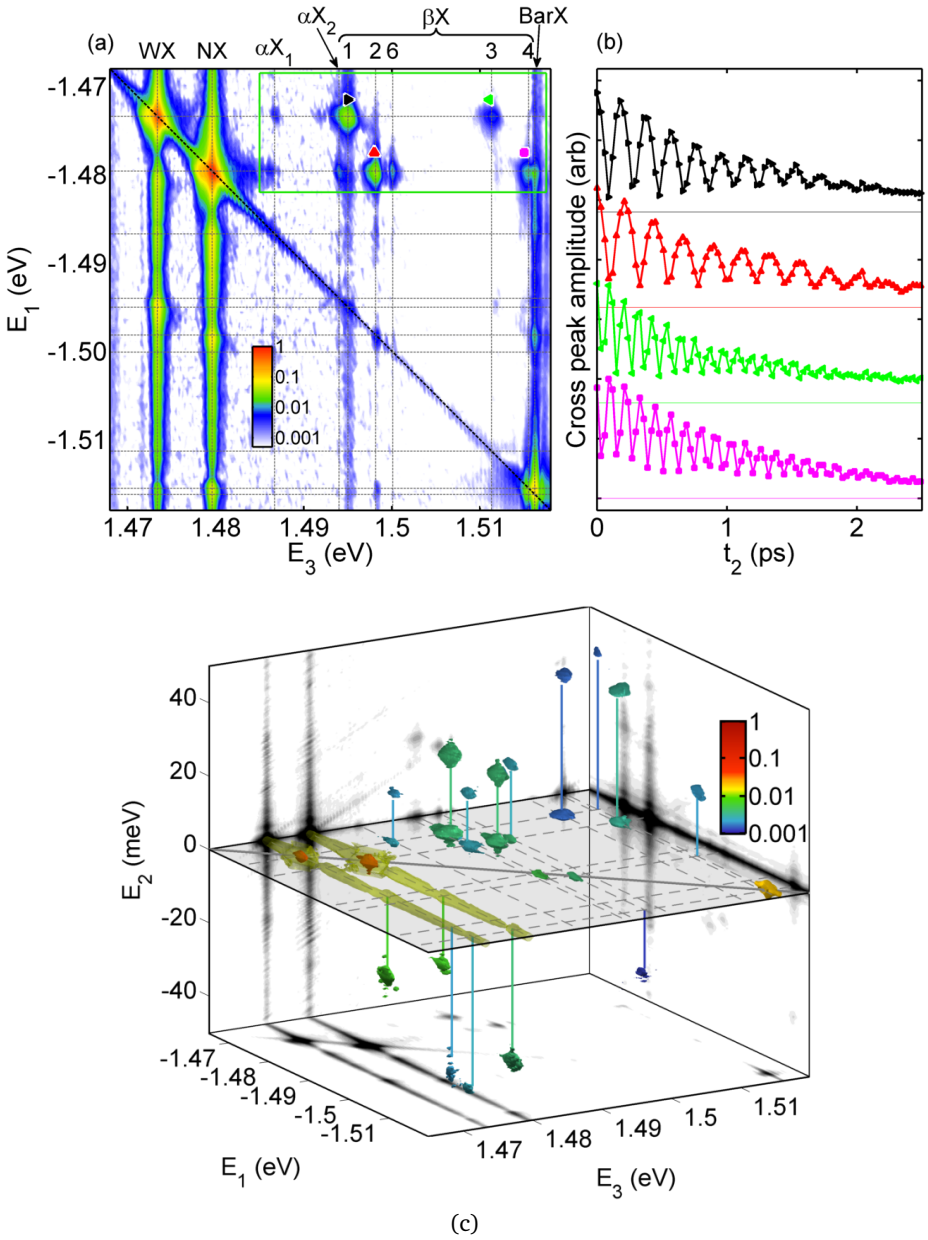

Figure 6.8: (a) shows the 3D spectrum integrated along E_2, which is equivalent to a 1Q spectrum with $t_2=0$. The green square indicates the region with the bulk of the coherence CPs which will be examined in detail in Fig. 6.9. The CPs indicated by the markers are plotted as a function of t_2 in (b), showing clear and significant oscillations (indicating coherent superpositions)of the main four above diagonal CPs. A Fourier transform is applied along t_2 to generate a 3D spectrum. The spectrum has signals spanning several orders of magnitude, so each region is plotted on the isosurface that best suits the signal strength. A wide variety of signals are isolated and studied in detail in the following section.

If we look back at the 3D spectrum in Fig. 6.8b we also observe the below diagonal equivalents of all of the coherence peaks shown in Fig. 6.9 (except the coherences involving αX_1 and αX_2). We also observe coherence peaks for two other combinations of transitions in other areas of the 3D spectrum. Coherences of βX_1 and βX_3 can be seen at both (E_1, E_3) = (βX_1, βX_3) and (E_1, E_3) = (βX_3, βX_1). Similarly, coherences of βX_2 and either βX_4 or BarX can be seen at both (E_1, E_3) = (βX_2, βX_4 or BarX) and (E_1, E_3) = (βX_4 or BarX, βX_2). Whether these peaks

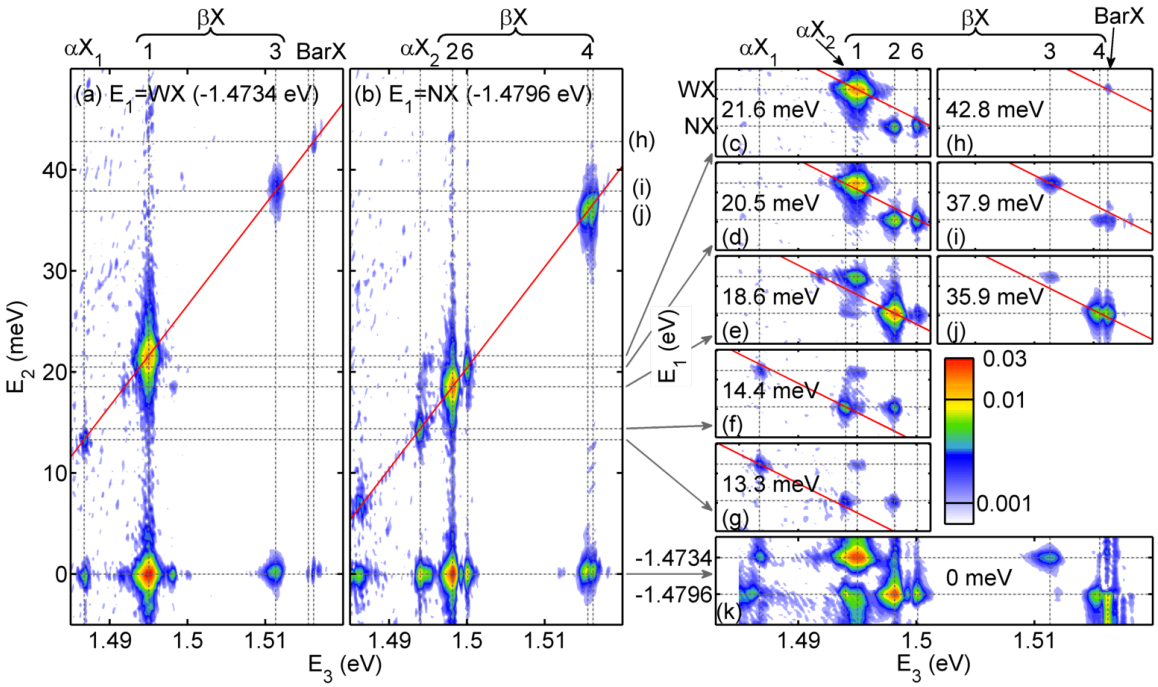

Figure 6.9: Slices of the 3D spectrum (Fig. 6.8) focussing on the region indicated by the green rectangle in Fig. 6.8. (a) and (b) show E_3 vs E_2 slices through the 3D spectrum at E_1 = WX and NX respectively. various population and coherence peaks are resolved. Coherence peaks appear along the red line ($E_2 = E_3 + E_1$). The horizontal dotted lines indicate the regions in which we expect to see coherence CPs based on the transition energies of the 1Q CPs (vertical dotted lines). (c)-(j) show slices of the 3D spectrum at each of these E_2 values, clearly showing that the coherence peaks appear at the expected positions along the red lines ($E_1 = E_2 - E_3$). The colors in all the plot are scaled according to the same logarithmic colorbar, and are normalized according to the largest amplitude peak in the figure.

involve BarX or βX_4 (or if both pairs of coherence peaks are present) cannot be determined due to the spectral overlap of the two. The below diagonal peak appears to be more centred on βX_4 whereas the above diagonal peak appears to be more centred on BarX.

We find in this 3D spectrum (as in all the previous 2D spectra), that the βX signals predominantly only couple to either WX or NX. As before, αX_1, βX_1 and βX_3 couple strongly to WX while αX_2, βX_2, βX_4 and βX_6 couple only to NX. We will look in more detail at some of the peak-shapes in the discussion section.

We now move on to Table 6.4, which presents the amplitudes of all of the peaks resolved in the 3D spectrum. The peak amplitudes are corrected to account for the spectral weight of the excitation spectra using the same method as in the previous chapter (Section 4.3.5). After the correction is applied, BarX is the strongest signal (it was much weaker than NX and WX, but it is also on the tail of the excitation spectrum). With the exception of the above diagonal BarX-NX, all of the CPs appear as pairs of population and coherence peaks. In general, the population and coherence peaks have amplitudes which are of similar orders of magnitude, with the coherence peak typically slightly weaker than the population peak.

E_1 \ E_3	WX	NX	αX_1	αX_2	βX_1	βX_2	βX_6	βX_3	βX_4	BARX
WX	16.8	✗	0.16 **0.1**	✗	1.06 **0.79**	✗	✗	0.94 **0.71**	✗	1.24 **0.59**
NX	✗	13.19	✗	0.13 **0.12**	✗	0.61 **0.56**	0.23 **0.2**	✗	1.22 **1.37**	✗ **1.57**
αX_1	✗	✗	✗	✗	✗	✗	✗	✗	✗	✗
αX_2	✗	✗	✗	✗	✗	✗	✗	✗	✗	✗
βX_1	1.77* **0.69**	✗	✗	✗	0.19	✗	✗	0.21 **0.11**	✗	✗
βX_2	✗	1.48* **0.56**	✗	✗	✗	0.17	✗	✗	✗	2.19 **1.03**
βX_6	✗	✗	✗	✗	✗	✗	✗	✗	✗	✗
βX_3	3.63* **0.75**	✗	✗	✗	0.88 **1.97**	✗	✗	✗	✗	✗
βX_4	✗	7.3* **2.74**	✗	✗	✗	1.26 **0.84**	✗	✗	✗	✗
BarX	8.16* **1.16**	✗	✗	✗	✗	✗	✗	✗	✗	100
(eV)	1.473	1.480	1.487	1.494	1.495	1.498	1.501	1.512	1.515	1.516

Table 6.4: A table listing of the amplitudes of all of the detected DPs, coherence CPs (bold) and population CPs (not bold). All values have been corrected to account for the different spectral weight in the excitation pulses according to the same method developed in section 4.3.5, and are presented as a percentage of the strongest peak (BarX). The *indicates signals which cannot be separated from the E_2=0 free carrier continua, so the values are likely significantly overestimated. The bottom row shows the transition energy that is associated with each transition in sample A.

E_1 \ E_3	WX	NX	αX_1	αX_2	βX_1	βX_2	βX_6	βX_3	βX_4	BarX
WX	61.8	✗	1.0 **0.61**	✗	5.84 **4.34**	✗	✗	1.14 **0.86**	✗	0.84 **0.40**
NX	✗	100	✗	1.08 **1.00**	✗	4.12 **3.79**	1.34 **1.19**	✗	1.25 **1.41**	✗ **1.52**
αX_1	✗	✗	✗	✗	✗	✗	✗	✗	✗	✗
αX_2	✗	✗	✗	✗	✗	✗	✗	✗	✗	✗
βX_1	9.71* **3.79**	✗	✗	✗	1.56	✗	✗	0.37 **0.20**	✗	✗
βX_2	✗	10.07* **3.81**	✗	✗	✗	1.03	✗	✗	✗	1.9 **0.89**
βX_6	✗	✗	✗	✗	✗	✗	✗	✗	✗	✗
βX_3	4.38* **0.91**	✗	✗	✗	1.6 **0.92**	✗	✗	✗	✗	✗
βX_4	✗	7.54* **2.83**	✗	✗	✗	1.17 **0.78**	✗	✗	✗	✗
BarX	5.5* **0.78**	✗	✗	✗	✗	✗	✗	✗	✗	12.4
(eV)	1.473	1.480	1.487	1.494	1.495	1.498	1.501	1.512	1.515	1.516

Table 6.5: Relative peak amplitudes for all population (not bold) and coherence peaks (bold) detected, before correction for spectral variation of the electric field amplitude is applied. The *indicates signals which cannot be separated from the $E_2=0$ free carrier continua, so the values are likely significantly overestimated. The bottom row shows the transition energy that is associated with each transition in sample A.

We can try to characterize the strength of the coupling of the various transitions by comparing peak amplitudes. Each of the DPs is proportional to the transition dipole moment of that transitions (μ_l) to the fourth power, multiplied by the product of the electric fields of the excitation pulses multiplied by the electric field of the LO. If all the pulses are identical, then the electric field amplitude for all four pulses can be written as $\mathbf{E}(\epsilon_n)$, (where $\mathbf{E}$ is the pulse electric field and ϵ_n is the transition energy of transition n) and the resulting signal strength is determined by:

$$A^{(n)} \propto \mathbf{E}(\epsilon_n)^4 \mu_n^4 \tag{6.3}$$

The correction we have applied above has effectively normalized all of the pulse spectra, meaning that for relative comparisons the dependence of the electric field on photon energy can be dropped. The electric field therefore drops out of the relative dipole moment $\widetilde{\mu}_n$:

$$\widetilde{\mu}_n = \frac{\mu_n}{\mu_0} = \left(\frac{\mathbf{E}^4 S_n}{\mathbf{E}^4 S_0}\right)^{1/4} = \left(\frac{S_n}{S_0}\right)^{1/4} \tag{6.4}$$

E_1 \ E_3	WX	NX	βX_1	βX_2	BarX
WX			0.59, **0.44**		0.03, **0.014**
NX				0.41, **0.37**	**0.04**
βX_1	**0.39**				
βX_2		**0.37**			0.53, **0.25**
BarX	**0.03**				

Table 6.6: Coherence ($J^C_{m,n}$ - bold) and population ($J^P_{m,n}$ - not bold) relative coupling strengths of CPs for which both of the associated DPs are detected.

Where μ_0 and S_0 are the dipole moment and spectral amplitude (respectively) of a reference transition, (in this case WX). $\widetilde{\mu}_n$ is proportional to the fourth root of the DP amplitude divided by the reference amplitude.

With the now flat spectra, we can approximate the amplitude of the CP signals $S_{n,m}$ based on the relative dipole moments calculated using equation.

$$\frac{A^{(n,m)}}{S_0} = \widetilde{\mu}_n^2 \widetilde{\mu}_m^2 J_{n,m} \tag{6.5}$$

where $J_{m,n}$ is a phenomenological coupling constant intended to characterize the strength of the interactions between the two transitions. This definition of J, based on the peak amplitude, does not incorporate different decay rates of the peaks. A more complete description would include a normalization based on the coherence and population lifetimes of the different excitons. In this scan, however, both lifetimes are limited by the experimental scan range, so an approximate normalization is intrinsically included. As the goal here is to calculate a rough comparison of coupling strengths, a more detailed inclusion of the lifetime normalisation is omitted. We can calculate J for each of the coherence ($J^C_{m,n}$) and population ($J^P_{m,n}$) CPs for which we have both of the associated DPs (and can therefore extract relative dipole moments). We can calculate phenomenological coupling strengths for the following CPs: WX/βX_1, NX/βX_1, WX/BarX, NX/BarX, βX_1/BarX βX_2/BarX.

The J values extracted from the 3D spectrum (Table 6.6) show that the WX/NX/BarX to βX coupling is much stronger than the BarX to WX/NX coupling. This stark difference (more than a factor of ten) can be explained in the following way. $\beta X_{1,2}$ each share an electron with NX or WX and the other with BarX. Furthermore, there is likely a large amount of wavefunction overlap of βX_1 (βX_2) with WX (NX) and also of $\beta X_{1,2}$ with BarX. On the other hand BarX does not share any states with WX or NX. BarX also likely has less spatial overlap with WX and NX.

6.4 10 nm barrier sample

Some of the same 2D spectroscopy and PLE experiments were performed on sample B, in which the QWs are separated by a 10 nm barrier instead of a 30 nm barrier, but is otherwise identical to sample A. The following sections will provide a brief overview of these results, which are used help justify the peak assignments, to add further constraints to the wavefunction calculations, and to investigate the way in which the coupling of WX and NX to αX and βX changes as the separation of the wells is reduced and hybridization of the wavefunctions increases.

6.4.1 *Relaxation pathways (PLE)*

A 2D PLE plot for DQW sample B is presented in Fig. 6.10. There are some significant differences between this and PLE from sample A (Fig. 6.5). First, there is strong emission from WX, but none from NX. In addition, there is a strong peak for excitation in NX and emission from WX. These two observations suggest that there is very efficient tunnelling from NX to WX, which is not unexpected given the narrow, low potential barrier separating the wells.

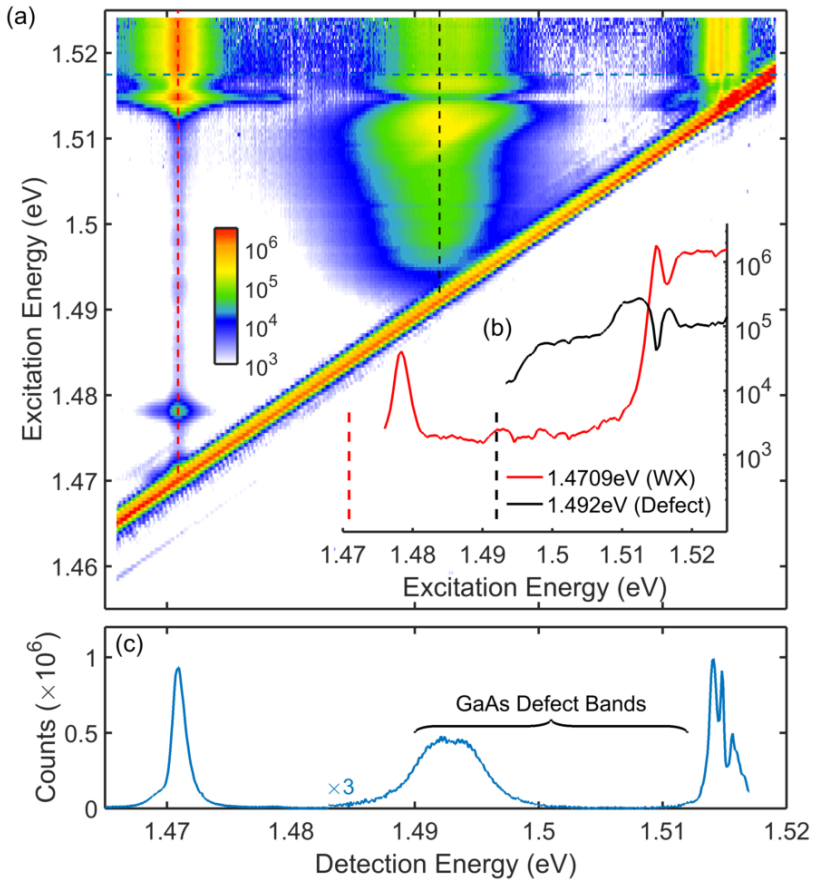

Figure 6.10: PLE on 10 nm barrier DQW. (a) shows the full 2D PLE spectrum which is discussed in detail in the text. Specific slices of the spectrum along the excitation axis (b) and emission axis (c) are discussed.

Second, there is a strong defect band centred between 1.490 eV and 1.493 eV with an emission profile similar to that of sample A. Unlike sample A, however, there is PL signal for this band even when the exciton energy is smaller than the GaAs band gap. The emission from the ~1.512 eV defect band is also missing. These differences suggest that the nature and concentration of defects in the GaAs epilayers is different for the two samples. This is not uncommon, as samples from different machines and even different runs on the same machine can have significant differences in defect incorporation ([128, 233]). More importantly (assuming defect density is uniform), this makes detection of emission from the βX states more difficult as the signal from the QWs is re-absorbed as it passes through the GaAs capping layer before leaving the sample.

There are also a range of different peaks along the excitation spectrum for emission in WX (shown in Fig. 6.10b). The most obvious of these peaks appears at 1.493 eV, but there are additional peaks above at 1.499 eV and 1.502 eV. These might represent the relaxation from the βX peaks down into the quantum wells. If they do, there is relaxation from βX_2 and βX_4 (which are predominantly localized in the narrow well) into WX (i.e. cross barrier relaxation). However, whether this is a two-step relaxation via NX, or tunnelling directly through the barrier to WX cannot be discerned from this measurement.

6.4.2 *1Q/2D spectrum of Sample B*

A 1Q spectrum for the 10 nm barrier sample B is shown in Fig. 6.11. Comparing this to the 1Q spectrum for the 30 nm barrier sample, there are several obvious differences. The peaks are all broader, the NX and WX DPs are tilted along the diagonal (indicating some inhomogeneous broadening), and a different array of above diagonal CPs are present.

The CPs at (E_3, E_1) = (WX, βX_1), (NX, βX_2) and (NX,βX_6) which appeared in the sample A 1Q spectrum are also resolved here, but are broadened and slightly tilted along the diagonal. The βX_3 and βX_4 peaks are missing entirely. Finally, an entirely new peak appears at $E_3 = 1.499$ eV, coupled only to WX. The width of the peaks makes exact identification difficult. This peak could be emission from the βX_5 peak that was missing in sample A, or $\beta X_{2,4}$ coupling to WX.

Closer inspection also shows that all of these peaks (WX, NX, βX_1, βX_2) are slightly spectrally shifted relative to the same peaks in sample A. As section 6.5.1.2 will show in more detail, these peak shifts can be explained by shifting splittings due to increased penetration of the wavefunctions (particularly $E_{1/2}$ and $H_{3/4}$) through the barrier.

The weaker βX above diagonal CPs (including some which are not resolved at all) could be in part the result of signal absorption in the GaAs capping layer. If that is the case, below diagonal CPs should be slightly easier to detect. Unfortunately,

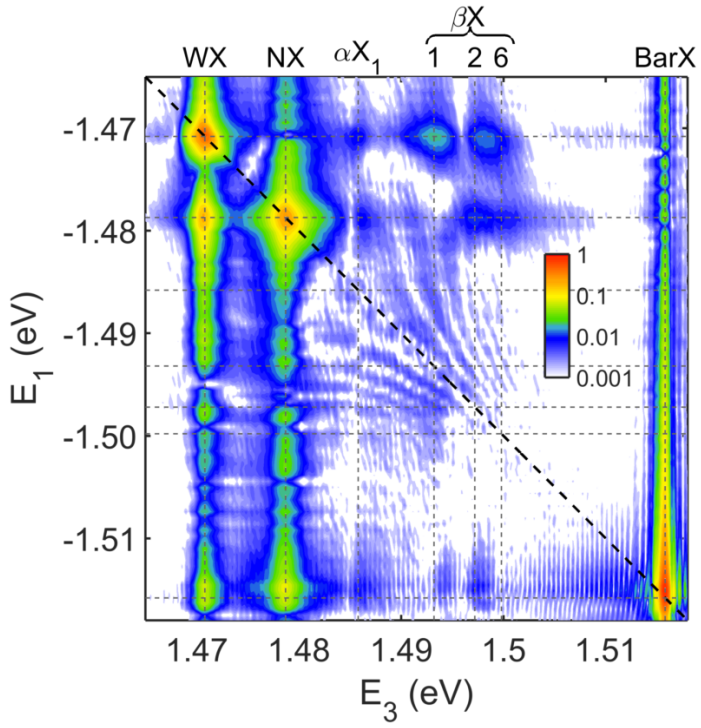

Figure 6.11: A 1Q/2D spectrum for sample B. It is similar to sample A, with a few differences. All peaks are broader, and fewer of the above diagonal CPs are resolved.

the NX and WX free-carrier continua makes detection of these peaks difficult in broadband spectra. There are certainly modulations of the free carrier continuum, but the precise location of these modulations is difficult to discern and depends heavily on the details of the windowing function which is used to remove the pulse overlap.

6.4.3 *Coherence-specific, Pathway-selective 3D spectroscopy*

Exciton signals can be separated from the free-carrier continuum by looking at the electronic coherent superposition pathways. The free-carrier coherence time is short enough that they do not contribute significantly to the coherent superposition pathway, while strongly coupled exciton transitions do generate coherent superposition signals. For that reason, we perform broadband and coherence-specific pathway selective 3D spectroscopy to better separate the below diagonal exciton signals.

A broadband 3D spectrum (not shown) does not resolve any resonances that could be coherent superpositions. The signal may be below the noise floor, preventing the detection of the signals. Chapter 4 showed that otherwise hidden coherence signals can be revealed by spectrally shaping excitation pulses to only excite the coherence pathways. Here we use the same approach to excite only the βX-NX/WX below diagonal coherent superposition pathways, using the pulse sequence shown

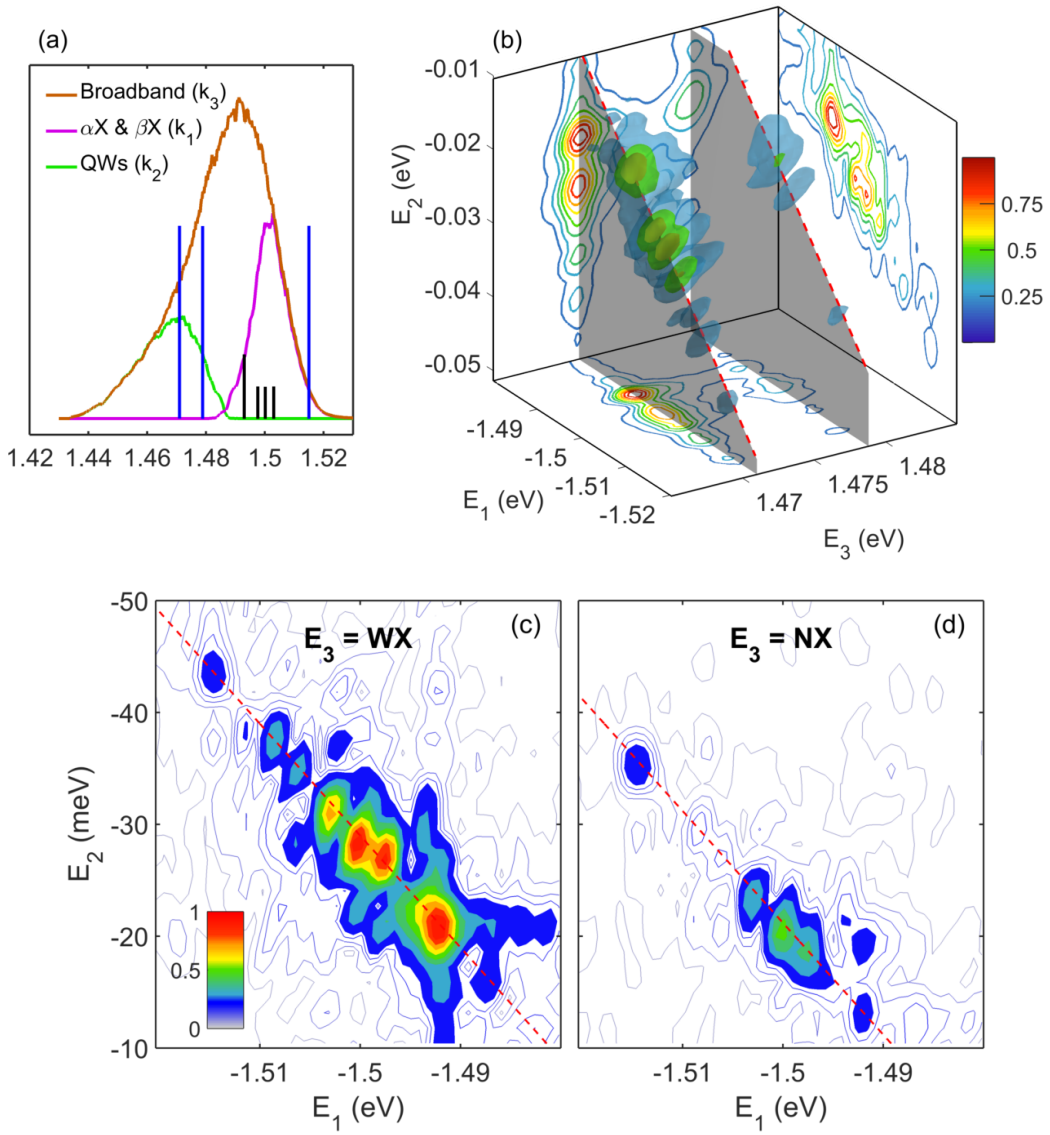

Figure 6.12: (a) Pulse sequence for pathway selective 3D spectrum. (b) Pathway selective 3D spectrum showing coherence below diagonal CPs of WX/NX with βX and BarX excitons. Vertical planes indicate slices displayed in (c) and (d) for emission from WX and NX respectively. The red diagonal lines in (b), (c) and (d) represent the $E_2 = E_3 + E_1$ line, which is where we expect coherence CPs.

in Fig. 6.12a[8]. The resulting 3D spectrum is presented in Fig. 6.12b. A wide range of coherence CPs are resolved. The E_2 vs E_1 slices for E_3 = WX and E_3 = NX are shown in Fig. 6.12c and 6.12d. The red line indicates the spectral positions where we expect to see coherent superposition signals.

The main peak in the 3D spectrum is at (E_1, E_2, E_3) = (-1.493 eV, -20 meV, WX), which is consistent with the β_1 above diagonal CP seen in the 2D spectrum. Like in the 1Q 2D spectrum this peak is stronger at E_3=WX, but there is also some signal

8 Pathway selection wasn't used on Sample A, because the above diagonal CS-CPs are evident even without the selective excitation. In Sample B, on the other hand, the CS-CPs are not clearly resolved, so selective excitation is more useful in that it can eliminate some of the diagonal peaks, reduce the noise floor and thereby reveal the CS-CPs.

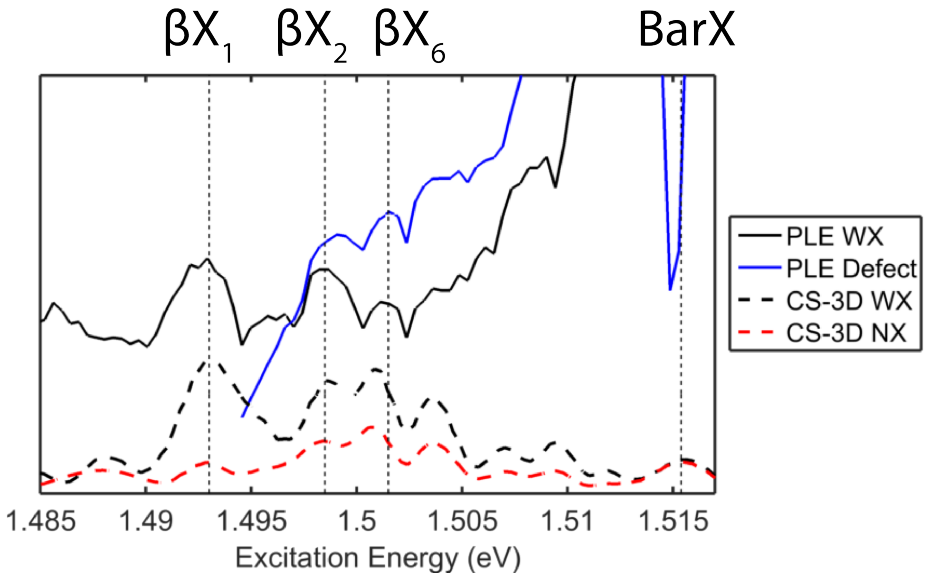

Figure 6.13: Traces of the PLE excitation spectra from Fig. 6.10 are superimposed on traces along the diagonal of the below diagonal coherence peaks in Fig. 6.12. They show a consistent set of transitions which are coupled to NX and WX

at (E_1, E_2, E_3) = (-1.493 eV, -20 meV, NX). Further down E_1, we see a set of three pairs of strong peaks at

E_1=-1.498 eV: (-1.498 eV, -26 meV, WX)& (-1.498 eV, -18 meV, NX),

E_1=-1.500 eV: (-1.500 eV, -28 meV, WX) & (-1.500 eV, -20 meV, NX),

E_1=-1.502 eV: (-1.502 eV, -30 meV, WX) & (-1.502 eV, -22 meV, NX).

There are then three weak pairs of peaks at

E_1=-1.507 eV: (-1.507 eV, -35 meV, WX) & (-1.507 eV, -27 meV, NX),

E_1=-1.509 eV: (-1.509 eV, -37 meV, WX) & (-1.509 eV, -29 meV, NX),

E_1=-1.516 eV: (-1.516 eV, -44 meV, WX) & (-1.516 eV, -36 meV, NX)

the final two of which correspond to coupling of WX and NX to BarX.

A slice along the diagonal line in in 6.12c and 6.12d is taken and superimposed on the PL excitation spectrum in Fig. 6.13, in which we see that peaks detected using PLE experiment with emission in WX match up with the range of peaks we see here in the PS-CMDS spectrum with emission at both WX and NX. Despite the relatively low signal to noise ratios of these spectra, the consistency of these very different experimental techniques supports taking them to be real peaks. The peaks at E_1=-1.498 eV and -1.500 eV roughly match up with the peaks that have been labelled βX_2 and βX_6 in the 1Q spectrum. However, some questions remain: what are the additional peaks E_1=1.507 eV and 1.510 eV? Why are these peaks slightly shifted compared to the above diagonal ones in the 1Q spectrum?

These questions aside, if we just look at the lowest frequency peaks (E_1=-1.493 eV, -1.498 eV and -1.502 eV) we can see here that the β_X excitons no longer only couple

to a single well (as they did in the 30 nm barrier sample): βX_1 and βX_2 are clearly coupled to *both* NX and WX in the PS-3D spectrum. In other words, a type-II exciton with one carrier localized in one well directly couples to the type-I exciton in the other well, through the central barrier. This also suggests that at least some of the βX peaks involve carriers localized in the central barrier which separates the two wells.

6.5 Discussion

6.5.1 *αX and βX peak assignments*

Within the array of CMDS and PLE data presented in the previous sections, there is a wide variety of evidence to support our asserted attribution of detected signals as α (parity forbidden) and β (type-II) 'dark' states. The aim of this first part of the discussion is to lay out that evidence.

A brief summary of the argument structure is provided first. The positions and widths of $\beta X_{1,2,6}$ and αX_1 (i.e. all of the αX and βX states which are detected in both samples) correlate with the positions and widths of WX and NX[9], which implies that they must involve states in the QWs, and rules out defect related states. The correlation of the inhomogeneous broadening, on the other hand is less apparent in βX CPs, suggesting that one of the βX carriers is not in the well. Since the αX and βX peaks must involve a state in one of the QWs, we use the calculated QW energy levels from section 6.2.2 to work out the expected transition energies of all possible exciton configurations involving at least one carrier in one of the QWs. From these calculations, we find very good agreement of the calculated αX and βX with the energies of the detected signals, and rule out all other possible exciton configurations.

6.5.1.1 *PLE and 1Q emission lines*

Figure 6.14 shows the emission spectra of the WX and NX for both samples in PLE (solid) and 1Q (dashed) experiments. In sample B, both WX and NX are shifted to slightly lower energy compared with sample A. The splitting between NX and WX is also increased by ~2 meV. This increased splitting is qualitatively consistent with increased coupling of the E_1/E_2 wavefunctions due to wavefunction penetration through the barrier. The splitting is also quantitatively consistent with the transition energies predicted by wavefunction calculations presented in Section 6.2, when a small difference between the samples' indium content is included in the calculations.

9 Note: The 'correlation' referred to here is **not** the correlation of the inhomogeneous broadening (angled peaks), but rather that the peaks shift in the same direction and broaden by the same amount from sample A to sample B.

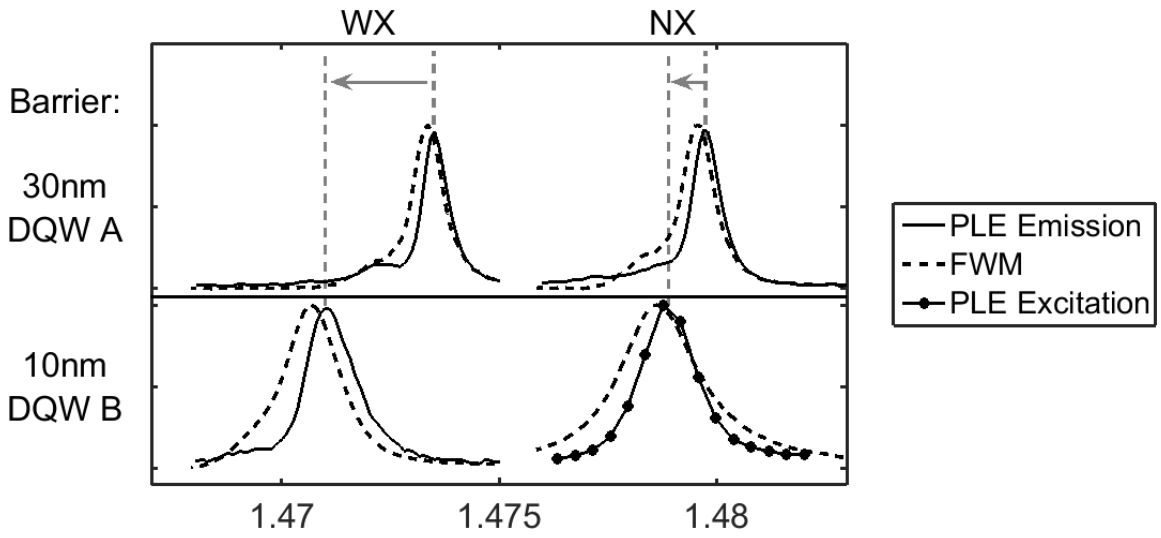

Figure 6.14: Emission lines WX and NX in both samples. This shows the increased splitting of WX and NX in sample B compared with sample A, as well as increased inhomogeneous linewidth. The increased width and slight detuning of the four-wave mixing signal compared with the PLE is an artifact of the data analysis procedures in which some of the signal is windowed out in the t_3 domain, resulting in a loss of resolution in the E_3.

The 1Q above diagonal CPs for both samples are shown in Fig. 6.15. Like the WX and NX DPs and PL emission in Fig. 6.14, the βX_1 and βX_2 CP emission energies are red shifted in sample B compared with sample A. This can be seen most clearly in the 1D plots of E_1 = WX (NX) in Fig. 6.15b. The CPs that are mostly localized in the wide well are shifted by ~2-3 meV, while the CPs that are mostly localized in the narrow well are shifted by ~0.5-1 meV. The emission linewidths of αX_1 βX_1, βX_2 and βX_6 are also all much broader in sample B than in sample A. This is consistent with the broadening observed for the WX and NX emission lines due to structural disorder.

The emission characteristics (transition energy and linewidth) of βX and αX are correlated to the bright direct excitons in the same well (which is to say, they change in the same way from sample A to sample B). This correlation[10] then suggests that the βX and αX transitions involve at least one state within the QW. They are therefore not intrinsic defect states in the GaAs epilayers, which would have emission characteristics uncorrelated to the QW excitons. Furthermore, the nature of the defects with emission in this spectral range also precludes them as an explanation. The 1.490 eV and 1.493 eV defect peaks arise from recombination of a free electron with a hole on an accepter defect [233], which would be unlikely to produce the well resolved excitonic resonances with long coherence times.

The peak-shapes of α_1 and α_2 in sample A contain some additional evidence for the proposed assignments as parity forbidden dark states. Looking more closely at the coherence peaks peaks (Fig. 6.16), we can see that both peaks are tilted along the diagonal. This tilt (like the HH-LH coupling in chapter 4) is generated by

10 Again, referring to the correlation of the emission properties (central energy and linewidth), not the correlation of the inhomogeneous broadening.

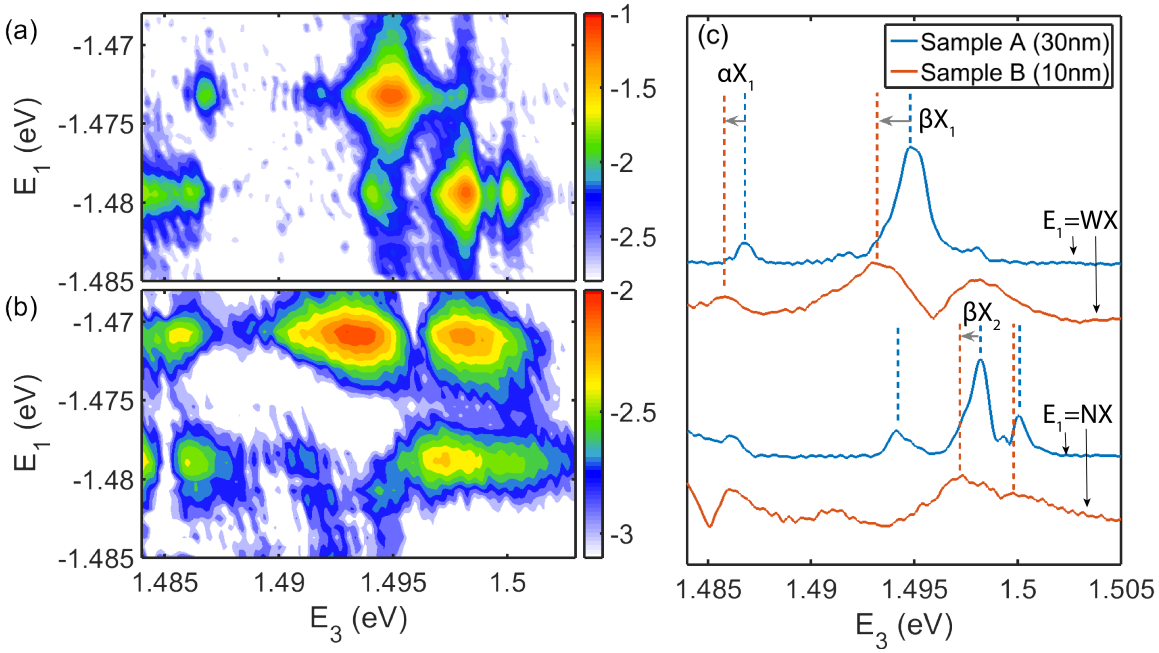

Figure 6.15: a comparison of the above diagonal βX CPs in sample A (a) and B(b), showing the increased separation of βX_1 and βX_2, as well as the increased inhomogeneous width (like in the WX and NX DPs). (c) shows slices through E_1=WX (top) and E_1=NX (bottom) for sample A (blue) and sample B (red). The vertical dotted lines indicated the position of the peak to show increased width and change in peak-shape and position.

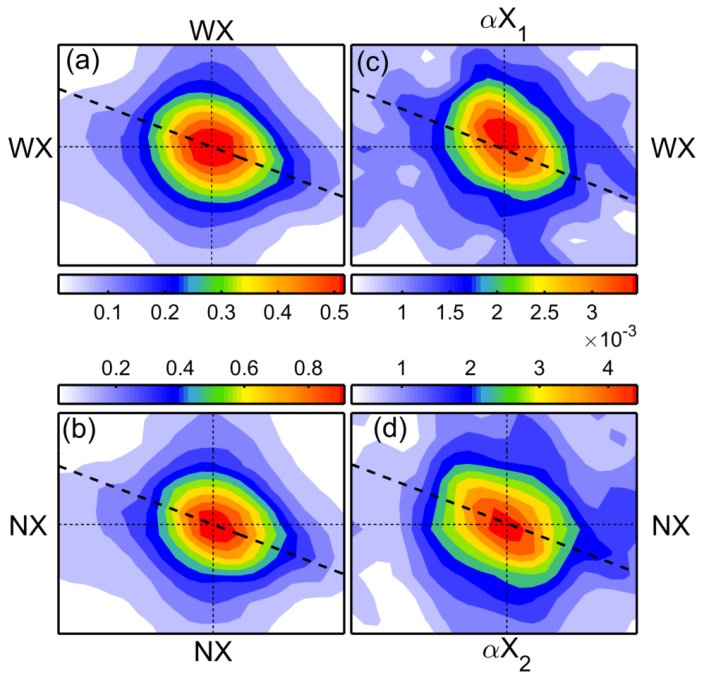

Figure 6.16: Diagonal and WX/NX - αX coherence CP show some elongation along the diagonal. This is strong evidence supporting the attribution of these signals to αX parity forbidden transitions. The x axis is E_3, and the y axis is E_1. The diagonal dashed lines are the E_1=-E_3 lines.

correlated inhomogeneity, which occurs when both transitions experience the same structural disorder. The correlation of the structural disorder is further confirmation that the αX peaks are indeed states in the QWs. In QWs, the structural disorder is

dominated by well-width fluctuations, so correlation suggests that the two excitons are in the same part of the same QW. As we described in the previous chapter, non-local coupling (i.e. inter-well or barrier-QW) would not demonstrate tilted CPs indicative of correlated inhomogeneity.

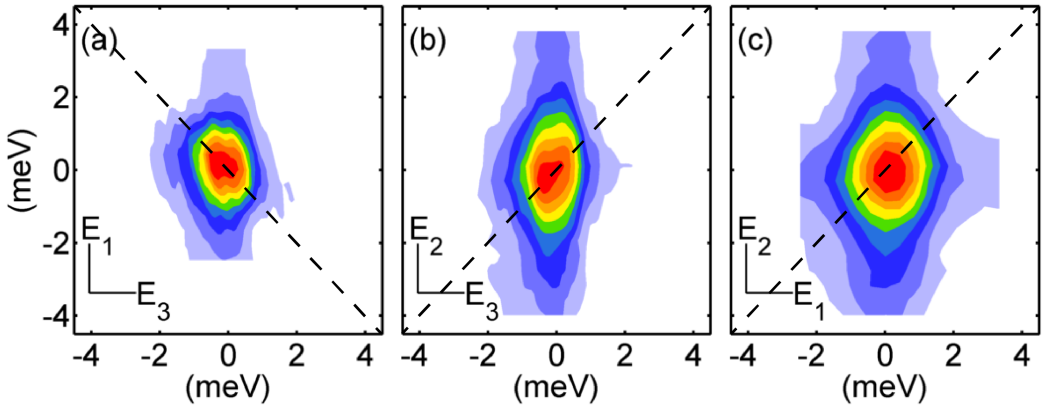

Figure 6.17: Projections of the (E_1,E_3) = (WX,βX_1) coherent superposition peak onto the (a) (E1,E3),(b) (E3,E2), and (c) (E1,E2) planes. (d) shows Lorentzian fits of the integrated peak profile in the three different directions along with a the three different energy directions. Fits show that E_2 is the largest, roughly double the size of the E_3.

The projections of the CS-CP onto the three different frequency axes is shown in Fig. 6.17. The shape of the E_1 vs E_3 projection (which is shown in Fig. 6.17a), is not significantly tilted, suggesting uncorrelated inhomogeneous broadening. There is a small amount of tilt in the E_3 vs E_2 peak-shape in Fig. 6.17b, but no observable tilt in the E_1 vs E_2 peak-shape in Fig. 6.17c. The peak-shapes of the projections of the NX-βX_2 CS-CP are similar. These shapes are consistent with the results in the previous chapter for CS-CPs where the inhomogeneous broadening is uncorrelated. They are, however, inconsistent with the simulations for uncorrelated broadening, which predict an observable tilt in E_3 vs E_2 and E_1 vs E_2 peak-shapes. It is not clear whether we should expect correlation of βX_1 (βX_2) and WX (NX) broadening. We might expect some correlation because βX_1 (βX_2) involves the same electron state as WX (NX). However, we also would not expect perfect correlation because the energy of the hole state in βX_1 (E_b) will be essentially independent of the well width. These results appear to indicate that there is little to no correlation of the inhomogeneous broadening of the WX (NX) and βX_1 (βX_2) transitions and that broadening in the E_2 domain exceeds the contributions from the individual excitons.

6.5.1.2 *Ruling out other peak assignments*

There are in principle two other excitons which involve carriers in the QW that we should consider as alternative assignments for the detected βXs and αXs: inter-well excitons and higher energy direct excitons. As described previously, there are four possible Inter-well excitons (E_1-H_2, E_2-H_1, E_1-H_4 and E_2-H_3). Assignment of either

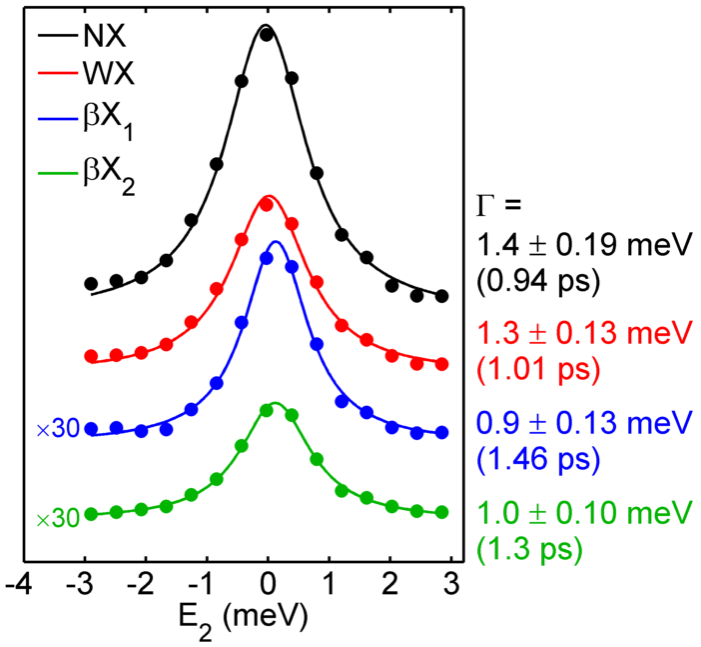

Figure 6.18: Lorentzian fits along E_2 of the $E_2 = 0$ DPs to determine the bright excitons (WX, NX) and the dark CT-like excitons (βX_1, βX_2) reveal that the dark state lifetime is at least as long if not slightly longer than the bright states.

any βX or αX as inter-well excitons can be ruled out based on the wavefunction calculations presented in section 6.2.2: Regardless of which value for QC is used, and for the entire range of reasonable indium content, the lowest two transitions (E_1-H_2 and E_2-H_1) have energies far below the detected bands while the other two (E_1-H_4 and E_2-H_3) have energies far too high. Secondly, we also consider the possibility of direct transitions involving higher energy electron states (E_3-H_3 to E_4-H_4). According to these calculations, both E_3 and E_4 are unconfined, above the GaAs bandgap for the entirety of the parameter space covered by these calculations, and therefore cannot account for the βX or αX. With these other possible peak assignments ruled out, the only transitions we are left with which involve at least one carrier in the QW are the βX and αX transitions.

Finally, we note that while our calculations have been constrained primarily so that they fit the WX, NX βX_1 and βX_2 transition energies, we get very good agreement with all of the detected states with the same set of parameters.

6.5.2 *Population dynamics*

Using the 3D spectrum of sample A presented in section 6.3.4 we can put a lower bound on some of the population lifetimes and make some inferences about population dynamics. During t_2, population pathways exhibit a decay along t_2 ($\hat{T}_1$) which is proportional to the population relaxation (T_1) and exciton diffusion (T_d).

$$\frac{1}{\hat{T}_1} = \frac{1}{T_1} + \frac{1}{T_d} \tag{6.6}$$

When this decay is Fourier transformed (as it is in a 3D spectrum) it results in a Lorentzian peak along E_2 with a width $\Gamma_2 = 2/\hat{T}_1$. As a result, we can measure the population lifetime by fitting the E_2 projection of population peaks (peaks occurring at E_2=0) to a Lorentzian function. In our experiment, however, the time window of the pulse-shaper introduces an additional decay along t_2, which we can approximate as another exponential decay with a decay constant T_{tw}. The Γ_2 that we measure is therefore a convolution of the population decay, the exciton diffusion and the experimentally limited delay range.

$$\Gamma_2 = \frac{2}{T_1} + \frac{2}{T_d} + \frac{2}{T_{tw}} \tag{6.7}$$

T_{tw} is around 1 ps, T_d is in the 10's of ps [48] and the T_1 can be up to several ns for 'bright' QW excitons [46]. We can therefore only put a lower bound on the population and exciton lifetimes and compare lifetimes of different transitions measured using the same experimental apparatus.

Lorentzian fits of the E_2 projections of the population peaks (shown in Fig. 6.18) show that the βX_1 and βX_2 population lifetimes are at least 1.5 ps and 1.3 ps respectively, which are the same as or slightly longer than the population lifetimes of WX and NX which are 1.0 ps and 0.9 ps respectively. Previously conducted experiments using a delay stage put the decay as a function of t_2 for WX in sample B[11] at around 20 ps [54]. The large discrepancy between the 20 ps measured previously and the ~1 ps reported here emphasizes that this 1 ps 'lifetime' is almost entirely a measurement of the experiment delay window function (T_{tw}) rather than the sample response. However, it still stands to reason that if either T_1 or T_d of βX were significantly shorter than those of NX, we would expect to measure broader Γ_2. Surprisingly, based on the fits in Fig. 6.18 the βX Γ_2 are actually slightly narrower than the WX and NX Γ_2's.

We might expect shorter lifetimes for βX_1 (βX_2) because relaxation into WX (NX) should be very efficient. This relaxation step only involves the hole being captured by the well, since the electron is already in $E_{1(2)}$. Carrier capture times are typically expected to be between 2 ps and 20 ps [240, 241, 277], so we would expect relaxation of the hole into the well to somewhat shorten the $\beta X_{1(2)}$ lifetimes. However, it is clear that this relaxation is not occurring on a timescale less than 5 ps.

If population relaxation into the QW is the main limit on the βX lifetimes (which we expect based on the PLE measurement, and because the reduced wavefunction overlap should lead to larger radiative lifetimes), we would expect to see below diagonal CPs in the 1Q/2D spectrum that grow in as a function of t_2. By examining the 1Q/2D spectra as a function of t_2 we can look for such a population relaxation CP in the first 5 ps. Though the overlapping free carrier continuum and strong co-

11 We assume that the exciton diffusion times and lifetimes are comparable between sample A and sample B. Other measurements of the linewidth of the sample B population peaks using the experiment at Swinburne measured similar Γ_2 for sample A and sample B.

herent oscillations make detection of the peak difficult, we don't see any indications of population relaxation in the 3D dataset. This again suggests that the population relaxation lifetime is much longer than 5 ps.

These longer than expected lifetimes suggest that the carrier states in $\beta X_{1(2)}$ are $E_{1(2)} - L_b$ and not $E_{1(2)} - H_b$, as the confinement of the LH in the barrier would decrease the relaxation rate into the QW, compared with the HH which is not confined in the barrier. Further experiments to measure the population dynamics over a longer range will be necessary to obtain a precise determination of the lifetimes.

6.5.3 *What are the βX excitons?*

The βX excitons can be separated into two groups, those which involve a hole in the barrier and an electron in the well ($\beta X_{1,2}$) and those which involve an electron in the barrier and a hole in the well (βX_{3-6}). Based on the results and analysis in this chapter,βX_1 and βX_2 are most likely type-II LH excitons (Fig. 6.19a). Although in principle there is no way of telling based on the experimental results whether $\beta X_{1,2}$ involve a HH or a LH in the GaAs layer, the 1Q DPs and long population lifetime strongly point to the latter. The inverted potential for LHs would explain these surprisingly long lifetimes, since the LH could not relax into the QW without a change in angular momentum.

The second group (βX_{3-6}) involving an electron in the barrier and a hole in the well cannot be explained by type-II LHs, so they are more difficult to classify. The missing DPs might be below the noise, or the populations do not last long enough to generate a measurable signal. Either way, we don't have a way to measure the population lifetimes directly. However, we might be able to approximate the lifetimes another way. Population relaxation has been shown in previous work on semiconductor nanostructures to shorten coherent superposition lifetimes [215, 221, 278]. This effect would manifest as a linewidth along E_2 which is significantly larger than the sum of the homogeneous linewidths along E_1 and E_3. Similar to the $\beta X_{1,2}$ coherence CPs, the $\beta X_{3,4}$ coherence CPs have roughly the expected 3D peak widths (i.e. $\Gamma_2 \approx \Gamma_1 + \Gamma_3$), so we can assume that the βX_{3-6} lifetimes are at least not vanishingly short, suggesting that the excitons are stabilized somehow.

State filling of NX and WX could explain the stability of the βX excitons. However, at the low excitation densities we are using, we wouldn't expect to be nearing this limit. Also, a coarse power dependence (not shown) over 1.5 orders of magnitude showed no appreciable change in the relative amplitude of the βX CP signals. The stability of βX_{3-6} could come from some sort of ridge in the potential which weakly confines the electron in the barrier (see Fig. 6.19c) which would make the βX_{3-6} excitons appear to be more like type-II excitons, though fundamentally different from the type-II LH excitons. However, if there is no ridge in the potential at the edge of the QW, (as in Fig. 6.19b), then there is no confinement of the electron

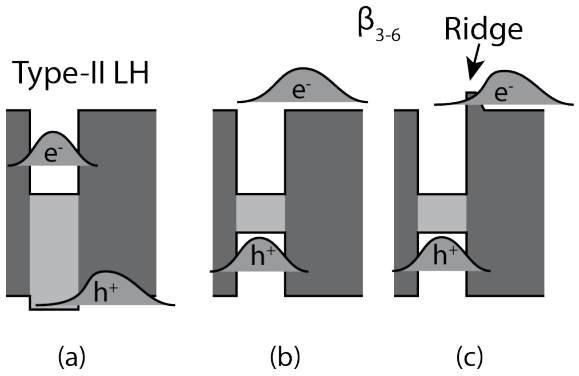

Figure 6.19: Potential profiles for different configurations of the βX excitons.

wavefunction in the barrier. The electron's wavefunction could therefore spread across the interface into the QW, making the exciton more type-I like. If this is the case, however, its hard to imagine that we would see such long lived coherent superpositions (with >1 ps lifetimes) given and there is nothing stabilizing the β_X and preventing the electron from relaxing into the QW (into WX or NX).

The physical effect that would create this ridge along the GaAs/InGaAs interface is less clear. Pockets and ridges can occur at heterojunctions, but typically only when one or both of the materials is doped (n-type or p-type) [244]. All of the materials used here are nominally undoped so this seems less unlikely. Strain induced electric fields can perturb the potential, but in zinc-blende crystals this only occurs along the growth direction when substrates other than (100) are used [279]. These samples are grown on (100) oriented GaAs, so the strain induced internal electric field also seems unlikely. Finally, if the GaAs layer is not uniformly strained (or even unstrained as is typically assumed when calculating strained energy levels [170]), there might be some perturbation of the GaAs potential near the interface. Calculations involving a more thorough incorporation of strain would be required to properly consider this possibility.

It also possible that the parity consideration make relaxation of the electron into the well partially forbidden. The $H_{3,4}$ holes (the holes that combine with E_b to form $\beta X_{3,4}$) have odd parity, while E_b (an unbound electron in the barrier) is not restricted to a particular parity. However, the excitons are created by the promotion of an electron from the valence band to the conduction band, However, it is likely that when the absorption of a photon creates the exciton by promoting the electron from the valence band to the conduction band, the electron will retain its parity. As a result, although the GaAs electrons can in principle have either parity, the ones bound to odd parity holes also necessarily have odd parity. The only available electron states in the well (E_1 and E_2) have even parity. The relaxation of the electron into the well is therefore inhibited by the lack of spatial overlap of odd parity E_b and the even parity E_1 and E_2.

6.5.4 *CMDS to detect dark states*

Based on the DPs in the 3D spectrum of sample A, the relative dipole moment of βX_1 and βX_2 are much weaker than the relative dipole moments of NX and WX, and the relative dipole moments of βX_{3-6}, $\alpha X_{1,2}$ are so low that they cannot be determined because no DPs are resolved. The presence of such strong CPs including CS-CPs indicates that they must be strongly coupled to NX and WX (respectively). In fact, in the case of all but $\beta X_{1/2}$ the only way that we know these transitions exist is because they form coherent superpositions with WX, NX and BarX. This emphasizes a little discussed potential application of CMDS and particularly coherence specific CMDS. Using these approaches, we can isolate signals from dark states that that are otherwise difficult to access optically. The dark states uncovered using CMDS in this chapter (particularly βX, but also αX) are a good demonstration of how this amplification of weak signals can be useful.

While other techniques can also exploit this coupling to study these dark transitions (e.g. the PLE shown in Fig. 6.5 and 6.10), CMDS is well placed to extract additional information that other techniques cannot. As detailed in this chapter, CMDS provides us a variety of information beyond what PLE offers. First, it allows us to directly identify coupling where PLE only shows us that there are relaxation pathways available to relax from the transition that is originally excited to the transition from which we detect photoluminescence. The exact pathway followed cannot be directly discerned. Furthermore, it allows us to identify coherent coupling pathways, and to measure both coherence and population dynamics. Finally, because CMDS drives emission from the dark states, and PLE does not, we are able to fully separate the dark states from the spectrally overlapped free-carrier continua, which absorbs strongly but does not emit, even in CMDS experiments.

Pump-probe measurements would also be able to identify the coherent superpositions of the dark and bright states as oscillations as a function of the pump-probe delays (as in Ref. [184]). However, CMDS allows us to access several additional details that pump-probe does not: 1. We can unambiguously identify the energy of the transitions which are coupled, where in pump-probe there are in principle multiple combinations of transitions that can lead to oscillations with the same frequency. 2. We can access peak shape information which is not available in pump-probe measurements, which as shown in this chapter and in Section 4.3.4 can provide a variety of additional physical insights. 3. The ability of the CMDS to separate different pathways along multiple frequency directions allows us to more easily separate out the signals involving dark states from all of the other signals, which in many cases are overlapped in pump-probe experiments.

6.5.5 *The role of the dark states in relaxation of excitons into QWs*

Now that we have identified these states we can explore their dynamics and understand how significant a role they play in the relaxation of excitons from the barrier into the QWs. These states could influence relaxation dynamics in a number of ways: they could act as 'sinks' which trap carriers that would otherwise relax into the QWs, and which instead eventually dissociate into free carriers or relax non-radiatively. On the other hand, they might represent a step between the barrier excitons (or more likely free carriers) and the QW excitons which allows more efficient and faster relaxation into the wells. Quantitative experiments will be required to determine the exact role these states play, and how significant that role is in the overall DQW dynamics. Identification and routine detection of these states is an important step towards that ultimate goal, which we have achieved through CMDS.

6.6 Summary

We have detected CS-CPs indicative of coherent coupling of a wide variety of types of transitions. We have detected coherent coupling of the barrier excitons to the direct QW excitons the details of which may be useful for understanding the specific relaxation pathways from the GaAs 3D excitons into the 2D QW excitons. We have also detected coherent coupling of type-II LH excitons (in which the hole is localized in the barrier) to the type-I HH excitons. The charge oscillations due to the strong coupling of the type-I HHs and type-II LHs could also be used as a terahertz source. We have also detected symmetry/parity forbidden direct transitions in both QWs through their coupling to the allowed QW excitons. Finally, we have observed a set of transitions that involve an unconfined electron in the GaAs barriers bound to holes confined in the InGaAs QWs. The nature of these excitons is not yet fully understood, and may have a type-I or type-II character. While the exact details of how to understand these states are as yet uncertain, what is clear is that these states are coherently coupled to BarX and the QW excitons, so they will be involved in the coherent dynamics of both.

All these results put together show that what appears on the surface to be a simple electronic structure (NX, WX, BarX) is actually much more complex. CMDS allows us to reveal this rich structure of dark states that is otherwise hidden and opens the door to previously unexplored physics and a more precise understanding of the exciton dynamics in shallow, strained InGaAs QWs.

7

EXCITON DYNAMICS IN THE VERY LOW EXCITATION DENSITY REGIME

7.1 Introduction

The coherent dynamics of excitons in semiconductors is very sensitive to excitation density, in part due to many-body contributions to the non-linear response [186]. For this reason, considerable effort has been put towards investigations of the intensity dependence of non-linear signals in semiconductor QWs. Previous work has mostly focused on the upper end of the accessible range (10^9-10^{12} carriers cm^{-2}) [89, 157, 175, 176, 280–283]. In the mid to high excitation range, the response can be well explained using mean field theories where excitonic interactions are introduced through phenomenological inclusion of excitation induced shift (EIS) [79, 188, 189], excitation induced dephasing (EID) [176, 177] and local field effects (LFE) [186]. The mean field approach, however cannot directly account for some recent reports of higher order correlations, including triexcitons (3 holes and 3 electrons) [190, 191], long range coherent interactions [73] and liquid-like coherent droplets [193]. Although direct detection of these effects is only possible through specialized techniques, they may still play a role in the standard FWM response. Furthermore - and perhaps counter-intuitively - it has also been suggested that many-body interactions are likely to play a larger role at low excitation densities where the dephasing time is much shorter than the exciton scattering time [186]. While some experiments have been performed at excitation densities below 10^9 carriers cm^{-2}, to our knowledge, the systematic studies of coherent dynamics as a function of excitation density have been limited to 10^9 carriers cm^{-2} and above [156–159].

In this chapter, we exploit the ability of the SLM based coherent multidimensional spectroscopy (CMDS) setup to make measurements of the coherent response at extremely low excitation densities. We also measure the excitation density dependence of three separate double quantum well (DQW) samples. 1-quantum (1Q), 0-quantum (0Q), and/or 2-quantum (2Q) 2D spectra were collected across three orders of magnitude of excitation densities. The range extends from the high end where excitation induced line-broadening and $\chi^{(5)}$ responses creep in, down three

orders of magnitude to a regime not previously explored fully with CMDS or FWM spectroscopy.

We don't have precise measurements of the absolute absorption for these samples at low temperature, so the signals are presented as a function of the photon density rather than the excitation density. If we assume an absorption coefficient of $\sim 1\%$ per well for the exciton transitions [284], we can estimate the carrier densities to be about two orders of magnitude lower than the given photon densities[1]. The ability of 2D spectroscopy to easily separate different signals allows us to simultaneously measure the excitation density dependence of inter-well and intra-well interactions as well as signals involving only one transition.

In these low density and density dependent measurements we find three surprising results: First, the relative strengths of different signals change with the excitation density. Some signals have a well defined $\mathbf{E}^3$ excitation dependence (where $\mathbf{E}$ is the pulse electric field amplitude) expected for $\chi^{(3)}$ signals, while others clearly do not. In particular, it is evident that signals representing interactions between excitons which are localized to different layers of the heterostructure (e.g. inter-well coupling and coupling of QW excitons to barrier excitons) follow a decidedly sub-$\mathbf{E}^3$ density dependence. Second, we find that there are two exciton sub-populations which contribute to a diagonal-peak (DP) in an AlGaAs/GaAs DQW. One sub-population generates a tilted DP while the other generates a round DP. The tilted peak dominates at intermediate densities, while the round peak dominates at low densities (below $\sim 10^9 \mathrm{cm}^{-2}$). We propose that the tilted and round signals are generated by excitons localized and delocalized (respectively) in the plane of the QW. Based on comparisons of the excitation density dependence of the delocalized exciton state and the inter-well cross-peaks (CPs), it appears that the majority of the inter-well signal also involves the in-plane delocalized exciton states. Finally, we demonstrate that down to $\sim 5 \times 10^8 \mathrm{cm}^{-2}$, the 2Q linewidths are limited by exciton-exciton and/or exciton-free carrier scattering. We find that below this density, dephasing is limited by the one-exciton linewidths.

While a complete understanding of these results will require further work in the form of experiments, simulations and theory, what is clear is that the coherent response of excitons in QWs changes in many ways when experiments are performed with extremely low energy pulses (and subsequently low excitation density). The stability of the CMDS apparatus has allowed us to make these new observations even though the coherent dynamics of excitons in semiconductors have been studied for decades.

1 Unless otherwise noted, all experimental densities reported here are photons cm^{-2} per pulse, but for legibility's sake, they will be displayed simply as cm^{-2}.

7.2 AlGaAs DQWs

In this section we will investigate the dependence on excitation density of two different $Al_{0.35}Ga_{0.65}As$/GaAs samples using 1Q 2D spectroscopy. In both samples we observe that the inter-well CPs follow a sub-$\mathbf{E}^3$ power dependence, while intra-well CPs and DPs follow a (predominantly) $\mathbf{E}^3$ dependence. In addition, in one of the AlGaAs DQWs we find evidence for the presence of a spatially extended, delocalized exciton state which is generated by the coherent coupling of separately localized excitons. This extended delocalized state dominates at low excitation density as seen through changes to the DP shape. The DP for the delocalized state has a dependence on excitation density nearly identical to that of the inter-well CPs. This similar density dependence suggests that the extended delocalized state is involved in the inter-well interactions.

7.2.1 *Excitation density dependence of AlGaAs/GaAs DQWs*

We will first present results for the 6 nm barrier AlGaAs/GaAs DQW sample, for which the inter-well coherence signal was isolated in Ch. 4. This sample is given the Al_1 label for the purposes of this chapter. Full details of the sample structure can be found in Section 4.3.1. 2D spectra were recorded using the approach outlined above for excitation densities of $5 \times 10^{11} \mathrm{cm}^{-2}$, where $\chi^{(5)}$ signals are involved, down to $5 \times 10^{8} \mathrm{cm}^{-2}$ beyond which the signal to noise was no longer sufficient to record satisfactory 2D spectra. Spectra were collected using collinear polarized beams.[2] The transition labels are the same as those used in Ch. 4.

The amplitude of each signal was characterized by summing across the 2D peak. The electric field of a four-wave mixing signal[3] should scale with the product of the pulse electric fields. If all the pulse intensities are shifted together, the FWM signal should therefore scale according to $S_{FWM} \propto \mathbf{E}^3 = \sqrt{I^3}$ where I is the intensity of the pulse. All of the acquisition parameters were kept constant while these spectra were acquired, so we can plot the absolute power dependence of the various signals[4].

The measured dependence of selected spectral peaks on excitation density are presented in Fig. 7.2. The absolute power dependence of the DPs are presented in Fig. 7.2a. The dotted angled line indicates the $\mathbf{E}^3$ dependence we might expect for third order process. The upper (lower) solid gray lines indicate $\mathbf{E}^5$ ($\mathbf{E}^1$) dependence. Due to their lower oscillator strengths, the WW_{lh} and WW_{hh} DPs disappear into the background noise earlier than the NW_{hh} DP. They are only plotted for the

2 The pertinent experimental parameters for these measurements (and the rest of the measurements in this chapter) can be found in Table A1.4 in Appendix A1

3 This experiment utilizes heterodyne detection, which directly measures the signal electric field and not intensity.

4 The CCD integration time and LO amplitude were changed to optimize the signal to noise at each power. These changes are accounted for using two linear corrections in the data analysis. This approach was justified by control experiments in which we attenuated the LO+FWM signal after the sample (or the LO alone before the sample) with a wide range of neutral density filters, and integration times. The signals were then normalized according to the acquisition parameters used and were found not to vary significantly.

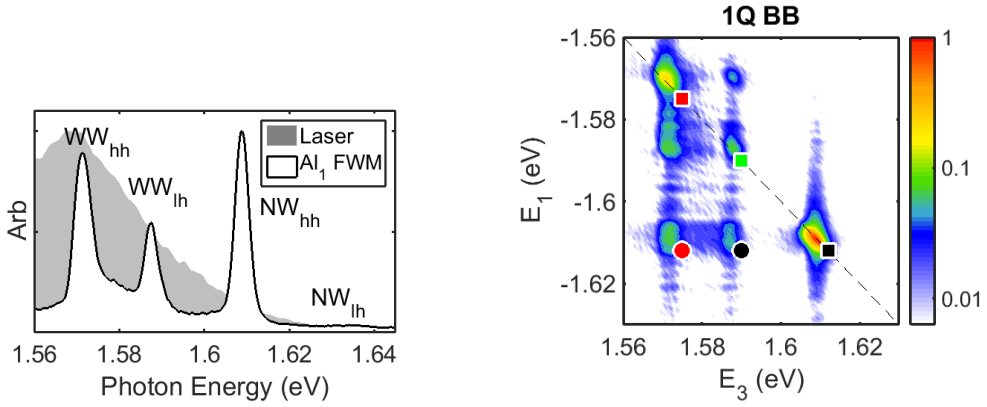

Figure 7.1: (a) Excitation spectrum and Al_1 FWM response. (b) A 2D spectrum for Al_1 (1×10^{10} cm^{-2}).

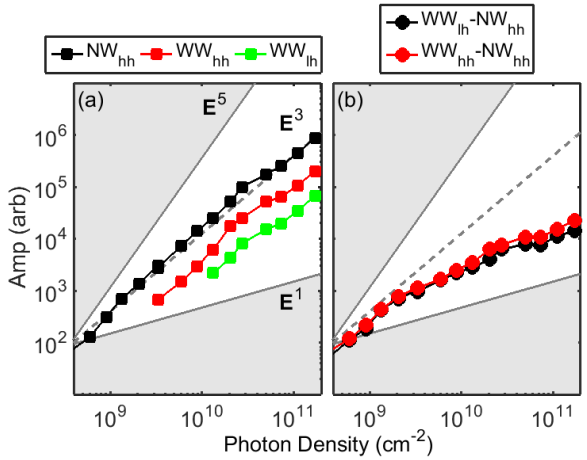

Figure 7.2: Density dependence of AlGaAs sample Al_1 for various 1Q BB (a) DPs and (b) inter-well CPs. The symbols are plotted next to the associated peak in Fig. 7.1b.

powers where the peak can be clearly resolved. All three DPs demonstrate a clear $\mathbf{E}^3$ dependence across the measured density range. The below diagonal inter-well CPs (Fig. 7.2b) on the other hand have a clearly sub-$\mathbf{E}^3$ dependence. Interestingly, these peaks can be resolved even down to the lowest excitation densities, long after the WW_{hh} and WW_{lh} DPs have disappeared.

We repeated this measurement on a second MOCVD grown AlGaAs/GaAs DQW sample (which we will label Al_2). This sample was not spun for a portion of the growth process to reduce the macroscopic uniformity of the width of the wide well. By measuring the photoluminescence across the sample we found that the center of the WW_{hh} transition shifted systematically by ~0.4 meV/mm at the most. The systematic variation of the transition energy across the focal spot (with has a diameter or 0.15 mm) is therefore at most ~0.06 meV. This value is negligible compared with the width of the transition(~4 meV), and we can therefore consider the sample to have a distribution of well widths which is roughly uniform across the focal spot of the laser. Interface morphology has been shown to be very dependent on growth parameters [146, 285], so it would not be surprising if the different growth param-

eters used to grow Al_2 modified the the lateral size[5] distribution of the well width fluctuations. We are unable to directly measure the lateral size of the well width fluctuations, so exactly how these differences have changed the interface morphology is unknown. The coherent dynamics do change in several ways, which will be detailed in the remainder of this section and in Section 7.2.2. This sample was also grown with slightly larger nominal barrier (8 nm) and well widths of 8.5 nm (WW) and 6 nm (NW) leading to a ~25 meV red shift of all of the transitions with respect to Al_1 (which has a nominal barrier width of 6 nm, and well widths of 8 nm and 5.7 nm).

In addition to standard 2D 1Q spectra using broadband excitation pulses (labelled BB), we also collect 1Q and 0Q pathway selective (PS) spectra for this sample. The 1Q PS spectra are collected by using spectral amplitude shaping in the manner demonstrated in Section 4.3.3. The 0Q spectra are collected using the same pulse sequence with the same spectral shaping, but by scanning t_2 instead of t_1. As demonstrated previously, both of these spectra can be used to isolate the portion of the signal which is generated by coherent superpositions of excitons localized in different QWs, while suppressing population pathways.

Fig. 7.3a shows the excitation spectrum, and FWM signal from Al_2 at $t_1=t_2=0$. Fig. 7.3b shows a 1Q 2D spectrum for Al_2 when broadband excitation is used. Fig 7.3c and Fig 7.3d show 1Q and 0Q 2D spectra (respectively) when spectral shaping has been used to isolate the inter-well coherent superposition CPs (CS-CPs). The excitation densities for these 2D spectra are given in the caption.

The excitation density dependence for this sample is shown in Fig. 7.4. Unlike Al_1, the DPs do not show an $\mathbf{E}^3$ dependence across the entire measured range. Indeed, it only appears to follow $\mathbf{E}^3$ from around $1 \times 10^{10} cm^{-2}$ to $1 \times 10^{11} cm^{-2}$. Above $1 \times 10^{11} cm^{-2}$, the signal falls off - presumably due to EID (which results in faster dephasing and hence less total signal) and/or $\chi^{(5)}$ signal[6]. Below $\sim 1 \times 10^{10} cm^{-2}$, the DPs diverge significantly from the $\mathbf{E}^3$ line, following a clearly sub-$\mathbf{E}^3$ dependence which is qualitatively very similar to the CPs. This change in dependence on excitation density will be discussed in more detail in the following section.

Like Al_1, this sample shows a clearly sub-$\mathbf{E}^3$ (in fact, closer to $\mathbf{E}^1$) dependence for the inter-well CPs. The signals for two of the intra-well CPs has also been plotted (green and blue triangles). Unlike the inter-well CPs, the intra-well CPs follow a nearly $\mathbf{E}^3$ dependence, similar to the DPs. This suggests that the nearly linear dependence of the inter-well CPs on excitation density is not a change in the prevalence of exciton interactions generally, but instead is specifically related to excitons localized in separate QWs. Furthermore, this striking difference between the intra-well

5 The size of the 2D interface roughness 'islands'. The size of these islands has been shown to vary between 1 nm and 1000 nm on average depending on the growth parameters [146, 149, 285, 286].

6 Although a pure $\chi^{(5)}$ signal should have an $\mathbf{E}^5$ dependence, the interference between $\chi^{(5)}$ and $\chi^{(3)}$ signals can lead to a sub-$\mathbf{E}^3$ dependence, which is likely part of the cause of the divergence at high excitation density.

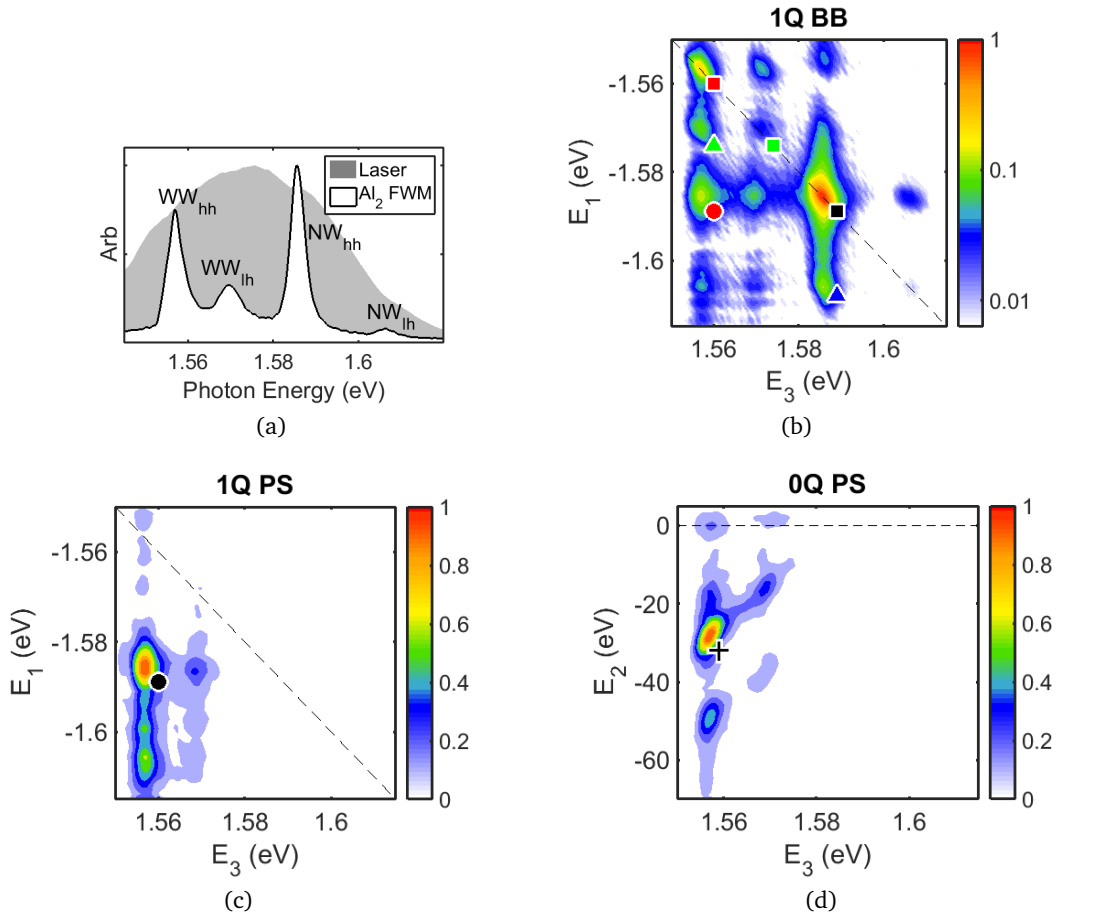

Figure 7.3: (a) Excitation spectrum for Al_2 density dependence (Fig. 7.4) and an Al_2 FWM spectrum at $t_1 = t_2 = 0$. (b-d) shows 2D spectra at a selected excitation density. (b) 1Q BB at 7×10^{10} cm^{-2}, (c) 1Q pathway selective at 5×10^{10} cm^{-2}, (d) 0Q pathway selective at 5×10^{10} cm^{-2}. The excitation spectra in the pathway selective experiments are shaped to isolate the inter-well CS-CPs. The symbols by the peaks are used to plot the power dependence of the peaks in Fig. 7.4.

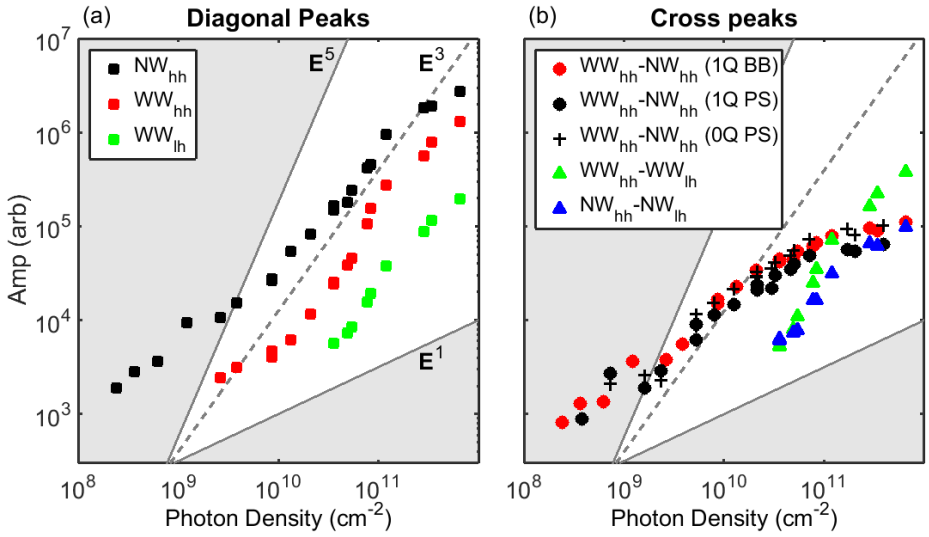

Figure 7.4: Excitation density dependence of AlGaAs/GaAs sample Al_2 for various 1Q and 0Q peaks: (a) DPs and (b) CPs. The inter-well (filled circles and crosses) and intra-well (triangles) CPs in (b) show very different dependence on excitation density. The peaks associated with the amplitudes plotted in (a) and (b) are indicated by the placement of symbols in Fig. 7.3b-d

and inter-well CPs also suggests that the inter-well and intra-well interactions are mediated by different coupling mechanisms.

The results of the pathway selective 1Q and 0Q spectroscopy (black filled circles and black crosses) show the same power dependence as the BB 1Q inter-well peaks. Furthermore, the 1Q PS peak and 1Q BB inter-well peaks are nearly the same amplitude. This suggests that the bulk of the BB inter-well CP signal amplitude is a result of the coherent superposition pathway.

To summarize this result, we have performed the same power dependence measurements on two AlGaAs samples, which have both demonstrated inter-well CPs that follow a clearly sub-$\mathbf{E}^3$ dependence on excitation density, while DPs and intra-well CPs more closely follow an $\mathbf{E}^3$ dependence on excitation density. In Al_2, we have shown that the bulk of the inter-well signal is a result of coherent superpositions of excitons localized in different QWs through a comparison of 1Q BB, 1Q PS and 0Q PS measurements.

7.2.2 *An extended delocalized exciton state in Al_2*

In addition to the anomalous power dependence, sample Al_2 also demonstrates changes in peak-shapes as a function of excitation density. Selected 2D spectra at a range of different densities are shown in Fig. 7.5. The WW_{hh} and the NW_{hh} DPs both are tilted along the diagonal due to inhomogeneous broadening at intermediate and high density, but the peaks become much rounder as the density is reduced. It is typically reported that DP broaden along the cross-diagonal direction as excitation density is *increased* due to exciton-exciton interactions which shorten the pure dephasing time and broaden the homogeneous linewidth[46, 216]. As expected, we do see broadening of the tilted peak at high density. At low excitation densities, the homogeneous linewidth is commonly shown to continue narrowing as exciton-exciton interactions play a smaller role in dephasing of the excitons. The broad, round peaks we report here at low density are therefore the *opposite* of what is typically expected for the coherent response of dilute excitons. However, we also go to lower excitation densities than previous experiments.

In this section, we will first demonstrate through frequency-domain and time-domain analysis that the DP-shapes we see here are the result of two distinct signals - one which leads to a round peak and one which leads to a tilted peak. Although the WW_{hh} and the NW_{hh} both demonstrate similar peak-shape changes, we focus in this section on the NW_{hh} peak because it can be detected over a larger range of densities. We show that the changes to the peak-shape that we observe are a result of the relative amplitude of these two contributions changing. Combining results from the fits to the peak-shape with the excitation density dependence data in Fig. 7.4a, we show that the tilted peak follows the expected $\mathbf{E}^3$ dependence while the round shaped peak follows a sub-$\mathbf{E}^3$ (nearly linear) dependence. Furthermore, we

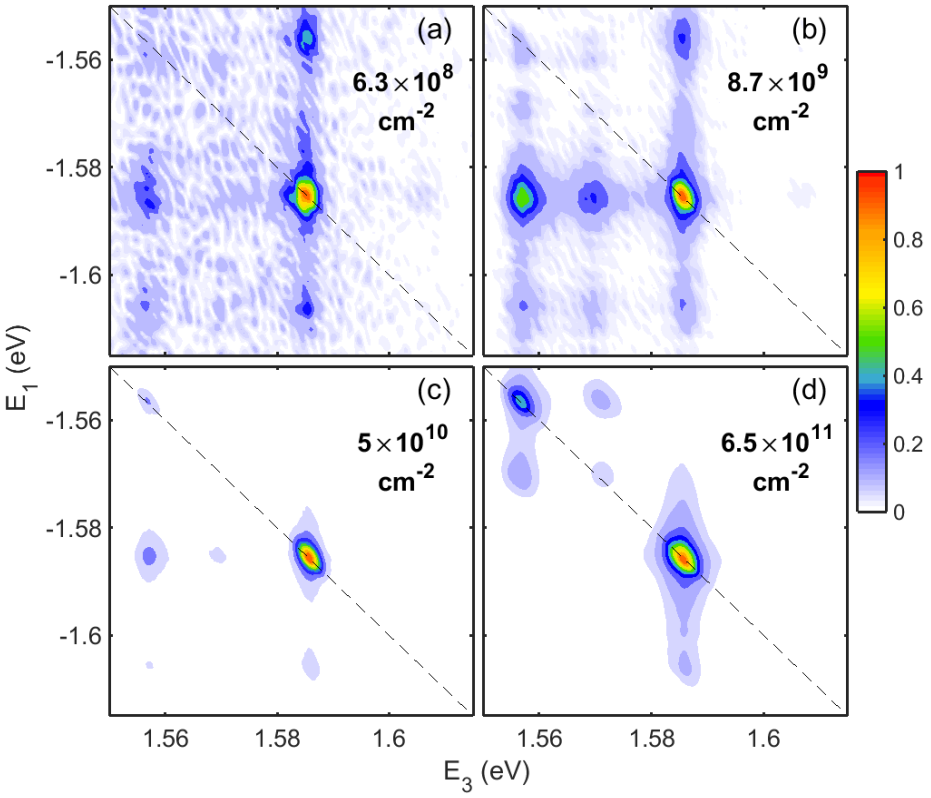

Figure 7.5: 2D spectra for AlGaAs DQW sample Al_2 at a range of different excitation densities.

show that the density dependence of the round peak is nearly the same as that of the inter-well CPs, suggesting that the two signals are related.

Before continuing on the detailed analysis of these peak-shapes, we will describe how round and tilted DP shapes are typically interpreted in QWs. The tilted peak-shapes we see at intermediate densities here are typical of disordered QWs. They are typically interpreted as ensemble averages of excitons (with narrow homogeneous linewidths) in different regions of the QW with different widths. The ensemble average across the Gaussian distribution of QW widths results in inhomogeneous broadening of the otherwise spectrally narrow exciton line. In 2D spectroscopy, this results in peaks tilted along the diagonal with a width along the diagonal equal to the inhomogeneous width and a cross-diagonal width equal to the homogeneous linewidth. On the other hand, round peak-shapes are taken to indicate that the inhomogeneous broadening is negligible compared with the homogeneous broadening. In the data presented here, the linewidths of the round and tilted peak-shapes along the diagonal are comparable. This suggests that the homogeneous linewidth of the round peak (which dominates at low excitation densities) is roughly equal to the inhomogeneous linewidth of the tilted peak (which dominates at intermediate and high excitation densities).

A zoomed in view of the NW_{hh} peak is plotted in Fig. 7.6a-d. It is hard to tell just by looking at the peak-shapes whether this change in shape is the result of a single signal whose E_1 linewidth is changing as a function of the excitation density or a combination of two signals whose relative contributions to the peak change.

To separate these two possibilities, the peaks were fit by two different 2D functions. First, the peaks were fit to Eq. 7.1, which represents a single tilted peak:

$$S(E_3, E_1) = C_1 + \exp\left[\frac{-(E_3-\mu_3)^2}{2\sigma_3^2}\right] \cdot \left[\frac{\Gamma_T^2}{(E_1-(-E_3-\delta))^2+\Gamma_T^2} + C_2\right] \tag{7.1}$$

The inhomogeneous broadening is represented by the first term which is a Gaussian distribution centred at μ_3 with a width σ_3. This term is multiplied by a Lorentzian function representing the homogeneous broadening centred along the diagonal with a width equal to Γ_T. δ allows for a slight shift of the peak away from the diagonal. C_1 is a constant offset to account for background signal. The constant C_2 provides an additional offset which is Gaussian in E_3 but independent of E_1. The physical origin of this signal is a very broad CP which overlaps the NW_{hh} DP. This signal corresponds to coupling of free carriers in the wide well to NW_{hh} excitons. This broad feature can be more clearly seen in Fig. 4.4, and only contributes very weakly here.

The other possible explanation for the changing peak-shapes is that the broadening at low density is due to a combination of two different peaks (one round, one tilted) which have different excitation density dependences. In Eq. 7.2 an extra term is added to account for this possibility.

$$\begin{aligned} S(E_3, E_1) = C_1 + A_T \cdot \exp\left[\frac{-(E_3-\mu_3)^2}{2\sigma_3^2}\right] \cdot \left[\frac{\Gamma_T^2}{(E_1-(-E_3-\delta))^2+\Gamma_T^2} + C_2\right] \\ + A_R \cdot \frac{\Gamma_R^2}{(E_1+\mu_R)+\Gamma_R^2} \cdot \frac{\Gamma_R^2}{(E_3-\mu_R)+\Gamma_R^2} \end{aligned} \tag{7.2}$$

The additional term (which accounts for the round peak) is a 2D Lorentzian distribution, centred at μ_R with a width equal to Γ_R in E_1 and E_3. A_T and A_R are the relative amplitudes of the tilted and round peaks, respectively.

The results of fits to Eq. 7.1 and Eq. 7.2 for different excitation densities can be seen in Fig. 7.6e-h and Fig. 7.6i-l respectively. When fit to Eq. 7.1, the round-ness of the peak at low intensities results in an increase of the cross diagonal width (Γ_T). As can be seen from the plots in Fig. 7.6e-h, this does not agree particularly well with the experimental data.

The results of the two component fits (Fig. 7.6i-l) show better agreement with the experimental data, and better capture the round peak-shapes at low density. Beyond the visual comparison, the quality of the fits can be assessed based on their root-mean-squared error (RMSE), which can be seen in Fig. 7.7a. Clearly Eq. 7.2 results in a better fit with reduced RMSE across all excitation densities. The increase of the RMSE of both fits at low densities is likely a result of the decreased signal to noise ratio of the data, rather than the quality of the fit.

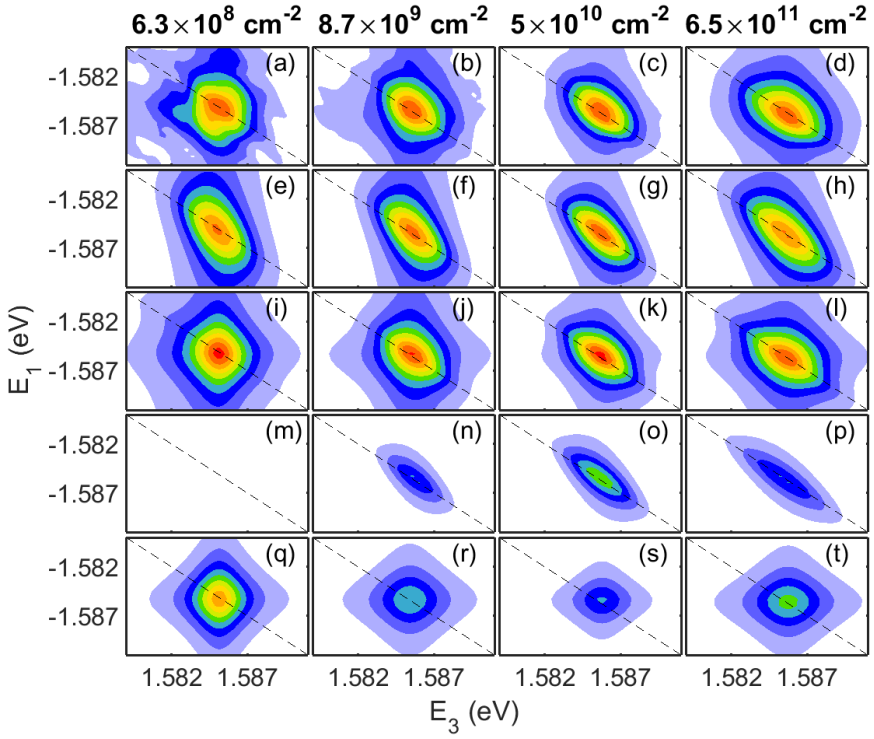

Figure 7.6: (a-d) A zoomed-in plot of the Al_2 NW_{hh} peak-shape at the same densities plotted in Fig. 7.5. (e-h) fits of the data in (a-d) to Eq. 7.1 which is a single tilted peak. (i-l) fits the data in (a-d) to Eq. 7.2 which is the combination of a tilted (m-p) and a round (q-t) peak.

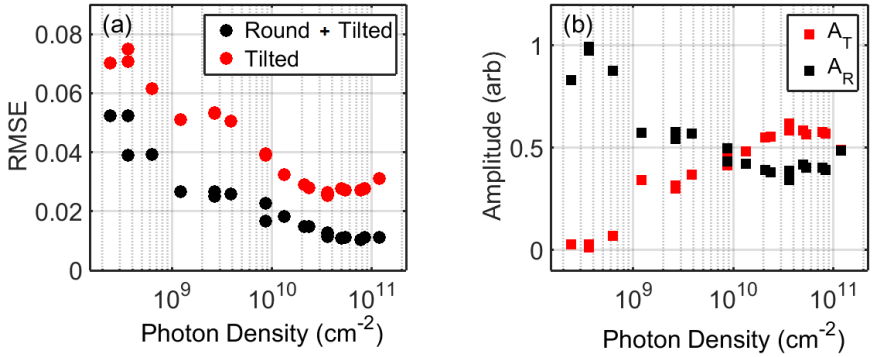

Figure 7.7: (a) Root mean squared error of the fits to Eq. 7.1 (tilted) and Eq. 7.2 (tilted + round). (b) Coefficients for the amplitude of the tilted (A_T) and round (A_R) peaks taken from the fit to Eq. 7.2.

The resulting A_R and A_T amplitude coefficients across the full set of data are plotted in Fig. 7.7b. It is clear that between $10^9 cm^{-2}$ and $10^{10} cm^{-2}$ there is a significant change in the relative amplitude of the tilted and round signals: the tilted peak diminishes and the round peak increases as the density is reduced.

Based on these frequency-domain fits we conclude that these peak-shape changes are a result of contributions from two separate exciton sub-populations, whose relative amplitudes change with excitation density. To confirm this conclusion, we can equivalently explore this effect in the time domain instead of the frequency domain. Based on the different peak-shapes (round vs diagonal) we would expect the t_3 dynamics of the two sub-populations to be quite different. The round peak should have a free polarization decay (FPD) signal which has a rapid rise after the third

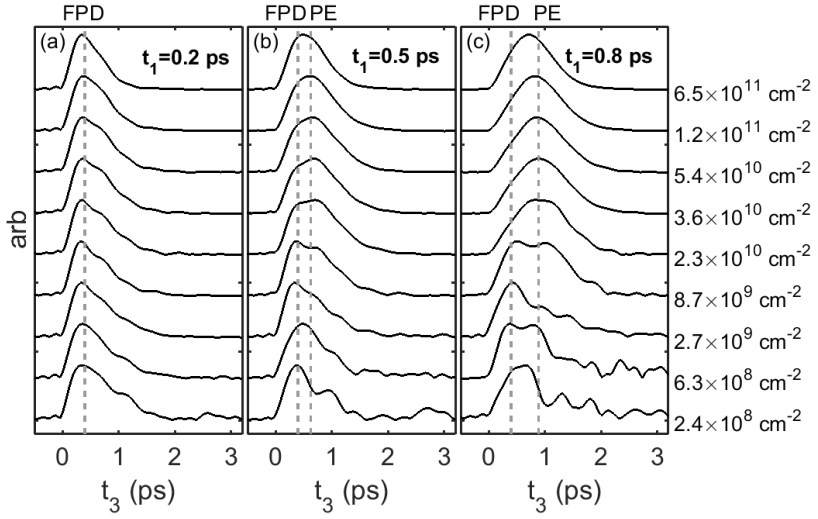

Figure 7.8: Time domain representation of the Al_2, NW_{hh} DP 2D. A series of plots as a function of t_3 and the excitation density for different t_1. All the peaks have an FPD shape at t_1 = 0.2 ps (a) as no photon echo has formed. At t_1 = 0.5 ps (b) and t_1 = 0.8 ps (c), the peaks at high density have a PE shape, while peaks at low density have an FPD shape.

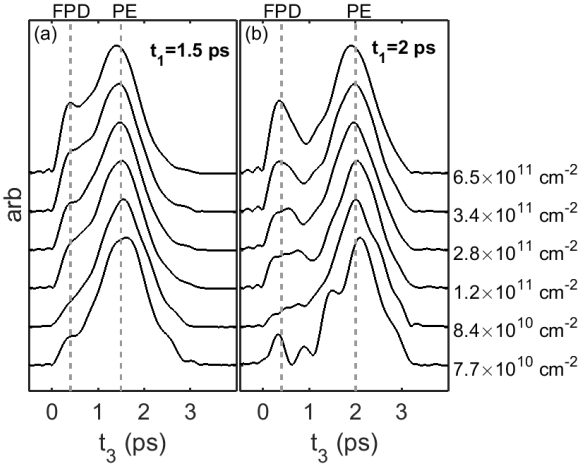

Figure 7.9: Time domain representation of the Al_2 NW_{hh} DP for high excitation densities at t_1 = 1.5 ps (a), t_1 = 2 ps (b). Although PE dominates, there is also a re-emergence of the FPD signal at the highest densities.

pulse followed by an exponential decay. The tilted peak-shape on the other hand should have a photon echo (PE) like signal in the time domain, appearing as a peak centred at t_3=t_1, which has a Gaussian shape in t_3 (except at short t_1, in which the photon echo overlaps the third pulse in t_3). We should, therefore, be able to separate and identify the FPD and PE contributions by looking at the signal as a function of t_3 for different t_1 and at different excitation densities.

To analyse the data in the time domain, we window out everything in the 2D spectrum except for the NW_{hh} DP and then apply a 2D inverse Fourier transform. The time domain data is presented in Fig. 7.8 as plots of t_3 for different t_1 and different excitation density. At t_1=0.2 ps (Fig. 7.8a), all the signals have FPD like shapes. At this short delay, the photon echo mostly overlaps the third pulse and has not yet fully formed. When t_1 is increased to 0.5 ps (Fig. 7.8b), and then 0.8 ps (Fig. 7.8c) more of the photon echo is visible. At the intermediate and higher powers, we

see a partially formed photon echo. At lower densities, an FPD signal with an earlier peak begins to appear. At $\sim 1 \times 10^{10} cm^{-2}$ the two contributions are roughly equal, and the signal has a flat topped shape which is a combination of the FPD and PE. At the lowest recorded densities, the signal appears to be almost completely FPD.

At the intermediate densities ($5 \times 10^9\, cm^{-2}$ to $5 \times 10^{10}\, cm^{-2}$) it is difficult to fully separate the FPD and PE contributions. As t_1 increases and the photon echo is more well separated from the final pulse, but the FPD is also nearly fully decayed. This is unavoidable by definition: the width of the PE and the decay of the FPD signal are both dictated by the inhomogeneous linewidth. However, in some cases and at high powers, the FPD and PE contributions can be separated as has been demonstrated previously by Weber et al [157]. They saw this effect only at high excitation densities ($5 \times 10^9 cm^{-2}$ excitons per well) but not at low excitation densities ($5 \times 10^7 cm^{-2}$ excitons per well). They were unable to explain the presence of this signal, but suggested it may have to do with either a delocalized exciton state or different regions of the samples which have different degrees of interface roughness. This result is similar to what we have demonstrated here except that in the results presented thus far the FPD appears at low power instead of high power. As it turns out, in sample Al_2 we also see the same effect at the highest powers. Figure 7.9 shows t_3 plots at $t_1 = 1.5\,ps$ (a) and $t_1 = 2\,ps$ (b) at the highest excitation densities. Both FPD and PE signals are clearly present. Assuming an absorption of around 1% for the the exciton transition, the excitation density in which we see the change from FPD to PE at high density would correspond to around the same excitation density reported in [157].

Sample Al_1 NW_{hh} DP does *not* have a round shape at any excitation density, so it should not have any FPD signal in the time domain. For comparison with Al_2, selected plots of the amplitude of the inverse Fourier transformed Al_1 NW_{hh} DP are plotted as a function of t_3 for various t_1 values and excitation densities in Fig. 7.10. Unlike Al_2, the t_3 signal here is predominately PE, even at the lowest and highest densities. There are some indications of FPD below $\sim 3 \times 10^9 cm^{-2}$, visible just above the noise, but still much lower in amplitude than the PE signal. Thus, the time domain and frequency domain analysis for Al_1 are consistent, and both indicate a photon echo signal across all excitation densities.

The results of the frequency and time domain analysis also both support the assertion that there are two signals contributing to the coherent response of the NW_{hh} transition in Al_2. The physical origin of these signals will be discussed later, but they likely represent different exciton populations [157].

The transition from a predominately PE peak-shape to a predominately FPD peak-shape and the deviation from an $\mathbf{E}^3$ excitation density dependence both occur at $\sim 1 \times 10^{10} cm^{-2}$. From this similarity, we infer that the FPD signal has a sub-$\mathbf{E}^3$ density dependence while the PE signal has a roughly $\mathbf{E}^3$ density dependence. We can test this inference by estimating the density dependence of each sub-population. This is accomplished by scaling the measured NW_{hh} DP density dependence according to

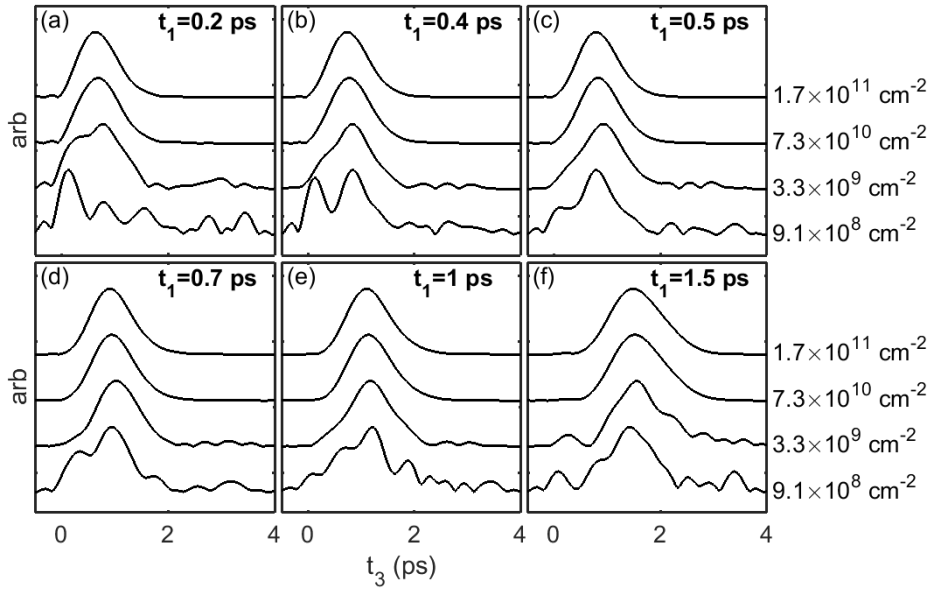

Figure 7.10: Time domain representation of the Al_1 NW_{hh} DP across the full range of measured excitation densities. We observe a PE dominated response across all densities. There is some indication of FPD in the at the lowest density, but it is near the noise limit and much weaker than the PE signal.

the fits from Fig. 7.7. The PE (FPD) fraction is calculated by multiplying the NW_{hh} signal by the ratio $I_{FPD}/[I_{PE}+I_{FPD}]$ ($I_{FPD}/[I_{PE}+I_{FPD}]$) where I_{PE} and I_{FPD} are the integrated photon echo peak Fig. 7.7m-p and FPD peak from 7.7q-t, respectively. When we apply this scaling we get the dependencies shown in Fig. 7.11, which show the as-measured data (black circles), the same data scaled for FPD (red circles) and PE (green circles) sub-populations. The as-measured data for the inter-well CP is also plotted (blue circles). The coloured solid lines are exponential fits of the different datasets. From this plot, it is clear that the PE signal follows a nearly $\mathbf{E}^3$ dependence, while the FPD signal follows a sub-$\mathbf{E}^3$ dependence, which closely matches the dependence of the inter-well CPs.

We now take a moment to re-iterate some of the main results from Al_1 and Al_2. Al_1 (which shows nearly pure PE signal based on the DP shape) demonstrates an excitation dependence which very closely follows $\mathbf{E}^3$. The PE fraction of Al_2 also closely follows $\mathbf{E}^3$. On the other hand, the FPD fraction of the Al_2 DP matches the same sub-$\mathbf{E}^3$ dependence of the CPs. Taken together, this suggests that the inter-well CPs arise (at least in part) from the same sub-population of exciton states that result in the round DP.

But what is the physical origin of this additional sub-population? At this point the answer to this question is not entirely clear. Further experiments and theoretical investigations are needed to narrow down several possibilities. In the following paragraphs (with these caveats in mind) we propose the following explanation for the FPD signal: that it is generated by the coupling of multiple localized exciton states which can equivalently be viewed as a single extended, delocalized state

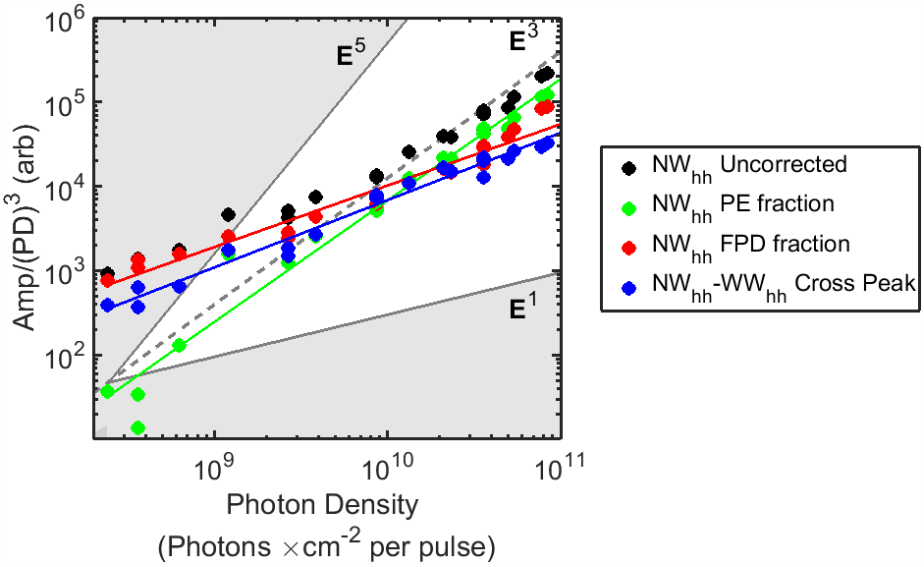

Figure 7.11: Al_2 NW_{hh} density dependence of the as measured data (black circles) and the measured data scaled according the A_R and A_T fit coefficients (red and green circles, respectively) in Fig. 7.7 to separate the FPD and PE signals, respecively. The inter-well CPs (blue circles) are also plotted. The solid colored lines represent single exponential fits to the data. The PE fraction goes roughly with $\mathbf{E}^3$, while the FPD fraction goes with the same sub-$\mathbf{E}^3$ dependence of the inter-well CP.

(EDS). There is, however, further work that is needed before this conclusion can be satisfactorily proven, and we recognize there may be alternative explanations.

The tilted/PE peak-shapes are typically taken to imply excitons with a homogeneous linewidth much smaller than the inhomogeneous linewidth. We therefore take the high density signal to arise from homogeneously broadened excitons localized in regions of the QW with well-defined widths, but which exhibit inhomogeneous broadening when a large ensemble is measured.

The round/FPD peak-shape can then be explained through the coupling of separately localized exciton states in parts of the well with different widths and with correspondingly different central transition energies (e.g. E_A and E_B). The coupling of an exciton with transition energy E_A to an exciton with energy E_B leads to CPs at (E_3, E_1) = (E_A,-E_B) and (E_B,-E_A) with widths along E_1 and E_3 equal to the homogeneous linewidth. If E_A and E_B both represent excitons in different parts of a QW, then they could each independently represent any energy within the inhomogeneous linewidth. If both E_A and E_B are integrated stochastically across the inhomogeneous linewidth, these CPs merge with the DP to form a single round peak centred on the diagonal with a width equal to the inhomogeneous linewidth. The signal resulting from these coupled excitons can then be viewed as the collective interaction of an ensemble of exciton states with the light rather than an ensemble of localized states interacting individually.

In a qualitative way, this collective interaction with light is similar to superradiance, a concept in quantum optics (first proposed by Dickey in 1954 [287]), which predicts an enhancement of the transition dipole moment of collective coherent

states compared with the sum of the emission from the individual states. Superradiance was originally explored theoretically and demonstrated experimentally in atoms [288]. It has since been extended to ions [289], Bose-Einstein condensates [290] and more recently self-assembled quantum dots [291]. The enhanced coupling of the collective state to the light field leads to much shorter photoluminescence decay times and larger absorption and fluorescence yields. The results presented in Fig. 7.11 at low excitation density show a significant enhancement of the FPD signal with respect to the PE signal. This is consistent with our interpretation of the FPD representing signal from a superradiant-like collective state and the PE representing signal from individual localized states.

In atomic systems, the individual emitters are all identical, so the superradiant emission is not different from the emission line-shape of the individual atoms[288]. On the other hand, the emitters that make up the collective state in this QW have a range of different emission energies. As a result, the collective state has some different properties than the individual states; the most notable difference being that the homogeneous linewidth broadens to match the inhomogeneous linewidth. In Ref. [291] they report superradiant emission from inhomogeneously broadened quantum dots. While they do not measure the homogeneous linewidth of the superradiant state or the individual emitters, they note that as long as the homogeneous linewidth is broader than the energetic separation of the dots, the radiative coupling required for superradiance can be achieved. That criteria is likely met for the NW_{hh}, as it has a homogeneous linewidth of $\sim 0.6\,meV$.

As the density increases, the signal from the localized states increase with $\mathbf{E}^3$. Since superradiant emission scales with the n^2 (where n is the number of coupled emitters) we might expect that the superradiant state would increase with $\mathbf{E}^6$. This is very different from the excitation dependence we observe for the collective state ($\sim \mathbf{E}^1$). This discrepancy can be understood qualitatively as follows. The dipole moment of the collective state depends on the number of exciton states that make up the collective state (i.e. the number of emitters). The number of localized states that can be involved in the collective state depends on the range over which the coherent interactions extend. As the excitation density is increased, exciton screening prevents the interactions of distant excitons. The reduced interaction distance leads to a fewer localized states in the cooperative state and consequently a reduced dipole moment.

The criteria used for identifying Dickey superradiance is typically a signal that increases with the square of the number of emitters ($S \propto n^2$). We cannot determine whether this condition is met in the data presented here, as the suppression of the collective state through carrier screening complicates the determination of the number of coupled emitters. Further experiments and theoretical studies are needed to fully understand the interplay of these two competing factors affecting the number of coupled excitons and the spectral variation.

A complementary way to understand the power dependence of the FPD signal is using the concept of coherence area [220, 292–294] - which has been explored in the context of self assembled quantum dots [293], QWs [292, 294] and nanoplatelets [215, 220]. It has been shown that the dipole moment of excitons in self assembled quantum dots is dependent on the lateral size the dot (d) relative to the exciton Bohr radius (α_B). The dipole moment is found to be large for $d \ll \alpha_B$ and $d \gg \alpha_B$ [293]. Similarly, it has been shown in QWs that increasing extension of the centre of mass motion of the wavefunction can lead to an enhancement of the dipole moment [292, 294]. This enhancement in QWs with large coherence area was explained by the effective lateral size of the exciton (which is called the coherence area) increasing in the plane of the QW.

The coherence area concept can be qualitatively applied to explain the EDS in our results in the following way. At low densities, the coherence area of the excitons is large relative to the Bohr radius. Based on the argument given above, the round peak-shape could be a result of coherent coupling of excitons which are spatially separated in the plane of the QW. Since at low densities these coupled excitons might be separated by μm distances, we can assume that the centre of mass wavefunction of the excitons (and therefore the coherence area) is much larger than the standard exciton Bohr radius. Due to the Pauli exclusion principle, multiple excitons cannot share the same state, so as the density of the excitons increases the size of the exciton center of mass wavefunction (and the coherence area) necessarily decrease [295, 296]. This shrinking of the coherence area then reduces the transition dipole moment, and the signal from this state therefore follows a sub-$\mathbf{E}^3$ dependence on excitation density. As with superradiance, it is not yet clear whether the results here quantitatively match the expected density dependence on coherence area.

It is worth noting that this result - a large coherence area at low exciton density - is apparently in contradiction with previous micro-photoluminescence experiments which have observed emission dominated by localized states at low densities, and only observe emission dominated by non-localized states at densities much higher than we report here[297–300]. We contend that these results are not contradictory, however, because the previous experiments at low excitation densities are time integrated incoherent emission experiments, whereas the experiment here is time resolved and involves coherent emission. An extended state would likely relax into a single localized state before photoluminescence, and would therefore be more difficult to detect in an emission experiment. An alternative way of looking at this would suggest that the coherently coupled emitters would lose their phase coherence rapidly and effectively become isolated, localized emitters once again. We would therefore expect photoluminescence emission from our sample to come from a localized state even if a delocalized state with large coherence area was originally excited. In the current experimental setup we do not have enough spatial

or spectral resolution to resolve the emission lines from individual localized states, so we cannot make such a measurement.

Such EDS has been invoked by Kazprzak et al to explain long range (approaching μm length scales) coupling between excitons localized to different monolayer islands [73]. Their explanation relied on radiative coupling of excitons which inhabit different parts of the same mesoscopic monolayer island in a sort of laterally localized polariton. This explanation relies on the radiative coupling renormalization energy exceeding the residual disorder potential, which it clearly does for the nearly atomically flat interfaces in the MBE grown QW used in that experiment. How these values would compare for a far more disordered sample such as the MOCVD grown Al_2 is less clear, and a calculation would have to include the typical length scales of the disorder which are unknown for this sample. Other papers have detected coherent coupling between excitons localized to different monolayer islands, which could be mediated by a delocalized state as described by Kazprzak [44, 46, 181]. However, these experiments lacked the spatial resolution to determine the distances between the excitons, and focused on weakly disordered MBE grown samples, so they are not necessarily relevant to the current results.

We note again that the FPD exciton sub-population and the inter-well signals have roughly the same sub-$\mathbf{E}^3$ excitation dependence, which suggests that the inter-well coupling also involves an EDS in both QWs. Speculatively, one plausible explanation of the involvement of EDS in the inter-well coupling is in the geometry of the exciton states. Dipole-dipole coupling between two point dipoles separated by a distance r goes with $1/r^6$ [301, 302]. The localized excitons are spherical and relatively small in size compared with the separation of the wells, suggesting that the point dipole approximation is reasonable. The EDS, however is larger in the plane of the QW than in the out of plane directions (i.e. like a disk). The large lateral extent, which is much larger than the QW separation means that the point dipole approximation is no longer reasonable. Coupling between two aligned planar dipoles (or disk dipoles) should thus scale differently with separation than point dipoles, and likely with a lower power (i.e. $1/r^{<6}$). A calculation of the exact expected dependence of the coupling of disk dipoles will be conducted in future work, but this could explain in part why the inter-well coupling appears to be related to the EDS.

In the other two samples discussed in this chapter we do observe evidence of a sub-$\mathbf{E}^3$ dependence of the inter-well signals, but no evidence of a round component of the DP[7]. The round DP itself, however, isn't a requirement for there to be a delocalized state, but rather an indicator that only occurs when the in-plane size of the delocalized state is large compared with the in-plane size of the disorder (i.e. the in plane size of the monolayer islands). In other words, the EDS state might appear in the other samples as well, but we just cannot separate it from the other PE pathways. Therefore the lack of a round DP does not in itself preclude the

7 We do see some indication of FPD in Al_1 at low densities, but it is difficult to differentiate from the noise floor, and is clearly much weaker relative to the PE than the FPD in Al_2.

inter-well and QW-barrier coupling in these other samples from being related to an in-plane delocalized state. However, the lack of sub-$\mathbf{E}^3$ signal in the DPs of the other two samples is unexplained and merits further investigation.

7.3 Excitation density dependence of the 10 nm barrier InGaAs/GaAs DQW

We have also measured the excitation dependence of 1Q, 0Q and 2Q spectra for the 10 nm barrier InGaAs DQW sample which we have studied extensively in previous chapters in this thesis (Ch. 4, Ch. 6, Ch. 5). A number of 2D spectra (1Q, 0Q, 2Q) representing the high, middle and low ends of the excitation range are shown in Fig. 7.13 (a,d,g) (b,e,h) and (c,f,i) respectively. Each spectrum is normalized according to the highest signal in the spectrum and plotted over the same logarithmic color range. The excitation spectrum and sample FWM spectrum is shown in Fig. 7.12. The CMDS experiments were performed with collinear polarized beams.

The spectra change in several significant ways as a function of excitation density:

1. The WX and NX line-shapes broaden at higher density, most notably for 1Q and 2Q, but also 0Q DPs.
2. Fringes appear across all the signals with emission in WX and NX at high density for all three types of 2D spectra. These fringes may be due to interference between $\chi^{(3)}$ and $\chi^{(5)}$ signals.
3. Many of the interaction signals (particularly the above diagonal ones) are much more evident at low powers. Of these signals, the clearest increase comes in the 0Q inter-well coherent superposition signals. These peaks are invisible at high powers, but grow in significantly at lower powers (at the lowest power, the strength of the WX diagonal and (WX-NX) CP are comparable).
4. The DP and CP shapes in the 2Q spectra change from un-tilted and broad along E_{2Q} at high power to tilted and narrow along E_{2Q} at low power.
5. The relative intensities of the WX and NX DPs flip at low power in all three types of spectra.

Items 1 and 2 are not surprising, but tell us that at the highest intensities we are moving into a regime where $\chi^{(5)}$ and excitation induced broadening are important. Item 3 is more surprising. It is telling us that the relative strength of the peaks that represent WX-NX interactions and WX/NX-BarX interactions are increasing relative to the DPs as the power is reduced. This indicates either a sub-$\mathbf{E}^3$ density dependence for the inter-well signals (similar to what we observed in the AlGaAs DQWs in Section 7.2.1) or a super-$\mathbf{E}^3$ dependence for all the other signals. The rest of this section will differentiate between these two possibilities and look into this effect in more detail. Item 4 will be discussed in detail in Section 7.3.1. Item 5 will not be

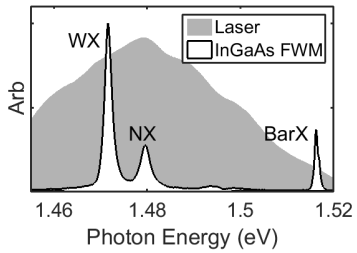

Figure 7.12: The FWM emission spectrum at $t_1=t_2=0$ and the spectrum of the excitation beams used for the 2D spectra in Fig. 7.13 and for measurements of the dependence on excitation density in Fig. 7.14, 7.15 and 7.16.

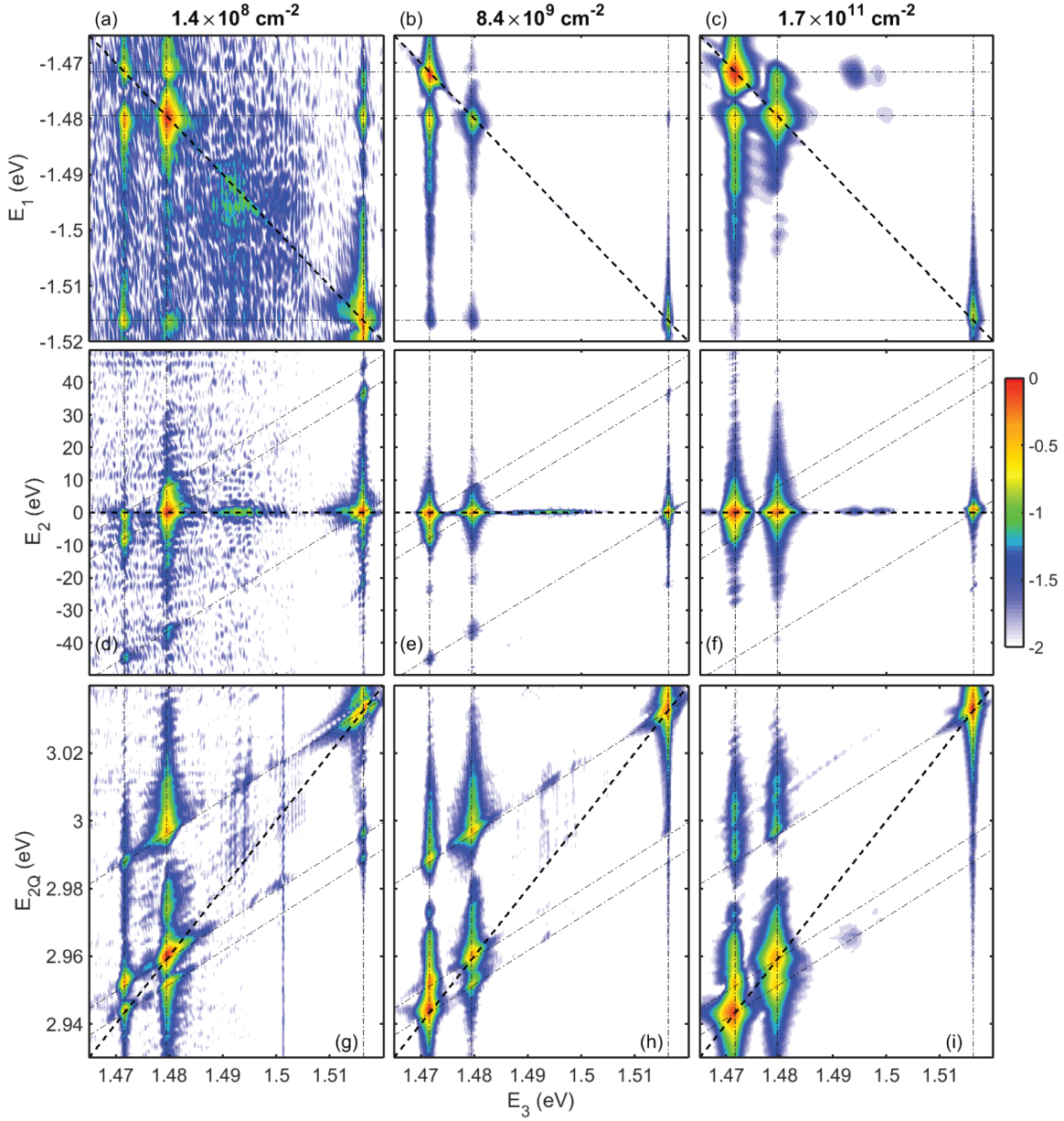

Figure 7.13: 1Q (a-c), 0Q (d-f) and 2Q (g-i) 2D spectra for low (a, d, g), mid (b, e, h), and high (c, f, i) excitation densities. Changes in the spectra are discussed in the text.

discussed in detail in this thesis, but is an interesting effect as it suggests that the relative dipole moments of the different transitions are excitation dependent. We will attempt to address this effect with simulations in future work.

The increase of the 0Q CPs relative to the DPs is perhaps the most interesting change we see at low densities. In previous experiments on this sample with higher excitation density ourselves (Ch. 4) and Nardin et al [54] were not even able to detect inter-well coherences when using broadband excitation.

For now, we are not interested in the 2D peak-shapes, so it is more convenient to discuss the data as slices of the 0Q 2D spectra at different emission energies. Slices along E_2 at emission energies corresponding to WX, NX and BarX are plotted in Fig. 7.14a-c, respectively. At each emission energy, we observe three peaks marked by vertical dotted lines. There is one main peak at $E_2=0$ meV (population pathways) as well as two peaks at $E_2 \neq 0$ (where we expect to see coherence pathways), which become more clear at lower powers[8]. At the highest powers, the WX-NX coherence and NX-WX coherence CPs are small shoulders on the $E_2=0$ population peak[9]. As the power is reduced, these shoulders grow in to fully fledged peaks, even surpassing the $E_2=0$ peak for the E_3=WX at the lowest powers. The tails of the Lorentzian $E_2=0$ peak can be seen all the way out to the $E_2 = \pm 40$ meV where we see the BarX-WX/NX coherences. These BarX-WX/NX coherences are completely missing at the highest power, and only grow in as the excitation density drops into the 10^{10} photons$\times$cm^{-2} per pulse range.

In all three types of 2D spectra, the increase of the CP amplitude relative to the DP amplitude could indicate that the DPs follow a super-$\mathbf{E}^3$ excitation dependence, that the CPs have a sub-$\mathbf{E}^3$ dependence, or both.

Figure 7.15a shows the measured density dependence of the WX DP in the 1Q spectrum. The deviation from $\mathbf{E}^3$ dependence can be more clearly seen when signals are divided by third power of the photon density, which has been done in Fig. 7.15b. In this plot, $\mathbf{E}^3$ dependence is indicated by the horizontal line, linear and fifth order signals are now indicated by the solid grey lines angling up and down, respectively. This signal generally follows the expected $\mathbf{E}^3$ dependence, with some non-uniform deviations which are be discussed further on.

Figure 7.16 shows the power dependence of the various signals divided by the third power of the photon density (as in Fig. 7.15b). The three rows are signals from the 1Q, 0Q and 2Q spectra, respectively. The first column shows the amplitude of the DPs (located on the $E_1=-E_3$ line in the 1Q, on the $E_2=0$ in the 0Q and on the

8 There are also peaks corresponding to interactions with the βX states discussed in Ch. 6. This chapter is focusing on the inter-well and BarX-QW interactions, so we will ignore these for now.

9 It might seem surprising that we can detect inter-well CPs here, even at high density when we could not detect them using broadband 2D spectroscopy in Ch. 4. These results can be reconciled in three ways: 1. the 0Q spectrum reported previously is actually a 3D spectrum projected onto the E_2 vs E_3 plane, which could in certain circumstances introduce additional noise. 2. We made improvements to the environmental stability of the lab between the two experiments (which were separated by about 6 months), which improved the experimental signal to noise. 3. There is some variability from spot to spot on the sample. The results presented in this chapter were recorded consecutively over the course of two days at the same position on the sample.

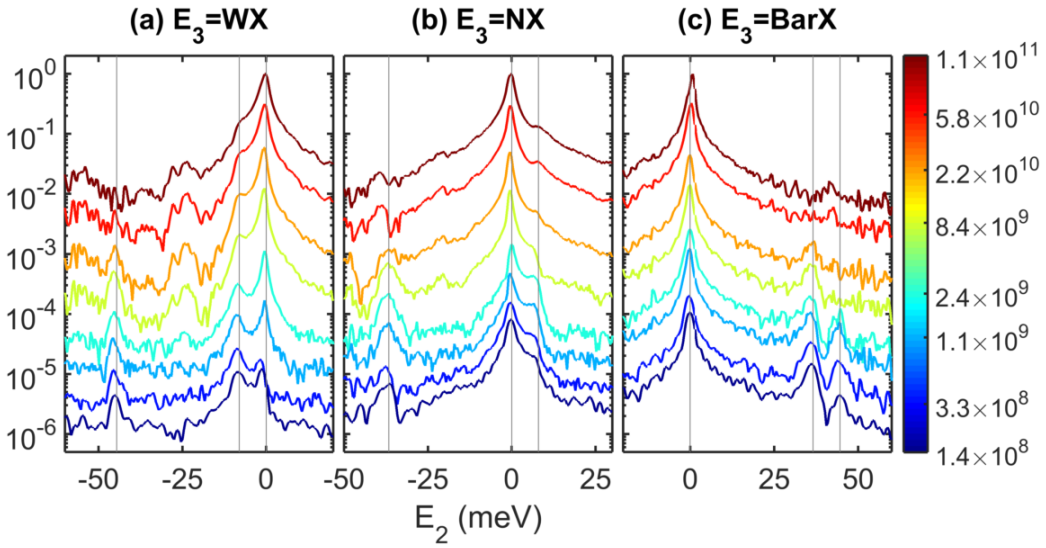

Figure 7.14: Slices of the 0Q spectrum along E_2 for emission at each of the strong excitonic transitions: WX (a) NX (b) and BarX (c). The signals are normalized to the highest signal from the highest power scan. The y-axis scale is in absolute units, and the different scans are **not** shifted. The gray lines at $E_2 \neq 0$ indicate coherent superpositions of excitonic states, and the photon density is given in the legend (in units of cm^{-2}).

$E_{2Q}=2E_3$ in the 2Q). The second column shows the amplitude of the inter-well CPs, and the third column shows the amplitude of CPs between WX/NX and BarX.

We will start by considering the DPs. In the 1Q and 0Q scans (Fig. 7.16a and Fig. 7.16d), the sum of the three peak amplitudes generally follows the $\mathbf{E}^3$ line, but the individual signals vary up and down out of phase with each other. For example, where the WX DP amplitude is large (e.g. at $\sim 10^{10} cm^{-2}$) the amplitude of the NX and BarX DPs are small. Conversely, at excitation densities where the amplitude of the WX DP is low (e.g. at $\sim 10^{8} cm^{-2}$), the amplitude of the NX and BarX DPs are comparatively large. The relative amplitudes of the three DPs in the 2Q scans also change. However, the sum of the three peak amplitudes clearly follows a sub-$\mathbf{E}^3$ dependence in this case.

The 1Q inter-well CPs show a roughly $\mathbf{E}^3$ dependence on excitation density above $\sim 10^{9} cm^{-2}$, and a sub-$\mathbf{E}^3$ dependence below that point. The excitation density dependences of the 0Q inter-well CPs are sub-$\mathbf{E}^3$ below $\sim 10^{9} cm^{-2}$, but cannot be satisfactorily separated from the DPs above this point. However, based on a qualitative analysis of the plots in Fig. 7.14 the coupling peaks do appear to continue to decrease as the excitation density increases, suggesting that the dependence continues to be sub-$\mathbf{E}^3$ even above $\sim 10^{10} cm^{-2}$.

The large 1Q CPs and non-existent 0Q CP suggests that incoherent coupling mechanisms dominate at high density. Furthermore, the significant mismatch of the below and above diagonal CPs is consistent with incoherent pathways such as population transfer. This is also consistent with the proposed mechanism in Ref. [54], which found that the CP is a result of many-body effects. At low densities, both 1Q and 0Q CPs are simultaneously increasing, and both above and below diagonal

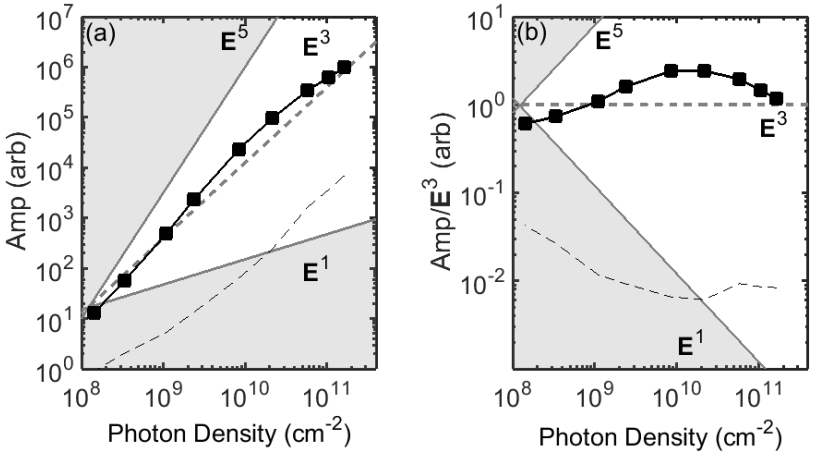

Figure 7.15: (a) Power dependence of the 1Q WX DP. It roughly follows follows $\mathbf{E}^3$ density dependence, which is indicated by the dashed gray line. The dotted black line is an estimate of the background noise. (b) Deviations from $\mathbf{E}^3$ dependence can be seen more clearly when the signal is divided by $\mathbf{E}^3$. The upper (lower) gray lines in both (a) and (b) indicate $\mathbf{E}^5$ ($\mathbf{E}^1$) power dependence, which we expect for χ^5 (linear) response.

CPs are of comparable amplitude. This suggests that coherent coupling mechanisms dominate at low density, which is consistent with what we have measured in Al_1 and Al_2. The dependence above $\sim 10^9 cm^{-2}$ is, however, complicated by the combination of coherent and incoherent signals which are not as strong in Al_1 and Al_2.

This interplay between coherent and incoherent coupling can also explain the changes in the NX and WX DP amplitudes. At low density the amplitude of the NX DP is much larger than that of the WX DP, which is expected because the dipole moment should increase as the well width decreases[10]. The incoherent coupling of the wells at high density reduces the signal from the NX DP, as efficient tunnelling into WX occurs, thereby weakening the NX DP.

We also observe an increase in the coupling of BarX to WX and NX at low excitation density (shown in Fig. 7.16c,f,i). Unlike the inter-well CPs, at high density the 1Q, 0Q and 2Q QW-Bar CPs (the CPs indicating interactions between the barrier and the QWs) all follow similar well-defined sub-$\mathbf{E}^3$ dependence on excitation density. This suggests that there is no increase of incoherent coupling at high density. This in-turn suggests that the Bar-QW coupling is predominately coherent across the entire range of measured excitation densities. This result is consistent with the results from Al_1 and Al_2, in that coherent coupling between the excitons localized to different layers (in this case one exciton localized in a QW and the other in the barrier) is much weaker relative to single-transition signals at high densities.

To summarize this section: although the interpretation is slightly more complicated, the results in the GaAs/InGaAs DQW are consistent with the results from Al_1 and Al_2. The amplitude of the CPs indicating coherent coupling of excitons predominately localized in different layers (both inter-well coupling and coupling of QW excitons to barrier excitons) is comparable to the amplitude of the DPs at low

10 The dipole moment only increases up to a point. For very narrow wells the dipole moment decreases as there is more leaking of the wavefunction into the barrier.

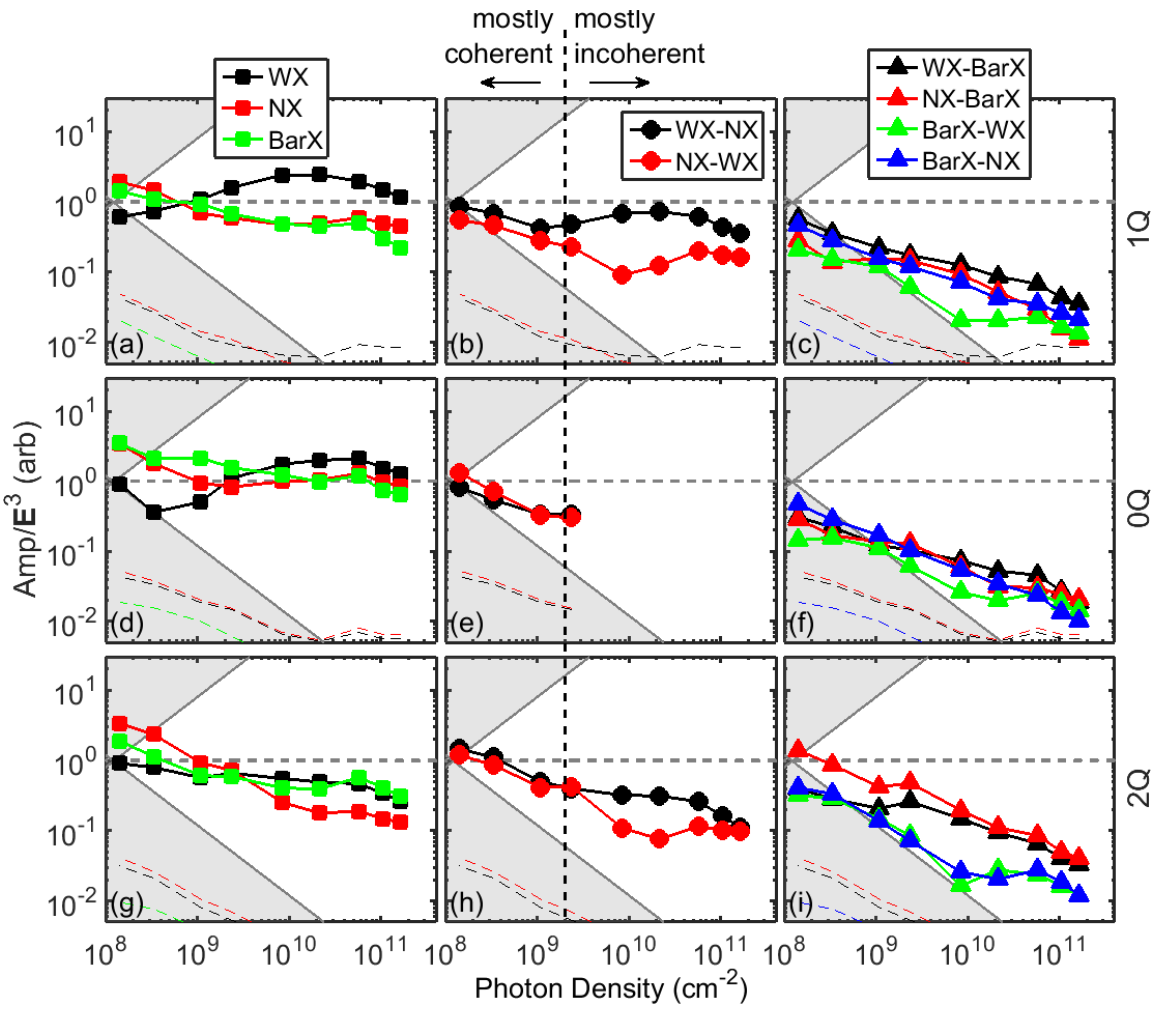

Figure 7.16: Excitation dependence of various signals in 1Q, 0Q and 2Q signals. The left column is the density dependence of DPs, the center column is the density dependence of inter-well peaks and the right column is the density dependence of barrier-QW CPs. The CPs are designated in the following way: emission axis - Fourier transform axis (E_3-$E_1/E_2/E_{2Q}$). The colored dashed lines indicate an estimate of the background signal.

density, but increases with a distinctly sub-$\mathbf{E}^3$ dependence as the density increases, while the DPs increase as $\mathbf{E}^3$.

7.3.1 *2Q peak-shape changes in the GaAs/InGaAs DQW*

In this section, we will take a closer look at the changes in the 2Q peak-shapes of the 10 nm barrier GaAs/InGaAs DQW as a function of excitation density. At low densities, we observe peaks which become much narrower along the E_{2Q} axis and exhibit a line-shape which is tilted along the diagonal. In the dataset presented here, the excitation laser spectrum has been shaped to excite only the WX and NX resonance while avoiding most of the free-carrier continua, the βX states and the barrier states.[11] The beams are co-circularly polarized to suppress biexciton signals.

11 The 2Q spectra from the dataset used in the previous section shows similar peak-shapes and amplitudes, even though broader excitation spectra were used.

Figure 7.17: Excitation spectrum for the 2Q 2D spectra in Fig. 7.18.

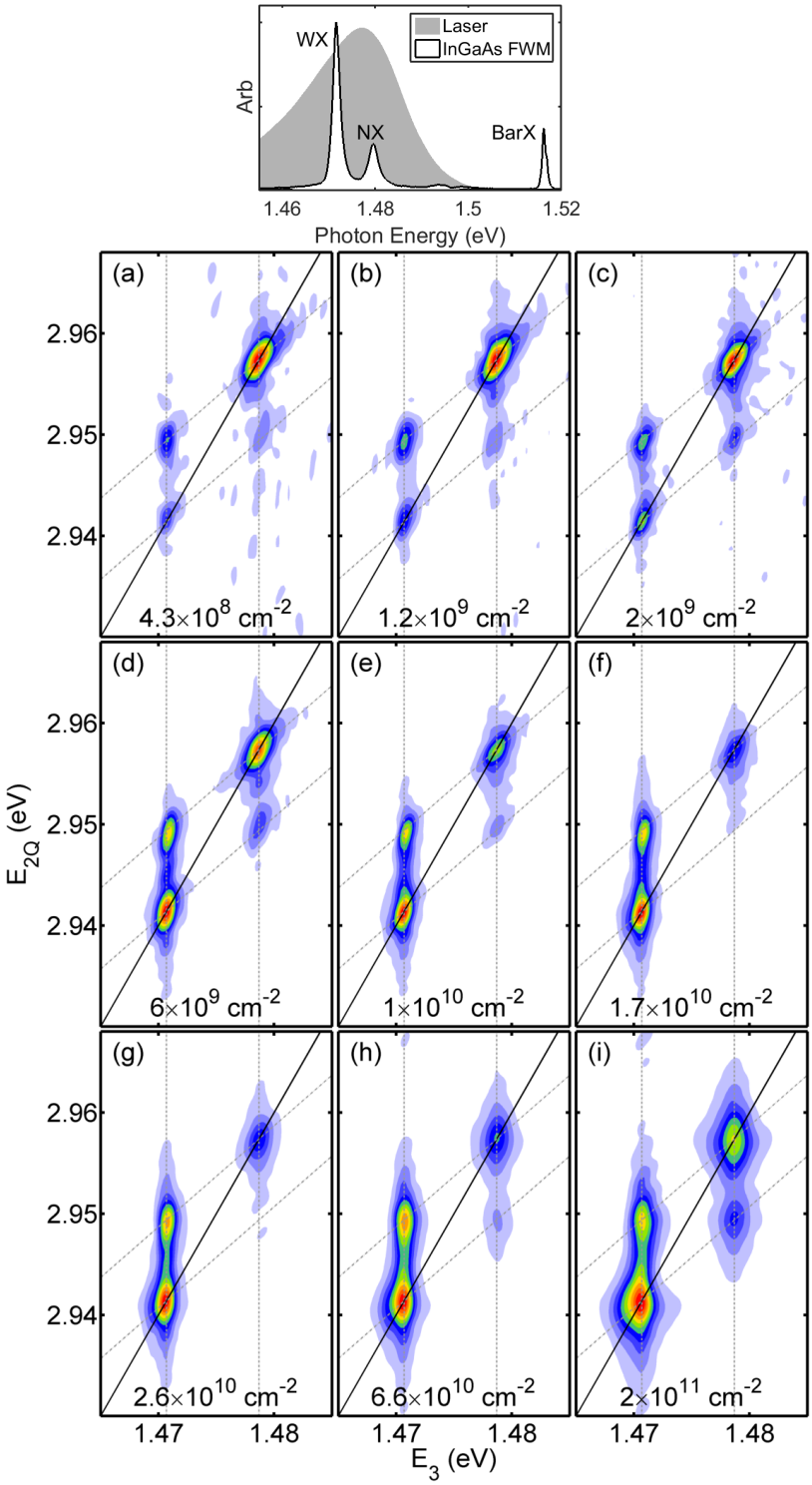

Figure 7.18: 2Q 2D spectra of the InGaAs DQW for a range of excitation densities. peak-shapes change from round/broad along E_{2Q} at high densities, to narrower peaks tilted along the diagonal at low densites. The beams are circularly polarized to suppress biexciton signals.

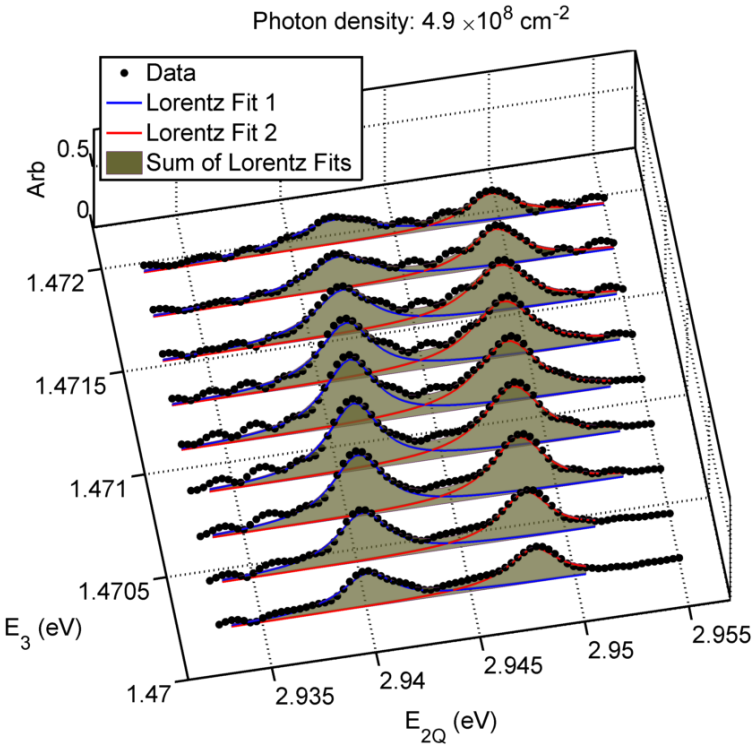

Figure 7.19: An example of fits to slices of the 2Q peaks in Fig. 7.18 along the E_{2Q} axis at each E_3 using Eq. 7.3.

The excitation spectrum and some 2Q 2D spectra at different excitation densities are plotted in Fig. 7.17 and Fig. 7.18 respectively. The plots go from a low density of $\sim 1 \times 10^8$ up to $\sim 5 \times 10^{10}$. Although the peak amplitudes change, each of the spectra show four peaks corresponding to the two DPs and the two CPs possible for this pair of transitions. A cursory look at the spectra show that the DPs broaden at the highest pulse energies, both in the E_3 and E_{2Q} directions (as in Fig. 7.13, which used broader excitation spectra). As the power decreases, the diagonal and CPs become more well resolved, and a tilt along the diagonal becomes more visible.

To quantify the width of the DPs and CPs along the E_{2Q} axis, a fit of slices along E_{2Q} was conducted for each detected E_3. The DPs and CPs which share the same emission energy are overlapped along the E_{2Q} direction (especially at high powers), so the E_{2Q} line-shape was fit to a sum of two Lorentzian functions according to the following two equations:

$$S^{WX}(E_{2Q}, E_3) = C + \frac{A_{2Q}^{WX}(\Gamma_{2Q}^{WX})^2}{(E_{2Q} - \mu_{2Q}^{WX})^2 + (\Gamma_{2Q}^{WX})^2} + \frac{A_{2Q}^{CP_1}(\Gamma_{2Q}^{CP_1})^2}{(E_{2Q} - \mu_{2Q}^{CP_1})^2 + (\Gamma_{2Q}^{CP_1})^2} \tag{7.3}$$

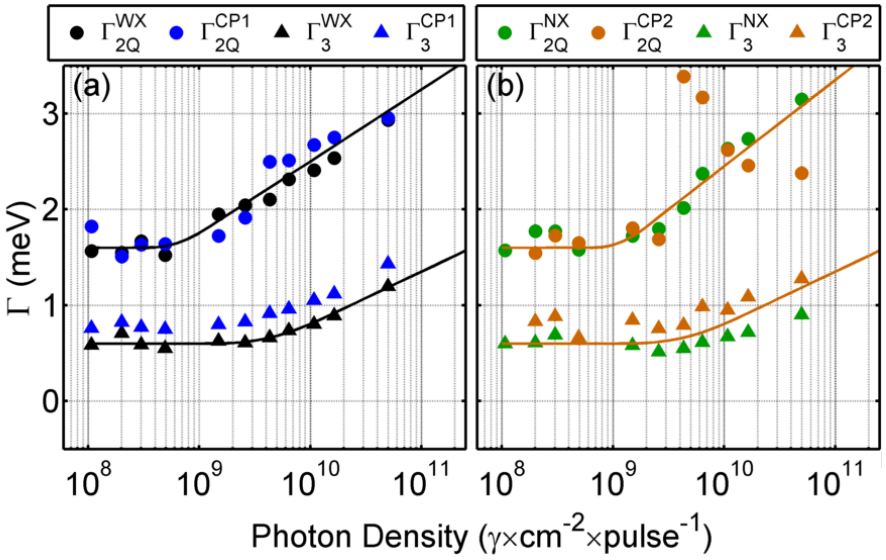

Figure 7.20: Density dependent E_{2Q} (circles) and E_3 (triangles) linewidths of peaks emitting at E_3=WX (a) and NX (b).

$$S^{NX}(E_{2Q}, E_3) = C + \frac{A_{2Q}^{NX}(\Gamma_{2Q}^{NX})^2}{(E_{2Q} - \mu_{2Q}^{NX})^2 + (\Gamma_{2Q}^{NX})^2} + \frac{A_{2Q}^{CP_2}(\Gamma_{2Q}^{CP_2})^2}{(E_{2Q} - \mu_{2Q}^{CP_2})^2 + (\Gamma_{2Q}^{CP_2})^2} \tag{7.4}$$

Where A_{2Q}, μ_{2Q} and Γ_{2Q} are the amplitude center and width along the E_{2Q} axis for the transition indicated in the superscript and a given E_3. CP_1 (CP_2) indicates the CP with emission from transition WX (NX). An example can be seen in Fig. 7.19, where slices of the WX DP and CP1 are fit to Eq. 7.3 (Eq. 7.4).

The emission line-shape for each peak was characterized by projecting the peak onto the E_3 axis and then fitting to a Lorentzian peak[12].

$$S_3^p(E_3) = C^p + \frac{A_3^p(\Gamma_3^p)^2}{(E_3 - \mu_3^p)^2 + (\Gamma_3^p)^2} \tag{7.5}$$

Where A_3^p, μ_3^p and Γ_3^p are the amplitude center and width along the E_3 axis, for peak 'p'.

The linewidths extracted from the fits along E_{2Q}[13] and E_3 are plotted as a function of the excitation density in Fig. 7.20a-b. The linewidths demonstrate roughly linear dependence on the log of the excitation density above a certain value, and are roughly independent of it below this value. The transition between the two regimes happens around $10^9 cm^{-2}$ for E_{2Q} and closer to around $10^{10} cm^{-2}$ for E_3. The solid

12 The line-shape is truly a Voigt shape, but the deviations are not significant as the sample is only weakly inhomogeneously broadened, so a Lorentzian fit is sufficient.

13 A single E_{2Q} is calculated by taking the average of the E_{2Q} widths across the emission linewidth.

lines are a guide to the eye indicating the transition from one behaviour to the other.

Kim et al reported 2Q spectra of Blue Nile laser dye which exhibited a tilt along the diagonal [88], and a similar tilt was also observed in 2Q spectra of β-Carotene [234] and Rhodamine 6G laser dye [303]. To our knowledge this is the first report of tilted DPs or CPs in 2Q 2D spectra of semiconductor QWs. Most 2Q spectra previously reported have round peaks with some broadening along the 2Q axis [81, 86, 191, 304]. However, no other previously reported results have been conducted with comparably low excitation densities.

We will now try to better understand these peak-shapes, starting with the single transition signals (DPs). In a rephasing 1Q spectrum, a tilted DP peak-shape is generated when the transition is inhomogeneously broadened and a photon echo is generated. This same interpretation does not extend to the 2Q DPs. There is no rephasing in the 2Q pulse ordering, so the tilted peak-shape cannot be the result of a photon echo. The t_{2Q} dephasing time is therefore limited by inhomogeneous dephasing (the systematic shifting of the phase of the different spectral components)

Instead, the tilted peak-shape can be understood as follows. Two interactions are required to excite the system into the two exciton state, each involving a single exciton transition. The range of available 2Q energies is therefore a convolution of the distributions of the two one-exciton transitions (ignoring biexciton contributions). The spectral width of the two-exciton state will therefore be equal to twice the single exciton linewidth. This can be seen graphically in the first part of Fig. 7.21a, which shows a cartoon illustrating the origin of the 2Q linewidth. The inhomogeneous dephasing of a DP as a function of t_{2Q} will therefore be $\propto 1/(2 \times \Gamma^{(tot)})$ where $\Gamma^{(tot)}$ is the full linewidth of the single exciton transition (including both homogeneous and inhomogeneous contributions).

For the signal pathway to obey energy conservation, the signal photon energy (E_s) for a given E_{2Q} is $E_s = E_{2Q} - E_{k_1}$ where E_{k_1} is the energy of the third pulse interaction. E_{k_1} is limited to the width of the transition it is exciting, or from which it is emitting. Both E_s and E_{k_1} must also be within the one-exciton linewidth. The combination of these two requirements causes the tilting of the 2Q DPs. For example, if we consider energies near the top of the E_{2Q} distribution (Fig. 7.21a), the available distribution of single exciton transition energies would lead to the range of signal energies shown by the blue bar. However, only the portion of these which overlap the ground-excited state distribution can conserve energy. A similar argument can be made for the low energy side of the E_{2Q} distribution (Fig. 7.21b). Extended smoothly across the entire E_{2Q} this leads to a correlation of E_{2Q} and E_3 which manifests in the 2Q spectrum as a tilted DP.

By the same token, tilted CPs don't tell us anything about the correlation of the inhomogeneous broadening. The fact that the CPs have E_{2Q} widths and tilt that are roughly equal to the DPs is not surprising in this case. For the CPs, instead of an auto-convolution, the E_{2Q} distribution is the convolution of the WX and NX

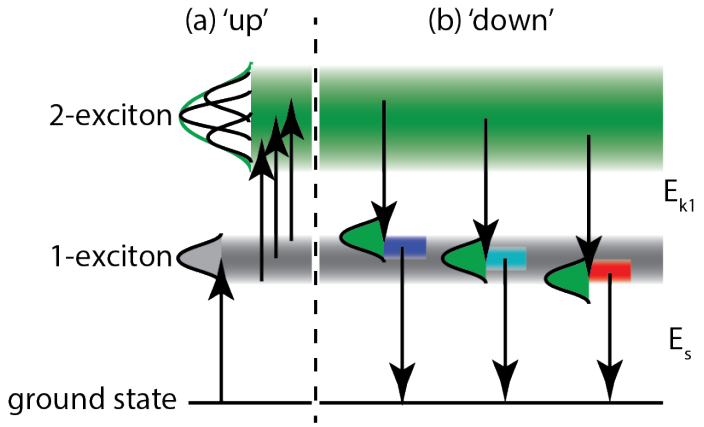

Figure 7.21: An graphical explanation of 2Q peakshapes tilted along the diagonal. (a) As described in the text, the two-exciton state has a lineshape equal to the auto-convolution of the single exciton lineshape. 2Q energies near the (top, middle, bottom) of the 2Q line are forced to generate signal from a smaller subset of the available single exciton energies given by the (blue, teal, red) bars. This leads to a correlation of the E_2Q and E_s, which exists even when the inhomogeneous broadening is uncorrelated. More details given in the text.

single exciton distributions, so the CP E_{2Q} widths are $\Gamma^{WX} + \Gamma^{NX}$. Since $\Gamma^{WX} \approx \Gamma^{NX}$, the CP widths are therefore expected to be similar to the DPs (in the absence of additional interactions which increase the dephasing rate of the mixed two-exciton state relative to the non-mixed two-exciton states).

The fit parameters in Fig. 7.20 do not change below $\sim 5^8 cm^{-2}$. We interpret this to mean that below this density these are the 'natural' peak-shapes and linewidths for this sample, and that above this the broadening along E_{2Q} and E_3 is excitation induced. This conclusion is supported by the fact that the Γ_{2Q} approaches $2\Gamma_3$ at low density, which is what we might expect for a t_{2Q} dephasing time which is limited by the 1-exciton transition linewidth. This interpretation suggests that steady increase in E_{2Q} linewidth above $\sim 5^8 cm^{-2}$ is a result of dephasing which is limited by exciton-exciton and/or exciton-free carrier scattering. This result suggests that most previous experiments in the 2Q pulse ordering have been conducted in a regime in which the excitation induced dephasing (EID) is the dominant broadening mechanism and the resulting peak-shapes and linewidths are therefore very excitation dependent. In the low density range, the dephasing is limited by the single exciton linewidths, so the resulting linewidths are less dependent on density.

The fact that exciton-exciton interactions cause dephasing the two-exciton state at an order of magnitude lower intensity than the single exciton state is somewhat intuitive in that the two-exciton state likely involves interactions over much larger lateral areas than single excitons. Due to their larger in-plane size, these two-exciton state (which are four-particle correlations) therefore will have more opportunity to scatter with other carriers. The CPs have the same widths as the DPs, indicating that the mixed 2-exciton state is no more sensitive to carrier-carrier scattering than the single-well 2-exciton states. Therefore, the larger out-of-plane size of the mixed 2-exciton state does not appear to increase the carrier-carrier scat-

tering rate. Simulations incorporating EID and EIS are being developed, which will help us to understand the origins of the excitation induced dephasing in a more detailed way.

7.4 Summary

In summary, the stability of this CMDS apparatus has allowed us to make measurements of a variety of different types of coherent dynamics at extremely low excitation densities At these low densities we have found a variety of interesting changes to the coherent dynamics of excitons in DQWs. These measurements have led to three main results:

First, in three separate DQW samples, we have observed sub-$\mathbf{E}^3$ dependence on excitation density for coherent coupling of excitons localized predominately in different QWs. These samples are made up of different material systems with different growth techniques and parameters, and have vastly different well depths. These similar results in vastly different samples suggest that this effect may be more general, and not just a peculiarity of any single sample. In the InGaAs DQW, we also observe this same phenomenon in signals generated by coherent coupling of the barrier excitons to the QW excitons. The intra-well signals by comparison (both intra-well CPs and DPs), do not deviate significantly from an $\mathbf{E}^3$ dependence except at high densities (where excitation induced broadening and $\chi^{(5)}$ signals contribute significantly). Regardless of the physical origin of this anomalous excitation dependence, this result shows that inter-well coherent interactions can be better resolved at lower excitation densities, and that excitation density should be carefully considered in investigations of coherent inter-well interactions.

Second, in AlGaAs DQW sample Al_2 we have observed that two sub-populations of excitons contribute to the NW_{hh} DP. At intermediate densities, photon echo signal dominates, at the lowest densities a free polarization decay dominates, while at the highest densities both signals contribute. Furthermore, the FPD signal follows an excitation density dependence similar to that of the inter-well CPs suggesting that the two effects are connected. We tentatively attribute the PE (FPD) signals to localized (extended, delocalized) exciton states. We also note the qualitative similarities of the extended, delocalized state to a superradiant state composed of many coherently coupled emitters. We however also recognize that other explanations for these changes in peak-shape and density dependence may exist.

Finally, in the InGaAs DQW studied at low density we have observed 2Q dephasing which is limited by the single exciton linewidths, and shown that excitation induced broadening of the 2Q line extends to much lower densities than the broadening of the 1Q line. Put another way, this means that by using excitation densities orders of magnitude lower than previous experiments, we are finally in a regime in which the exciton dephasing induced by the single exciton linewidth is fast com-

pared with the average exciton-exciton or exciton-free carrier scattering rate. This should allow us to explore multi-particle correlations in a regime where they are less affected by carrier scattering.

These results have one important factor in common: they all suggest the presence (or even dominance) of signals resulting from the interaction of distant excitons (separated at the lowest excitation densities by up to μm distances on average). The density of these dilute exciton ensembles is well below the range where it is typically assumed that the single-exciton response dominates. Although the coherent response of excitons in QWs have been studied for decades now, CMDS has enabled us to access this previously unexplored regime and gain new insight.

8

SUMMARY AND OUTLOOK

In this thesis, we have presented several different investigations into coherent effects in semiconductor double quantum wells (DQWs), and developed a pathway selective multidimensional spectroscopy approach. While they are in many ways interrelated, the nature of these investigations do not conveniently lend themselves to a single, tidy summary. For this reason, the major conclusions have been summarized at the end of each chapter. In this section, we will reiterate some of the conclusions and discuss the outlook, grouping interrelated results together.

8.1 Pathway-selective coherent multidimensional spectroscopy

As a part of this PhD project we implemented a coherent multidimensional spectroscopy (CMDS) experiment using spatial light modulators. The experiment was setup in such a way that spectral shaping could be used to perform pathway-selective CMDS. Using this experimental apparatus, we showed that it is possible to isolate signals involving a coherent superposition in 1-quantum (1Q) and 0-quantum (0Q) spectroscopy. We also showed that new details regarding the nature of transition broadening can be extracted from projections of coherent superposition cross-peaks (CS-CPs) onto the E_3 vs. E_2 and E_1 vs. E_2 planes.

We also showed that signals from mixed two-exciton states could be isolated by using spectral shaping based pathway selection in 2-quantum (2Q) spectroscopy. This approach can also be used to suppress rapidly dephasing free-carrier and defect related signals. We also explained how this could be used to deterministically generate mixed two-exciton states in a controlled order, which is important for the extension of the technique to higher order correlations.

Now that we have demonstrated the capabilities of selection in CMDS, we can use it to study other systems. Work is currently ongoing to use this technique to study coherent effects in PC645 light harvesting complex (LHC). The techniques developed here are very promising for studying light harvesting complexes for a few reasons. The ability to selectively excite particular pathways will help to clean up 2D spectra that are often congested by multiple overlapping signals, while still providing the varied benefits of multidimensional spectroscopy. As selective FWM experiments have shown, there is a lot to be gained by using narrowband excitation

to study coherent interactions, and the addition of CMDS tools should allow those interactions to be studied in more detail (e.g. by analyzing peak shapes). One example of where peak shape analysis my provide additional insights is in the question of whether correlated fluctuations in the electronic states of different chromophores can account for the longer than expected excited state coherences that have been experimentally measured in LHCs. The analysis of peak shapes in 0Q and 3D spectra could potentially allow such correlated fluctuations to be directly measured.

As demonstrated in Ref. [67], the ability to isolate signals from excited state coherent superpositions in a fast 2D scan will also be useful in exploring their dependence on other parameters (e.g. excitation density, temperature, excitation wavelength). Finally, the ability to perform measurements at extremely low photon densities is potentially very important as well, as recent work has shown that the coherences measured in PC645 demonstrate a surprisingly pronounced dependence on photon density and saturation behaviour at lower powers than previously expected [305].

It should also be useful in studying coherence in other samples, such as nanoplatelets [215, 220] and heterostructures made of monolayer dichalcogenides [212, 235, 236]. The latter, in particular, is a rapidly evolving field where many of the measurements of coherent effects either have not been performed while others have produced conflicting results. The ability of selective CMDS to separate out overlapping signals may be very useful in isolating interactions between different monolayers in the TMD heterosctructures.

One of the main limitations of the pulse-shaper based CMDS experiment is the delay range. We are currently in the process of implementing translation stage delays (similar to those used in Refs. [57, 58]), which can be used along with the pulse-shaper. This would overcome the delay limitations while still allowing us to use the pulse-shaper for spectral amplitude shaping. Work is also ongoing on the extension of the pathway-selective 2Q experiment into a 3Q, 5^{th} order experiment.

8.2 Inter-well coherent superpositions in double quantum wells

In this thesis we have shown that coherent superpositions can be observed in AlGaAs/GaAs DQWs even when the wells are separated so that there is no hybridization of the wavefunctions. This result suggests some sort of dynamic excited state coupling of the excitonic states. This work does not point to a particular coupling mechanism, but the routine detection of these signals is an important tool for future investigations.

Nardin et al. [54] have proposed that coupling in an InGaAs/GaAs DQW is a result of many-body effects. Using pathway-selective CMDS, we measured the amplitude of the 0Q CS-CP in this same sample, and found that it is much larger than predicted by the simulations involving many-body interactions. We therefore spec-

ulate that the inter-well coupling may be a result (at least in part) of some type of two-body coupling. We showed in Ch. 7 that the relative amplitude of the 0Q CS-CP depends on excitation density, and becomes much more prevalent at low densities. As a result, to accurately represent the sample response a density dependence must be considered in the simulations. The experiments and simulations in Ref. [54] were only reported for a single excitation density.

Speculatively, the excitation density dependence measured in Ch. 7 may suggest that inter-well coupling is related to an extended delocalized state in each of the QWs. However, coupling due to many-body-effects may also lead to a sub-$\mathbf{E}^3$ density dependence. A way to separate these two effects would be by performing pump-CMDS experiments [193]. In pump-CMDS, a pre-pulse (the pump) excites populations of excitons before standard CMDS techniques are used with low power excitation pulses. The pre-pulse arrives several ps before the first excitation pulse so that the coherent polarization from the pump has dephased before the first pulse in the CMDS experiment arrives at the sample. Thus, no coherent signals are generated involving the pump. CMDS is then performed as a function of the excitation density generated by the prepulse. This reduces the complexity of the interpretation of the data, as the excitation density remains roughly the same throughout the experiment if the pump power is larger than the CMDS power.

All of the inter-well coupling results would benefit from simulations involving density-dependent incorporation of many-body effects. Efforts towards developing these simulations at Swinburne are ongoing.

8.3 Spatially indirect 'dark' excitons

We observed a range of 'dark' states in two InGaAs DQWs: type-II LH excitons, parity forbidden direct excitons and spatially indirect states involving an electron in the barrier and a hole in one of the QWs. We were able to observe these states primarily as CPs generated by absorption in a 'bright' QW or barrier state and emission from the 'dark' state. We are therefore able to unambiguously detect these states primarily due to CMDS's sensitivity to coherent coupling. By fitting population peaks in a 3D spectrum, we were able to put a lower bound on the exciton population lifetimes, and found that the type-II LH 'dark' excitons and type-I HH 'bright' excitons have nearly equal lifetimes within the parameters used in the experiment. Given the spatially indirect states strongly couple to both QW excitons and barrier excitons, they might play a role in relaxation of barrier excitons into the QWs. We may be able to determine what that role is if we can capture the full coherence and population decays. The addition of translation stage based delays should allow us to make this measurement.

The demonstrated ability to identify and measure these dark states could impact applications of DQW systems. For example, the strong coupling of the Type-I HHs

and Type-II LHs could be used as a THz source, or a THz detector. Such could have benefits compared with purely type-I systems in that spatial separation of the charged carriers could induce larger electric fields. Second, if the dark type-II states do play a key role in relaxation into the quantum wells, this knowledge could be useful in designing more efficient quantum cascade lasers, where rapid repopulation of the lasing state from the bulk is one of the key aspects of the device.

Finally, this electronic system also presents a good way to test the selective 3Q experiments. We can test if the two wells are indirectly coupled through the barrier or through spatially indirect exciton states by using pulse sequences that selectively excite different sets of transitions: WX→BarX→NX, and WX→ βX →NX. Furthermore, we could use the BarX→ βX →WX to help us determine whether the βX mediate a coupling of the barrier and QW excitons. Finally, we could also use spectral shaping and 5^{th} order $\chi^{(5)}$ 3D rephasing experiment to directly track the multi-step relaxation pathways as was recently demonstrated (using broadband non-selective excitation) in Ref. [68].

8.4 Low density experiments

We have observed two important additional changes to the coherent response at low excitation densities: a narrowing of the 2Q linewidth in GaAs/InGaAs DQW and an extended delocalized exciton state in an AlGaAs/GaAs DQW. The tilted 2Q peaks which are narrow along E_{2Q} are a result of an inherent correlation of E_{2Q} and E_3, and not indicative of inhomogeneous broadening. We show that above 5×10^8 photons cm^{-2}, the E_{2Q} linewidths continuously increase with excitation density, which implies that the E_{2Q} linewidths are limited by carrier-carrier interactions.

Although tilted 2Q peaks have been observed previously [88, 234, 303], this is the first time they have been observed in QWs. This suggests that previous 2Q experiments were performed in regimes where the excitation induced broadening is the primary factor in determining the peak-shapes and linewidths. This result also indicates that exciton-exciton interactions are still prevalent even when the average inter-excitonic distance is nearly 1 μm.

In an AlGaAs/GaAs DQW, we have observed that the shape of the diagonal-peaks change from tilted at high power to un-tilted at low power, in apparent contradiction to typical experiments. We posit that this changing peak-shape is evidence of an extended delocalized exciton state, which dominates the coherent response at low densities. Though the results are not shown, we also observe this same peak-shape at low density in two additional samples. We discuss how this state can be thought of as coupling of localized states spatially separated in the plane of the QW, and as such this state is conceptually similar to a superradiant state. The apparently much larger dipole moment of this delocalized state is also consistent with superradiance. We explain the diminishing of this state as power increases to screening

of the interactions that mediate the coupling of the localized states. Going forward, a detailed calculation of the screening as a function of excitation density should be conducted. We also observe that the inter-well coherent interactions and the delocalized state scale with excitation density almost identically, suggesting that the inter-well interactions are related to the delocalized state. The fact that we only observe the delocalized state in samples which were grown with particular growth parameters suggests this effect may be related to the interface morphology. To explore this possibility in more detail, a systematic study of samples with different degrees structural disorder should be conducted.

The unexpected behaviour of the excitons at low excitation densities implies some of the physics is quite different from that which is typically expected for excitons in QWs. It is typically considered that when an exciton is confined in one direction, the separation of the electron and hole is reduced, but the aspect ratio stays the same (i.e. the radius of the exciton in the unconfined direction remains the same as the radius in the confined direction). The results here seem to suggest that the effective size of the exciton in the plane of the QW (the unconfined direction) is actually much larger, as it strongly interacts with excitons over distances hundreds of times larger than the expected radius. This is an important physical insight, and suggests that there is much to learn in this excitation regime which has remained largely unexplored.

BIBLIOGRAPHY

[1] W. H. Zurek. Decoherence and the transition from quantum to classicalDecoherence and the Transition from Quantum to Classical-Revisited. *Phys. Today*, **44**(27): 36 (1991).

[2] J. Faist, F. Capasso, D. Sivco, and C. Sirtori. Quantum cascade laser. *Science*, **264**(5158): 553–556 (1994).

[3] E. R. Brown, J. R. Soderstrom, C. D. Parker, L. J. Mahoney, K. M. Molvar, and T. C. McGill. Oscillations up to 712 GHz in InAs / AISb resonant-tunneling diodes. *Applied Physics Letters*, **58**(20): 2291–2293 (1991).

[4] M. A. Nielson and I. L. Chuang. *Quantum Information and Quantum Computation*. Cambridge University Press, Cambridge (2000).

[5] A. Chenu and G. D. Scholes. Coherence in energy transfer and photosynthesis. *Annual Review of Physical Chemistry*, **66**(1): 69–96 (2014).

[6] G. S. Engel, T. R. Calhoun, E. L. Read, T.-K. Ahn, T. Mancal, Y.-C. Cheng, R. E. Blankenship, and G. R. Fleming. Evidence for wavelike energy transfer through quantum coherence in photosynthetic systems. *Nature*, **446**(7137): 782–6 (2007).

[7] E. Collini, C. Y. Wong, K. E. Wilk, P. M. G. Curmi, P. Brumer, and G. D. Scholes. Coherently wired light-harvesting in photosynthetic marine algae at ambient temperature. *Nature*, **463**(7281): 644–647 (2010).

[8] G. Panitchayangkoon, D. Hayes, K. a. Fransted, J. R. Caram, E. Harel, J. Wen, R. E. Blankenship, and G. S. Engel. Long-lived quantum coherence in photosynthetic complexes at physiological temperature. *Proceedings of the National Academy of Sciences of the United States of America*, **107**(29): 12,766–12,770 (2010).

[9] E. Harel and G. S. Engel. Quantum coherence spectroscopy reveals complex dynamics in bacterial light-harvesting complex 2 (LH2). *Proceedings of the National Academy of Sciences*, **109**(3): 706–711 (2012).

[10] H. Lee, Y.-C. Cheng, and G. R. Fleming. Coherence dynamics in photosynthesis: protein protection of excitonic coherence. *Science*, **316**(5830): 1462–1465 (2007).

[11] S. Westenhoff, D. Palecek, P. Edlund, P. a. Smith, and D. Zigmantas. Coherent picosecond exciton dynamics in a photosynthetic reaction center. *Journal of the American Chemical Society*, **134**(40): 16,484–16,487 (2012).

[12] S. Gu, H. Neugebauer, and N. S. Sariciftci. Conjugated polymer-vased organic solar cells. *Chemical Reviews*, **107**(1): 1324–1338 (2007).

[13] W. Aue, E. Bartholdi, and R. Ernst. Two-dimensional spectroscopy: application to nuclear magnetic resonance. *The Journal of Chemical Physics*, **64**(5): 2229–2246 (1976).

[14] R. Ernst. Nuclear magnetic resonance Fourier transform spectroscopy. *Bioscience Reports*, **12**(3): 12–57 (1992).

[15] K. Wüthrich. NMR studies of structure and function of biological macromolecules (Nobel Lecture). *Journal of Biomolecular NMR*, **27**(1): 13–39 (2003).

[16] M. T. Zanni and R. M. Hochstrasser. Two-dimensional infrared spectroscopy: a promising new method for the time resolution of structures. *Current Opinion in Structural Biology*, **11**(5): 516–522 (2001).

[17] M. Cho. Coherent two-dimensional optical spectroscopy. *Chemical Reviews*, **108**: 1331–1418 (2008).

[18] D. M. Jonas. Two-dimensional femtosecond spectroscopy. *Annual Review of Physical Chemistry*, **54**: 425–463 (2003).

[19] J. D. Hybl, A. W. Albrecht, S. M. Gallagher Faeder, and D. M. Jonas. Two-dimensional electronic spectroscopy. *Chemical Physics Letters*, **297**: 307–313 (1998).

[20] J. D. Hybl, A. Albrecht Ferro, and D. M. Jonas. Two-dimensional Fourier transform electronic spectroscopy. *The Journal of Chemical Physics*, **115**(14): 6606 (2001).

[21] G. M. Clore and A. M. Gronenborn. Structures of larger proteins in solution: three- and four-dimensional heteronuclear NMR spectroscopy. *Science*, **252**(5011): 1390–1399 (1991).

[22] M. Hofmann, S. D. Brorson, J. Mork, and a. Mecozzi. Time resolved four-wave mixing technique to measure the ultrafast coherent dynamics in semiconductor optical amplifiers. *Applied Physics Letters*, **68**(23): 3236 (1996).

[23] A. Mecozzi and J. Mork. Theory of heterodyne pump-probe experiments with femtosecond pulses. *Journal of the Optical Society of America B*, **13**(11): 2437 (1996).

[24] J. Davis, J. Wathen, V. Blanchet, and R. Phillips. Time-resolved four-wave-mixing spectroscopy of excitons in a single quantum well. *Physical Review B*, **75**(3): 1–8 (2007).

[25] D. R. Herriott and H. J. Schulte. Folded optical delay lines. *Applied Optics*, **4**(8): 883 (1965).

[26] C. V. Shank and E. P. Ippen. Subpicosecond kilowatt pulses from a mode-locked cw dye laser. *Applied Physics Letters*, **24**(8): 373–375 (1974).

[27] D. E. Spence, P. N. Kean, and W. Sibbett. 60-fsec pulse generation from a self-mode-locked Ti : sapphire laser. *Optics Letters*, **16**(1): 42–44 (1991).

[28] T. Brabec and F. Krausz. Intense few-cycle laser fields: Frontiers of nonlinear optics. *Reviews of Modern Physics*, **72**(2): 545–591 (2000).

[29] A. Wirth, M. T. Hassan, I. Grguras, J. Gagnon, A. Moulet, T. T. Luu, S. Pabst, R. Santra, Z. a. Alahmed, A. M. Azzeer, V. S. Yakovlev, V. Pervak, F. Krausz, and E. Goulielmakis. Synthesized light transients. *Science*, **334**(6053): 195–200 (2011).

[30] L. Schultheis, M. Sturge, and J. Hegarty. Photon echoes from two dimensional excitons in GaAs-AlGaAs quantum wells. *Applied physics letters*, **47**(November): 995–997 (1985).

[31] K. Leo, M. Wegener, J. Shah, and D. Chemla. Effects of coherent polarization interactions on time-resolved degenerate four-wave mixing. *Physical Review Letters*, **65**(11): 1340–1343 (1990).

[32] K. Leo, J. Shah, E. Göbel, T. Damen, S. Schmitt-Rink, W. Schäfer, and K. Köhler. Coherent oscillations of a wave packet in a semiconductor double-quantum-well structure. *Physical Review Letters*, **66**(2): 201–204 (1991).

[33] E. Göbel, K. Leo, T. Damen, J. Shah, S. Schmitt-Rink, W. Schäfer, J. F. Muller, and K. Kohler. Quantum beats of excitons in quantum wells. *Physical Review Letters*, **64**(15): 1801–1804 (1990).

[34] I. D. Abella, N. A. Kurnit, and S. R. Hartmann. Photon Echoes. *Physical Review*, **141**(1): 391–406 (1966).

[35] R. M. Hochstrasser, G. R. Meredith, and H. P. Trommsdorff. Resonant four wave mixing in molecular crystals. *The Journal of Chemical Physics*, **73**(3): 1009 (1980).

[36] R. K. Jain and R. C. Lind. Degenerate four-wave mixing in semiconductor-doped glasses. *Journal of the Optical Society of America*, **73**(5): 647 (1983).

[37] A. M. Weiner, S. D. Silvestri, and E. P. Ippen. Three-pulse scattering for femtosecond dephasing studies: theory and experiment. *Journal of the Optical Society of America B*, **2**(4): 654 (1985).

[38] W. P. de Boeij, M. S. Pshenichnikov, and D. A. Wiersma. Ultrafast solvation dynamics explored by femtosecond photon echo spectroscopies. *Annual Review of Physical Chemistry*, **49**(1): 99–123 (1998).

[39] K. A. Nelson, R. Casalegno, R. Miller, and M. Fayer. Laser-induced excited state and ultrasonic wave gratings: Amplitude and phase grating contributions to diffraction. *Journal of Chemical Physics*, **77**(3): 1144 (1982).

[40] P. Kukura, D. W. McCamant, and R. A. Mathies. Femtosecond stimulated Raman spectroscopy. *Annual Review of Physical Chemistry*, **58**(1): 461–488 (2007).

[41] H. Hamaguchi and T. L. Gustafson. Ultrafast time-resolved spontaneous and coherent Raman spectroscopy: The structure and dynamics of photogenerated transient species. *Annual Review of Physical Chemistry*, **45**(1): 593–622 (1994).

[42] R. Berera, R. van Grondelle, and J. T. M. Kennis. Ultrafast transient absorption spectroscopy: Principles and application to photosynthetic systems. *Photosynthesis Research*, **101**(2): 105–118 (2009).

[43] S. T. Cundiff. Transient four-wave mixing spectroscopy. In R. P. Prasankumar and A. J. Taylor (editors), *Optical Techniques for Solid State Materials Characterization*, chapter 10, pp. 371–398. CRC Press, London (2012).

[44] M. Koch, J. Feldmann, and E. Göbel. Coupling of exciton transitions associated with different quantum-well islands. *Physical Review B*, **48**(15): 480–483 (1993).

[45] D. S. Kim, J. Shah, D. A. B. Miller, T. C. Damen, W. Schäfer, and L. Pfeiffer. Femtosecond-pulse distortion in quantum wells. *Physical Review B*, **48**(24): 17,902–17,905 (1993).

[46] J. Shah. *Ultrafast spectroscopy of semiconductors and semiconductor nanostructures*. Springer Verlag, Berlin (1999).

[47] N. A. Kurnit, I. D. Abella, and S. R. Hartmann. Observations of a Photon Echo. *Physical Review Letters*, **13**(9): 567–569 (1964).

[48] A. Miller, R. Manning, P. Milsom, D. Hutchings, D. Crust, and K. Woodbridge. Transient grating studies of excitonic optical non-linearities in GaAs/AlGaAs multiple quantum well structures. *Journal of Optical Society of America B*, **6**(4): 567–578 (1988).

[49] K. Ferrio and D. Steel. Raman quantum beats of interacting excitons. *Physical Review Letters*, **80**(4): 786–789 (1998).

[50] L. Yang, T. Zhang, A. D. Bristow, S. T. Cundiff, and S. Mukamel. Isolating excitonic Raman coherence in semiconductors using two-dimensional correlation spectroscopy. *The Journal of Chemical Physics*, **129**(23): 234,711 (2008).

[51] S. Mukamel. *Principles of Nonlinear Optical Spectroscopy*. Oxford University Press, Oxford (1995).

[52] P. Hamm. Principles of Nonlinear Optical Spectroscopy: A Practical Approach or: Mukamel for Dummies (2005).

[53] X. Li, T. Zhang, C. Borca, and S. Cundiff. Many-body interactions in semiconductors probed by optical two-dimensional Fourier transform spectroscopy. *Physical Review Letters*, **96**(5): 1–4 (2006).

[54] G. Nardin, G. Moody, R. Singh, T. M. Autry, H. Li, F. Morier-Genoud, and S. T. Cundiff. Coherent excitonic coupling in an asymmetric double InGaAs quantum well arises from many-body effects. *Physical Review Letters*, **112**(4): 1–5 (2014).

[55] F. D. Fuller and J. P. Ogilvie. Experimental implementations of two-dimensional Fourier transform electronic spectroscopy. *Annual Review of Physical Chemistry*, **66**(1): 667–690 (2013).

[56] T. Zhang, C. Borca, X. Li, and S. Cundiff. Optical two-dimensional Fourier transform spectroscopy with active interferometric stabilization. *Optics Express*, **13**(19): 7432–7441 (2005).

[57] M. Cowan, J. Ogilvie, and R. Miller. Two-dimensional spectroscopy using diffractive optics based phased-locked photon echoes. *Chemical Physics Letters*, **386**(1-3): 184–189 (2004).

[58] U. Selig, F. Langhojer, F. Dimler, T. Lorig, C. Schwarz, B. Gieseking, and T. Brixner. Inherently phase-stable coherent two-dimensional spectroscopy using only conventional optics. *Optics Letters*, **33**(23): 2851–2853 (2008).

[59] T. Brixner, T. Mancal, I. V. Stiopkin, and G. R. Fleming. Phase-stabilized two-dimensional electronic spectroscopy. *The Journal of Chemical Physics*, **121**(9): 4221–36 (2004).

[60] E. Collini and G. D. Scholes. Coherent intrachain energy migration in a conjugated polymer at room temperature. *Science*, **323**(5912): 369–373 (2009).

[61] J. C. Vaughan, T. Hornung, T. Feurer, and K. A. Nelson. Diffraction-based femtosecond pulse shaping with a two-dimensional spatial light modulator. *Optics Letters*, **30**(3): 323–5 (2005).

[62] D. B. Turner, K. W. Stone, K. Gundogdu, and K. A. Nelson. Invited article: The coherent optical laser beam recombination technique (COLBERT) spectrometer: coherent multidimensional spectroscopy made easier. *The Review of Scientific Instruments*, **82**(8): 081,301 (2011).

[63] D. Turner. *Investigating exciton correlations using coherent multidimensional optical spectroscopy*. Ph.D. thesis, Massachusetts Institute of Technology (2010).

[64] L. P. Deflores, R. A. Nicodemus, and A. Tokmakoff. Two-dimensional Fourier transform spectroscopy in the pump-probe geometry. *Optics Letters*, **32**(20): 2966–2968 (2007).

[65] J. A. Myers, K. L. M. Lewis, P. F. Tekavec, and J. P. Ogilvie. Two-color two-dimensional Fourier transform electronic spectroscopy with a pulse-shaper. *Optics Express*, **16**(22): 17,420–17,428 (2008).

[66] P. F. Tekavec, J. a. Myers, K. L. M. Lewis, and J. P. Ogilvie. Two-dimensional electronic spectroscopy with a continuum probe. *Optics Letters*, **34**(9): 1390–1392 (2009).

[67] S. S. Senlik, V. R. Policht, and J. P. Ogilvie. Two-color nonlinear spectroscopy for the rapid acquisition of coherent dynamics. *The Journal of Physical Chemistry Letters*, **6**(13): 2413–2420 (2015).

[68] Z. Zhang, P. H. Lambrev, K. L. Wells, G. Garab, and H.-S. Tan. Direct observation of multistep energy transfer in LHCII with fifth-order 3D electronic spectroscopy. *Nature Communications*, **6**: 7914 (2015).

[69] G. Nardin, T. Autry, K. Silverman, and S. Cundiff. Multidimensional coherent photocurrent spectroscopy of a semiconductor nanostructure. *Optics Express*, **21**(23): 625–628 (2013).

[70] K. J. Karki, J. R. Widom, J. Seibt, I. Moody, M. C. Lonergan, T. Pullerits, and A. H. Marcus. Coherent two-dimensional photocurrent spectroscopy in a PbS quantum dot photocell. *Nature Communications*, **5**(5869): 1–7 (2014).

[71] P. Tian, D. Keusters, Y. Suzaki, and W. S. Warren. Femtosecond phase-coherent two-dimensional spectroscopy. *Science*, **300**(5625): 1553–1555 (2003).

[72] P. F. Tekavec, G. A. Lott, and A. H. Marcus. Fluorescence-detected two-dimensional electronic coherence spectroscopy by acousto-optic phase modulation. *Journal of Chemical Physics*, **127**(21): 214,307 (2007).

[73] J. Kasprzak, B. Patton, V. Savona, and W. Langbein. Coherent coupling between distant excitons revealed by two-dimensional nonlinear hyperspectral imaging. *Nature Photonics*, **5**: 57–63 (2010).

[74] M. Aeschlimann, T. Brixner, A. Fischer, C. Kramer, P. Melchior, W. Pfeiffer, C. Schneider, C. Strüber, P. Tuchscherer, and D. V. Voronine. Coherent two-dimensional nanoscopy. *Science*, **333**(6050): 1723–1727 (2011).

[75] J. Davis, L. Dao, M. Do, P. Hannaford, K. Nugent, and H. Quiney. Noninterferometric two-dimensional Fourier-transform spectroscopy of multilevel systems. *Physical Review Letters*, **100**(22): 227,401 (2008).

[76] J. A. Davis, C. R. Hall, L. V. Dao, K. A. Nugent, H. M. Quiney, H. H. Tan, and C. Jagadish. Three-dimensional electronic spectroscopy of excitons in asymmetric double quantum wells. *The Journal of chemical physics*, **135**(4): 044,510 (2011).

[77] C. R. Hall, J. O. Tollerud, H. M. Quiney, and J. A. Davis. Three-dimensional electronic spectroscopy of excitons in asymmetric double quantum wells. *New Journal of Physics*, **15**(4): 045,028 (2013).

[78] D. Keusters, H. S. Tan, and W. S. Warren. Role of pulse phase and direction in two-dimensional optical spectroscopy. *Journal of Physical Chemistry A*, **103**(49): 10,369–10,380 (1999).

[79] J. Shacklette and S. Cundiff. Role of excitation-induced shift in the coherent optical response of semiconductors. *Physical Review B*, **66**(4): 1–6 (2002).

[80] A. D. Bristow, D. Karaiskaj, X. Dai, R. P. Mirin, and S. T. Cundiff. Polarization dependence of semiconductor exciton and biexciton contributions to phase-resolved optical two-dimensional Fourier-transform spectra. *Physical Review B - Condensed Matter and Materials Physics*, **79**(16): 1–4 (2009).

[81] D. Karaiskaj, A. D. Bristow, L. Yang, X. Dai, R. P. Mirin, S. Mukamel, and S. T. Cundiff. Two-quantum many-body coherences in two-dimensional Fourier-transform spectra of exciton resonances in semiconductor quantum wells. *Physical Review Letters*, **104**(11): 1–4 (2010).

[82] G. Moody, I. a. Akimov, H. Li, R. Singh, D. R. Yakovlev, G. Karczewski, M. Wiater, T. Wojtowicz, M. Bayer, and S. T. Cundiff. Coherent coupling of excitons and trions in a photoexcited CdTe/CdMgTe quantum well. *Physical Review Letters*, **112**(9): 1–5 (2014).

[83] K. Nagayama, P. Bachmann, K. Wuthrich, and R. Ernst. The use of cross-sections and of projections in two-dimensional NMR spectroscopy. *Journal of Magnetic Resonance (1969)*, **31**(1): 133–148 (1978).

[84] S. G. Faeder and D. Jonas. Two-dimensional electronic correlation and relaxation spectra: Theory and model calculations. *The Journal of Physical Chemistry A*, **103**(49): 10,489–10,505 (1999).

[85] F. Milota, C. Lincoln, and J. Hauer. Precise phasing of 2D-electronic spectra in a fully non-collinear phase-matching geometry. *Optics Express*, **21**(13): 15,904–15,911 (2013).

[86] K. W. Stone, K. Gundogdu, D. B. Turner, X. Li, S. T. Cundiff, and K. A. Nelson. Two-quantum 2D FT electronic spectroscopy of biexcitons in GaAs quantum wells. *Science*, **324**(5931): 1169–73 (2009).

[87] X. Dai, M. Richter, H. Li, A. Bristow, C. Falvo, S. Mukamel, and S. Cundiff. Two-dimensional double-quantum spectra reveal collective resonances in an atomic vapor. *Physical Review Letters*, **108**(19): 1–5 (2012).

[88] J. Kim, S. Mukamel, and G. Scholes. Two-dimensional electronic double-quantum coherence spectroscopy. *Accounts of Chemical Research*, **42**(9): 1375–1384 (2009).

[89] K. Bott, O. Heller, and D. Bennhardt. Influence of exciton-exciton interactions on the coherent optical response in GaAs quantum wells. *Physical Review B*, **48**(23): 17,418 (1993).

[90] E. J. Mayer, G. O. Smith, V. Heuckeroth, J. Kuhl, K. Bott, A. Schulze, T. Meier, D. Bennhardt, S. W. Koch, P. Thomas, R. Hey, and K. Ploog. Evidence of biexcitonic contributions to four-wave mixing in GaAs quantum wells. *Physical Review B*, **50**(19): 14,730–14,733 (1994).

[91] D. Chemla and J. Shah. Ultrafast dynamics of many-body processes and fundamental quantum mechanical phenomena in semiconductors. *Proceedings of the National Academy of Sciences*, **97**(6): 2437–2444 (2000).

[92] D. Hayes and G. S. Engel. Extracting the excitonic Hamiltonian of the Fenna-Matthews-Olson complex using three-dimensional third-order electronic spectroscopy. *Biophysical Journal*, **100**(8): 2043–2052 (2011).

[93] H. Li, A. D. Bristow, M. E. Siemens, G. Moody, and S. T. Cundiff. Unraveling quantum pathways using optical 3D Fourier-transform spectroscopy. *Nature communications*, **4**: 1390 (2013).

[94] S. T. Cundiff. Optical three dimensional coherent spectroscopy. *Physical chemistry chemical physics*, **16**(18): 8193–8200 (2014).

[95] J. O. Tollerud, C. R. Hall, and J. A. Davis. Isolating quantum coherence using coherent multi-dimensional spectroscopy with spectrally shaped pulses. *Optics Express*, **22**(6): 6719–6733 (2014).

[96] D. B. Turner, K. W. Stone, K. Gundogdu, and K. A. Nelson. Three-dimensional electronic spectroscopy of excitons in GaAs quantum wells. *The Journal of Chemical Physics*, **131**(14): 144,510 (2009).

[97] G. Richards, K. Wilk, P. Curmi, and J. Davis. Disentangling electronic and vibrational coherence in the phycocyanin-645 light-harvesting complex. *Journal of Physical Chemistry Letters*, **5**(1): 43–49 (2014).

[98] G. Richards, K. Wilk, P. M. G. Curmi, H. M. Quiney, and J. A. Davis. Coherent vibronic coupling in light-harvesting complexes from photosynthetic marine algae. *Physical Chemistry Letters*, **3**(2): 272–277 (2012).

[99] N. A. Mathew, L. A. Yurs, S. B. Block, A. V. Pakoulev, K. M. Kornau, and J. C. Wright. Multiple quantum coherence spectroscopy. *The Journal of Physical Chemistry. A*, **113**(33): 9261–9265 (2009).

[100] J. C. Wright. Multiresonant coherent multidimensional spectroscopy. *Annual Review of Physical Chemistry*, **62**(1): 209–230 (2011).

[101] D. D. Kohler, S. B. Block, S. Kain, A. V. Pakoulev, and J. C. Wright. Ultrafast dynamics within the 1s exciton band of colloidal PbSe quantum dots using multiresonant coherent multidimensional spectroscopy. *Journal of Physical Chemistry C*, **118**(9): 5020–5031 (2014).

[102] A. M. Weiner and D. E. Leaird. Generation of terahertz-rate trains of femtosecond pulses by phase-only filtering. *Optics Letters*, **15**(1): 51–53 (1990).

[103] T. Baumert, T. Brixner, V. Seyfried, M. Strehle, and G. Gerber. Rapid communication: Femtosecond pulse shaping by an evolutionary algorithm with feedback. *Applied Physics B*, **65**(6): 779–782 (1997).

[104] H. Kawashima. Femtosecond pulse shaping, multiple-pulse spectroscopy, and optical control. *Annual Review of Physical Chemistry*, **46**(1): 627–656 (1995).

[105] C. Brif, R. Chakrabarti, and H. Rabitz. Control of quantum phenomena: Past, present and future. *New Journal of Physics*, **12**(7): 075,008 (2010).

[106] M. Luo, S. Chuang, and P. Planken. Coherent double-pulse control of quantum beats in a coupled quantum well. *Physical Review B*, **48**(15): 43–50 (1993).

[107] A. P. Heberle, J. J. Baumberg, and K. Köhler. Ultrafast coherent control and destruction of excitons in quantum wells. *Physical Review Letters*, **75**(13): 2598–2601 (1995).

[108] X. Marie, P. Le Jeune, T. Amand, M. Brousseau, J. Barrau, M. Paillard, and R. Planel. Coherent control of the optical orientation of excitons in quantum wells. *Physical Review Letters*, **79**(17): 3222–3225 (1997).

[109] N. H. Bonadeo, J. Erland, D. Gammon, D. S. Katzer, D. Park, and D. G. Steel. Coherent optical control of the quantum state of a single quantum dot. *Optics and Photonics News*, **9**(12): 40 (1998).

[110] P. Wen and K. Nelson. Selective enhancements in 2D Fourier transform optical spectroscopy with tailored pulse shapes. *The Journal of Physical Chemistry A*, **117**(29): 6380–6387 (2013).

[111] V. I. Prokhorenko, A. Halpin, and R. J. D. Miller. Coherently-controlled two-dimensional photon echo electronic spectroscopy. *Optics express*, **17**(12): 9764–9779 (2009).

[112] V. I. Prokhorenko, A. Halpin, and R. J. D. Miller. Coherently-controlled two-dimensional spectroscopy: Evidence for phase induced long-lived memory effects. *Faraday Discussions*, **153**(0): 27–39 (2011).

[113] V. I. Prokhorenko, A. M. Nagy, and R. J. D. Miller. Coherent control of the population transfer in complex solvated molecules at weak excitation. An experimental study. *Journal of Chemical Physics*, **122**(18) (2005).

[114] E. L. Read, G. S. Engel, T. R. Calhoun, T. Mancal, T. K. Ahn, R. E. Blankenship, and G. R. Fleming. Cross-peak-specific two-dimensional electronic spectroscopy. *Proceedings of the National Academy of Sciences of the United States of America*, **104**: 14,203–14,208 (2007).

[115] S. Woutersen and P. Hamm. Structure determination of trialanine in water using polarization sensitive two-dimensional vibrational spectroscopy. *Journal of Physical Chemistry B*, **104**(47): 11,316–11,320 (2000).

[116] M. T. Zanni, N. H. Ge, Y. S. Kim, and R. M. Hochstrasser. Two-dimensional IR spectroscopy can be designed to eliminate the diagonal peaks and expose only the crosspeaks needed for structure determination. *Proceedings of the National Academy of Sciences of the United States of America*, **98**(20): 11,265–11,270 (2001).

[117] M. Khalil, N. Demirdöven, and A. Tokmakoff. Coherent 2D IR spectroscopy: Molecular structure and dynamics in solution. *The Journal of Physical Chemistry A*, **107**(27): 5258–5279 (2003).

[118] N. S. Ginsberg, J. a. Davis, M. Ballottari, Y.-C. Cheng, R. Bassi, and G. R. Fleming. Solving structure in the CP29 light harvesting complex with polarization-phased 2D electronic spectroscopy. *Proceedings of the National Academy of Sciences of the United States of America*, **108**(10): 3848–3853 (2011).

[119] K. Gundogdu, K. W. Stone, D. B. Turner, and K. A. Nelson. Multidimensional coherent spectroscopy made easy. *Chemical Physics*, **341**(1-3): 89–94 (2007).

[120] R. L. Fork, O. E. Martinez, and J. P. Gordon. Negative dispersion using pairs of prisms. *Optics Letters*, **9**(5): 150–152 (1984).

[121] E. W. Weisstein. Fourier Transforms. *MathWorld–A Wolfram Web Resource* (2015).

[122] J. Vaughan. Ultrafast pulse shaping. In R. Trebino (editor), *Ultrafast Optics Textbook*, chapter 13, pp. 1–25. Online: http://frog.gatech.edu/prose.html (2015).

[123] J. C. Vaughan, T. Hornung, K. W. Stone, and K. A. Nelson. Coherently controlled ultrafast four-wave mixing spectroscopy. *Journal of Physical Chemistry A*, **111**(23): 4873–4883 (2007).

[124] A. M. Weiner. Femtosecond pulse shaping using spatial light modulators. *Review of Scientific Instruments*, **71**(5): 1929 (2000).

[125] J. Vaughan, T. Feurer, K. Stone, and K. Nelson. Analysis of replica pulses in femtosecond pulse shaping with pixelated devices. *Optics Express*, **14**(3): 323–325 (2006).

[126] F. Frei, A. Galler, and T. Feurer. Space-time coupling in femtosecond pulse shaping and its effects on coherent control. *The Journal of Chemical Physics*, **130**(3): 034,302 (2009).

[127] B. Sussman, R. Lausten, and A. Stolow. Focusing of light following a 4-f pulse shaper: Considerations for quantum control. *Physical Review A*, **77**(4): 1–11 (2008).

[128] G. Gilliland. Photoluminescence spectroscopy of crystalline semiconductors. *Materials Science and Engineering: R: Reports*, **18**(3-6): 99–399 (1997).

[129] W. Kaye. A universal spectrophotometer. *Applied Optics*, **2**(12): 1295–1302 (1963).

[130] J. Lefebvre and P. Finnie. Polarized photoluminescence excitation spectroscopy of single-walled carbon nanotubes. *Physical Review Letters*, **98**(16): 167,406 (2007).

[131] D. Kundys, S. Schulz, F. Oehler, D. Sutherland, T. J. Badcock, P. Dawson, M. J. Kappers, R. a. Oliver, and C. J. Humphreys. Polarized photoluminescence excitation spectroscopy of a-plane InGaN/GaN multiple quantum wells grown on r-plane sapphire. *Journal of Applied Physics*, **115**(11): 113,106 (2014).

[132] R. E. Smalley, L. Wharton, and D. H. Levy. The fluorescence excitation spectrum of rotationally cooled NO2. *The Journal of Chemical Physics*, **63**(11): 4977 (1975).

[133] M. Squared. Solstis ultra narrow linewidth cw ti:sapphire laser. `http://www.m2lasers.com/media/74139/solstis_datasheet_1014.pdf` (2015). Original document from Coherent. Viewed: Sixth of September, 2015.

[134] Coherent. Mbr-pe narrow linewidth ti:sapphire laser. `https://www.coherent.com/downloads/MBR110PE_DS_0913revB_1.pdf` (2015). Original document from Coherent. Viewed: Sixth of September, 2015.

[135] S.-w. Chiow, S. Herrmann, H. Müller, and S. Chu. 6W, 1 kHz linewidth, tunable continuous-wave near-infrared laser. *Optics Express*, **17**(7): 5246–5250 (2009).

[136] Newport. Cornerstone 130 1/8 m monochromators. `http://assets.newport.com/webDocuments-EN/images/Oriel%20Cornerstone%20130%20Datasheet.pdf` (2015). Original document from Newport Corporation. Viewed: Sixth of September, 2015.

[137] McPherson. Model 2062 high-resolution spectrometrometer. `http://www.mcphersoninc.com/spectrometers/uvvisir/2062%20with%20DP.pdf` (2015). Original document from Mcpherson. Viewed: Sixth of September, 2015.

[138] R. Hildner, D. Brinks, J. B. Nieder, R. J. Cogdell, and N. F. van Hulst. Quantum coherent energy transfer over varying pathways in single light-harvesting complexes. *Science*, **340**(6139): 1448–1451 (2013).

[139] H. P. Sardesai and A. M. Weiner. A femtosecond code-division multiple-access communication system test bed. *Journal of Lightwave Technology*, **16**(11): 1953–1964 (1998).

[140] A. Monmayrant, S. Weber, and B. Chatel. A newcomer's guide to ultrashort pulse shaping and characterization. *Journal of Physics B: Atomic, Molecular and Optical Physics*, **43**(10): 103,001 (2010).

[141] A. Efimov, M. D. Moores, B. Mei, J. L. Krause, C. W. Siders, and D. H. Reitze. Minimization of dispersion in an ultrafast chirped pulse amplifier using adaptive learning. *Applied Physics B*, **70**(1): 133–141 (2000).

[142] J. Davis and C. Jagadish. Semiconductors and their Nanostructures. In R. P. Prasankumar and A. J. Taylor (editors), *Optical Techniques for Solid State Materials Characterization*, chapter 2, pp. 39–78. CRC Press, London (2012).

[143] O. Zitouni, K. Boujdaria, and H. Bouchriha. Band parameters for GaAs and Si in the 24-k sdot p model. *Semiconductor Science and Technology*, **20**(9): 908–911 (2005).

[144] D. Strauch and B. Dorner. Phonon dispersion in GaAs. *Journal of Physics: Condensed Matter*, **2**(6): 1457–1474 (1999).

[145] A. Y. Cho and J. R. Arthur. Molecular beam epitaxy. *Progress in Solid State Chemistry*, **10**(3): 157–191 (1975).

[146] M. J. Ludowise. Metalorganic chemical vapor deposition of III-V semiconductors. *Journal of Applied Physics*, **58**(8) (1985).

[147] T. Kuech and E. Veuhoff. Mechanism of carbon incorporation in MOCVD GaAs. *Journal of Crystal Growth*, **68**(1): 148–156 (1984).

[148] P. Harrison. *Theoretical and Computational Physics of Semiconductor Nanostructures*. Wiley, Chichester, 2 edition (2005).

[149] D. Gammon, B. V. Shanabrook, and D. S. Katzer. Interfaces in GaAs/AlAs quantum well structures. *Applied Physics Letters*, **57**(25): 2710 (1990).

[150] M. Tanaka and H. Sakaki. Atomistic models of interface structures of GaAs-AlxGa1-xAs (x = 0.2-1) quantum wells grown by interrupted and uninterrupted MBE. *Journal of Crystal Growth*, **81**(1-4): 153–158 (1987).

[151] S. Koshiba, S. Nanao, O. Tsuda, Y. Watanabe, Y. Sakurai, H. Sakaki, H. Kawata, and M. Ando. Effects of growth interruption on structure of MBE grown GaAs/AlAs hetero-interfaces studied by x-ray diffraction. *Journal of Crystal Growth*, **95**(1-4): 51–54 (1989).

[152] J. Hegarty, L. Goldner, and M. D. Sturge. Localized and delocalized two-dimensional excitons in GaAs-AlGaAs multiple-quantum-well structures. *Physical Review B*, **30**(12): 7346–7348 (1984).

[153] J. Hegarty and M. Sturge. Studies of exciton localization in quantum-well structures by nonlinear-optical techniques. *Journal of Optical Society of America B*, **2**(7): 1143–1154 (1985).

[154] S. Lan, S. Nishikawa, O. Wada, K. Akahane, Y. Okada, and M. Kawabe. Different responses of localized and extended excitons to exciton-exciton scattering manifested in excitation density-dependent photoluminescence excitation spectra. *Journal of Applied Physics*, **89**(11): 6171–6176 (2001).

[155] A. J. Fischer, D. S. Kim, J. Hays, W. Shan, J. J. Song, D. B. Eason, J. Ren, J. F. Schetzina, H. Luo, and J. K. Furdyna. Femtosecond four-wave-mixing studies of exciton localization and exciton-exciton interaction in ZnSe/ZnxCd1-xSe quantum wells. *Physical Review B*, **50**(23): 17,643–17,646 (1994).

[156] M. D. Webb, S. T. Cundiff, and D. G. Steel. Stimulated-picosecond-photon-echo studies of localized exciton relaxation and dephasing in GaAs/AlxGa1-xAs multiple quantum wells. *Physical Review B* (1991).

[157] M. Webb, S. Cundiff, and D. Steel. Observation of time-resolved picosecond stimulated photon echoes and free polarization decay in GaAs/AlGaAs multiple quantum wells. *Physical Review Letters*, **66**(7): 934–937 (1991).

[158] S. Cundiff, H. Wang, and D. Steel. Polarization-dependent picosecond excitonic nonlinearities and the complexities of disorder. *Physical Review B*, **46**(11) (1992).

[159] S. Cundiff and D. Steel. Coherent transient spectroscopy of excitons in GaAs-AlGaAs quantum wells. *IEEE Journal of Quantum Electronics*, **28**(10): 2423–2433 (1992).

[160] B. M. Ashkinadze, E. Linder, E. Cohen, A. Ron, and L. N. Pfeiffer. Free-carrier effect on exciton dynamics in GaAs/AlxGa1-xAs quantum wells. *Physical Review B*, **51**(3): 1938–1941 (1995).

[161] J. Erland, J. Kim, N. Bonadeo, D. Steel, D. Gammon, and D. Katzer. Nonexponential photon echo decays from nanostructures: Strongly and weakly localized degenerate exciton states. *Physical Review B*, **60**(12): 8497–8500 (1999).

[162] S. T. Cundiff. Coherent spectroscopy of semiconductors. *Optics Express*, **16**(7): 4639–4664 (2008).

[163] C. Lonsky, P. Thomas, and A. Weller. Localization effects in dephasing experiments. *Journal of Luminescence*, **45**(1): 77–79 (1990).

[164] D. Bennhardt, P. Thomas, and A. Weller. Influence of Coulomb interaction on the photon echo in disordered semiconductors. *Physical Review B*, **43**(11): 8934–8945 (1991).

[165] C. Lonsky, P. Thomas, and a. Weller. Optical dephasing in disordered semiconductors. *Physical Review Letters*, **63**(6): 652–655 (1989).

[166] F. Jahnke, M. Koch, T. Meier, J. Feldmann, W. Schafer, P. Thomas, S. Koch, E. Gobel, and H. Nickel. Simultaneous influence of disorder and Coulomb interaction on photon echoes in semiconductors. *Physical Review B*, **50**(11): 8114–8117 (1994).

[167] D. Bimberg, H. Münzel, A. Steckenborn, and J. Christen. Kinetics of relaxation and recombination of nonequilibrium carriers in GaAs: Carrier capture by impurities. *Physical Review B*, **31**(12): 7788–7799 (1985).

[168] M. Skolnick, C. Tu, and T. Harris. High-resolution spectroscopy of defect-bound excitons and acceptors in GaAs grown by molecular-beam epitaxy. *Physical Review B*, **33**(12) (1986).

[169] J.-Y. Marzin, M. Charasse, and B. Sermage. Optical investigation of a new type of valence-band configuration in In_{x}Ga_{1-x}As-GaAs strained superlattices (1985).

[170] G. Ji, D. Huang, U. Reddy, T. Henderson, R. Houdre, and H. Morkoc. Optical investigation of highly strained InGaAs-GaAs multiple quantum wells. *Journal of Applied Physics*, **62**(8): 3366 (1987).

[171] J. Davis and C. Jagadish. Ultrafast spectroscopy of ZnO/ZnMgO quantum wells. *Laser & Photonics Review*, **3**(1-2): 85–96 (2009).

[172] K. F. Huang, K. Tai, S. N. G. Chu, and A. Y. Cho. Optical studies of InxGa1-xAs/GaAs strained-layer quantum wells. *Applied Physics Letters*, **54**(20): 2026 (1989).

[173] D.-S. Kim, J. Shah, J. Cunningham, T. Damen, W. Schäfer, M. Hartmann, and S. Schmitt-Rink. Giant excitonic resonance in time-resolved four-wave mixing in quantum wells. *Physical Review Letters*, **68**(7): 1006–1009 (1992).

[174] L. Schultheis, a. Honold, J. Kuhl, K. Köhler, and C. W. Tu. Optical dephasing of homogeneously broadened two-dimensional exciton transitions in GaAs quantum wells. *Physical Review B*, **34**(12): 9027–9030 (1986).

[175] A. Honold, L. Schultheis, J. Kuhl, and C. W. Tu. Collision broadening of two-dimensional excitons in a GaAs single quantum well. *Physical Review B*, **40**(9): 6442–6445 (1989).

[176] H. Wang, K. Ferrio, D. Steel, Y. Hu, R. Binder, and S. Koch. Transient nonlinear optical response from excitation induced dephasing in GaAs. *Physical Review Letters*, **71**(8): 1261–1264 (1993).

[177] H. Wang, K. B. Ferrio, D. G. Steel, P. R. Berman, Y. Z. Hu, R. Binder, and S. W. Koch. Transient four-wave-mixing line shapes: Effects of excitation-induced dephasing. *Physical Review A* (1994).

[178] V. G. Lyssenko, J. Erland, I. Balslev, K. H. Pantke, B. S. Razbirin, and J. M. Hvam. Nature of nonlinear four-wave-mixing beats in semiconductors. *Physical Review B*, **48**(8): 5720–5723 (1993).

[179] K. Leo, T. Damen, and J. Shah. Quantum beats of light hole and heavy hole excitons in quantum wells. *Applied Physics Letters*, **57**(1): 19–21 (1990).

[180] B. F. Feuerbacher, J. Kuhl, R. Eccleston, and K. Ploog. Quantum beats between the light and heavy hole excitons in a quantum well. *Solid State Communications*, **74**(12): 1279–1283 (1990).

[181] K. Leo, T. Damen, J. Shah, and K. Köhler. Quantum beats of free and bound excitons in GaAs/AlxGa1-xAs quantum wells. *Physical Review B*, **42**(17): 359–361 (1990).

[182] C. R. Hall. *Ultrafast Dynamics In Semiconductor quantum wells*. Ph.D. thesis, Swinburne University of Technology (2011).

[183] I. Mashkov, C. Gourdon, P. Lavallard, and D. Roditchev. Exciton quantum beats in type-II GaAs/AlAs superlattices in longitudinal and in-plane magnetic fields. *Physical Review B*, **55**(20): 761–770 (1997).

[184] O. Kojima, K. Mizoguchi, and M. Nakayama. Quantum beats of type-I and type-II excitons in an InxGa1-xAs/GaAs strained single quantum well. *Journal of Applied Physics*, **112**(4): 043,522 (2012).

[185] M. Hübner, J. Kuhl, T. Stroucken, A. Knorr, S. Koch, R. Hey, and K. Ploog. Collective effects of excitons in multiple-quantum-well Bragg and anti-Bragg structures. *Physical Review Letters*, **76**(22): 4199–4202 (1996).

[186] D. S. Chemla and J. Shah. Many-body and correlation effects in semiconductors. *Nature*, **411**(6837): 549–557 (2001).

[187] D.-S. Kim, J. Shah, T. Damen, W. Schäfer, F. Jahnke, S. Schmitt-Rink, and K. Köhler. Unusually slow temporal evolution of femtosecond four-wave-mixing signals in intrinsic GaAs quantum wells: Direct evidence for the dominance of interaction effects. *Physical Review Letters*, **69**(18): 2725–2728 (1992).

[188] D. Chemla, W. Knox, D. Miller, S. Schmitt-Rink, J. Stark, and R. Zimmermann. The excitonic optical Stark effect in semiconductor quantum wells probed with femtosecond optical pulses. *Journal of Luminescence*, **44**: 233–246 (1989).

[189] G. Manzke, Q. Peng, K. Henneberger, U. Neukirch, K. Hauke, J. Wundke, J. Gutowski, and D. Hommel. Density dependence of the exciton energy in semiconductors. *Physical Review Letters*, **80**(22): 4943–4946 (1998).

[190] S. Bolton, U. Neukirch, L. Sham, D. Chemla, and V. Axt. Demonstration of sixth-order Coulomb correlations in a semiconductor single quantum well. *Physical Review Letters*, **85**(9): 2002–2005 (2000).

[191] D. B. Turner and K. A. Nelson. Coherent measurements of high-order electronic correlations in quantum wells. *Nature*, **466**(7310): 1089–1092 (2010).

[192] R. Miller, D. Kleinman, A. Gossard, and O. Munteanu. Biexcitons in GaAs quantum wells. *Physical Review B*, **25**(10): 6545–6547 (1982).

[193] A. E. Almand-Hunter, H. Li, S. T. Cundiff, M. Mootz, M. Kira, and S. W. Koch. Quantum droplets of electrons and holes. *Nature*, **506**(7489): 471–475 (2014).

[194] C. N. Borca, T. Zhang, X. Li, and S. T. Cundiff. Optical two-dimensional Fourier transform spectroscopy of semiconductors. *Chemical Physics Letters*, **416**(4-6): 311–315 (2005).

[195] M. Erementchouk, M. N. Leuenberger, and L. J. Sham. Many-body interaction in semiconductors probed with two-dimensional Fourier spectroscopy. *Physical Review B*, **76**(11): 115,307 (2007).

[196] R. Singh, T. M. Autry, G. Nardin, G. Moody, H. Li, K. Pierz, M. Bieler, and S. T. Cundiff. Anisotropic homogeneous linewidth of the heavy-hole exciton in (110)-oriented GaAs quantum wells. *Physical Review B*, **88**(4): 3–8 (2013).

[197] X. Li, T. Zhang, S. Mukamel, R. P. Mirin, and S. T. Cundiff. Investigation of electronic coupling in semiconductor double quantum wells using coherent optical two-dimensional Fourier transform spectroscopy. *Solid State Communications*, **149**(9-10): 361–366 (2009).

[198] J. Paul, P. Dey, T. Tokumoto, J. L. Reno, D. J. Hilton, and D. Karaiskaj. Exploring two-dimensional electron gases with two-dimensional Fourier transform spectroscopy. *The Journal of Chemical Physics*, **141**(13): 134,505 (2014).

[199] Y. Glinka, M. Erementchouk, K. Chandriker, M. Leuenberger, A. Bracker, and X. Li. Non-local coherent coupling between excitons in a disordered quantum well. *New Journal of Physics*, **15**(7): 075,026 (2013).

[200] E. Collini, C. Y. Wong, K. E. Wilk, P. M. G. Curmi, P. Brumer, and G. D. Scholes. Coherently wired light-harvesting in photosynthetic marine algae at ambient temperature. *Nature*, **463**(7281): 644–647 (2010).

[201] G. H. Richards, K. E. Wilk, P. M. G. Curmi, H. M. Quiney, and J. A. Davis. Excited state coherent dynamics in light-harvesting complexes from photosynthetic marine algae. *Journal of Physics B*, **45**(15): 154,015 (2012).

[202] P. Dapkus, J. Coleman, W. D. Laidig, N. Holonyak, B. A. Vojak, and K. Hess. Continuous room temperature photopumped laser operation of modulation doped AlxGa1-xAs/GaAs superlattices. *Applied Physics Letters*, **38**(3): 118–120 (1981).

[203] F. Capasso, K. Mohammed, and A. Cho. Electronic transport and depletion of quantum wells by tunneling through deep levels in semiconductor superlattices. *Physical review letters*, **57**(18): 2303–2306 (1986).

[204] D. K. Kim and D. S. Citrin. Strong excitonic mixing effect in asymmetric double quantum wells: On the optimization of electroabsorption modulators. *Physica Status Solidi (C)*, **5**(7): 2400–2403 (2008).

[205] K. Leo, J. Shah, T. Damen, A. Schulze, T. Meier, S. Schmitt-Rink, P. Thomas, E. O. Gobel, S. L. Chuang, M. S. C. Luo, W. Schafer, K. Kohler, and P. Ganser. Dissipative dynamics of an electronic wavepacket in a semiconductor double well potential. *IEEE Journal of Quantum Electronics*, **28**(10): 2498–2507 (1992).

[206] H. Roskos, M. Nuss, J. Shah, K. Leo, D. A. B. Miller, A. Fox, S. Schmitt-Rink, and K. Kohler. Coherent submillimeter-wave emission from charge oscillations in a double-well potential. *Physical Review Letters*, **68**(14): 2216–2219 (1992).

[207] F. Eickemeyer, K. Reimann, M. Woerner, T. Elsaesser, S. Barbieri, C. Sirtori, G. Strasser, T. Müller, R. Bratschitsch, and K. Unterrainer. Ultrafast coherent electron transport in semiconductor quantum cascade structures. *Physical Review Letters*, **89**(4): 047,402 (2002).

[208] M. Woerner, K. Reimann, and T. Elsaesser. Coherent charge transport in semiconductor quantum cascade structures. *Journal of Physics: Condensed Matter*, **16**(4): 25–48 (2004).

[209] J. Yuen-Zhou, D. H. Arias, D. M. Eisele, C. P. Steiner, J. J. Krich, M. G. Bawendi, K. a. Nelson, and A. Aspuru-Guzik. Coherent exciton dynamics in supramolecular light-harvesting nanotubes revealed by ultrafast quantum process tomography. *ACS Nano*, **8**(6): 5527–5534 (2014).

[210] F. Harris. On the use of windows for harmonic analysis with the discrete Fourier transform. *Proceedings of the IEEE*, **66**(1): 51–83 (1978).

[211] G. Heinzel, A. Rüdiger, and R. Schilling. Spectrum and spectral density estimation by the Discrete Fourier transform (DFT), including a comprehensive

list of window functions and some new flat-top. Technical report, The Max Planck Institute for Gravitational Physics (2002).

[212] K. Mak, C. Lee, J. Hone, J. Shan, and T. Heinz. Atomically thin MoS2: A new direct-gap semiconductor. *Physical Review Letters*, **105**(13): 2–5 (2010).

[213] S. Cundiff. Effects of correlation between inhomogeneously broadened transitions on quantum beats in transient four-wave mixing. *Physical Review A*, **49**(4): 3114–3119 (1994).

[214] M. Koch, R. Hellmann, S. T. Cundiff, J. Feldmann, E. O. Gijbel, D. R. Yakovlev, A. Waag, and G. Landwehr. Excitonic quantum beats in CdTe/Cd1-xMnxTe quantum wells. *Solid State Communications*, **88**(7): 515–519 (1993).

[215] E. Cassette, R. D. Pensack, B. Mahler, and G. D. Scholes. Room-temperature exciton coherence and dephasing in two-dimensional nanostructures. *Nature Communications*, **6**(1): 6086 (2015).

[216] S. Cundiff, A. Bristow, M. Siemens, H. Li, G. Moody, D. Karaiskaj, X. Dai, and T. Zhang. Optical 2-D Fourier transform spectroscopy of excitons in semiconductor nanostructures. *IEEE Journal of Selected Topics in Quantum Electronics*, **18**(1): 318–328 (2012).

[217] A. D. Bristow, T. Zhang, M. E. Siemens, S. T. Cundiff, and R. P. Mirin. Separating homogeneous and inhomogeneous line widths of heavy- and light-hole excitons in weakly disordered semiconductor quantum wells. *Journal of Physical Chemistry B*, **115**(18): 5365–5371 (2011).

[218] A. D. Bristow, D. Karaiskaj, X. Dai, T. Zhang, C. Carlsson, K. R. Hagen, R. Jimenez, and S. T. Cundiff. A versatile ultrastable platform for optical multidimensional Fourier-transform spectroscopy. *Review of Scientific Instruments*, **80**(7): 073,108 (2009).

[219] A. Singh, G. Moody, S. Wu, Y. Wu, N. J. Ghimire, J. Yan, D. G. Mandrus, X. Xu, and X. Li. Coherent electronic coupling in atomically thin MoSe2. *Physical Review Letters*, **112**(21): 1–5 (2014).

[220] A. Naeem, F. Masia, S. Christodoulou, I. Moreels, P. Borri, and W. Langbein. Giant exciton oscillator strength and radiatively limited dephasing in two-dimensional platelets. *Physical Review B*, **91**(12): 8–12 (2015).

[221] J. R. Caram, H. Zheng, P. D. Dahlberg, B. S. Rolczynski, G. B. Griffin, A. F. Fidler, D. S. Dolzhnikov, D. V. Talapin, and G. S. Engel. Persistent interexcitonic quantum coherence in CdSe quantum dots. *Journal of Physical Chemistry Letters*, **5**(1): 196–204 (2014).

[222] D. Kim, H. Ko, Y. Kim, S. Rhee, and S. Hohng. Percolation of carriers through low potential channels in thick Al x Ga 1-x As (x< 0.35) barriers. *Physical Review B*, **54**(20): 580–588 (1996).

[223] S. Mukamel. Multidimensional femtosecond correlation spectroscopies of electronic and vibrational excitations. *Annual Review of Physical Chemistry*, **51**(1): 691–729 (2000).

[224] S. Mukamel, D. Abramavicius, L. Yang, W. E. I. Zhuang, I. V. Schweigert, and D. V. Voronine. Coherent Multidimensional Optical Probes for Electron Correlations and Exciton Dynamics : From NMR to X-rays. *Accounts of Chemical Research*, **42**(4): 553–562 (2009).

[225] M. Ikura, L. E. Kay, and a. Bax. A novel approach for sequential assignment of 1H, 13C, and 15N spectra of proteins: heteronuclear triple-resonance three-dimensional NMR spectroscopy. Application to calmodulin. *Biochemistry*, **29**(19): 4659–4667 (1990).

[226] L. E. Kay, M. Ikura, R. Tschudin, and A. Bax. Three-dimensional triple-resonance NMR Spectroscopy of isotopically enriched proteins. *Journal of Magnetic Resonance*, **89**(3): 496–514 (1990).

[227] W. Commons. 1h nmr ethyl acetate coupling shown (2007). File: 1HNMREthylAcetateCouplingshown.png.

[228] A. Maudsley and R. R. Ernst. Indirect detection of magnetic resonance by heteronuclear two-dimensional spectroscopy. *Chemical Physics Letters*, **50**(3): 368–372 (1977).

[229] L. Müller. Sensitivity enhanced detection of weak nuclei using heteronuclear multiple quantum coherence. *Journal of the American Chemical Society*, **101**(16): 4481–4484 (1979).

[230] M. Robin Bendall, D. T. Pegg, and D. M. Doddrell. Pulse sequences utilizing the correlated motion of coupled heteronuclei in the transverse plane of the doubly rotating frame. *Journal of Magnetic Resonance*, **52**(1): 81–117 (1983).

[231] C. D. Schwieters, J. J. Kuszewski, N. Tjandra, and G. M. Clore. The Xplor-NIH NMR molecular structure determination package. *Journal of magnetic resonance*, **160**(1): 65–73 (2003).

[232] C. Scheurer and S. Mukamel. Infrared analogs of heteronuclear nuclear magnetic resonance coherence transfer experiments in peptides. *The Journal of Chemical Physics*, **116**(15): 6803 (2002).

[233] M. Alessi, A. Patane, A. Polimeni, and M. Capizzi. Formation and relaxation of exciton-carbon acceptor complexes in GaAs. *Physical Review B*, **56**(7): 3834–3837 (1997).

[234] N. Christensson, F. Milota, A. Nemeth, I. Pugliesi, E. Riedle, J. Sperling, T. o. Pullerits, H. F. Kauffmann, and J. Hauer. Electronic double-quantum coherences and their impact on ultrafast spectroscopy: The example of β-carotene. *Journal of Physical Chemistry Letters*, **1**(23): 3366–3370 (2010).

[235] Q. H. Wang, K. Kalantar-Zadeh, A. Kis, J. N. Coleman, and M. S. Strano. Electronics and optoelectronics of two-dimensional transition metal dichalcogenides. *Nature Nanotechnology*, **7**(11): 699–712 (2012).

[236] L. Britnell, R. M. Ribeiro, A. Eckmann, R. Jalil, B. D. Belle, A. Mishchenko, Y. Kim, R. V. Gorbachev, T. Georgiou, S. V. Morozov, A. N. Grigorenko, A. K. Geim, C. Casiraghi, A. H. C. Neto, and K. S. Novoselov. Strong light-matter interactions in heterostructures of atomically thin films. *Science*, **340**(6138): 1311–1314 (2013).

[237] H. Hirayama, J. Yoshida, Y. Miyake, and A. Masahiro. Carrier capture time and its effect on the efficiency of quantum-well lasers. *IEEE Journal of Quantum Electronics*, **30**(1): 54–62 (1994).

[238] H. Schneider and C. L. Liu. *Quantum Well Infrared Photodetectors*. Springer-Verlag, Berlin (2007).

[239] S. Weiss, J. M. Wiesenfeld, D. S. Chemla, G. Raybon, G. Sucha, M. Wegener, G. Eisenstein, C. A. Burrus, A. G. Dentai, U. Koren, B. I. Miller, H. Temkin, R. A. Logan, and T. Tanbun-Ek. Carrier capture times in 1.5 μm multiple quantum well optical amplifiers. *Applied Physics Letters*, **60**(1): 9 (1992).

[240] B. Deveaud, A. Chomette, D. Morris, and A. Regreny. Carrier capture in quantum wells. *Solid State Communications*, **85**(4): 367–371 (1993).

[241] P. Blom, C. Smit, J. Haverkort, and J. Wolter. Carrier capture into a semiconductor quantum well. *Physical Review B*, **47**(4): 2072–2081 (1993).

[242] D. Reynolds, K. Evans, K. Bajaj, and B. Jogai. Direct coupling of heavy-hole free excitons in In x Ga 1- x As/GaAs quantum wells with free excitons in the GaAs barrier. *Physical Review B*, **43**(2): 1871–1874 (1991).

[243] D. C. Reynolds, B. Jogai, P. W. Yu, and C. E. Stutz. Excitation of optical transitions in the InxGa1-xAs-GaAs quantum well system by the free exciton in the barrier. *Journal of Applied Physics*, **74**(2): 1453 (1993).

[244] J. H. Davies. *The Physics of Low-dimensional Semiconductors: An Introduction*. Cambridge University Press, Cambridge (1997).

[245] J. E. Golub, K. Kash, J. P. Harbison, and L. T. Florez. Long-lived spatially indirect excitons in coupled GaAs/AlxGa1-xAs quantum wells. *Physical Review B*, **41**(12): 8564–8567 (1990).

[246] S. Charbonneau, M. L. W. Thewalt, E. S. Koteles, and B. Elman. Transformation of spatially direct to spatially indirect excitons in coupled double quantum wells. *Physical Review B*, **38**(9): 6287–6290 (1988).

[247] A. A. High, J. R. Leonard, A. T. Hammack, M. M. Fogler, L. V. Butov, A. V. Kavokin, K. L. Campman, and A. C. Gossard. Spontaneous coherence in a cold exciton gas. *Nature*, **483**(7391): 584–8 (2012).

[248] L. Butov, C. Lai, A. Ivanov, A. Gossard, and D. Chemla. Towards Bose-Einstein condensation of excitons in potential traps. *Nature*, **417**(May): 47–52 (2002).

[249] D. Snoke, S. Denev, Y. Liu, L. Pfeiffer, and K. West. Long-range transport in excitonic dark states in coupled quantum wells. *Nature*, **418**(August): 754–757 (2002).

[250] A. Larionov and V. Timofeev. Condensation of interwell excitons in GaAs/AlGaAs double quantum wells. *Journal of Experimental and Theoretical Physics*, **73**(6): 301–308 (2001).

[251] S. Pan, H. Shen, Z. Hang, F. Pollak, and W. Zhuang. Photoreflectance study of narrow-well strained-layer In x Ga 1- x As/GaAs coupled multiple-quantum-well structures. *Physical Review B*, **38**(5): 3375–3382 (1988).

[252] J. Menendez, A. Pinczuk, and D. Werder. Large valence-band offset in strained-layer In x Ga 1- x As-GaAs quantum wells. *Physical Review B*, **36**(15): 8165–8168 (1987).

[253] A. Ksendzov, H. Shen, F. Pollak, and D. Bour. Photoreflectance study of In x Ga 1-x As/GaAs single quantum wells. *Surface science*, **228**: 326–329 (1990).

[254] B. Jogai and P. W. Yu. Energy levels of strained In_ {x} Ga_ {1-x} As-GaAs superlattices. *Physical Review B*, **41**(18): 650–658 (1990).

[255] M. Moran, P. Dawson, and K. Moore. The nature of the light hole potential profile in GaAs-InGaAs double quantum well structures. *Solid State Communications*, **107**(3): 119–123 (1998).

[256] K. Kim, G. L. W. Hart, and A. Zunger. Negative band gap bowing in epitaxial InAs/GaAs alloys and predicted band offsets of the strained binaries and alloys on various substrates. *Applied Physics Letters*, **80**(17): 3105 (2002).

[257] A. Kavokin, M. Kaliteevski, and S. Goupalov. Quantum wells with zero valence-band offset: Drastic enhancement of forbidden excitonic transitions. *Physical Review B*, **54**(16): 78–81 (1996).

[258] Z. Piao, M. Nakayama, and H. Nishimura. Binding energies and envelope functions of light-hole excitons in GaAs/InxGa1-xAs/GaAs strained quantum wells. *Physical Review B*, **54**(15): 10,312–10,315 (1996).

[259] M. Nakayama and T. Nakanishi. Oscillator strength of type-II light-hole exciton in In x Ga 1- x As/GaAs strained single quantum wells. *Physica E*, **7**(3): 567–571 (2000).

[260] P. C. M. Planken, M. C. Nuss, I. Brener, K. W. Goosen, M. S. C. Luo, S. L. Chuang, and L. Pfeifer. Terahertz emission in single quantum wells after coherent optical excitation of light hole and heavy hole excitons. *Physical Review Letters*, **69**(26): 3800–3804 (1992).

[261] I. Vurgaftman, J. R. Meyer, and L. R. Ram-Mohan. Band parameters for III-V compound semiconductors and their alloys. *Journal of Applied Physics*, **89**(11): 5815–5875 (2001).

[262] W. S. Chi and Y. S. Huang. The determination of the band offsets in strained-layer InX Ga1-x As / GaAs quantum wells by low-temperature modulation spectroscopy. *Semiconductor Science and Technology*, **10**(1): 127–137 (1995).

[263] D. J. Arent, K. Deneffe, C. Van Hoof, J. De Boeck, and G. Borghs. Strain effects and band offsets in GaAs/InGaAs strained layered quantum structures. *Journal of Applied Physics*, **66**(4): 1739 (1989).

[264] K. Moore, G. Duggan, A. Raukema, and K. Woodbridge. Miniband dispersion in (In, Ga) As-GaAs strained-layer superlattices. *Physical Review B*, **42**(2): 1326–1331 (1990).

[265] M. Joyce, Z. Xu, and M. Gal. Photoluminescence excitation spectroscopy of as-grown and chemically released In 0.05 Ga 0.95 As/GaAs quantum wells. *Physical Review B*, **44**(7): 3144–3149 (1991).

[266] L. P. Ramberg, P. M. Enquist, Y.-K. Chen, F. E. Najjar, L. F. Eastman, E. a. Fitzgerald, and K. L. Kavanagh. Lattice-strained heterojunction InGaAs/GaAs bipolar structures: Recombination properties and device performance. *Journal of Applied Physics*, **61**(3): 1234 (1987).

[267] M. Joyce, M. Johnson, M. Gal, and B. Usher. Concentration-dependent band offset in In_{x}Ga_{1-x}As/GaAs strained quantum wells. *Physical Review B*, **38**(15): 10,978–10,980 (1988).

[268] S. Niki, C. L. Lin, W. S. C. Chang, and H. H. Wieder. Band-edge discontinuities of strained-layer InxGa1-xAs/GaAs heterojunctions and quantum wells. *Applied Physics Letters*, **55**(13): 1339 (1989).

[269] D. Gershoni, J. Vandenberg, and S. Chu. Excitonic transitions in strained-layer In x Ga 1- x As/GaAs quantum wells. *Physical Review B*, **40**(14): 10,017–10,020 (1989).

[270] D. P. Wang, C. T. Chen, H. Kuan, S. C. Shei, and Y. K. Su. Study on symmetry forbidden transitions in an InxGa1-xAs/GaAs single quantum well by temperature dependence. *Journal of Applied Physics*, **77**(12): 6500 (1995).

[271] J.-L. Yu, Y.-H. Chen, C.-G. Tang, C. Jiang, and X.-L. Ye. Observation of strong anisotropic forbidden transitions in (001) InGaAs/GaAs single-quantum well by reflectance-difference spectroscopy and its behavior under uniaxial strain. *Nanoscale Research Letters*, **6**(1): 210 (2011).

[272] H. Shen, P. Parayanthal, and F. Pollak. Observation of symmetery forbidden transitions in the room temperature photoreflectance spectrum of a GaAs/-GaAlAs multiple quantum well. *Solid State Communications*, **59**(8): 557–560 (1986).

[273] Y. Chen, Z. Yang, Z. Wang, X. Bo, and J. Liang. Quantum-well anisotropic forbidden transitions induced by a common-atom interface potential. *Physical Review B*, **60**(3): 3–6 (1999).

[274] S. Kwok, H. Grahn, K. Ploog, and R. Merlin. Giant electropleochroism in GaAs-(Al, Ga) As heterostructures: the quantum-well pockels effect. *Physical Review Letters*, **69**(6): 973–976 (1992).

[275] W. Z. Shen, W. G. Tang, S. C. Shen, S. M. Wang, and T. Andersson. Absorption spectroscopy studies of strained InGaAs/GaAs single-quantum wells. *Applied Physics Letters*, **65**(21): 2728 (1994).

[276] K. Ferrio and D. Steel. Observation of the ultrafast two-photon coherent biexciton oscillation in a GaAs/Al x Ga 1- x As multiple quantum well. *Physical Review B*, **54**(8): 5231–5234 (1996).

[277] O. Heller and G. Bastard. Exciton capture by shallow quantum wells in separate confinement heterostructures. *Physical Review B*, **54**(8): 5629–5636 (1996).

[278] G. B. Griffin, S. Ithurria, D. S. Dolzhnikov, A. Linkin, D. V. Talapin, and G. S. Engel. Two-dimensional electronic spectroscopy of CdSe nanoparticles at very low pulse power. *The Journal of chemical physics*, **138**(1): 014,705 (2013).

[279] D. Smith. Strain-generated electric fields in growth axis strained-layer superlattices. *Solid state communications*, **57**(12): 919–921 (1986).

[280] D. H. Levi, D. R. Wake, M. V. Klein, S. Kumar, and H. Morkoç. Density dependence of nonresonant tunneling in asymmetric coupled quantum wells. *Physical Review B*, **45**(8): 4274–4279 (1992).

[281] R. Eccleston, B. F. Feuerbacher, J. Kuhl, W. W. Ruhle, and K. Ploog. Density-dependent exciton radiative lifetimes in GaAs quantum wells. *Physical Review B*, **45**(19): 11,403–11,406 (1992).

[282] D. R. Wake, H. W. Yoon, J. P. Wolfe, and H. Morkoç. Response of excitonic absorption spectra to photoexcited carriers in GaAs quantum wells. *Physical Review B*, **46**(20): 13,452–13,460 (1992).

[283] R. Eccleston, J. Kuhl, D. Bennhardt, and P. Thomas. Intensity dependent four-wave-mixing polarization rules in quantum wells. *Solid State Communications*, **86**(2): 93–97 (1993).

[284] W. T. Masselink, P. J. Pearah, J. Klem, C. K. Peng, H. Morkoç, G. D. Sanders, and Y. C. Chang. Absorption coefficients and exciton oscillator strengths in AlGaAs-GaAs superlattices. *Physical Review B*, **32**(12): 8027–8034 (1985).

[285] P. M. Petroff and S. P. Denbaars. MBE and MOCVD growth and properties of self-assembling quantum-dot arrays in III-V semiconductor structures (1994).

[286] D. S. Katzer, D. Gammon, and B. V. Shanabrook. Modification of the microroughness of molecular-beam epitaxially grown GaAs/AlAs interfaces through changes in the growth temperature. *Journal of Vacuum Science & Technology B*, **10**(2): 800 (1992).

[287] R. H. Dicke. Coherence in spontaneous radiation processes. *Physical Review*, **93**(1): 99–110 (1954).

[288] S. Haroche. Controlling photons in a box and exploring the quantum to classical boundary (Nobel Lecture). *Reviews of Modern Physics*, **85**(3): 10,158–10,178 (2013).

[289] R. DeVoe and R. Brewer. Observation of superradiant and subradiant spontaneous emission of two trapped ions. *Physical Review Letters*, **76**(12): 2049–2052 (1996).

[290] K. Baumann, C. Guerlin, F. Brennecke, and T. Esslinger. Dicke quantum phase transition with a superfluid gas in an optical cavity. *Nature*, **464**(7293): 1301–1306 (2010).

[291] M. Scheibner, T. Schmidt, L. Worschech, A. Forchel, G. Bacher, T. Passow, and D. Hommel. Superradiance of quantum dots. *Nature Physics*, **3**(2): 106–110 (2007).

[292] T. Takagahara and E. Hanamura. Giant-oscillator-strength effect on excitonic optical nonlinearities due to localization. *Physical Review Letters*, **56**(23): 2533–2536 (1986).

[293] J. Hours, P. Senellart, E. Peter, A. Cavanna, and J. Bloch. Exciton radiative lifetime controlled by the lateral confinement energy in a single quantum dot. *Physical Review B*, **71**(16): 1–4 (2005).

[294] V. Savona and W. Langbein. Realistic heterointerface model for excitonic states in growth-interrupted GaAs quantum wells. *Physical Review B*, **74**(7): 1–18 (2006).

[295] F. Intonti, V. Emiliani, C. Lienau, T. Elsaesser, V. Savona, E. Runge, R. Zimmermann, R. Nötzel, and K. H. Ploog. Quantum mechanical repulsion of exciton levels in a disordered quantum well. *Physical Review Letters*, **87**(7): 1–4 (2001).

[296] F. Intonti, V. Emiliani, C. Lienau, T. Elasaesser, V. Savona, E. Runge, R. Zimmermann, R. Nötzel, and K. H. Ploog. Quantum mechanical repulsion of exciton levels in a disordered quantum well evidenced by near-field spectroscopy. *Physica E: Low-Dimensional Systems and Nanostructures*, **13**(2-4): 178–181 (2002).

[297] K. Brunner, G. Abstreiter, and G. Böhm. Sharp-line photoluminescence and two-photon absorption of zero-dimensional biexcitons in a GaAs/AlGaAs structure. *Physical Review Letters*, **73**(8): 1138–1141 (1994).

[298] R. Grousson, V. Voliotis, and N. Grandjean. Microroughness and exciton localization in (Al, Ga) As/GaAs quantum wells. *Physical Review B*, **55**(8): 5253–5258 (1997).

[299] U. Bockelmann, W. Heller, a. Filoramo, and P. Roussignol. Microphotoluminescence studies of single quantum dots. I. Time-resolved experiments. *Physical Review B*, **55**(7): 4456–4468 (1997).

[300] R. Zimmermann, F. Groß e, and E. Runge. Excitons in semiconductor nanostructures with disorder. *Pure and Applied Chemistry*, **69**(6): 1179–1186 (1997).

[301] R. M. Clegg. *The history of FRET : From conception through the labors of birth*. Springer US (2006). ISBN 978-0-387-33016-7.

[302] L. Novotny and B. Hecht. Optical Interactions. In *Principles of Nano-Optics*, chapter 8, pp. 35–46. Cambridge University Press, Cambridge, 2 edition (2012).

[303] A. Nemeth, F. Milota, T. Mančal, T. Pullerits, J. Sperling, J. Hauer, H. F. Kauffmann, and N. Christensson. Double-quantum two-dimensional electronic spectroscopy of a three-level system: Experiments and simulations. *Journal of Chemical Physics*, **133**(9) (2010).

[304] K. W. Stone, D. B. Turner, K. Gundogdu, S. T. Cundiff, and K. A. Nelson. Exciton - exciton correlations revealed by two-dimensional Fourier transform optical spectroscopy. *Accounts of Chemical Research*, **42**(9): 1452–1461 (2009).

[305] F. Novelli, A. Nazir, G. H. Richards, A. Roozbeh, K. E. Wilk, P. M. G. Curmi, and J. A. Davis. Vibronic resonances facilitate excited-state coherence in light-harvesting proteins at room temperature. *The Journal of Physical Chemistry Letters*, **6**(22): 4573–4580 (2015).

[306] J. L. M. Quiroz Gonzalez and D. Thompson. Getting started with Numerov's method. *Computers in Physics*, **11**(5): 514 (1997).

[307] E. W. Weisstein. Sifting Property. *MathWorld–A Wolfram Web Resource* (2015).

A1

EXPERIMENTAL PARAMETERS

	Scan type	t_1 step, range	t_2 step, range	t_{2Q} step, range	Density (Photons·cm^{-2})	CF (nm)	Temp (K)	Polarization	Figure
AlGaAs BB 2D	1Q	10 fs, 2000 fs	$t_2 = 0$ fs		7×10^{11}	795	20	Co-linear	4.4
AlGaAs BB 3D	1Q	10 fs, 2000 fs	15 fs, 900 fs		7×10^{11}	795	20	Co-linear	4.5, 4.6, 4.7
AlGaAs CS 2D	1Q	10 fs, 2000 fs	$t_2 = 0$ fs		3×10^{11}	795	20	Co-linear	4.9
InGaAs BB 2D	1Q	50 fs, 5000 fs	$t_2 = 0$ fs		2.4×10^{10}	850	6	Co-circular	4.18
	0Q	$t_1 = 0$ fs	50 fs, 5000 fs		2.4×10^{10}	850	6	Co-circular	4.18
	2Q	$t_1 = 0$ fs		40 fs, 2000 fs	2.4×10^{10}	850	6	Co-circular	4.18
InGaAs CS-3D	1Q	50 fs, 2000 fs	50 fs, 2000 fs		1.5×10^{10}	850	6	Co-circular	4.19

Table A1.1: Experimental parameters in Ch. 4.

	Scan type	t_1 step, range	t_2 step, range	t_{2Q} step, range	Density (Photons·cm^{-2})	CF (nm)	Temp (K)	Polarization	Figure
InGaAs BB 2D	2Q	$t_2 = 300$ fs		10 fs, 2000 fs	3.4×10^{10}	810	6	Co-linear	5.9
InGaAs CS 2D	2Q	$t_2 = 300$ fs		10 fs, 2000 fs	2.2×10^{10}	810	6	Co-linear	5.9

Table A1.2: Experimental parameters in Ch. 5.

	Scan type	t_1 step, range	t_2 step, range	t_{2Q} step, range	Density (Photons·cm^{-2})	CF (nm)	Temp (K)	Polarization	Figure
30nm Barrier BB 2D	1Q	20 fs, 5000 fs	$t_2 = 0$ fs		4.5×10^{10}	850	6	Co-linear	6.6
	0Q	$t_1 = 0$ fs	30 fs, 5010 fs		4.5×10^{10}	850	6	Co-linear	6.7
	2Q	$t_1 = 0$ fs		15 fs, 3000 fs	4.5×10^{10}	850	6	Co-linear	6.7
30nm Barrier BB 3D	1Q	20 fs, 5000 fs	30 fs, 5010 fs		4.5×10^{10}	850	6	Co-linear	6.8, 6.9
10nm Barrier BB 2D	1Q	30 fs, 5010 fs	$t_2 = 0$ fs		4.5×10^{10}	812	6	Co-linear	6.11
10nm Barrier CS 3D	1Q	20 fs, 2000 fs	50 fs, 2000 fs		1.6×10^{11}	850	6	Co-linear	6.8, 6.9

Table A1.3: Experimental parameters in Ch. 6.

	Scan type	t_1 step, range	t_2 step, range	t_{2Q} step, range	Density (Photons·cm^{-2})	CF (nm)	Temp (K)	Polarization	Figure
Al_1 2D BB	1Q	25 fs, 4000 fs	$t_2 = 0$ fs		Varied	800	6	Co-linear	7.2, 7.1
Al_2 2D BB	1Q	15 fs, 2500 fs	$t_2 = 0$ fs		Varied	805	6	Co-linear	7.4, 7.3
Al_2 2D CS	1Q	15 fs, 2500 fs	$t_2 = 0$ fs		Varied	805	6	Co-linear	7.4, 7.3
	0Q	$t_1 = 0$ fs	15 fs, 2500 fs		Varied	805	6	Co-linear	7.4, 7.3
InGaAs 2D BB	1Q	25 fs, 4000 fs	$t_2 = 0$ fs		Varied	812	6	Co-linear	7.13, 7.16
InGaAs 2D BB	0Q	$t_1 = 0$ fs	25 fs, 5000 fs		Varied	812	6	Co-linear	7.13, 7.16, 7.14
InGaAs 2D BB	2Q	$t_1 = 0$ fs		15 fs, 2000 fs	Varied	812	6	Co-linear	7.13, 7.16
InGaAs 2D DQW only	2Q	$t_1 = 0$ fs		10 fs, 2000 fs	Varied	850	6	Co-circular	6.8 6.9

Table A1.4: Experimental parameters in Ch. 7.

A2

EXPERIMENT LAYOUT

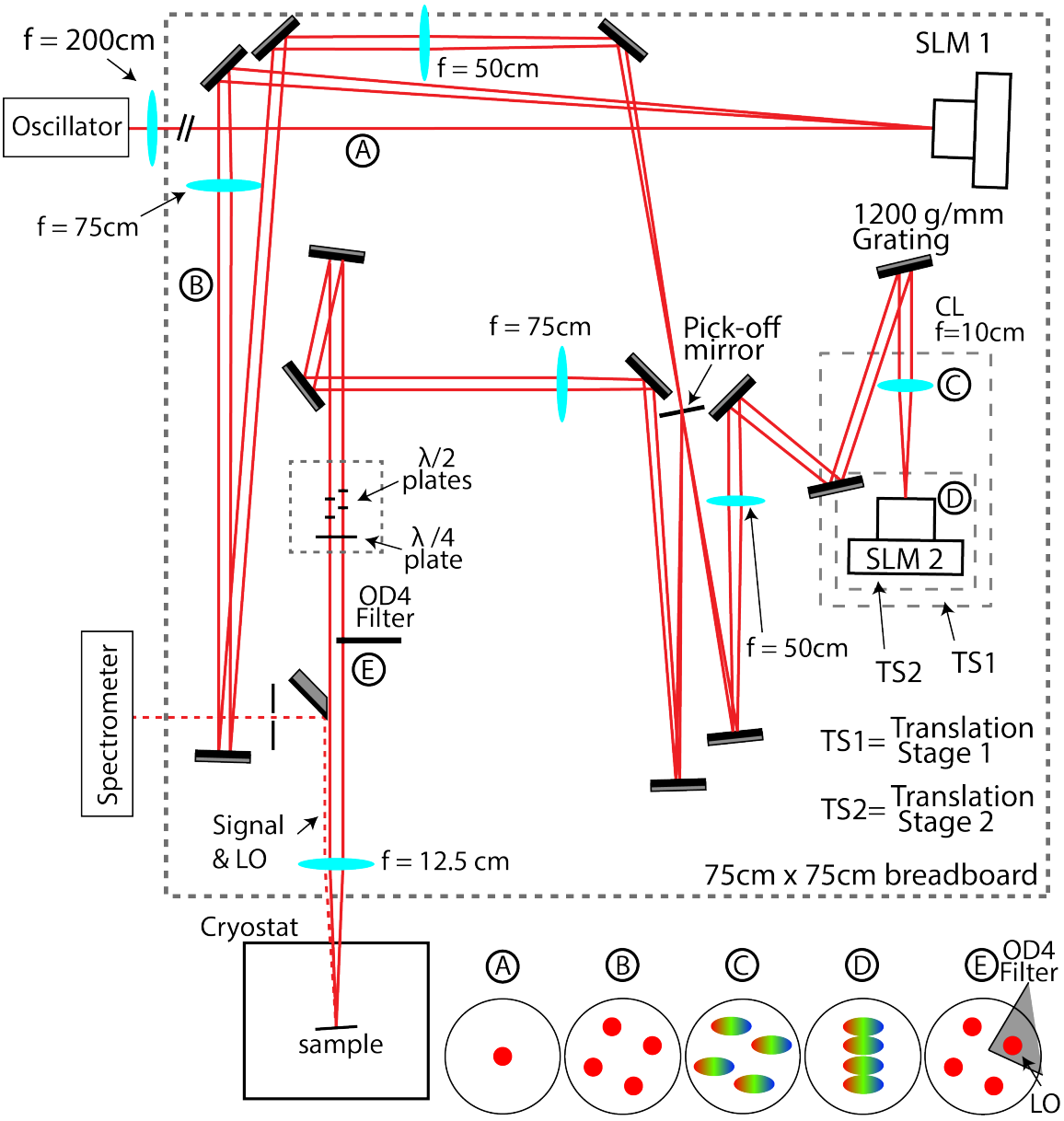

Figure A2.1: Full layout of the CMDS experiment

A3

WAVEFUNCTION CALCULATIONS

To find the allowed solutions to the 1D TISE, we use the Numerov algorithm and shooting method. A brief description of these methods are provided here, and full details of this calculation can be found in Refs. [76, 77, 182]. To calculate the wavefunction for a state S with an energy E_S we use the Numerov algorithm [306]. The Numerov algorithm is a general a method for solving differential equations of the form of the TISE. Specifically applied to the TISE, the Numerov algorithm can be used to generate the wavefunction $\psi(z)$ associated with a particular energy for a chosen potential V(z) (in this case V(z) is the DQW). Given an initial value at $\psi(z_0)$, the Numerov algorithm is used to propagate the wavefunction along z in a stepwise fashion. Each subsequent step is calculated based on the previous $\psi(z)$ and the parameters in the TISE and V(z). The Numerov method can be used to generate a wavefunction for any E, regardless of whether the resulting wavefunction is an allowed solution of the TISE.

To be an allowed solution of the TISE, ψ must be normalizable and therefore $\psi(\infty) = \psi(-\infty) = 0$. The shooting method can be used to find valid solutions to the TISE (which we will call E_S). The shooting method is an iterative process in which the Numerov algorithm is used many times. First, two wavefunctions ($\psi_{min}(z)$ and $\psi_{max}(z)$) are calculated for two energies (E_{min} and E_{max}), which are chosen such that E_{max}>E_S>E_{min}. The Numerov algorithm is used starting from z_0 (which is typically 20-50 nm into the barrier on one side of the DQW), with $\psi(z_0)$=0 and then propagated through to z_f. If the chosen energies are not allowed solutions of the TISE, then $\psi(z_f) \neq 0$. Depending on the parity and value of E_s, value of $\psi(z_f)$ will be either positive or negative (assuming E_{max}>E_S>E_{min}).

- If $\psi_s z$ has even parity, then $\psi_{max}(z_f) < 0$ and $\psi_{min}(z_f) > 0$
- If $\psi_s z$ has odd parity, then $\psi_{max}(z_f) > 0$ and $\psi_{min}(z_f) < 0$

As a result, $\psi_{max}(z_f) \cdot \psi_{min}(z_f) < 0$, regardless of the parity of $\psi_s(z)$. A third wavefunction ($\psi_{mid}(z)$) is calculated using the Numerov algorithm for an energy E_{mid}=(E_{max}-E_{mid})/2. One of three possibilities now must be true:

1. E_{max}>E_S>E_{mid}
2. E_{mid}>E_S>E_{min}
3. E_{mid}=E_S

We can determine which of the three options is true by calculating $\psi_{max}(z_f) \cdot \psi_{mid}(z_f)$ and $\psi_{mid}(z_f) \cdot \psi_{min}(z_f)$ and using the conditions above (i.e. which one is <0) to determine in which range E_s lies. If $\psi_{max}(z_f) \cdot \psi_{mid}(z_f) < 0$ (and $\psi_{mid}(z_f) \cdot \psi_{min}(z_f) > 0$), then item 1 is true and E_{mid} becomes the new E_{min}. If $\psi_{mid}(z_f) \cdot \psi_{min}(z_f) < 0$ (and $\psi_{max}(z_f) \cdot \psi_{mid}(z_f) > 0$), then item 2 is true and E_{mid} becomes

the new E_{max}. If $\psi_{max}(z_f) \cdot \psi_{mid}(z_f) = \psi_{mid}(z_f) \cdot \psi_{min}(z_f) = 0$, then item 3 is true and we have found the solution so we stop.

If $E_{mid} \neq E_s$, a new E_{mid} is defined ($E_{mid}=(E_{min} + E_{max})/2$), and the Numerov algorithm is used to calculate $\psi_{mid}(z)$, $\psi_{min}(z)$, and $\psi_{max}(z)$. This process is repeated until $\psi(z_f)=0$ (and therefore $E_{mid}=E_S$) within a given tolerance.

A4

SPECTRAL CORRECTION

To quantitatively compare the signals in CMDS spectra, the differing spectral intensity of the excitation pulses must be taken into account. This section describes how that is accomplished for the quantitative quantitative comparisons in this thesis. From Eq. 2.22 (in Section 2.1.1), we know that the amplitude of the signal from a particular pathway P in the response function ($S_P^{(3)}$) is given by:

$$\begin{aligned} P^{(3)}(\vec{r},t) = &\int_0^\infty dt_3 \int_0^\infty dt_2 \int_0^\infty dt_1 S_P^{(3)}(t_3,t_2,t_1)\cdot \\ &\mathbf{E}^{(-k_1)}(\vec{r},t-t_3)\mathbf{E}^{(k_2)}(\vec{r},t-t_3-t_2)\mathbf{E}^{(k_3)}(\vec{r},t-t_3-t_2-t_1) \end{aligned} \tag{A4.1}$$

where the pulse electric fields can be separated into a time dependent part and a time-independent amplitude ($E_0^{(k_1)}$)

$$\mathbf{E}^{(-k_1)}(\vec{r},\tau) = E_0^{(-k_1)} \cdot e^{\frac{-(\tau-\tau_{k_1})^2}{2T^2}} \cdot e^{-ik_1\vec{r}+i\omega(\tau-\tau_A)} = E_0^{(-k_1)} \cdot \bar{E}^{(-k_1)}(\vec{r},\tau) \tag{A4.2.1}$$

$$\mathbf{E}^{(k_2)}(\vec{r},\tau) = E_0^{(k_2)} \cdot e^{\frac{-(\tau-\tau_{k_2})^2}{2T^2}} \cdot e^{ik_1\vec{r}-i\omega(\tau-\tau_A)} = E_0^{(k_2)} \cdot \bar{E}^{(k_2)}(\vec{r},\tau) \tag{A4.2.2}$$

$$\mathbf{E}^{(k_3)}(\vec{r},\tau) = E_0^{(k_3)} \cdot e^{\frac{-(\tau-\tau_{k_3})^2}{2T^2}} \cdot e^{ik_1\vec{r}-i\omega(\tau-\tau_A)} = E_0^{(k_3)} \cdot \bar{E}^{(k_3)}(\vec{r},\tau) \tag{A4.2.3}$$

The electric field amplitudes can therefore be pulled out front of the integral in Eq. A4.1.

$$\begin{aligned} P^{(3)}(\vec{r},t) = &E_0^{(-k_1)}E_0^{(k_2)}E_0^{(k_3)} \int_0^\infty dt_3 \int_0^\infty dt_2 \int_0^\infty dt_1 S_P^{(3)}(t_3,t_2,t_1)\cdot \\ &\bar{E}^{(-k_1)}(\vec{r},t-t_3)\bar{E}^{(k_2)}(\vec{r},t-t_3-t_2)\bar{E}^{(k_3)}(\vec{r},t-t_3-t_2-t_1) \end{aligned} \tag{A4.3}$$

The third order polarization is therefore proportional to the product of the three electric field amplitudes:

$$P^{(3)} \propto E_0^{(-k_1)}E_0^{(k_2)}E_0^{(k_3)} \tag{A4.4}$$

The polarization is therefore proportional to the electric field amplitude at the energy of the transition involved in each interaction (ϵ_1, ϵ_2 and ϵ_3)[1].

$$P^{(3)}(\vec{r},t) \propto E_0^{(-k_1)}(\epsilon_1)E_0^{(k_2)}(\epsilon_2)E_0^{(k_3)}(\epsilon_3) \tag{A4.5}$$

The amplitude of the FWM signal from each of the different pathways is therefore proportional to the product of the amplitudes of the three electric fields at the transition energies of the three interactions. The electric field of the excitation pulse is

$$E_0(\epsilon) = \sqrt{I(\epsilon)} \tag{A4.6}$$

where $I(\epsilon)$ is the measured spectrally dependent intensity of the pulses. Combining Eq. A4.5 and Eq. A4.6 with the fact that the measured signal (E_0^{sig}) is proportional to $P^{(3)}$, we get:

$$\begin{aligned}\tilde{E}_0^{sig} &\propto E_0^{sig} \cdot E_0^{LO}(\epsilon_{sig}) \\ &\propto E_0^{(-k_1)}(\epsilon_1) \cdot E_0^{(k_2)}(\epsilon_2) \cdot E_0^{(k_3)}(\epsilon_3) \cdot E_0^{LO}(\epsilon_{sig}) \\ &\propto \sqrt{I^{(-k_1)}(\epsilon_1) \cdot I^{(k_2)}(\epsilon_2) \cdot I^{(k_3)}(\epsilon_3) \cdot I^{(LO)}(\epsilon_{sig})}\end{aligned} \tag{A4.7}$$

We can then define a factor $\eta^{(P)}$ which is the electric field contribution to the signal P:

$$\eta^{(P)} = \sqrt{I^{(-k_1)}(\epsilon_1^{(P)}) \cdot I^{(k_2)}(\epsilon_2^{(P)}) \cdot I^{(k_3)}(\epsilon_3^{(P)}) \cdot I^{(LO)}(\epsilon_{sig}^{(P)})} \tag{A4.8}$$

If we define $A^{(P)}$ as the amplitude of the signal from pathway P (assuming a flat uniform spectrum), then the measured signal amplitude ($\tilde{A}^{(P)}$) is given by

$$\tilde{A}^{(P)} = \eta^{(P)} \cdot A^{(P)} \tag{A4.9}$$

The physics that we are after is embedded in $A^{(P)}$ (which contains all of the integrals of $S_P^{(3)}$. To compare the strength of different signal pathways which for which $\eta^{(P)}$ is not identical, we need to calculate $A^{(P)}$. We can do this by dividing the measured signal amplitude by the contribution from electric amplitudes:

$$A^{(P)} = \frac{\tilde{A}^{(P)}}{\eta^{(P)}} \tag{A4.10}$$

Using Eq. A4.10 we can compare different amplitudes within the same 3D spectrum. We can also compare different 3D spectra as long as certain criteria are met:

1. The 3D spectra must be collected consecutively with no changes to the optical setup
2. The acquisition parameters (eg. CCD integration time) and delay sampling (both t_1 and t_2) must be the same for the different 3D spectra.

1 This method of incorporating the spectral dependence of the electric field amplitude is not rigorous because the spectral dependence comes from the interaction of the dipole operator with the electric field. However, this result could also be reached rigorously by considering the spectral dependence of the dipole operators as delta functions in frequency. $P^{(3)}$ can then can then be Fourier transformed along t_1, t_2 and t_3 using the Fourier sifting property [307]. This would result in a spectrally dependent electric field amplitude which can be pulled out of the integrals in Eq. A4.2.1, resulting in Eq. A4.4.

3. The excitation spectra used in both 3D spectra must be measured in such a way that they can be quantitatively compared (i.e. they must all be recorded using the same acquisition parameters).

Using the pulse shaper based CMDS experiment, these requirements can all be satisfied, so comparisons between 3D spectra can be made as long as they are made consecutively and with no changes to the optical setup.

Publications:

[1–3]

Conference Presentations:

[4–7]

References

[1] J. O. Tollerud, C. R. Hall, and J. A. Davis. Isolating quantum coherence using coherent multi-dimensional spectroscopy with spectrally shaped pulses. *Optics Express*, **22**(6): 6719–6733 (2014).

[2] C. R. Hall, J. O. Tollerud, H. M. Quiney, and J. A. Davis. Three-dimensional electronic spectroscopy of excitons in asymmetric double quantum wells. *New Journal of Physics*, **15**(4): 045,028 (2013).

[3] J. Tollerud, C. Hall, and J. Davis. Isolating quantum coherence using coherent multi-dimensional spectroscopy with spectrally shaped pulses. In K. Yamanouchi, S. Cundiff, R. de Vivie-Riedle, M. Kuwata-Gonokami, and L. DiMauro (editors), *Ultrafast Phenomena XIX*, volume 162 of *Springer Proceedings in Physics*, pp. 793–796. Springer International Publishing (2015). ISBN 978-3-319-13241-9.

[4] J. O. Tollerud, C. R. Hall, and J. A. Davis. Isolating quantum coherence in semiconductor quantum wells with pathway selective multidimensional spectroscopy. *Australian Instutute of Physics Congress*, (10 December 2014).

[5] J. O. Tollerud, C. R. Hall, and J. A. Davis. Isolating coherent coupling with pathway selective coherent multi-dimensional spectroscopy. *Australian and New Zealand Conference on Optics and Photonics*, (9 December 2013).

[6] J. O. Tollerud, C. R. Hall, and J. A. Davis. Isolating quantum coherence in semiconductor quantum wells with pathway selective multi-dimensional spectroscopy. *Nonlinear Optics and Excitation Kinetics in Semiconductors*, (25 September 2014).

[7] J. O. Tollerud, C. R. Hall, and J. A. Davis. Isolating quantum coherence in semiconductor quantum wells with pathway selective multi-dimensional spectroscopy. *Photon14*, (3 September 2014).

A5

PERMISSION TO USE COPYRIGHTED WORK

Copyright Clearance Center RightsLink® Home Account Info Help Live Chat

ACS Publications Most Trusted. Most Cited. Most Read.

Title: Coherent Two-Dimensional Optical Spectroscopy
Author: Minhaeng Cho
Publication: Chemical Reviews
Publisher: American Chemical Society
Date: Apr 1, 2008
Copyright © 2008, American Chemical Society

Logged in as:
Jonathan Tollerud
LOGOUT

PERMISSION/LICENSE IS GRANTED FOR YOUR ORDER AT NO CHARGE

This type of permission/license, instead of the standard Terms & Conditions, is sent to you because no fee is being charged for your order. Please note the following:

- Permission is granted for your request in both print and electronic formats, and translations.
- If figures and/or tables were requested, they may be adapted or used in part.
- Please print this page for your records and send a copy of it to your publisher/graduate school.
- Appropriate credit for the requested material should be given as follows: "Reprinted (adapted) with permission from (COMPLETE REFERENCE CITATION). Copyright (YEAR) American Chemical Society." Insert appropriate information in place of the capitalized words.
- One-time permission is granted only for the use specified in your request. No additional uses are granted (such as derivative works or other editions). For any other uses, please submit a new request.

If credit is given to another source for the material you requested, permission must be obtained from that source.

BACK CLOSE WINDOW

American Physical Society
License Details

Sep 27, 2015

This is an Agreement between Jonathan Tollerud ("You") and American Physical Society ("Publisher"). It consists of your order details, the terms and conditions provided by American Physical Society, and the payment instructions.

License Number	3717340731313
License date	Sep 27, 2015
Licensed content publisher	American Physical Society
Licensed content publication	Physical Review Letters
Licensed content title	Coherent Excitonic Coupling in an Asymmetric Double InGaAs Quantum Well Arises from Many-Body Effects
Licensed copyright line	© 2014 American Physical Society
Licensed content author	Gaël Nardin et al.
Licensed content date	Jan 28, 2014
Volume number	112
Type of Use	Thesis/Dissertation
Requestor type	Student
Format	Print, Electronic
Portion	chart/graph/table/figure
Number of charts/graphs/tables/figures	2
Portion description	1, 3
Rights for	Main product
Duration of use	Life of current edition
Creation of copies for the disabled	no
With minor editing privileges	no
For distribution to	Worldwide
In the following language(s)	Original language of publication
With incidental promotional use	no
The lifetime unit quantity of new product	0 to 499
The requesting person/organization is:	Jonathan Tollerud / Swinburne University
Order reference number	None
Title of your thesis / dissertation	Understanding quantum processes in semiconductors through the use of selective multidimensional spectroscopy
Expected completion date	Oct 2015
Expected size (number of	250

From: Kathryn Shaw on behalf of Permissions
To: Jonathan Tollerud
Subject: Re: Perimission Request
Date: Tuesday, 29 September 2015 5:59:56 PM

Dear Jonathan Tollerud,

Thank you for your request to reproduce IOP Publishing material in your thesis.

Regarding:

Figure (Semicond. Sci. Technol. 20 (2005) 908–911)

Figure 2 (J. Phys.: Condens. Matter 2 (1990) 1457-1474)

We are happy to grant permission for the use you request on the terms set out below.

Conditions

Non-exclusive, non-transferrable, revocable, worldwide, permission to use the material in print and electronic form will be granted **subject to the following conditions:**

- Permission will be cancelled without notice if you fail to fulfil any of the conditions of this letter.
- You will make reasonable efforts to contact the author(s) to seek consent for your intended use. Contacting one author acting expressly as authorised agent for their co-authors is acceptable.
- You will reproduce the following prominently alongside the material:
  - the source of the material, including author, article title, title of journal, volume number, issue number (if relevant), page range (or first page if this is the only information available) and date of first publication. This information can be contained in a footnote or reference note; or
  - a link back to the article (via DOI); and
  - if practical and IN ALL CASES for works published under any of the Creative Commons licences the words "© IOP Publishing. Reproduced with permission. All rights reserved""
- The material will not, without the express permission of the author(s), be used in any way which, in the opinion of IOP Publishing, could distort or alter the author(s)' original intention(s) and meaning, be prejudicial to the honour or reputation of the author(s) and/or imply endorsement by the author(s) and/or IOP Publishing.
- Payment of £0 is received in full by IOP Publishing prior to use.

Special Conditions – For STM Signatories ONLY (as agreed as part of the STM Guidelines)

Any permissions granted for a particular edition will apply also to subsequent editions and for editions in other languages, provided such editions are for the work as a whole in situ and does not involve the separate exploitation of the permitted illustrations or excerpts.

If you have any questions, please feel free to contact our Permissions team at permissions@iop.org.

I should be grateful if you would acknowledge receipt of this email.

Kind regards,

Kathryn Shaw

From: pubscopyright
To: Jonathan Tollerud
Subject: RE: Copyright Permissions request
Date: Tuesday, 29 September 2015 4:32:11 AM

Dear Dr. Tollerud,

Thank you for contacting The Optical Society.

OSA considers your requested use of its copyrighted material to be Fair Use under United States Copyright Law. It is requested that a complete citation of the original material be included in any publication.

Let me know if you have any questions.

Kind Regards,

Susannah Lehman

Susannah Lehman
September 28, 2015
Authorized Agent, The Optical Society

From: Jonathan Tollerud [mailto:jtollerud@swin.edu.au]
Sent: Sunday, September 27, 2015 8:22 PM
To: pubscopyright
Subject: Copyright Permissions request

Hello,

I would like to request permission to use a figure in my PhD Thesis:

"Understanding quantum processes in semiconductors through the use of selective multidimensional spectroscopy"
To be published in print and online, but not for a fee

I would like to use:

Figure 1

From:
J. Vaughan, T. Hornung, T. Feurer, and K. Nelson, "Diffraction-based femtosecond pulse shaping with a two-dimensional spatial light modulator," Opt. Lett. 30, 323-325 (2005).

https://www.osapublishing.org/ol/abstract.cfm?uri=ol-30-3-323

Best Regards,

From: Joshua Vaughan
To: Jonathan Tollerud
Subject: Re: Perimission to Re-use a figure in my PhD Thesis
Date: Monday, 28 September 2015 10:56:42 AM

Dear Jonathan,

fine by me as long as you cite the source. I hope the chapter was helpful and I wish you good luck with your defense!

Best regards,
Josh

On Sun, Sep 27, 2015 at 5:42 PM, Jonathan Tollerud <jtollerud@swin.edu.au> wrote:

> Dear Professor Vaughan,
>
> I would like to request permission to use two figures from the chapter you wrote for Rick Trebino's online ultrafast textbook in my PhD thesis:
>
> "Understanding quantum processes in semiconductors through the use of selective multidimensional spectroscopy"
>
> Specifically I would like to use Fig. 1 and Fig. 5.
>
> Best Regards,
>
> Jonathan Tollerud
>
> Swinburne University of Technology

--
Joshua C. Vaughan
Assistant Professor
Department of Chemistry
Box 351700
University of Washington
Seattle, WA 98195
206-543-4644

Copyright Clearance Center RightsLink® Home | Create Account | Help | Live Chat

ACS Publications Most Trusted. Most Cited. Most Read.

Title: A novel approach for sequential assignment of proton, carbon-13, and nitrogen-15 spectra of larger proteins: heteronuclear triple-resonance three-dimensional NMR spectroscopy. Application to calmodulin

Author: Mitsuhiko Ikura, Lewis E. Kay, Ad Bax

Publication: Biochemistry

Publisher: American Chemical Society

Date: May 1, 1990

LOGIN
If you're a copyright.com user, you can login to RightsLink using your copyright.com credentials. Already a RightsLink user or want to learn more?

PERMISSION/LICENSE IS GRANTED FOR YOUR ORDER AT NO CHARGE

This type of permission/license, instead of the standard Terms & Conditions, is sent to you because no fee is being charged for your order. Please note the following:

- Permission is granted for your request in both print and electronic formats, and translations.
- If figures and/or tables were requested, they may be adapted or used in part.
- Please print this page for your records and send a copy of it to your publisher/graduate school.
- Appropriate credit for the requested material should be given as follows: "Reprinted (adapted) with permission from (COMPLETE REFERENCE CITATION). Copyright (YEAR) American Chemical Society." Insert appropriate information in place of the capitalized words.
- One-time permission is granted only for the use specified in your request. No additional uses are granted (such as derivative works or other editions). For any other uses, please submit a new request.

If credit is given to another source for the material you requested, permission must be obtained from that source.

BACK CLOSE WINDOW